Nanoscale Tools for Biosensing and Treatment of Bacterial Biofilms and Eukaryotic Cells

Inaugural-Dissertation
to obtain the academic degree
Doctor rerum naturalium (Dr. rer. nat.)

submitted to the Department
of Biology, Chemistry, Pharmacy
of Freie Universität Berlin

by
Charlotte Kromer

Berlin, 2024

The experimental work for this thesis was carried out at the German Federal Institute for Risk Assessment (BfR) in Berlin from January 2020 to December 2023 under the supervision of Prof. Dr. Dr. Andreas Luch.

1st Reviewer:	Prof. Dr. Dr. Andreas Luch
2nd Reviewer:	Prof. Dr. Burkhard Kleuser

Date of defence: 22.07.2024

Declaration of Authorship

I hereby declare that I alone am responsible for the content of my doctoral dissertation and that I have only used the sources or references cited in the dissertation entitled:

“Nanoscale Tools for Sensing Cellular Functions and Treatment of Bacterial Biofilms and Eukaryotic Cells”

Berlin, 11.04.2024

Acknowledgment

I would like to express my gratitude towards the many people who have supported me during my thesis.

First of all, I would like to thank Prof. Dr. Dr. Andreas Luch for the opportunity to conduct my doctoral thesis in his department and for his support and supervision. While providing a research environment where I had the opportunity and the freedom to pursue my research independently, he was always there to offer guidance. Furthermore, I would like to thank Prof. Dr. Burkhardt Kleuser for acting as the second reviewer for this thesis.

I am extremely grateful to Dr. Harald Tschiche, without whom this work would not have been possible. He deserves endless praise for being my research supervisor, project enabler, and an endless optimist for all the projects we concurred. I thank him for always being there for me to discuss my research, day and night, in the office, and from home. He shared his knowledge with me, challenged me, and made me laugh, even when things didn't go as planned.

A special thanks also goes out to my cooperation partners at BAM. Dr. Karin Schwibbert has always supported me with scientific ideas, motivation, and the opportunity to carry out endless experiments in their laboratories. Dorothea Thiele was a fantastic technical support and documented everything with a precision that any observation team could learn from.

Dr. Sebastian Radunz also supported me with ideas and also spent many hours in the lab cooking up nanoparticles.
I am grateful to Aaron Katz, not only for his technical assistance, but also for sharing his knowledge, proofreading several manuscripts, and always helping us with his great programming skills.

I would also like to thank Dr. Nina Glaser, who supervised me during my training as an expert pharmacist for toxicology and ecology.

A big thank you goes to all my dear colleagues at the BfR, especially Aline Rosin, Maya Kissner, Philipp Reichard, Dr. Thomas Tietz, Dr. Lukas Patalag, and Dr. Gregor Nagel as well as former colleagues Dr. Fabian Kriegel, Dr. Benjamin Krause, and Yves Hachenberger for moral support, good advice, but also for many coffee breaks with good conversations and jokes, and the one or other drink that was enjoyed even without an occasion.

However, the biggest and most positive influence on my time at the BfR were my two colleagues and now some of my best friends, Dr. Franziska Riedel and Konstantin Simon. They have made every day at the BfR and outside better and brighter, motivated me, and were always there for me. I hope to keep you for many years to come.

I would like to thank my partner Markus Bimüller from the bottom of my heart. He is always there for me, motivating me, making me laugh, but also taking care of me. He is the best thing that has ever happened to me.

Finally, I would like to thank my parents for always supporting and encouraging me in everything I do. I have learnt a lot from you, maybe everything. You have shaped the person I am today and for that I am forever grateful.

Thank you all for making this possible!

Table of Contents

Zusammenfassung

Nanopartikel sind aufgrund ihrer geringen Größe und ihrer physikalisch-chemischen Eigenschaften ideal für die Herstellung von Diagnostika und als Wirkstoffträger für therapeutische Ansätze. Sie bieten Funktionen, die viele konventionelle Ansätze nicht bieten können. Dazu gehören die hochauflösende Bildgebung mit Nanosensoren, die verbesserte Bioverfügbarkeit von nanopartikulären Formulierungen für therapeutische Wirkstoffe und die Möglichkeit, Substanzen gezielt an den Wirkort zu bringen. Insbesondere polymere Nanopartikel können leicht strukturell modifiziert werden, um bestimmte Eigenschaften maßzuschneidern. Aus ihnen können eine Vielzahl funktioneller Nanopartikel für unterschiedlichste Anwendungen gefertigt werden. Im Rahmen dieser Dissertation wurden drei Studien durchgeführt, in denen die vielfältigen Einsatzmöglichkeiten von Polystyrol-Nanopartikeln als Nanosensoren für die Biosensorik in Biofilmen und eukaryotischen Zellen sowie als Nanocarrier für die Behandlung pathogener Biofilme aufzeigt werden.

In der ersten Studie wurde ein pH-Nanosensor auf Basis von biokompatiblen Polystyrol-Nanopartikeln für die Messung und bildliche Darstellung des pH-Werts in Biofilmen entwickelt. Der Nanosensor nutzt ein ratiometrisches Prinzip zur pH-Wert Bestimmung, basierend auf den Fluoreszenz-Intensitätsverhältnissen des pH-unempfindlichen Farbstoffs Nilrot und des pH-empfindlichen Farbstoffs Fluorescein-Isothiocyanat (FITC). Die Bestimmung der Fluoreszenzen erfolgt mittels konfokaler mikroskopischer Bildgebung. Damit ist es möglich, den pH-Wert sowohl dreidimensional als auch über lange Zeiträume zu messen und abzubilden, z.B. um dynamische Prozesse in Biofilmen genauer zu untersuchen. In der Studie wurde die Funktionalität des pH Nanosensors an einem Anwendungsbeispiel demonstriert, bei dem die zeitabhängigen pH-Änderungen, die durch die Stoffwechselaktivität von *Escherichia coli* Biofilmen ausgelöst werden, abgebildet wurden. Die Anwendung des Nanosensors ist unkompliziert, es wird kein besonderes Equipment benötigt und trotzdem sind die Messungen sehr genau und der Sensor robust. Dies ist unter anderem auf das durchdachte Designkonzept des Sensors mit seinem ratiometrischen Messprinzip zurückzuführen und macht ihn zu einem wertvollen Werkzeug für die Charakterisierung der chemischen Mikroumgebung von Biofilmen. Der pH-Nanosensor kann dazu beitragen, die Dynamik von Biofilmen besser zu verstehen und die Entwicklung verbesserter Strategien zur Bekämpfung von durch Biofilme verursachten Gesundheitsproblemen zu ermöglichen.

In der zweiten Studie wurde ein Nanosensor für die Bestimmung des extrazellulären pH-Werts und der extrazellulären pH-Mikroumgebung von eukaryotischen Zellen beschrieben. Dieser funktioniert nach dem gleichen Prinzip wie der Sensor der ersten Studie, doch eine entscheidende Weiterentwicklung ermöglicht die Messung des pH-Wertes direkt auf der Zelloberfläche. Der Nanosensor ist mit einem Lektin konjugiert, welches an die Zellmembran bindet und den Nanosensor dort verankert. Dadurch wird die präzise und räumlich aufgelöste Messung des extrazellulären pH-Werts an der Zelloberfläche einzelner Zellen ermöglicht. Die Studie zeigt die Vielseitigkeit und Kompatibilität dieses pH Nanosensors mit verschiedenen Zelllinien aus unterschiedlichen Organen in Verbindung mit einem effektiven Targeting. Dieser Nanosensor hat großes Potenzial für die Erforschung der extrazellulären Mikroumgebung und für ein tieferes Verständnis von zellulären Prozessen eingesetzt zu werden. Die Anwendungen des Nanosensors finden sich in der biomedizinischen Forschung, wie beispielsweise in der Krebsforschung oder zur Untersuchung von Stoffwechselstörungen sowie für diagnostische oder therapeutische Zwecke.

In der dritten Studie wurde ein neuartiges Tool zur Eradikation von Biofilmen mittels photodynamischer Therapie entwickelt und angewendet. Polystyrol-Nanopartikel dienen als Träger, um den lipophilen Photosensibilisator (ein Bordipyrromethen-Derivat) einzubetten und zur Aktivierung am Zielort in den Biofilm zu bringen. Die Studie zeigte, dass die mit Photosensibilisator beladenen Nanopartikel hochwirksam gegen planktonische Bakterien und bakterielle Biofilme pathogener Bakterien wie *Escherichia coli*, *Staphylococcus aureus* und *Streptococcus mutans*, sind. Darüber hinaus wurden in der Studie die Wechselwirkungen der Nanopartikel mit den Biofilmen charakterisiert, um das Wissen über die Wirkmechanismen der antimikrobiellen photodynamischen Therapie mit nanopartikulären Wirkstoffen gegen Biofilme zu erweitern. Die mit Photosensibilisatoren beladenen Nanopartikel haben sich als wertvolle Hilfsmittel zur Verhinderung und Vernichtung von Biofilmen erwiesen. Sie zeigten dabei eine höhere Wirksamkeit als viele Systeme aus bereits publizierten Studien zur antimikrobiellen photodynamischen Therapie, sowohl mit als auch ohne Nanopartikel. Damit besitzen sie ein großes Potenzial als wirksames Mittel im Kampf gegen Biofilme eingesetzt zu werden. Sie stellen eine praktische und unkomplizierte Alternative zu bestehenden Methoden dar und haben gleichzeitig ein deutlich geringeres Risiko, zur Entwicklung bakterieller Resistenzen beizutragen.

Zusammenfassend zeigen die drei Studien das Potenzial von polymeren Nanopartikeln als Träger für eine wirksame antimikrobielle Behandlung und als Sensoren, die z.B. wertvolle Einblicke in die Mikroumgebung von Biofilmen ermöglichen. Weiterhin ermöglichen diese Sensoren präzise extrazelluläre pH-Messungen in verschiedenen Zelllinien. Diese Fortschritte sind vielversprechend für künftige Forschungen und Anwendungen in Bereichen, die von der Charakterisierung von Biofilmen bis zur biomedizinischen Forschung und antimikrobiellen Therapie reichen.

Abstract

Nanoparticles are well-suited for developing diagnostic and therapeutic tools due to their small size and favorable physicochemical properties. They provide unique features that many conventional approaches cannot, such as high-resolution imaging utilizing nanosensors, improved bioavailability of nanoformulated therapeutics, and targeted delivery. Polymeric nanoparticles can be easily structurally modified to tailor specific properties, making them suitable for a wide range of applications. Three studies were carried out as part of this thesis, demonstrating the diverse applications of polystyrene nanoparticles as nanosensors for biosensing in biofilms and eukaryotic cells, and as nanocarriers for the treatment of pathogenic biofilms.

In the first study, a pH nanosensor based on biocompatible polystyrene nanoparticles was developed to determine and visualize the pH in biofilms. The nanosensor employs a ratiometric principle to determine pH, based on the fluorescence intensity ratio of the pH-insensitive dye nile red and the pH-sensitive dye fluorescein isothiocyanate (FITC). The fluorescence is acquired by confocal laser scanning microscopy. This method allows for three-dimensional measurement of pH over extended time periods, enabling detailed studies of dynamic processes in biofilms. The study demonstrated the functionality of the pH nanosensor by imaging the time-dependent pH changes induced by the metabolic activity of *Escherichia coli* biofilms. The nanosensor is easy to use, no special equipment is required, yet the measurements are precise, and the sensor is very robust. This is achieved by the smart design concept with its ratiometric working principle, making it a valuable tool for characterizing the chemical microenvironment of biofilms. The pH nanosensor can improve the understanding of biofilm dynamics and enable the development of improved strategies to combat biofilm-associated health problems in industry and for clinical settings.

The second study describes a nanosensor for the determination of extracellular pH and the extracellular pH microenvironment of eukaryotic cells. The nanosensor operates on the same principle as the sensor in the first study, but a significant addition enables the direct measurement of pH at the cell surface. The nanosensor is conjugated to a lectin, which binds to the cell membrane and anchors the nanosensor to the cell surface. This method enables a precise and spatially resolved measurement of extracellular pH at the cell surface of individual cells. The study demonstrates the versatility and compatibility of this pH nanosensor with

different cell lines from various organs, combined with effective targeting. It has great potential for studying the cellular microenvironment and gaining a deeper understanding of cellular processes based on these microenvironments. Its applications are found in biomedical research, particularly in cancer research, for understanding and studying metabolic disorders, and for diagnostic or therapeutic purposes.

In the third study, a novel tool for the photodynamic eradication of biofilms was developed and applied. Polystyrene nanoparticles were used as carriers to embed the lipophilic photosensitizer (a boron-dipyrromethene derivative) and deliver it to the biofilm for activation at the target site. The study demonstrated that the photosensitizer-loaded nanoparticles were highly effective against planktonic bacteria and bacterial biofilms of pathogenic bacteria such as *Escherichia coli*, *Staphylococcus aureus*, and *Streptococcus mutans*. Furthermore, the study aimed to characterize the interactions between nanoparticles and biofilms to enhance the understanding of the mechanisms behind antimicrobial photodynamic therapy using nanoscale treatment agents against biofilms. The photosensitizer-loaded nanoparticles were found to be a highly effective tool in the prevention and removal of biofilms. They showed even higher efficacy than many tools in previously published studies about antimicrobial photodynamic therapy, both with and without nanoparticles. The nanoparticles presented in this study have great potential to be used as effective tools in the fight against biofilms. They offer a practical and straightforward alternative to existing methods, with a lower risk of bacterial resistance developing in the future.

In summary, these studies highlight the potential of polymeric nanoparticles as carriers for effective antimicrobial treatment and as sensors for providing valuable insights into biofilm microenvironments. Furthermore, they enable precise extracellular pH measurements in diverse cell lines. These advancements hold promise for future research and applications in fields ranging from biofilm characterization to biomedical research and antimicrobial therapy.

Abbreviations

aPDT	antimicrobial photodynamic therapy
BODIPY	boron-dipyrromethene
DLS	dynamic light scattering
EPR	Enhanced Permeability and Retention
EPS	extracellular polymeric substances
FITC	fluorescein isothiocyanate
MIC	microbially induced corrosion
NPs	nanoparticles
NR	nile red
PDT	photodynamic therapy
PEG	polyethylene glycol
pH_e	extracellular pH
pH_i	intracellular pH
PS	polystyrene
PTS	photosensitizers
QS	quorum sensing
ROS	reactive oxygen species
SEM	scanning electron microscopy
UV	ultraviolet light
WGA	wheat germ agglutinin
WHO	World health organization

1. Introduction

1.1. Nanosensors for biosensing

A biosensor is an analytical tool that detects, monitors, or quantifies a biological component, biological molecule, or biochemical reaction in or produced by a biological system. Biosensors have been developed for a wide range of biological systems, including eukaryotic cells, tissues, fungi, bacteria, and biofilms, for both *in vitro* and *in vivo* applications. They have proven to be highly valuable in many areas including the medical field, pharmaceutics, biotechnology, food safety, environmental monitoring, and forensics [1,2].

Biosensors on the nanoscale are often referred to as nanobiosensors or short nanosensors and will be the topic of the following chapter of this work. They are often fabricated from nanoparticles (NPs). The materials used to produce nanosensors are diverse, including biological and synthetic polymers, metals, metal oxides, carbon, and many others, depending on the requirements of the application [3]. Some sensors consist of a single material, while others are composed of a mixture of materials. The core-shell nanosensor is a widely used design, where the core of the particle is made of one material and the shell is made of another. This design can improve the interaction with the analyte and allows for the combination and fine-tuning of various material properties within a single sensor or particle [4].

1.1.1. Rationale for using nanoparticles

Nanomaterials are materials with at least one dimension in the nanometer scale, typically less than 100 nm. While some nanomaterials occur naturally, such as oxides, minerals, or rock abrasion, the majority of nanomaterials used in research and the production of nanosensors are man-made. The fabrication of materials and particles in nanometer size is motivated by the fact that NPs have significantly different properties compared to the same material with larger dimensions. For instance, NPs have a higher surface-to-volume ratio than their respective bulk material. This results in new material properties in chemical, physical, optical, and mechanical aspects, such as increased reactivity, as more atoms or surface groups can interact with the environment. The size-dependent properties of NPs also vary depending on their composition. Gold NPs are a good example of size-dependent reactivity and optical properties. Gold is considered chemically inert in its solid form, and in particulate form in sizes as small as the double-digit nanometer range [5]. However, gold NPs smaller than approximately 5 nm exhibit a significantly increased reactivity, and these gold NPs are even used as catalysts [6]. On top, gold NPs can have a range of colors, including red, green, blue, and brown, depending on their size and shape [7]. When metals or semiconductor NPs interact with visible or near-infrared light, quantum effects dominate the material properties and a phenomenon called surface plasmon resonance occurs [8]. The plasmon oscillation generates strong electromagnetic fields at the particle surface. These surface plasmons can decay by photon emission resulting in the colored appearance of the NPs. Other types of NPs that use size-dependent photoemission are quantum dots, which exhibit size-dependent light absorption. Due to their distinctive optical properties, they are utilized in the production of displays and solar cells. Unfortunately, many inorganic NPs, including quantum dots, are toxic in biological systems, which limits their use in medical and diagnostic applications [9]. Figure 1 displays various classes of NPs, along with examples, advantages, and limitations of their use.

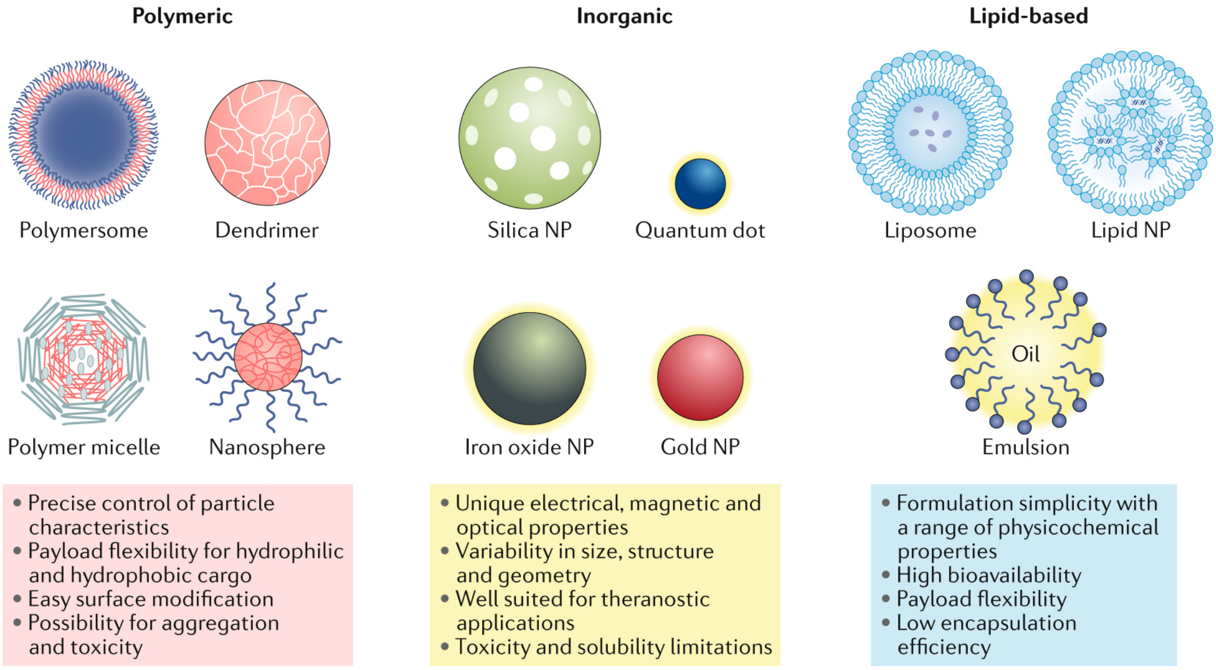

- Precise control of particle characteristics
- Payload flexibility for hydrophilic and hydrophobic cargo
- Easy surface modification
- Possibility for aggregation and toxicity

- Unique electrical, magnetic and optical properties
- Variability in size, structure and geometry
- Well suited for theranostic applications
- Toxicity and solubility limitations

- Formulation simplicity with a range of physicochemical properties
- High bioavailability
- Payload flexibility
- Low encapsulation efficiency

Figure 1. Common classes and subclasses of nanoparticles (NP) with some of the main advantages and disadvantages regarding cargo, delivery, and biological response. Reprinted with permission from reference [10]. Copyright by Springer Nature 2021.

Polymeric NPs, such as dendrimers or nanospheres, are a promising alternative for diagnostic use, as they can be labelled with dyes and used for imaging. Polymer particles have the potential to be used as drug delivery vehicles. However, not all types of polymers are biocompatible. Lipid-based NPs, such as liposomes or solid lipid NPs, are a better option due to their good biocompatibility. However, they have limitations in terms of the amount and type of cargo.

When utilizing nanomaterials, especially in biochemical research and the medical field, it is important to consider that most biological processes occur on the nanoscale. As a result, NPs interact differently with cells and cellular processes. This enables the optimization of interactions between NPs and biological targets, such as receptors, enzymes, or cells, leading to the development of new strategies for therapy and diagnosis. However, it is important to note that this increased interaction can cause the toxicological properties of NPs to differ significantly from those of larger particles. In addition, when NPs are exposed to biological fluids, particles generate a dynamic layer of biomolecules, mainly proteins, known as the protein corona [11]. The protein corona can impact the interaction of NPs with their surroundings and, consequently, their toxicity [12]. The protein corona's composition varies depending on the protein composition of the biological fluid. This variability makes it a complex task to evaluate the impact of the protein corona on NPs toxicity. Consequently, regulatory efforts aimed at evaluating the hazard posed by NPs should incorporate comprehensive assessments that account for the distinct toxicological properties arising from the size in the nanoscale.

1.1.2. Benefits of polystyrene nanoparticles

Polystyrene (PS) is a synthetic polymer composed of styrene monomers. Its applications are numerous. In its foamed form, it is commonly used as a packaging material and for thermal insulation. In its solid form, it is used as a disposable product in laboratory equipment and for the fabrication of NPs. In the following section, the specific properties of PS NPs and the resulting potential applications are discussed in detail.

PS NPs can be easily synthesized and are also commercially available in a broad size range, from several nanometers to large PS spheres in the micron range. They are known for their excellent size uniformity and narrow particle size distribution, which is achieved through controlled synthesis methods during manufacturing. Modern synthesis methods for PS NPs are emulsion polymerization and controlled radical polymerization techniques like atom transfer radical polymerization or reversible addition-fragmentation chain transfer [13]. Furthermore, the use of monodisperse initiators for polymerization can propagate to the growing polymer chains, resulting in NPs with a narrow size distribution. A narrow size distribution is an important factor for maintaining suspension stability, as phenomena such as agglomeration are minimized. The use of stabilizing agents or surfactants in the synthesis of NPs also helps to prevent agglomeration and aggregation of the particles.

PS NPs mostly possess a spherical morphology, irrespective of their size, a trait ascribed to the influence of surface tension during their synthesis through precipitation (Figure 2). The customization of PS NPs into non-spherical shapes, such as discs, rods, golf balls, or fiber-like structures, is feasible, catering to specific application requirements [14]. The morphology of NPs plays a critical role for biological interactions, impacting cellular uptake, as well as degradation processes [15-17].

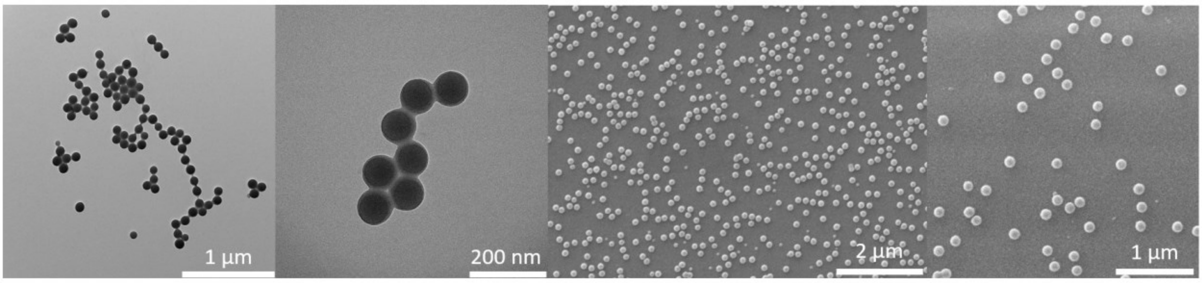

Figure 2. Transmission electron microscopy (left) and scanning electron microscopy images (right) of polystyrene nanoparticles displaying the uniform size and shape morphology.

The stability of NP suspensions is influenced by several factors, including van der Waals forces, Coulomb forces, and the distance between neighboring NPs (which is concentration dependent). When attractive forces dominate, NPs tend to agglomerate or aggregate, whereas a predominance of repulsive forces leads to stabilization. There are several methods of stabilizing NPs, such as electrostatic or steric repulsion. To enhance electrostatic repulsion, charged surface groups can be introduced to NPs trough covalent binding or adsorption. When neighboring NPs share the same surface charge, repulsion is induced, leading to stabilization of the NPs. Zeta potential is a measure of the surface charge of NPs, with values above +30 mV or below −30 mV considered indicative of high colloidal stability. Steric repulsion is achieved by attaching long chain polymers to the NPs to increase the distance between the particles. Electrosteric stabilization, which combines both electrostatic and steric effects, can also be used to stabilize NP dispersions [18].

One advantage of using synthetic polymers such as PS NPs is the wide range of options for equipping the NPs with functional groups. The properties of the particles such as colloidal stability (aggregation tendency), reactivity, biocompatibility, biodistribution, and pharmacodynamics can be influenced by the type and quantity of functional groups. In addition, the surface groups are the primary point of interaction between the particles and their environment. The terminal surface functionalities on the NPs, formed by co-polymerization of a monomer, act as anchoring points for subsequent surface functionalizations.

The most commonly used groups for surface functionalization of PS NPs are carboxyl and amino groups. Carboxyl groups turn the surface of the particles hydrophilic, resulting in excellent particle suspendability in water. This is particularly beneficial for application in biological systems, which are typically aqueous. In addition, the carboxyl groups give the NPs a negative zeta potential at neutral pH, which can be beneficial for the suspension stability. Carboxyl groups can also be utilized to conjugate other biomolecules to adapt the function of the particles. For the conjugation, the carboxyl groups must first be activated as they have a very low reactivity. A carbodiimide, such as 1-ethyl-3-(3-dimethylaminopropyl)carbodiimide, is typically used to convert the carboxyl group into an active ester. The resulting active ester can then react with the amino groups of the conjugation partner through an addition-elimination reaction to form an amide [19]. Dye molecules can be conjugated to create colored or fluorescent particles, which can be used for imaging or colorimetric quantification. Additionally, biomolecules such as proteins or antibodies can be conjugated for targeting purposes.

Another common surface functionalization for PS NPs are amino groups, which result in the particles having a positive zeta potential at a neutral pH value. Biomolecules, small molecules, or dyes containing amino-reactive groups can be conjugated to the particle’s amino groups, e.g. via addition-elimination reactions. Dyes commonly used for this type of conjugation are fluorescein isothiocyanate (FITC), Texas Red (with a sulfonyl chloride group) or 5-TAMRA-SE (with a succinimidyl ester group). Amino groups at the surface of PS NPs are most often synthesized from carboxyl groups through conjugation of a diamino compound resulting in a mixture of both surface groups instead of a pure amino group functionalization.

PS NPs can be functionalized with various other surface groups, such as thiol, aldehyde, maleimide, epoxide, azide, and vinyl groups. These groups can expand the range of conjugation partners that can be coupled using other conjugation reactions, such as click reactions with e.g. cyclooctyne derivatives reacting with azide groups.

The toxicity of PS NPs is relatively low compared to other polymeric NPs due to the inertness of PS as a material [20-22]. Therefore, the toxicity and biocompatibility of PS NPs are primarily determined by the surface chemistry, specifically the type and number of functional groups. The surface groups are crucial for biocompatibility and toxicity as they are the first point of interaction with the biological environment. The presence of free reactive groups on the NPs, such as those with a high cationic surface charge, can result in cytotoxicity. Numerous studies have demonstrated that a positive surface charge is linked to higher toxicity of PS NPs in comparison to neutral or negatively charged PS NPs [23-25]. Positively charged NPs interact more effectively with cell membranes. This is due to attractive electrostatic interactions with negatively charged phospholipids or membrane proteins. As a result, non-phagocytic cells can more easily take up NPs, which plays a critical role for toxicity [26,27]. In addition, due to the increased membrane interactions of cationic PS particles, cell membrane ruptures can occur, leading to cell death [21]. This relationship between cationic surface charge and increased toxicity is also observed in other types of NPs, including carbon nanotubes, silica NPs, and liposomes [28,29]. Additionally, surface groups with a highly hydrophobic character can interact more strongly with cell membranes, potentially leading to membrane disruption [27]. When assessing the toxicity of NPs for bacteria, the particle’s surface charge and hydrophilicity are the predominant factors to be considered. In addition, it should be noted that bacteria are not able to actively take up NPs in a size-dependent manner. Neutral and negatively charged PS NPs are generally considered non-toxic and non-inflammatory, making them suitable carriers for *in vitro* cell studies [30,31].

In summary, PS NPs are very versatile and can be easily and effectively structurally customized for various purposes. Most PS NPs exhibit a narrow particle size distribution and good biocompatibility. The possibility to easily load and conjugate PS NPs with different molecules such as dyes, drug molecules or targeting moieties make them a universally applicable platform for nanoscale tools for diverse applications.

1.1.3. Fluorescent nanoparticles as biosensors

Polymeric NPs are often used as nanosensors. Nanosensors are typically classified based on the stimuli they respond to, i.e. chemical stimuli (elements and molecules like glucose, lactate, oxygen or protons), biological stimuli (pathogens, enzymes, DNA), mechanical stimuli (position, force, pressure), optical stimuli (absorbance, fluorescence, refractive index), thermal stimuli (temperature), electrical stimuli (charge, potential), or magnetic stimuli (magnetic fields) [3,32]. Classification of nanosensors by the readout parameters is also common and the main categories are electrochemical, optical, piezoelectric, and thermometric readout [33]. This works focus is on optical nanosensors, more specifically on fluorescent nanosensors. These sensors are based on the readout of fluorescence signals, either after excitation of a fluorescent dye or by the inherent fluorescence of a sensor. The molecules absorb photons and undergo transition to an excited state. Upon returning to their ground state, they emit fluorescence at a characteristic wavelength. Fluorescence can be detected sensitively using instruments such as spectrometers and microscopes. The response to a stimulus can be measured by changes in fluorescence intensity or the shift in the wavelength of the fluorescence maximum. Commonly used fluorescent sensor dyes e.g., for measuring pH via fluorescence are fluorescein-based dyes, seminaphthorhodafluors (SNARF), naphthalimide dyes or rhodamine dyes [34,35].

Single-wavelength intensity-based probes are commonly used for sensing due to their simple instrumentation and operation [36]. However, the accuracy of their determination is often compromised by fluctuations in excitation light intensity, variations in dye concentration, and interference from other potential stimuli, such as high salt concentrations [34]. Ratiometric fluorescence sensors effectively overcome many limitations of the single-wavelength intensity-based sensors [37-39]. Ratiometric sensors measure the fluorescence intensity of an analyte-sensitive sensor dye and an analyte-insensitive reference dye simultaneously. The analyte value is then derived from the ratio of these two intensities. The advantage of this method is that the ratio is not affected by variations in dye concentration and excitation light intensity, making it a more accurate and robust measurement system.

To fabricate a ratiometric sensor, the sensor and reference dye can be incorporated into the same NP. When both dyes are embedded in the NP, a permeable NP matrix is required for the target analyte. Therefore, most ratiometric nanosensors embed the reference dye in the NP core and conjugate the sensor dye to the functional groups on the particles surface. The previous section 1.1.2. discussed the possibilities of dye conjugation to PS NPs. Various techniques can be used to embed dyes in polymer NPs, which are typically divided into polymerization-based strategies and strategies based on preformed polymers [40]. Polymerization-based strategies can involve chemical conjugation of the dyes to the monomers before polymerization, resulting in polymer particles with covalently bound dyes [41]. Techniques that employ preformed polymers can use one-step swelling procedures [42]. These one-step swelling procedures are both simple and effective and involve swelling the PS NPs in organic solvents, such as tetrahydrofuran, before adding a dye solution [43]. Once the dye has diffused into the swollen particles, the solvent is removed, and the NPs are deswollen in water, embedding the dye in the polymer structure. This technique is particularly advantageous for lipophilic dyes such as nile red (NR) or rhodamines, as their low affinity for water prevents leakage of the NPs in aqueous media.

Numerous fluorescent ratiometric nanosensors are used for various applications, such as nanosensors based on polymer or silica NPs labelled with stimuli-responsive sensor dyes. The benefits of such systems include enhanced brightness due to the incorporation of a large number of fluorophores into a particle as well as improved photostability [44,45]. Another advantage of NPs loaded with fluorescent dyes is the opportunity to easily customize them to suit the application’s requirements. Therefore, several sensing dyes for different analytes could also be incorporated in the same particle if they have spectrally discriminable fluorescence signals [46,47]. This characteristic facilitates multiplexing, wherein multiple dyes can be simultaneously detected in a single assay [48,49].

Fluorescent NPs have emerged as powerful biosensors due to their ability to enable three-dimensional imaging, their robustness, ease of fabrication and modification, and uncomplicated readout with standard laboratory equipment. The use of various types of NPs and fluorescent dyes provides flexibility in developing biosensor tools that are tailored to specific applications. However, it is important to ensure that biosensors do not interfere with the biological system under investigation. This is particularly important as it can lead to biased results or even render the measurement impossible. Therefore, a nanosensor system must be specifically designed and tested for use in a particular biological system. The following sections describe nanosensors for the application in two different biological systems, namely bacterial biofilms and eukaryotic cells.

1.1.4. Bacterial biofilms

Biofilms are communities of microorganisms that adhere to surfaces and are surrounded by a self-produced matrix. This matrix consists mainly of water and extracellular polymeric substances (EPS) such as polysaccharides, proteins, DNA and lipids [50]. The EPS matrix is vital in enhancing the resistance of biofilms to external influences, such as changes in temperature, desiccation, shear forces, and disinfection [51]. This is attributed to its role in fostering biofilm development, providing structural stability, and creating a diffusion barrier. In addition, it forms a reservoir for nutrients and allows the microorganisms to establish long-term synergistic interactions and to disperse further [52,53] (Figure 3).

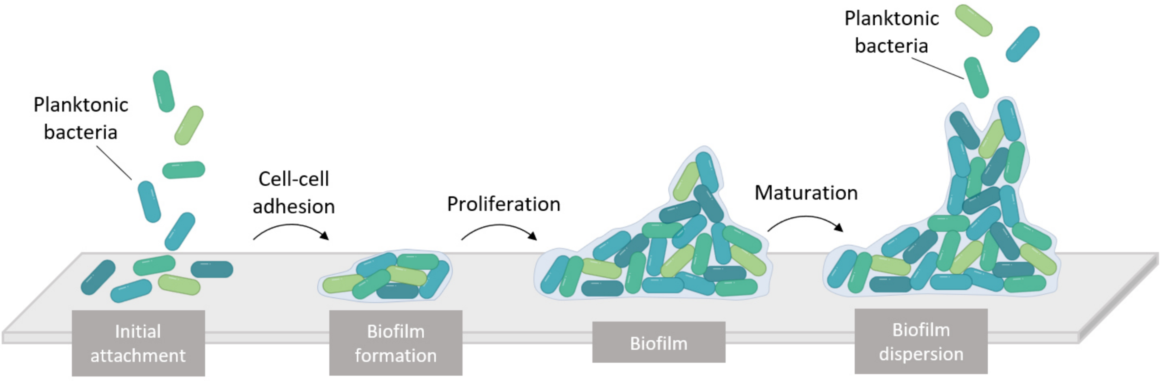

Figure 3. The phases of biofilm development and biofilm dispersion, starting with the adhesion of planktonic bacterial cells to a surface and to each other. The bacteria proliferate, the EPS matrix is produced, and the bacterial population matures to form a biofilm. The biofilm can disperse when bacteria detach and move as planktonic bacteria in the medium, adhering to new surfaces to repeat the cycle.

Bacterial species with the ability to form biofilms pose a significant challenge to various sectors including healthcare, the food industry, the marine industry as well as water treatment facilities (Figure 4). Biofilm formation shields and protects bacteria from typical cleaning agents such as soaps, alcohols, and other disinfectants, allowing them to persist even after cleaning. In the food industry, persistent bacteria colonize the interior of mixing tanks, drums, and hoses, thereby compromising the quality and safety of food. Biofilms on medical equipment may pose an even greater risk and are discussed in detail in section 1.2.1.

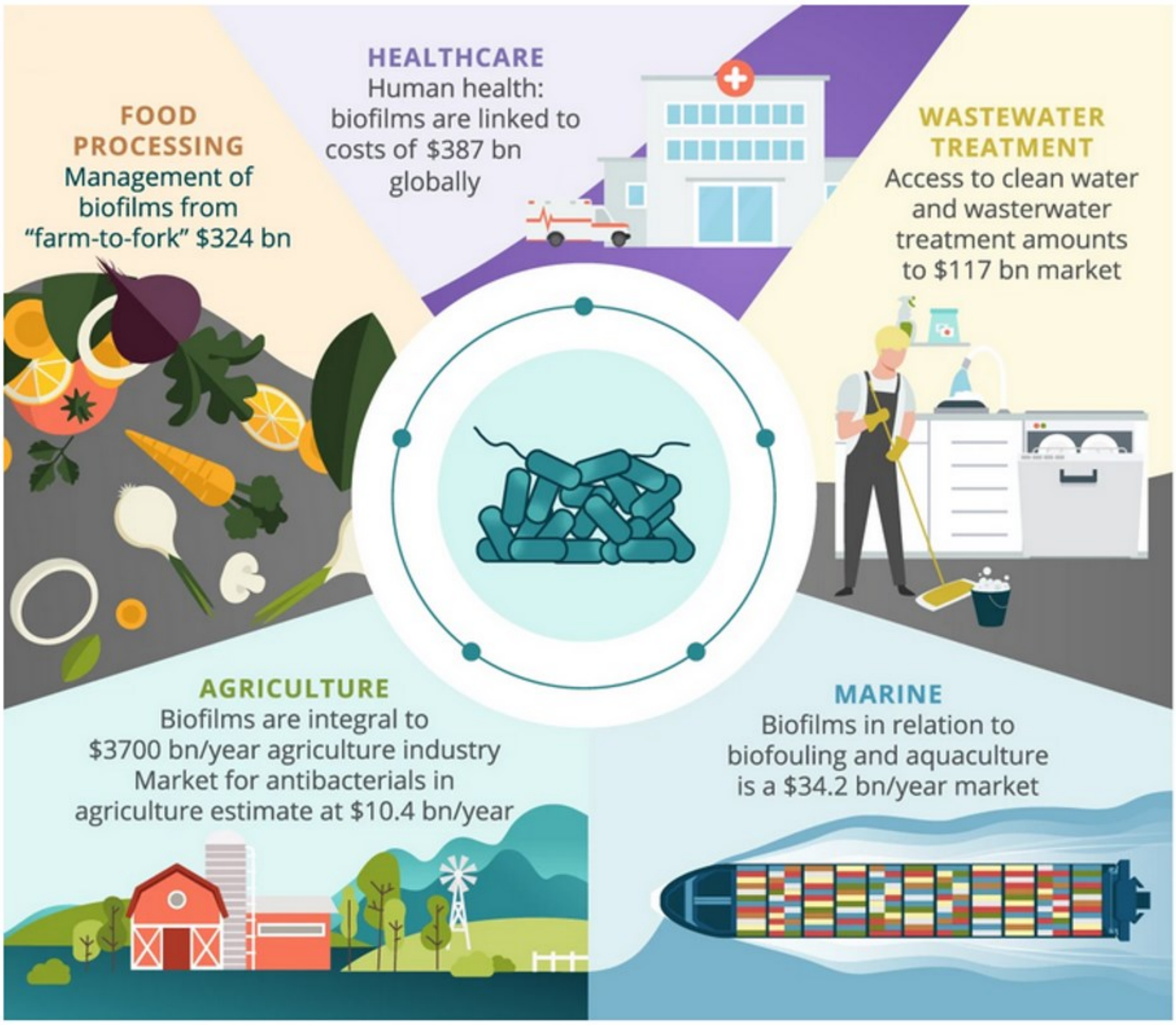

Figure 4. The figures of global economic impact estimated from an in-depth market analysis commissioned by the U.K. National Biofilms Innovation Centre in 2021. This perspective highlights the extensive reach of biofilm interactions across key sectors such as food production, agriculture, healthcare, wastewater treatment, and marine industries [71]. Adapted from reference [75] under the Creative Commons Attribution 4.0 International License. Copyright by Springer Nature 2022.

Generally, medical equipment, such as infusion bags, tubes, and plasters, can become contaminated with bacteria over time, leading to the formation of biofilms [54]. Despite significant advances in materials science leading to a reduction in biofilm formation on medical devices, bacterial colonization remains a concern. Bacteria are ubiquitous in many areas of the body, for instance the digestive tract and oral cavity. Therefore, it is always possible for planktonic bacterial cells to adhere to a surface, form a cell aggregate and ultimately form a biofilm. A prime example of a disease caused by a biofilm infection is dental caries. Although oral hygiene can reduce the formation of biofilms, it cannot permanently prevent the presence of bacteria.

Biofilms create microenvironments with different ion concentrations, redox potentials, oxygen levels, and pH values compared to the surrounding medium [55-57]. Even within a biofilm, there can be gradients and heterogeneities of these properties [58]. For instance, the pH value within a bacterial biofilm colony is crucial for many metabolic processes and is often regulated by the colony itself, ensuring optimal conditions for the survival and proliferation of the biofilm [59]. In dental caries, biofilms containing various microorganisms such as *Lactobacilli spp.* and different types of *Streptococci spp.*, especially *Streptococcus mutans*, metabolize low molecular weight carbohydrates from food, such as sugar, into organic acids [60,61]. This process can cause a drop in pH at the tooth-biofilm interface. If the pH of the tooth falls below a critical level of approximately 5.5, minerals such as calcium phosphates can leach from the tooth structure, resulting in a slow demineralization of the underlying enamel [62,63]. If this is left unattended, demineralization of the enamel will lead to the formation of a carious lesion. As the presence of sugars is necessary for this process, individuals who consume high amounts of sugar are more susceptible to plaque buildup [64]. It is therefore important to be able to measure and monitor pH, for example in biofilm models, for caries research and treatment strategies.

In addition to health-related applications, the ability to monitor the pH of biofilms is also important in industrial environments. Biofilms and their acidic metabolites can induce material corrosion, known as microbially induced corrosion (MIC), e.g., when they are present on metal surfaces such as aluminum or steel [65,66]. This problem is often associated with damage in power plants, refineries, petrochemical facilities, fuel tanks and maritime infrastructure, where it is also referred to as biofouling [67-69]. The annual damage caused by MIC is estimated to be around $500 billion [70,71]. Even on surfaces that are normally alkaline, such as concrete with a pH of 9-12, biofilms can colonize and lower the pH significantly through their metabolites, resulting in structural damage [72]. Thus, there is a growing need to investigate chemical gradients, such as pH in biofilm microenvironments in more detail [73,74].

1.1.5. Nanosensors for the measurement of pH in biofilms

Measuring extracellular pH within biofilms and pH gradients over extended time periods and areas can be challenging and time-consuming. Common monitoring methods include pH microelectrodes and indicator dyes. A pH microelectrode typically uses a membrane permeable to hydrogen ions. It measures the electrical potential difference between the hydrogen ions inside the electrode's internal electrolyte solution and outside the electrode [76,77]. Microelectrodes are suitable for bulk pH measurements in aqueous media. However, their applicability to measure pH inside biofilms is limited by the tip size and small electrode area, allowing only a single detection point per measurement [78]. To monitor pH levels across larger areas using an electrode, it is necessary to either move the electrode within the biofilm or apply multiple electrodes at different positions [79]. Therefore, microelectrode-based techniques are not suitable for dynamic pH measurements in biofilms due to their invasive nature and potential to cause irreversible damage [80]. In addition, electrodes often have slow response times, which makes them unsuitable for extended dynamic pH measurements. For pH imaging microfluidic chips and thin-film sensors are an improvement over microelectrodes as they can detect pH over large areas [81-83]. However, they are limited to measuring pH only at the chip-biofilm interface and cannot provide three-dimensional data, which is critical for understanding biofilm microenvironments.

In addition to microelectrodes, pH can also be determined optically using indicator dyes or pH-responsive fluorescent optical probes, which are both relatively inexpensive and easy to use [84]. The principle of functionality is based on the variation of their fluorescence or absorption, which is dependent on the protonation state of the dye molecule. The transition point is determined by the pK_a value of the dye molecule used. Typical indicators with pH-dependent absorption are e.g., phenolphthalein, bromothymol blue and litmus. However, if the measurement is based on the intensity of a single wavelength, as described in section 1.3.1, the determined pH is susceptible to variations in sensor dye concentration and excitation light intensity. Furthermore, it is important to note that the process of determining pH in a biofilm differs significantly from that of an aqueous bulk phase. Indicator dyes can be taken up by bacterial cells, which may affect the sensitivity of the indicator or harm the bacteria [85,86]. Internalized sensor dyes simultaneously generate signals for both the intracellular and extracellular compartments of a biofilm. Common readout methods, such as colorimetric, fluorescence, or absorption measurement with a plate reader, cannot distinguish signals locally between the two compartments. However, the pH of the intracellular and extracellular biofilm compartments often differs. Therefore, the pH determined by this method is a combination of the two signals, which does not represent the real pH in each compartment and is therefore inaccurate. Moreover, molecular dyes can suffer from relatively low photostability hampering the measurement of time-dependent pH changes.

As described in the previous section, the determination of pH via ratiometric fluorescence measurements with a nanosensor provides a highly functional, yet easy-to-use method. Encapsulating the reference and indicator dyes in the particle core can reduce their interaction with the biofilm and increase the robustness. However, many of the nanosensors described in literature to date tend to easily aggregate in biological systems, rendering them unsuitable for long-term measurements. In addition, many sensors are limited to imaging only very narrow pH ranges [57,87]. Nevertheless, these limitations can be overcome through rational design and careful selection of dyes and particles as presented in the study in chapter 3.1.

In summary, the numerous advantages of optical sensing methods have led to an increasing interest in easy-to-use but highly functional tools that can accurately determine pH in biofilms over extended periods of time. The widespread application of nanosensors for pH measurement in biofilms requires either commercially available systems, which are not yet on the market, or sensor particles that can be easily prepared in most laboratories using commercial components without complex synthesis [38,88]. Apart from biofilms, other biological systems also depend greatly on pH, hence there is a great interest for pH nanosensors as tools for their investigation.

1.1.6. Relevance of extracellular pH in eukaryotic cells

The regulation and maintenance of cellular pH is essential for cellular homeostasis. This applies to both intracellular pH (pH_i) and extracellular pH (pH_e). Various processes control and finely balance the maintenance of pH_i and pH_e. The pH_i of healthy cells is kept stable within a narrow range of 7.0–7.2 [89] or 7.0–7.4 [90] depending on the source and type of cells. It is worth noting that some cell types have pH_i values that deviate from this range. For example, skeletal muscle cells have a slightly lower pH range of 6.8–7.1, while gastric mucosal cells have a higher pH of approximately 8.0 [91]. The high pH_i is the result of the acid production by the cells. The produced acid is then released into the digestive tract, leaving an excess of alkaline ions within the cell.

Generally, the pH_i is regulated by active processes such as proton pumps, bicarbonate transporters, and cellular buffering systems and by passive processes such as ion diffusion e.g. through selective ion channels. These processes are interconnected by feedback mechanisms and keep each other in balance to maintain the pH_i. The pH_i plays an important role in many physiological processes such as enzyme activity, ion transport, and protein functionality. Therefore, pH_i also influences basic cellular functions such as cell signaling, metabolism, growth, proliferation, and apoptosis [92].

The pH_e microenvironment of cells is a critical parameter for cell function, both for individual cells and for cell populations such as tissues and organs. Physiologically healthy cells generally have a pH_e of around 7.2-7.4, whereas the pH_e of abnormal cells and tissues can vary significantly. For example, tumors often have an acidic pH_e of 6.2-6.9 [93]. Hypoxic conditions in a tumor and an increased metabolic capacity lead to increased lactic acid production due to increased glycolysis, resulting in a lower pH_e [94]. Other pathomechanisms that can cause an abnormal pH_e include inflammatory responses or metabolic disorders such as diabetic ketoacidosis, respiratory acidosis or hypoxia-induced acidosis. In these cases, the pH_e in the affected tissues is also significantly lowered. Deviation from normal pH_e can adversely affect cell health and cell-cell communication and lead to an altered immune response as well as triggering further photogenic cascades. Studies have shown that a tumor can develop a microenvironment of pH gradients and local pH heterogeneities [95,96]. These heterogeneities are believed to promote a tumor's invasive and metastatic phenotype and contribute to therapy resistance [97-100]. Efforts are being made to use pH_e as a predictive marker for tumor invasion, immune response, and treatment strategies [101]. Therefore, an accurate assessment of pH_e can help in the evaluation of the extent of tumor invasion and possible treatment strategies.

1.1.7. Nanosensors for the measurement of extracellular pH

Numerous tools are available for the measurement of pH_i [35,102-106]. However, there is a lack of functional tools for measuring pH_e. This may be due to the difficulties associated with accurately measuring pH in close proximity to the cell [107,108]. The limitations of conventional methods, such as pH microelectrodes, have been described in the previous section. In addition, nuclear magnetic resonance and positron emission tomography can also be utilized to measure pH_e [95,109]. However, due to their low spatial resolution, these methods are not suitable for determining pH_e at the cellular level. Instead, they are better suited for larger clinical samples such as whole organs or animals. It is important to note that these methods can be expensive and require the use of a contrast agent that must be injected into the tissue being analyzed.

Fluorescence-based methods are a promising option due to their ability to enable three-dimensional imaging, ease of use, and robustness, as well as their excellent spatial and temporal resolution [110,111]. A remaining challenge with many of fluorescent sensors, which use fluorescent dyes [103], proteins, lipids, and NPs [105,112] is their tendency to be taken up by cells. This internalization of the sensor prevents detection of pH_e [113]. Therefore, these sensors are more suitable for sensing pH_i rather than pH_e [114]. To overcome this challenge and enable pH detection on the surface of cells, targeting moieties that anchor the sensor to the cell surface are employed. Targeting moieties like certain bioligands can also be utilized, to further enhance the selectivity of such nanosensors [115]. Ideally, the sensor should accumulate at the target site to generate a high signal intensity. There are several mechanisms by which targeting can be achieved. These are discussed in the following section.

1.2. Nanoparticles as carriers for treatment agents

Effective treatment of disease is often limited by the shortcomings of newly developed drug candidates that cannot enter clinical trials due to their physico-chemical properties. Small molecule compounds, especially those with low water solubility, often require new formulation and modification approaches to improve therapeutic efficacy. Encapsulation of therapeutic molecules in NPs or nanocarriers can improve their solubility and bioavailability, alter their bio-distribution, and can also facilitate entry into the target cell [116]. Figure 5 displays the various properties of NPs that can be fabricated and adjusted to suit their use as carriers and delivery systems. These properties include surface and material properties, as well as the architecture of the NPs, particularly their size and shape. Targeting moieties can be attached to the NPs, and various stimuli-responsive entities can be integrated, allowing for the release of cargo. By the intelligent design of a NP, the platform can be tailored to a specific application, e.g., through combining different attributes in one particle.

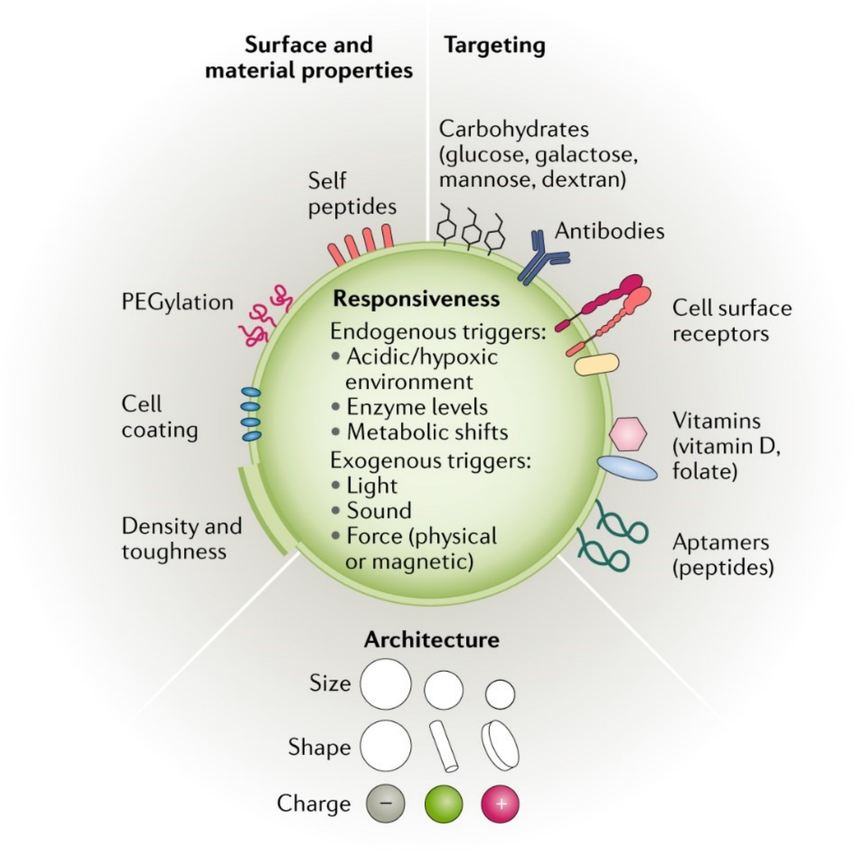

Figure 5. The properties of nanoparticle delivery systems that can be modified for an intelligent nanoparticle design include surface and material properties, targeting moieties, nanoparticle architecture, and responsiveness to stimuli. Reprinted with permission from reference [10]. Copyright by Springer Nature 2021.

To optimize biodistribution, the compound can be packaged in NPs with a size ranging from approx. 10–100 nm. NPs of this size can bypass the clearing mechanisms in the kidneys and liver, thereby increasing the drug's half-life in the body [117]. NPs smaller than 5.5 nm are renally excreted and particles larger than 100 nm phagocytosed in the liver [118]. Positively charged surfaces can enhance endocytosis [119]. Hydrophilic surfaces, such as polyethylene glycol (PEG), can be utilized to provide NPs with stealth properties thereby increasing the circulation times and the treatment effect [120]. Those properties can be useful in the treatment of tumors and are often used therapeutically. Examples of nanoformulations using PEG are Doxil® and Caelyx®, where doxorubicin hydrochloride is packaged in a PEGylated liposomal formulation [121]. Other drug formulations utilizing the nanoscale are (1) Abraxane®, albumin-bound paclitaxel NPs for the treatment of several cancer types, the NPs facilitate the delivery to the cancer cells; (2) Rapamune®, Sirolimus nanocrystals for immunosuppression therapy, the NPs increase the bioavailability due to increased solubility of the drug; and (3) Ritalin LA®, methylphenidate hydrochloride NPs for increased drug loading and increased bioavailability [122]. The development of new nano formulations has also made further progress in recent years. For example, in the Covid-19 vaccines, e.g. Comirnaty® mRNA was encapsulated in lipid NPs about 100 nm in size to protect the active ingredient and facilitate transport into the target cells [123].

Nanomedicine formulations can be designed to deliver therapeutics directly to a specific site in the body, resulting in a lower dose required to achieve a therapeutic effect and a reduction in unwanted side effects. This can be achieved, for example, by encapsulating substances in NPs with specifically designed properties for targeting. Two types of targeting are distinguished: passive and active targeting. Passive targeting with NPs, e.g., for cancer treatment typically employs the enhanced permeability and retention (EPR) effect. The EPR effect is a result of the tumor tissue's altered physiology compared to healthy tissue. The tumor's rapid cell division and increased metabolic activity require increased blood circulation, leading to the rapid formation of new, more permeable blood vessels. This increased permeability results in a greater transfer of nanoscale particles from the blood into the tumor tissue. Furthermore, the lymphatic drainage of the tumor is inferior to that of healthy tissue. This facilitates the retention of NPs in the tumor, resulting in their accumulation.

Active cellular targeting involves the application of targeting moieties (e.g. antibodies or aptamers) to the surface of the NPs. These targeting moieties are specific for certain cell structures such as receptors or antigens and allow for increased accumulation of the NPs at the target site or even facilitate uptake into the target cells. The target should either be present exclusively on diseased tissue or cells or be overexpressed in comparison to healthy cells to allow accumulation of the NPs at the target site. Commonly targeted receptors e.g. for cancer treatment include the HER2 receptor (found in breast and gastric cancer) [124], the folate receptor (found in ovarian and non-small cell lung cancer) [125], or the CD44 antigen (found in leukemia, pancreatic, and lung cancer) [126]. However, this approach is limited by the fact that active-targeted NPs must first reach the target site after systemic application in order to bind to their target. The approach can be combined with passive targeting to deliver the NPs to tumor-specific cells or other target tissues.

Several passively targeted NP formulations using the EPR effect have been approved for treatment in the last two decades, but to date none of the actively targeted NPs have yet passed clinical trials and been approved [116]. One reason might be that the delivery efficiency of NPs to a tumor, both with active and passive targeting approaches, is rather low. A study by Wilhelm et al. assessed the delivery efficiency of 224 scientific publications on targeted NPs and found that only a median of 0.7% of the administered NPs dose was found in the tumor [118]. This shows that there are still gaps in the translation from research to clinical application that will hopefully be bridged in the next years.

NPs can also be used *in vitro* or for medical purposes outside the human body, for example as carriers for antimicrobial substances, which often face similar challenges as newly developed drug compounds. Therefore, nanocarriers are also used to combat microbes and biofilms. This is particularly useful in the development of novel disinfection strategies. The following section describes the background, design, and use of such nanocarriers in combating biofilms.

1.2.1. Challenges and health threats of biofilms

According to the U.S. National Institutes of Health, approximately 65% of all microbial infections and 80% of all chronic infections are associated with biofilms [127-129]. Infections caused by biofilms can be life-threatening and difficult to treat. Endocarditis caused by

Staphylococcus aureus, infections of implants such as heart valves or prostheses, and lung infection including infections in patients with cystic fibrosis caused by *Pseudomonas aeruginosa* are only a few examples of biofilm-derived infections [130].

However, it is important to recognize that not all infections that contribute to the high prevalence of biofilm-associated diseases are life-threatening. Other examples of less critical biofilm-associated infections include: urinary tract infections caused mainly by *Escherichia coli* [131,132], the aforementioned dental plaques leading to caries (Figure 6A), keratitis caused by bacterial biofilms on contact lenses (Figure 6B) [133], and otitis media caused by *Haemophilus influenzae* [134]. Although not life-threatening these conditions still decrease quality of life.

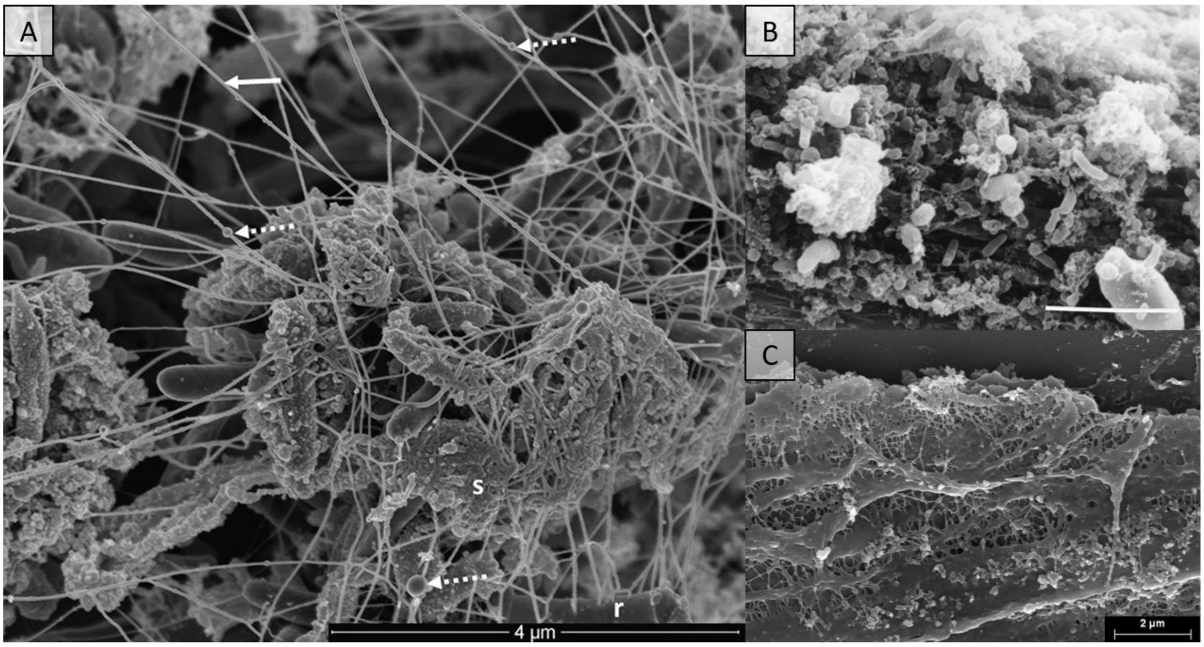

Figure 6. Scanning electron microscopy images of biofilms found in patients or medical equipment. A) A subgingival dental plaque biofilm. Extracellular polymeric matrix (solid arrow) with bead structures (dashed arrow) surrounds the rod-shaped bacterial cells (r) like a coating (s). Adapted from reference [139] under the Creative Commons CC-BY licence (CC-BY 4.0). Copyright by Springer Nature 2015. B) A biofilm found on a contact lens storage case from a patient with contaminated contact lenses. Adapted with permission from reference [133]. Copyright by Oxford University Press 1998. C) Biofilm found on the inner surface of an extubated endotracheal tube. Adapted with permission from reference [138]. Copyright by Springer Nature 2012.

Furthermore, biofilm infections caused by *Staphylococcus aureus*, *Staphylococcus epidermidis* or *Pseudomonas aeruginosa*, such as infections of endotracheal tubes or catheters, are often initially non-critical [135]. However, contamination of endotracheal tubes can lead to ventilator-associated pneumonia, which can prolong the intensive care unit stay and has a mortality rate of up to 30% [136,137]. Gil-Perotin et al. conducted a study in an intensive care unit in which they examined endotracheal aspirates from intubated patients and later performed microbiological assessment of extubated endotracheal tubes [138]. They found bacterial colonization in 87% of patients' endotracheal aspirates and biofilm formation in 95% of endotracheal tubes (example see Figure 6C). Catheter infections can lead to blood poisoning, which is often lethal even under treatment. Biofilm-associated infections have been shown to cause more severe infections, particularly in hospital settings. For instance, *Staphylococcus aureus* and its biofilms pose a significant challenge in hospitals, particularly in intensive care units, due to their high pathogenicity and tendency to develop antibiotic resistance.

Increasing antimicrobial resistance is a global threat that is also recognized by the World Health Organization (WHO). The WHO has published a report in 2017 containing a list of the prioritized multidrug-resistant pathogens for which research and development of new antibiotics is most urgent [140]. All three pathogens in the "*Priority 1: Critical*" category (*Acinetobacter baumannii, Pseudomonas aeruginosa, Enterobacteriaceae*) and most of the pathogens in the other two categories are known to be biofilm-forming [77,141]. The significance of managing and eliminating biofilms in the medical sector cannot be overstated. It is crucial for the global protection of human health, both presently and in the future.

Strategies currently used to combat biofilms include cleaning and disinfection, material selection, and surface treatments such as the use of ultraviolet light, plasma and ultrasonic treatment [142,143]. In the medical field, the use of antibiotics plays a fundamental role in the treatment and prevention of biofilm-associated infections. Most of these methods are primarily aimed at killing or inhibiting the growth of planktonic bacteria. Conventional methods for controlling and eradicating biofilms face two main challenges: (1) Bacteria in biofilms are more robust than planktonic bacteria, making therapeutic agents much less effective against bacteria living in biofilms [144]. These agents are often inadequate for complete biofilm control and eradication [145]. (2) The rapid and increasing emergence of antimicrobial resistance in many bacterial species poses a significant challenge for future eradication efforts. The primary concern is antibiotic resistance. Mechanisms of resistance include molecular modification of antibiotics, changes in binding sites or targets, changes in cell permeability that limit drug absorption, and increased drug efflux [146]. The formation of biofilms is also considered a strategy of resistance. Therefore, there is an urgent need for effective strategies to overcome bacterial persistence by inhibiting biofilm formation and eradicating mature biofilms.

1.2.2. Novel prevention and eradication strategies for biofilms

In the following section, three innovative methods that can be used to combat biofilms will be discussed: bacteriophage therapy, quorum sensing, and photodynamic therapy with NPs.

Due to the increasing prevalence of antibiotic resistance, research into bacteriophage therapy for treating bacterial infections and biofilms has increased. This is because conventional antibiotic resistance mechanisms do not apply to bacteriophage therapy [147].
Bacteriophages, also called phages, are viruses that utilize bacteria as host cells. They can be found in all natural environments in which bacteria occur and are bacteria species-specific. The bacteriophages multiply in the host bacteria resulting in cell death of the host [148]. As bacteriophages require living bacteria for replication, they cannot reproduce once a bacterial infection has been eliminated. This is an advantage regarding clinical applications of phages. Due to their small size and mobility, phages are capable of penetrating biofilms. Therefore, they can be effective against biofilms and can significantly reduce the number of viable cells [149]. Bacteriophages have already shown promise in preventing biofilm colonization of catheters by *Pseudomonas ssp.*[150] and of wound infections caused by *Staphylococcus ssp.*, *Pseudomonas ssp.* and *Acinetobacter ssp.* [151-153].
A limitation for the use of bacteriophages is that they typically have a narrow host range. Some phages are specific to a particular bacterial strain, while others can infect multiple strains or related species [154,155]. Although the specificity of phages can be advantageous in situations where the elimination of known bacterial species is required, it can also be a significant limitation, especially in the case of polymicrobial biofilms [148]. Firstly, the composition of a biofilm must be identified. Secondly, it is necessary to obtain the specific phages that can target the bacteria that need to be eliminated. In the future, genetic manipulation of phages may enhance their selectivity. Bacteriophages have the potential to treat bacterial and biofilm infections in a natural and species-specific way, including multi-drug resistant pathogens.

However, further research is needed before phages can be safely used in clinical practice and healthcare.

Quorum sensing (QS) is the ability of unicellular organisms to regulate gene expression of signaling molecules for chemical communication in response to environmental stimuli. This enables them to adapt cellular processes to, for example, fluctuations in cell population density helping their survival and competitive advantage. Most QS systems are activated by a simple positive feedback mechanism. Bacteria release autoinducers into the environment, and as the population density rises, the concentration of these signaling molecules increases. Once a threshold is reached, bacteria adjust their gene expression, influencing e.g. their phenotype, the promotion of biofilm formation, or reduced cell proliferation [156]. QS systems are used to combat biofilms based on natural signaling molecules. This approach has an advantage over bactericidal methods as it exerts less selection pressure, reducing the likelihood of developing resistance [157]. *Streptococcus mutans*, commonly referred to as the caries pathogen, has two QS communication pathways that could be used therapeutically. It was shown that the administration of high concentrations of QS molecules can induce the death of the *Streptococcus mutans* cell population [158]. Additional research has demonstrated that obstructing particular QS signaling pathways can impede the formation of biofilms, such as in *Pseudomonas aeruginosa* [159]. It is possible that these QS systems could be used to combat biofilms and utilize them for therapeutic purposes [160]. However, it should be noted that, as with bacteriophages, there is often species specificity, i.e. some QS molecules only act on very specific bacteria. In addition, further research is needed to make these QS methods clinically applicable.

The antimicrobial effect of light of certain wavelengths has long been recognized. The most prominent example is the use of ultraviolet light (UV), typically at a wavelength of 254 nm. The light is absorbed by DNA in microbial cells, leading to the formation of dimers between pyrimidine residues in nucleic acid chains. This alters the cell replication and ultimately leads to cell death [161]. However, DNA dimerization also occurs in mammalian cells, which results in mutagenic properties [162]. Therefore, disinfection with UV light is safe only for surfaces and not for the use on or in humans. Research has shown that blue light (wavelengths between 400 and 470 nm) can be effective against a range of bacteria and fungi, although to a lesser extent than light with shorter wavelengths [159].

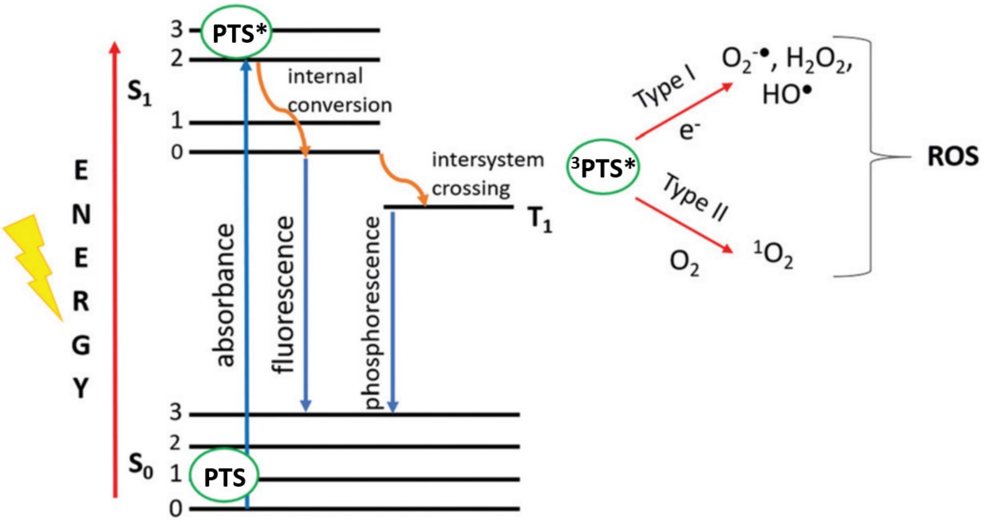

Figure 7. The Jablonski diagram illustrating the photochemical transitions that occur during photodynamic therapy. The diagram shows that in the ground state (S0), the photosensitizer (PTS) absorbs a photon and forms an excited singlet state (S1) PTS*. After internal transformation or intersystem crossing, the long-lived triplet state (T1) 3PTS* can be formed. The 3PTS* species can undergo either a type I electron transfer, forming radicals such as HO•, O_2•− and hydrogen peroxide, or a type II energy transfer, forming singlet oxygen $^1O_2$. Adapted with permission from reference [167]. Copyright by Royal Society of Chemistry 2020.

Photodynamic therapy (PDT) was discovered over 100 years ago and has since become a well-studied treatment for cancer, skin diseases, and various infectious diseases [163]. PDT is also applied to combat microbes, such as bacteria or biofilms, and is often referred to as antimicrobial photodynamic therapy (aPDT). Generally, PDT uses photosensitizers (PTS) which are activated by the absorption of visible light. Upon excitation, the PTS molecule initially reaches an excited singlet state, followed by a transition to the long-lived excited triplet state. The molecule then undergoes photochemical reactions in the presence of oxygen to form reactive oxygen species (ROS) (Figure 7). These ROS can destroy cancer cells, unwanted tissue and microbes such as bacteria in close proximity to the PTS [164]. When the PTS is activated with light, the lifetime of the generated singlet oxygen is very short, with diffusion distances of approximately 10-55 nm. Therefore, photoactivation of the PTS must be initiated at the target after prior delivery to the target site [165,166]. To effectively eliminate biofilms, the PTS should be introduced into and activated in the biofilm. The therapeutic performance improves with higher concentrations of PTS within the biofilm [167]. One significant advantage of aPDT is that ROS cause non-specific damage, therefore there is no known resistance to it. As a result, aPDT can be used to eradicate all types of bacteria, including polymicrobial biofilms, which are often difficult to eliminate [149].

Commonly used PTS are tetrapyrrole structures such as porphyrins, which can occur naturally, but many variations have been synthesized (Figure 8). Other synthetic dye classes used as PTS, include phenothiazines (e.g., methylene blue and toluidine blue), xanthenes and boron-dipyrromethene (BODIPY) derivatives [168]. Naturally occurring PTS substances are e.g., hypericin, riboflavin and curcumin. Most of the PTS molecules are dyes, due to the absorption of light in the visible spectrum (380 nm – 750 nm). The PTS have absorption maxima at different wavelengths, and some have multiple absorption maxima. Generally, absorption maxima at higher wavelengths have the advantage that the light needed for activation of the compound can penetrate deeper into tissues compared to light with shorter wavelengths [169]. This can be an advantage for medical applications but also biofilms.

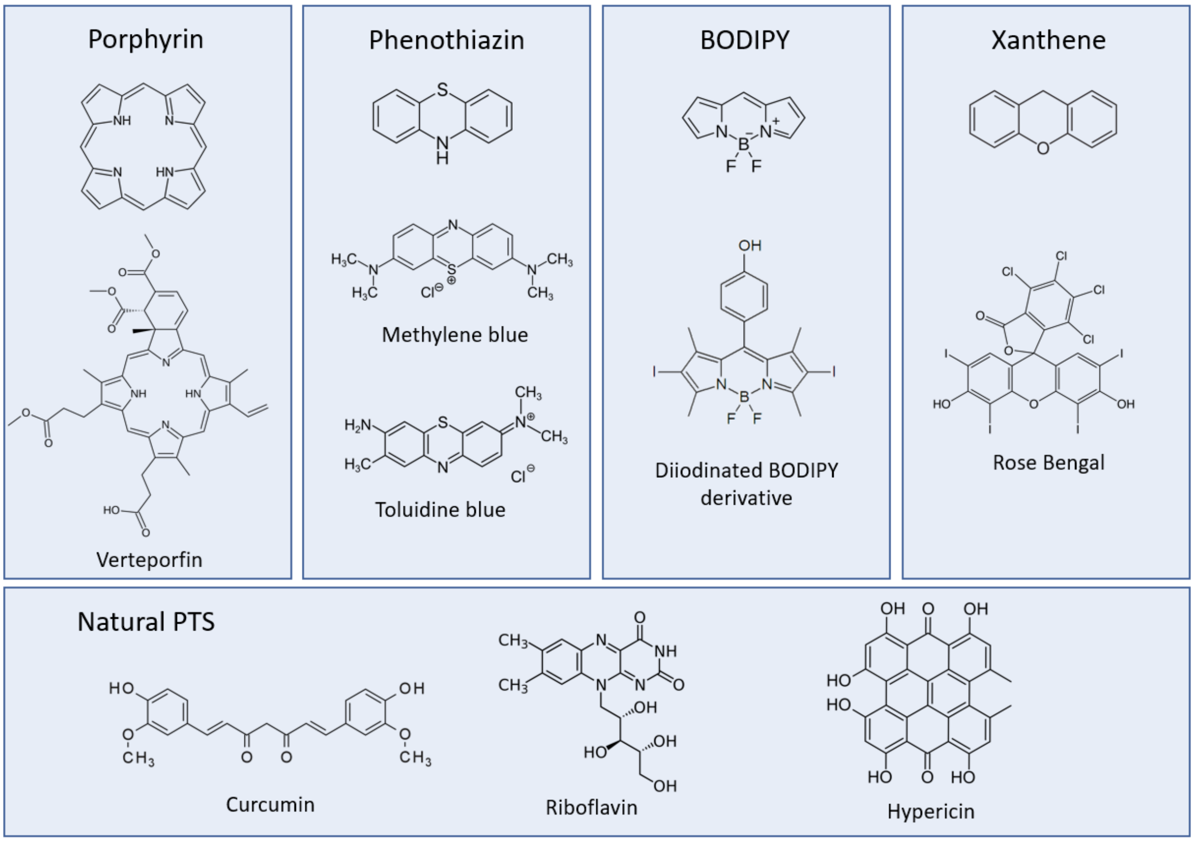

Figure 8. Chemical structures of different classes of photodynamic therapy molecules with the core structure and some prominent derivates.

In the absence of light, PTS molecules are typically not toxic. However, some PTS can be toxic even without exposure to light, which is known as dark toxicity. This applies, for example, to the widely used PTS rose bengal [170,171]. As dark toxicity is difficult to control and can interfere with PDT treatment, it is an undesirable effect in PDT. Therefore, PTS molecules should be highly effective but still controllable to be well suited for PDT of biofilms.

BODIPY dyes are excellent candidates as PTS for the development of modern aPDT methods due to their exceptional photophysical properties. BODIPY dyes can exhibit high molar absorption coefficients, high quantum yields for ROS generation (singlet oxygen), high photostability, and the dark toxicity is negligible [172-174]. Moreover, they are a versatile class of dyes that can be easily prepared and structurally modified for a variety of applications [175-177].

1.2.3. Treatment of biofilms utilizing nanoparticles for photodynamic therapy

Most often, the applicability of PTS molecules is limited by their poor water solubility, tendency to aggregate, and inability to penetrate tissues and biofilms adequately [163,178]. To address the issue of poor water solubility, compounds with more hydrophilic side chains can be synthesized, which may result in a reduction in phototherapeutic efficacy. To overcome both, the solubility and aggregation problems, one strategy is to incorporate the PTS into carriers or NPs that are suspendable in aqueous media. Various synthetic frameworks can be utilized, which have the necessary properties of introducing water solubility and the possibility of a high PTS loading. Some prominent examples of delivery systems are shown in Figure 9. Various nanomaterials, such as polymeric NPs (i.e. PS, poly(lactic-co-glycolic acid), polyacrilamide), liposomes, and spherical micelles can directly incorporate the PTS. Alternatively, the PTS can be conjugated to nanomaterials like carbon nanotubes, graphene sheets, or metal NPs, including gold, silver, or platinum. Metal NPs are often equipped with stabilizing agents such as amino acids or polymers. Macrocycles like cyclodextrins represent another category of nanomaterials capable of PTS conjugation. Furthermore, it is possible to combine multiple PTS in a single particle, which can be excited at different wavelengths.

Numerous studies have demonstrated the use of aPDT in conjunction with NPs against biofilms. For example, Usacheva et al. have demonstrated the treatment of *Staphylococcus* *aureus* and *Pseudomonas aeruginosa* bacteria and biofilms using alginate NPs loaded with toluidine blue [179]. The eradication was effective for planktonic gram-positive *Staphylococcus aureus*, but not as effective for planktonic gram-negative *Pseudomonas aeruginosa*.

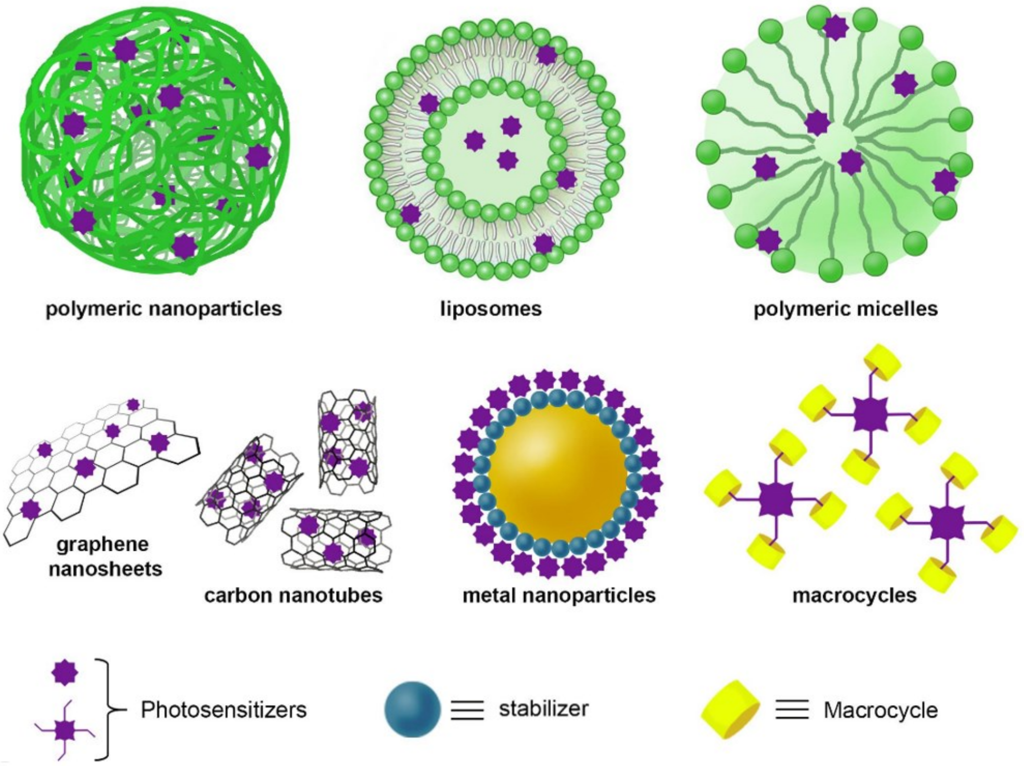

Figure 9. Delivery systems for antimicrobial photodynamic therapy are based on photosensitizers incorporated into polymeric nanoparticles, liposomes, and spherical micelles; and photosensitizers non-covalently conjugated to various nanomaterials. These include carbon nanotubes or graphene sheets, metal nanoparticles such as gold, silver, or platinum, combined with different stabilizing agents such as amino acids, proteins or polymers, and macrocycles such as cyclodextrins. Adapted from reference [161] under the Creative Commons CC-BY licence (CC-BY 4.0). Copyright by Frontiers 2021.

The eradication of the corresponding biofilms was rather low and in general the free dye had the same effect as the loaded NPs. Therefore, it can be assumed that the NPs selected in this study were not suitable to achieve significant effects on biofilm eradication. Other NP-PTS systems used include chitosan NPs loaded with methylene blue [174] and liposomes loaded with temoporfin [180]. These systems have a similar effect in that they easily eradicate gram-positive *Staphylococcus aureus* but are insufficient in eradicating gram-negative *Escherichia coli* and *Pseudomonas aeruginosa*. In many studies, only the eradication of planktonic bacteria is demonstrated [180-183]. One possible explanation is that the limited penetration of NPs into biofilms makes their eradication more challenging than that of planktonic bacteria. Studies have demonstrated that gold NP loaded with methylene blue [173], poly(lactic-co-glycolic acid) NP loaded with curcumin [184], and gelatin NP loaded with rose bengal [182] have been effective against planktonic bacteria. However, there is no available data on their effectiveness against biofilms.

The limitations mentioned in the described studies may be attributed to general challenges in eliminating bacteria and biofilms. Bacteria, and consequently biofilms, exhibit exponential growth with very high colony numbers when sufficient nutrients are available. Therefore, bacterial elimination is typically expressed in log units rather than percentages. A reduction in the bacterial population from 100% of bacteria to 1% is a reduction of 2 log units and from 100% to 0.001% is a reduction of 5 log units. Disinfection is only considered successful if all bacteria are eradicated, as even small amounts of surviving bacteria can rebuild the biofilm population within a short period of time. For instance, if only 0.01% of a biofilm containing 10 million bacteria (10^7 cells) survives disinfection (corresponding to a reduction of 4 log units), this still amounts to 1,000 bacteria. With a doubling time of e.g. 20 minutes (*Escherichia coli*), these bacteria can regain their previous colony strength in approximately 4.5 hours. Elimination rates of less than 2 log units (less than 99% eradicated) achieved with toluidine blue or methylene blue-loaded NPs are not considered sufficient for biofilm removal [179,185,186]. However, this is a general limitation of many studies for biofilm removal and not specific for aPDT.

In general, the effect of aPDT is greater on planktonic bacterial cells than on biofilms [187-189]. This effect is also known for antibiotic treatment and is due to several reasons [190]. Firstly, planktonic bacterial cells are typically in the proliferation stage, which means they have thinner cell walls and are therefore more vulnerable for aPDT agents. In a biofilm, bacteria exist in various physiological states, which means that not all of them are in a susceptible, proliferating state [145]. Some may be dormant with reduced metabolism, which limits the internalization of substances and the efficacy of many therapeutic agents. Secondly, planktonic bacteria are surrounded by a medium, whereas in biofilms the bacteria are densely packed and surrounded by the EPS matrix. The slimy nature of the EPS matrix makes it difficult for the PTS to penetrate the biofilm [191,192]. The effective penetration of the biofilm by the PTS is necessary to completely eradicate all bacteria, including the innermost and best protected cells.

While many published methods can reduce planktonic bacteria by several log units or even completely, the reduction in the case of biofilms is often only in the double-digit percentage range [171,186,193]. This level of reduction cannot be considered sufficient for eradication, let alone disinfection. Therefore, it is crucial to develop systems that can effectively eliminate all bacteria in biofilms.

Delivery of PTS can be achieved through active targeting or passive accumulation. Passive accumulation involves the passive accumulation of PTS-loaded NPs by diffusion, influenced by their charge, size, or hydrophobicity [38,194]. Although this process can take time (minutes to hours), it allows for high concentrations of PTS to be localized at the target site, particularly if the particles have a high dye loading. The active targeted aPDT approach involves the introduction of antibodies, peptides, proteins, and other ligands to the PTS-loaded particles. This enables the particles to bind to specific targets within the biofilm such as the bacterial cell walls or EPS components. This allows for faster and more controlled accumulation within the biofilm. Furthermore, the targeting ligand can be modified depending on the type of biofilm and the mode of action used for eradication.

Combining functional aPDT systems with other antibacterial agents, such as antibiotics, can increase treatment effectiveness [178,195]. NPs are also suitable vehicles for combining active substances, as they allow for the transport of both substances to the same site of action, enabling multitargeted treatment. However, it is equally important to consider the practicality of these developments. The systems should not only become more complex but also remain practical in terms of manufacture and application. This will enable their widespread use in laboratories, food production facilities, and other institutions on a large scale. In addition, the systems should be highly effective against both planktonic cells to prevent biofilm formation and biofilms themselves.

2. Objective

As outlined in the introduction, NPs are a diverse group of materials and their potential applications are vast. Their small size and unique properties make them ideal candidates for the development of biosensors, as they can acquire sensing data in three-dimensional space with high resolution. Particularly polymeric NPs are important and convenient tools for today's diagnostics and therapeutics due to their advantageous physicochemical properties and the ability to tailor their properties through synthesis. Different NP designs, e.g. surface functionalisations, enable optimal interaction with the biological system while ensuring biocompatibility. PS nanosensors exhibit excellent stability even in complex biological media and can be used for long measurement intervals. They are therefore ideal for the development of nanosensors that can measure the pH_e value in biofilms and eukaryotic cells. These nanosensors are easy to manufacture but still highly functional.

Currently, there is an urgent need for effective strategies to overcome bacterial and biofilm persistence. Most of the methods used to combat bacteria and biofilms have significant limitations, and no magic bullet has yet been found to combat the dramatic emergence of bacterial resistance. One promising approach is aPDT. Despite the potential benefits of aPDT for biofilm eradication, there are still significant challenges to overcome. The primary obstacle is the low water solubility of most PTS and the poor uptake of PTS into biofilms. As a result, most PTS have little or no effect against biofilms in their molecular form. PS NPs can act as carriers for PTS molecules and enable successful aPDT.

The objective of this work is to advance comprehension of the design, fabrication, and application of fluorescent dye-loaded PS NPs. These nanoscale tools aim to bridge methodological gaps in conventional approaches, thereby advancing the understanding of cellular microenvironments and biofilm dynamics and enabling advanced antimicrobial strategies.

For this purpose, the specific objectives of this thesis are outlined as follows:

1. **Design and fabrication of a pH-responsive nanosensor for biofilms:**
    - Development of a pH-responsive ratiometric nanosensor utilizing biocompatible PS NPs for the measurement of pH in biofilms

- Characterization of the pH nanosensor and the fluorescence properties of the fluorophores NR and FITC in the NPs
- Calibration and application of the pH nanosensor for the characterization of pH microenvironments in biofilms
- Demonstration of the functionality of the nanosensor through monitoring of time-dependent pH changes induced by the metabolic activity of *Escherichia coli* biofilms

2. **Development of an extracellular pH (pH_e) nanosensor for eukaryotic cells:**
    - Advancement of the pH nanosensor into a pH_e nanosensor suited for the measurement of pH_e in eukaryotic cells
    - Design and fabrication of the pH_e nanosensor using a cell membrane-targeting component for effective labelling of the cell surface to enable the precise and spatially resolved measurement of pH_e
    - Demonstration of the versatility and compatibility of the pH_e nanosensor with various eukaryotic cell lines from different tissues and organs, highlighting its broad applicability in biomedical research
3. **Utilization of PS NPs as carriers for PTS enabling aPDT against biofilms:**
    - Design and development of a novel aPDT tool for the eradication of biofilms using PS NPs as carriers
    - Demonstration of the NPs ability to embed lipophilic PTS, and the delivery directly into bacterial biofilms for on-site activation
    - Assessment of the effectiveness of these nanoscale aPDT tools for various pathogenic bacterial species and for the treatment of both planktonic bacteria and biofilms
    - Characterization of NP-biofilm interactions to advance the knowledge about the mechanisms of action of aPDT against biofilms
    - Effective eradication of pathogenic biofilms and demonstration of the suitability of the PTS-loaded NPs to be used as effective weapons in the battle against biofilms

3. Results

3.1. Monitoring and imaging pH in biofilms utilizing a fluorescent polymeric nanosensor

Charlotte Kromer, Karin Schwibbert, Ashish K. Gadicherla, Dorothea Thiele, Nithiya Nirmalananthan-Budau, Peter Laux, Ute Resch-Genger, Andreas Luch, Harald R. Tschiche

Published online on 14 June 2022 in:
Scientific Reports 12, 9823, 2022
DOI: 10.1038/s41598-022-13518-1
Link: https://doi.org/10.1038/s41598-022-13518-1

Involvement of the author within this publication: Study design, project execution, data analysis, writing and visualisation of the manuscript.

Author contributions as published: The study was designed by C.K., U.R.-G., A.L. and H.R.T. All experiments were performed by C.K., K.S., A.K.G., D.T. and N.N.-B.; C.K. and H.R.T. performed the data analysis. C.K., U.R.-G., and H.R.T. wrote the manuscript and K.S., P.L., and A.L. were involved in critically reviewing the manuscript.

Online Supplementary Material is presented in Annex I.

www.nature.com/scientificreports

scientific reports

OPEN

Monitoring and imaging pH in biofilms utilizing a fluorescent polymeric nanosensor

Charlotte Kromer[1,2], **Karin Schwibbert**[3], **Ashish K. Gadicherla**[4], **Dorothea Thiele**[3], **Nithiya Nirmalananthan-Budau**[5], **Peter Laux**[1], **Ute Resch-Genger**[5]✉, **Andreas Luch**[1,2] & **Harald R. Tschiche**[1]✉

Biofilms are ubiquitous in nature and in the man-made environment. Given their harmful effects on human health, an in-depth understanding of biofilms and the monitoring of their formation and growth are important. Particularly relevant for many metabolic processes and survival strategies of biofilms is their extracellular pH. However, most conventional techniques are not suited for minimally invasive pH measurements of living biofilms. Here, a fluorescent nanosensor is presented for ratiometric measurements of pH in biofilms in the range of pH 4.5–9.5 using confocal laser scanning microscopy. The nanosensor consists of biocompatible polystyrene nanoparticles loaded with pH-inert dye Nile Red and is surface functionalized with a pH-responsive fluorescein dye. Its performance was validated by fluorometrically monitoring the time-dependent changes in pH in *E. coli* biofilms after glucose inoculation at 37 °C and 4 °C. This revealed a temperature-dependent decrease in pH over a 4-h period caused by the acidifying glucose metabolism of *E. coli*. These studies demonstrate the applicability of this nanosensor to characterize the chemical microenvironment in biofilms with fluorescence methods.

Biofilms are consortia of microorganisms adhered to a surface and surrounded by a self-produced matrix of extracellular polymeric substances (EPS) [1]. This matrix facilitates their survival and increases the resistance to external influences such as disinfectants [2]. Such biofilms, that are ubiquitous both in nature and in the man-made environment, can be found on numerous surfaces, including water piping systems, food, household items, and medical devices [3,4].

Numerous factors can influence the formation, growth, and dispersion of biofilms and thus their harmful effects on human health, such as water and food contamination or infection [5–8]. This includes temperature, nutrient composition, shear forces or the pH of the media in which a biofilm is formed [9–11]. Also, these parameters can differ and change between the biofilm matrix and the environment surrounding the biofilm. Inside biofilms local microenvironments can be formed [12]. The pH in bacterial biofilms is of central importance for many metabolic processes. For example, for dental biofilms, the pH in the extracellular matrix is the key factor for the development of dental caries [13]. Extended periods with low pH (< 5.5) at the biofilm-tooth interface after sugar consumption can lead to slow demineralization of the underlying enamel [14,15]. Biofilms can also induce material corrosion (termed microbially induced corrosion) which can cause damage, e.g., in power plants, refineries, petrochemical facilities, and maritime infrastructure [16–18]. Therefore, there is a growing need to investigate chemical gradients in biofilm environments and the internal microenvironments in more detail [19].

The reliable measurement of extracellular pH within biofilms and the measurement of pH gradients over larger areas or longer periods of time are very challenging and tedious. Although microelectrode-based techniques are widely used in biological systems, their applicability is limited by the tip size and the small electrode area, enabling only a single point detection per measurement [20]. For the monitoring of larger areas, the electrode must either be moved within the biofilm or multiple electrodes at different positions of the biofilm must be applied [21]. In addition, measurements with microelectrodes are invasive and can lead to an irreversible

[1]Division 75 "Product Materials and Nanotechnology", Department Chemical and Product Safety, German Federal Institute for Risk Assessment (BfR), Max-Dorn-Str. 8-10, 10589 Berlin, Germany. [2]Institute of Pharmacy, Freie Universität Berlin, 14195 Berlin, Germany. [3]Department Materials and the Environment, Federal Institute for Materials Research and Testing, 12205 Berlin, Germany. [4]Department Biological Safety, German Federal Institute for Risk Assessment, 12277 Berlin, Germany. [5]Division 1.2 "Biophotonics", Department Analytical Chemistry, Reference Materials, Federal Institute for Materials Research and Testing (BAM), Richard-Willstaetter-Str. 11, 12489 Berlin, Germany. ✉email: ute.resch@bam.de; Harald.Tschiche@bfr.bund.de

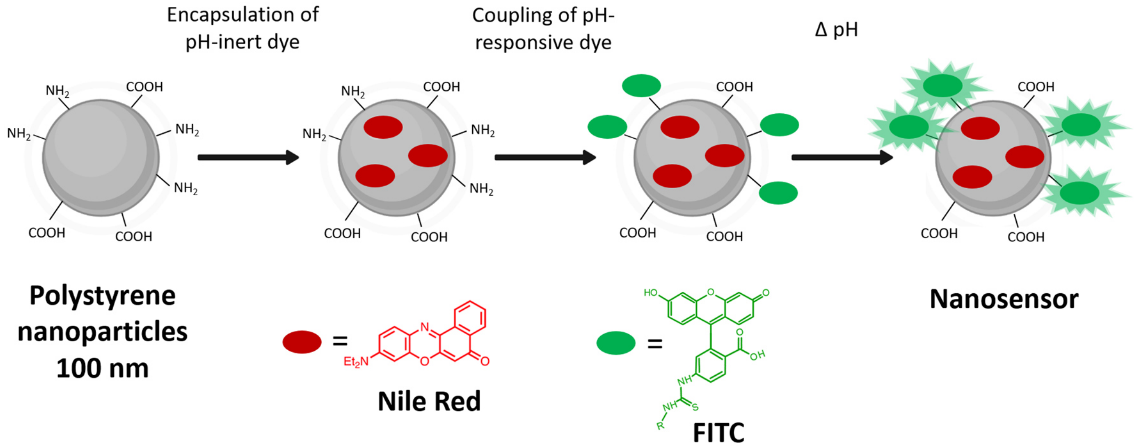

Figure 1. Schematic illustration of the nanosensor fabrication starting from a functionalized PS particle. NR is embedded into the particle by a swelling procedure and FITC is coupled to the PS NP by a thiourea bridge.

destruction of the biofilm. Alternatively, pH can be optically determined, utilizing, e.g. fluorescence techniques such as pH-responsive molecular optical probes and pH indicators which are relatively inexpensive and easy to use [22]. A general limitation of molecular sensors is the challenging preparation of ratiometric sensors that can account for signal fluctuations caused by fluctuations in the excitation light intensity and changes in sensor dye concentration. Moreover, many indicator dyes are taken up by bacterial cells [23]. This could alter the sensitivity of the indicator or have a damaging effect on the bacteria as well as prevent the determination of the extracellular pH e.g. in the biofilm matrix [24]. Moreover, molecular dyes can suffer from a relatively low photostability under microscopic conditions hampering the measurement of time-dependent pH changes. Fluorescent nanosensors can overcome some of these challenges [25–27]. Such nanosensors commonly rely on polymer or silica nanoparticles (NP) labelled or doped with stimuli-responsive luminophores. Advantages of such systems include an increased brightness due to the large number of luminophores per particle, the relative ease of combining two dyes for the design of ratiometric sensors, and an improved photostability [28,29]. Encapsulation of the reference and indicator dyes in the particle core can minimize their interaction with the biofilm. This approach requires a host or carrier matrix that is permeable for the target analyte in the case of encapsulated sensor molecules. Therefore, most ratiometric nanosensors are core stained with a reference dye and the functional groups at the particle surface are utilized for the covalent attachment of sensor molecules. Additionally, recognition moieties like certain bioligands can be utilized, to further enhance the selectivity of such nanosensors [30].

The many advantages of optical sensing schemes triggered an increasing interest in easy-to-prepare and simple-to-handle nanosensors to determine the pH in biofilms with a high accuracy and over extended periods of time. However, many nanosensors reported so far can only map very narrow pH ranges or have a relatively high aggregation tendency in biological systems, which makes them unsuitable for this task [20,31]. Moreover, the broad application of such nanosensors for pH measurements in biofilms requires either commercial systems, which are not yet available, or at least sensor particles that can be easily prepared from commercial components without the need for an elaborate synthesis [26,32].

Here, a facile pH nanosensor made from commercial premanufactured aminated 100 nm polystyrene (PS) NP was developed. The PS NP were loaded with a pH-inert hydrophobic reference dye, here Nile Red (NR), via a simple swelling procedure and subsequently labelled with a commercial pH-responsive fluorescein dye [33,34]. This design concept was also used in our previous work to fabricate oxygen nanosensors and can be realized under standard laboratory conditions [32,33]. As a pH-responsive dye, fluorescein isothiocyanate (FITC) was selected for its pKa value of 6.5 and pH efficient interval, which optimally covers the physiological pH ranges present in *Escherichia coli* (*E. coli*) biofilms. The resulting pH nanosensor has a high colloidal and photochemical stability in aqueous dispersion and in biological media. It does not aggregate in biofilms and shows a very homogeneous distribution in the biofilm matrix. With this nanosensor, a pH range from about 4.5–9.5 can be imaged by confocal laser scanning microscopy (CLSM) as a prerequisite to visualize metabolic pH changes within a biofilm made from *E. coli*.

Results and discussion

Design and preparation of the pH nanosensor.

To prepare the pH-responsive nanosensor, 100 nm PS NP were chosen, that are readily available in a broad size range from nm to µm and with different surface functionalizations. These PS NP are biocompatible and stable in cell culture media. Reportedly, plain and surface modified PS NP with an overall negative charge have no cytotoxic effect on *E. coli* [35,36]. To support this assumption, a live-dead staining of the biofilm was performed after 24 h of incubation of the PS NP used for the preparation of the nanosensor (Supplementary Fig. S4). This viability assessment confirms that the incubated PS NP have no cytotoxic effect on the biofilm.

The simple two-step strategy for the preparation of the pH nanosensor is shown in Fig. 1. First, the reference dye NR was embedded into the PS NP by a previously established swelling method [33]. Then, pH-responsive FITC was covalently attached to the amine groups on the PS NP surface via isothiocyanate amine coupling.

Dye loading was optimized, with respect to optimal signal intensities and intensity ratios of the reference and pH-responsive dye (data not shown).

For ratiometric fluorescence sensing of pH in the visible wavelength region, hydrophobic red emissive NR was chosen as a pH-inert dye and hydrophilic and biocompatible FITC as a pH-responsive dye. NR is known to provide a homogeneous particle loading, does not show leakage from the NP in aqueous dispersions and is photochemically stable [34,37]. FITC reveals a strong green fluorescence solely at basic and neutral pH values [38]. The dyes exhibit spectrally discriminable emission bands as prerequisite for ratiometric sensing and can be read out with a standard CLSM setup using standard lasers and filter settings. The chosen ratiometric design concept allows a correlation of the calculated intensity ratios of the nanosensors FITC and the NR fluorescence with pH neglecting local concentration differences of the sensor. Moreover, at the chosen excitation wavelengths of 520 nm and 560 nm, no autofluorescence of the *E. coli* model biofilm was observed.

Nanosensor characterization. The particle size of 100 nm provided by the manufacturer was confirmed with TEM and dynamic light scattering (DLS) (Table 1). The particle size was not altered by the introduction of NR and FITC. TEM images showed that both the PS NP and the nanosensor are monodisperse and have a spherical shape (Fig. 2a,b). The polydispersity index (PDI) assessed by DLS confirms the monodispersity of the particle suspension. Consequently, the particle size, shape, and agglomeration behavior of the NP were not affected by the dye loading and dye labelling of the NPs. The zeta potential of the PS NP before and after NR staining and FITC coupling was determined to – 30.6 ± 0.6 mV and – 38 ± 1.3 mV, respectively.

Subsequently, the fluorescence properties of the nanosensor were investigated at different pH values in Britton-Robinson (BR-) buffer. As shown in Fig. 2 (lower panels), NR exhibits a fluorescence maximum at 560 nm upon excitation at 530 nm, while FITC shows a fluorescence maximum at 520 nm upon excitation at 480 nm at neutral and basic pH. The pH-dependent fluorescence measurements confirmed that the fluorescence intensities

	Size (TEM) [nm]	Size (DLS) [nm]	PDI (DLS)	Zeta potential [mV]
PS NP	103 ± 9	133 ± 3	0.038 ± 0.023	– 30.6 ± 0.6
Nanosensor	101 ± 8	132 ± 1	0.017 ± 0.011	– 38 ± 1.3

Table 1. Comparison of the precursor PS NP with the dye loaded nanosensor by TEM and DLS.

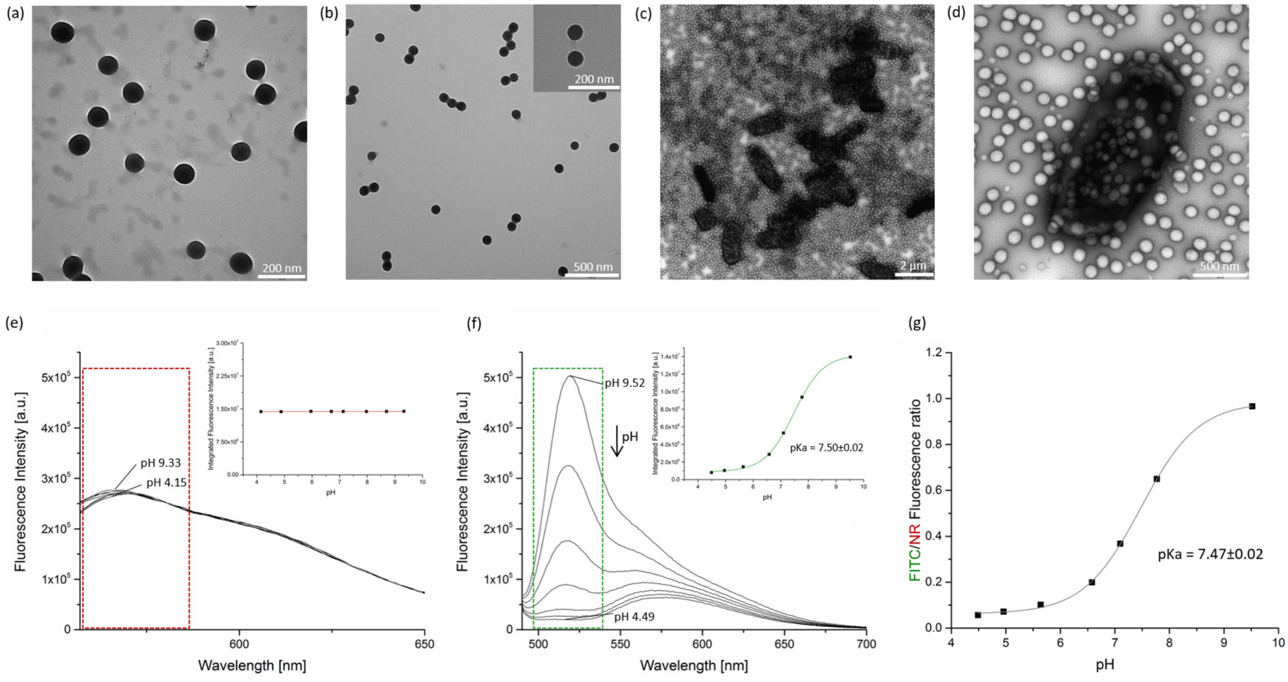

Figure 2. Characterization of the nanosensor. (**a**) TEM image of the precursor PS NP in water. (**b**) TEM image of the nanosensor in water. (**c**) and (**d**) TEM images of *E. coli* cells and nanosensor after 24 h incubation with 1 mg/ml nanosensor in M9 minimal medium. (**e**) Fluorescence spectra of the nanosensor excited at 530 nm (NR) in 7 buffers with different pH. Inset: Integrated FI (red box = area of signal integration) plotted against the pH value of the respective buffer. (**f**) Excited at 480 nm (FITC). Inset: Sigmoidal fit of the integrated FI (green box = area of integration) plotted against the pH value of the respective buffer. (**g**) Ratio of the integrated FI of the green FITC and the red NR emission plotted against the corresponding pH with sigmoidal curve fit.

(FI) of NR is pH-independent (Fig. 2e) while the FI of FITC correlates with changes in pH (Fig. 2f). The FITC fluorescence signal is highest at pH 9.5, decreases upon acidification, and eventually disappears at pH ≤ 4.5. Integrating the FI of FITC in the peak area (Fig. 2f, green box) and plotting against pH reveals a sigmoidal behavior (Fig. 2f, inset), whereas that of NR remains constant (Fig. 2e, inset). The plot of the ratio of the integrated FI of FITC and NR as function of pH (Fig. 2g) yields a pKa value of 7.47 ± 0.02 that is slightly shifted to basic pH values compared to unbound FITC (pKa value of 6.5) [39]. This shift is attributed to the coupling of FITC to a negatively charged particle [40]. Despite the pKa shift from 6.5 to 7.5, the working range of the nanosensor of about pH 4.5–9.5 is still relatively large. Thus, the sensor is well suited for fluorometric pH sensing in the physiological pH range of *E. coli* [41].

Evaluation of the nanosensor in model biofilms. Many factors can limit the functionality of a pH nanosensor in biological systems. Little is known about the interaction of NP with the EPS in the biofilm matrix [42]. Different biomolecules, such as proteins, polysaccharides, nucleic acids or lipids can adsorb on the NP surface forming a corona-like coating [43,44]. This can result in, e.g., particle agglomeration, shifts in the absorption or fluorescence maxima, changes in FI, and in the pH dependence of the optical properties used as readout parameters.

Escherichia coli were selected as the biological model system for assessing the nanosensors application potential. Although *E. coli* is a naturally occurring bacterium in the human intestine, it is the most common cause of bacterial urinary tract infections and is feared as a causative agent of blood poisoning and hospital infections [45–47]. *Escherichia coli* forms biofilms in many environments which can be easily reproduced under laboratory conditions. Also, *E. coli* has metabolic pathways that lead to natural pH changes within the biofilm. Glucose serves as the primary energy source for *E. coli* and is converted to lactate, acetate, succinate, etc. by mixed acid fermentation [48]. To test the metabolic activity of a lab grown *E. coli* biofilm, in a first experiment the pH shift after glucose inoculation was visualized with the pH indicator solution bromothymol blue. After 90 min, acidification of the medium surrounding the biofilm was clearly visible, confirming the suitability of *E. coli* biofilms for testing the nanosensor (Supplementary Fig. S5).

As a prerequisite for the functionality and performance studies with the ratiometric pH nanosensor, first a growth protocol for the biofilms in Ibidi slides was established, followed by an incubation protocol for the nanosensor. As criteria for the growth protocol, uniformity and reproducibility of biofilm growth, homogeneity of colonization on the slide and the biofilm thickness was chosen. Optimization of the nanosensor incubation focused on the homogeneous distribution of the NP in the biofilm and a sufficiently strong fluorescence signal for the CLSM studies, as this is essential for reliable pH measurements.

Within 24 h, the nanosensor accumulated in the biofilm but not inside the cells as revealed by CLSM experiments (see Supplementary Fig. S6). This supports the assumption that the nanosensor accumulates in the extracellular part of the biofilm. This extracellular accumulation points to previously described interactions of the NPs surface groups with the EPS in the biofilm matrix and is supported by the fact that negatively charged PS NP are not taken up by *E. coli* [49,50]. In addition, the combined results of CSLM and TEM studies of the biofilm supernatant after 24 h of incubation indicated that the nanosensor does not tend to accumulate inside the bacteria. (Fig. 2c,d). The hydrophilicity of the nanosensor in the cell culture medium seemed to change. This is suggested by the better adhesion of the nanosensor particles to the TEM grid when applying nanoparticles dispersed in cell culture medium (Fig. 2c,d), compared to nanosensor particles dispersed in water utilizing the same particle concentration (Fig. 2a, b). Nevertheless, the nanosensor particles do not agglomerate or aggregate even after 24 h in cell culture medium. This is an advantage over previously published nanosensors, which often show a high aggregation tendency under these conditions which limits their biosensing performance [20].

For the calibration of the nanosensor fluorescence inside the biofilm, the supernatant cell culture medium was replaced by a reference buffer with a well-defined pH prior to fluorescence imaging. The fluorescence signals of the nanosensor (FITC and NR) were imaged as Z-stacks at 8 different pH values (Fig. 3a). For better visualization of the FI, one representative image from each Z-stack is displayed. The yellow color of the overlayed images reflects an increased FITC signal relative to the NR signal. This ratio is highest at high pH values, here pH 9.33. The mean FI of each FITC and NR stack was calculated using the maximum intensity function for Z-stacks in ImageJ.

The FITC FI divided by the NR FI gave a FI ratio for each pH. These ratios were then plotted against the corresponding pH values (Fig. 3b). This plot was fitted with a four-parameter calibration curve to enable an inverse pH estimation from observed FI ratio values. These results confirm successful fluorometric pH sensing with the nanosensor in the pH range of about pH 4.5–9.5.

To demonstrate the potential of the nanosensor for fluorometrically imaging pH changes in active biofilms, the pH drop caused by the acidifying glucose metabolism of *E. coli* biofilms was investigated. Hence, the *E. coli* biofilms were supplemented with 10 mM glucose at 37 °C and the resulting fluorescence signals of the nanosensor were imaged over a time period of 4 h. A biofilm incubated only with the buffer but without glucose served as a control for potential non-glucose related changes in pH, e.g., due to CO_2.

The nanosensor fluorescence originating from pH-responsive FITC and pH-insensitive NR was measured immediately after glucose addition (time point 0 min) and then every 30–60 min over a period of 4 h (Fig. 4a). The fluorescence of the reference dye NR did not change over time in the glucose-containing biofilm and in the control samples. Contrary, the FITC fluorescence remained constant in the control sample even after 4 h but decreased significantly in the biofilm containing glucose and eventually disappeared completely. This results in a decrease in the FITC/NR FI ratio, signaling a decrease in pH.

The pH values derived from the measured fluorescence ratios of FITC and NR with the aid of the previously acquired calibration curve are shown as a function of time in Fig. 4b. In the biofilm supplemented with glucose, the pH drops significantly from about 7.5 to about 4.5 within 4 h. In the control, no significant pH drop can be

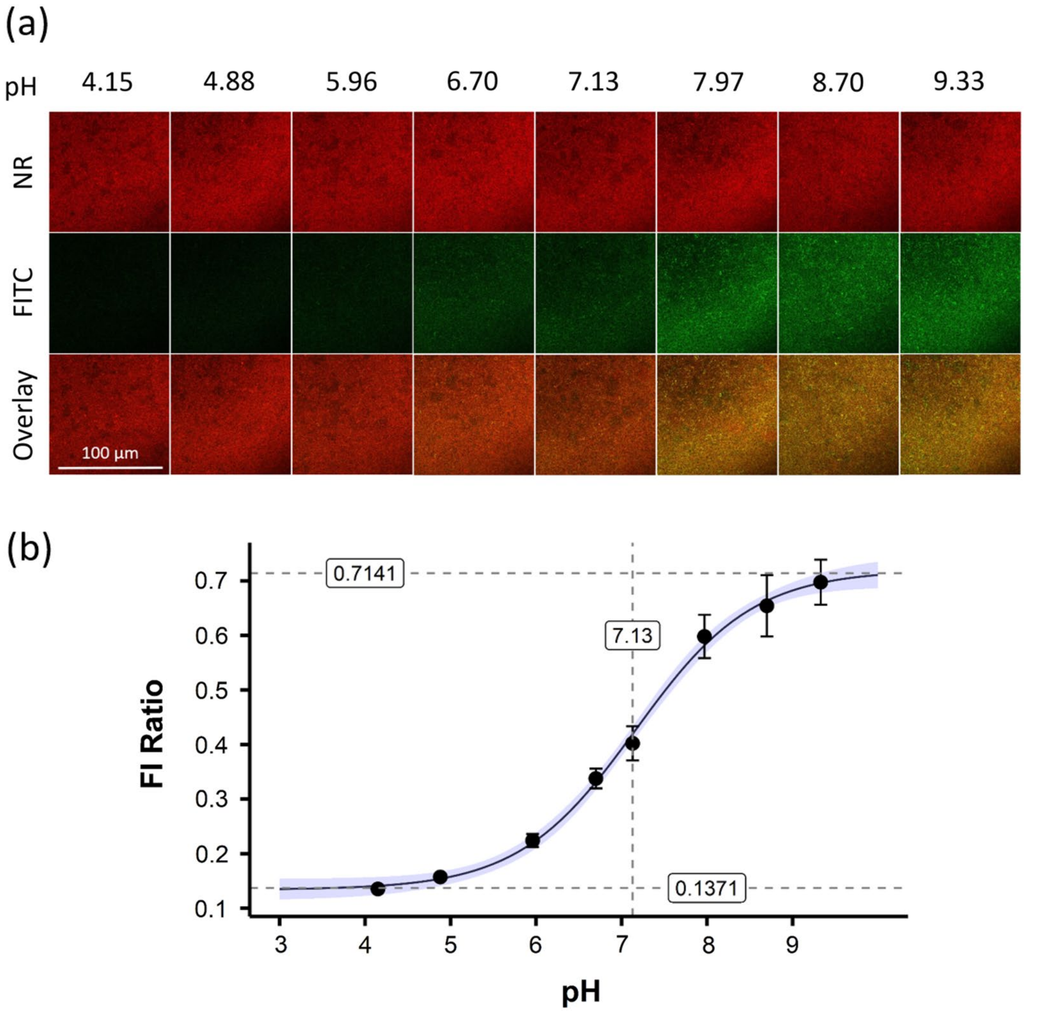

Figure 3. Fluorescence imaging of the nanosensor in reference buffers with CLSM. (**a**) The nanosensors FITC (green) and NR (red) fluorescence were imaged in 8 different reference buffers. For each pH value the entire depth of the biofilm was imaged as a Z-stack. A representative 2D image plus an overlay are shown for better visualization. The 100 µm scale bar applies to all images. (**b**) The FI ratio of the FITC to the NR signal was plotted against the respective pH. The blue area represents the confidence interval of the curve fit, and the error bars indicate the standard deviation. The experiments were performed as 3 independent replicates.

observed. Here, a maximum change from 7.5 to 7 was noticed, with no further change occurring after 1 h. When the *E. coli* biofilms are exposed to glucose at 4 °C, where their metabolism is considerably slowed down, the decrease in pH is significantly reduced compared to the studies done at 37 °C. This supports the assumption of a metabolism-induced drop in pH [51]. To confirm that the observed decrease of the FITC fluorescence with time is not caused by photobleaching of the dye or a leaking of the nanosensor from the biofilm, the reversibility of the nanosensor was controlled. Addition of the starting buffer after 4 h restored the initial nanosensor fluorescence at pH 7.5. This shows the proper functioning of the nanosensor in terms of stability and its accumulation inside the biofilm even after long exposure times.

Conclusion and outlook

In summary, the design, preparation, characterization, and application of a pH-responsive ratiometric nanosensor system was described utilizing commercial biocompatible polystyrene nanoparticles and the fluorescence intensity ratios of the pH-insensitive dye Nile Red, and pH-responsive FITC. The nanosensor enables fluorometric pH sensing in a range of about pH 4.5–9.5 and can monitor pH changes in biofilms over time. Thus, use of this simple nanosensor can greatly contribute to the characterization of the chemical microenvironment in biofilms.

In the future, this ratiometric pH sensor system will be used for studying other pH relevant processes in biofilms such as microbially influenced corrosion on surfaces or in depth investigations of acid stress effects in biofilms [52]. Furthermore, pH gradients present within a biofilm could be explored by calculating the FI ratio for every single pixel in imaging experiments. Thereby, even local chemical microenvironments within biofilms could be imaged [53]. In addition, the nanosensor can be further customized and modified as desired for specific applications, due to their ease of fabrication. For example, dyes with modified absorption or emission wavelengths

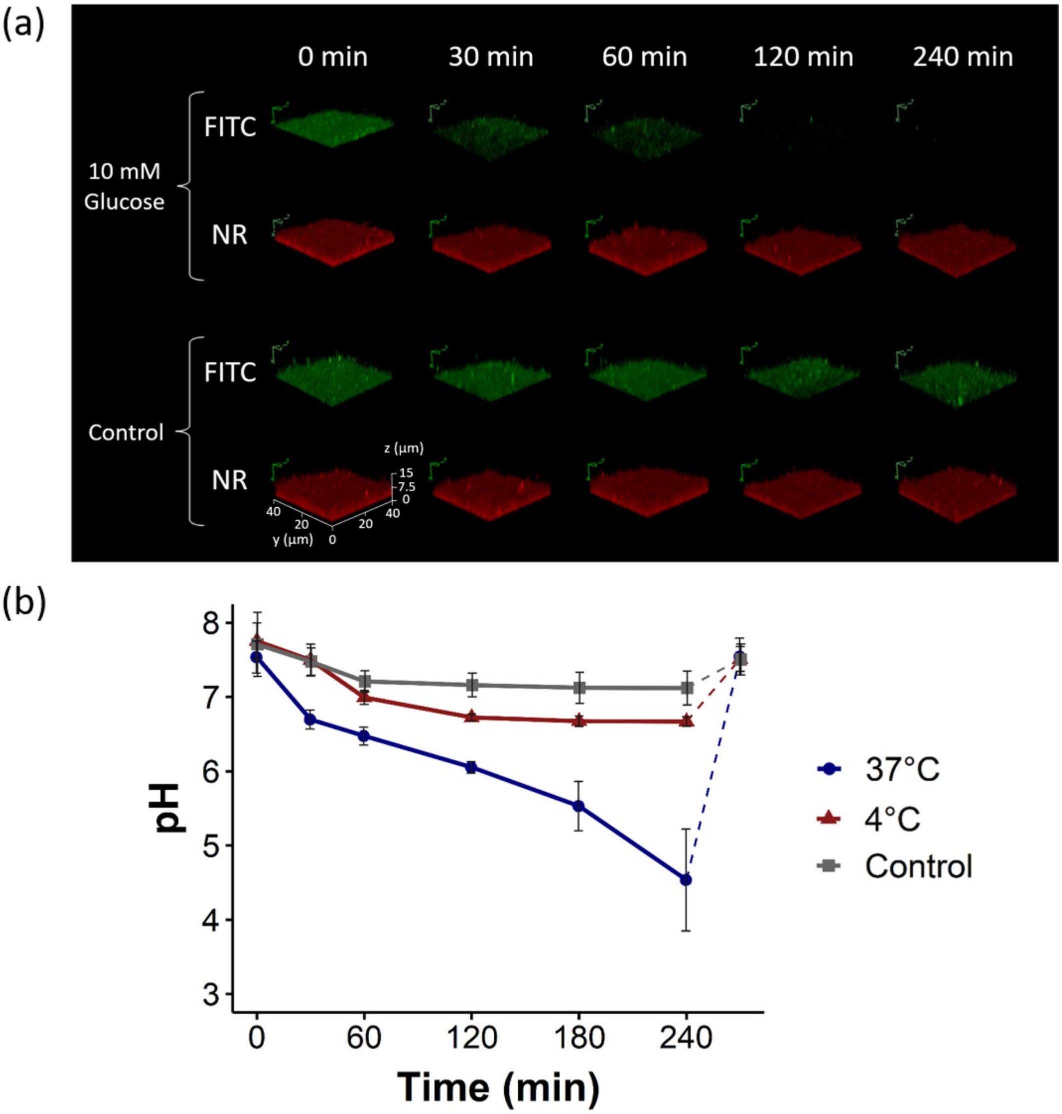

Figure 4. Fate of extracellular biofilm pH after glucose addition. (**a**) Z-stack CLSM images of *E. coli* biofilms after addition of 10 mM glucose (top) and control without glucose (bottom). Green = FITC signal and red = NR signal. The scale bar at the bottom right applies to all Z-stack images. (**b**) Derived pH values of the biofilm after incubation with 10 mM glucose at 37 °C, at 4 °C and the control samples without glucose. The experiments were performed as independent replicates with n = 3 and n = 6 for the control.

and pKa values for biofilms of organism with lower pH such as acidophiles can be easily introduced [54]. The utilization of more than two dyes as well as the combination with other imaging agents for multimodal imaging approaches is also possible.

Overall, this rational design approach for nanosensors utilizing simple and commercially available components can be beneficial for future research aimed at providing better insight into the biofilm microenvironment.

Experimental section

Materials and reagents. All solvents (tetrahydrofuran (THF) and ethanol (EtOH)) were of UV-spectroscopic grade, purchased from Sigma-Aldrich, and used as received. The 100 nm PS NP were purchased from Kisker Biotech and ultrasonically treated prior to use. The fluorescent dyes NR and FITC were purchased from Fluka and Sigma-Aldrich, respectively, and employed without further purification. *Escherichia coli* were purchased from DSMZ-German collection of microorganisms and cell cultures. All cell culture materials and ingredients were obtained from Sigma-Aldrich/Merck and Thermo Fisher Scientific.

Nanosensor preparation. The nanosensor was prepared from commercially available aminated PS NP and two commercial fluorescent dye molecules. The particles had a size of 100 nm, bearing 130 nmol/mg of primary amine surface groups as determined by a Fluram assay [55]. According to the particle manufacturer, the aminated PS NP are obtained by the reaction of carboxylated PS NP with short diamines. As this reaction is not quantitative, the PS NP bear a mixture of amine and carboxyl surface groups. The reference dye NR was incorporated into the PS NP via a swelling procedure published by Behnke et al. [33]. In brief, NR was first dissolved in THF in a concentration of 5×10^{-5} mol/L. Dye loading of the PS NP was performed by addition of 100 µL of the NR-containing solution to 600 µL of an aqueous suspension of the PS NP (0.5 weight percent (w%)). After 30 min, the occasionally shaken suspension was centrifuged with an Eppendorf centrifuge 5415D at 16,000 g for 40 min. The supernatant consisting of unembedded NR dye was removed from the accordingly separated PS NP followed by two washing steps with MilliQ water with a separation step after each washing step. Next, the covalently bound dye FITC was introduced through coupling to the amine groups at the particle surface. The NP suspension (390 nmol NH_2 groups, 1 equiv) was diluted to 5 mg/mL with phosphate buffer (0.1 M, pH 8). To this 1.5 mL suspension, 1.5 mL of a solution of FITC (2.1 µM, 5 equiv.) in PB containing 10 v% EtOH was added and shaken for 3 h with protection against light. The purification steps were the same as for the swelling procedure before, except that a total of 5 washing steps were performed and the first centrifugation/washing cycle was performed with PB containing 10 v% EtOH followed by MilliQ water.

pH dependent fluorescence measurements. Fluorescence spectra were recorded on a calibrated spectrofluorometer (FLS920, Edinburgh Instruments). For these measurements, an integration time of 0.1 s and slit widths of 2 and 6 nm were employed for excitation and emission, respectively. For the pH dependent fluorescence behavior of the nanosensor, 2 µl of nanosensor suspension (5 mg/mL) was added to 1 mL of buffer solution. The fluorescence spectra were recorded with excitation at either 480 nm or 530 nm, with pH values of 4.49, 4.96, 5.64, 6.58, 7.10, 7.77 and 9.52, using the BR-buffer. All measurements were carried out in Hellma quartz cuvettes (QS, 10×10 mm^2). The pH values of the BR-buffer solutions were adjusted with a pH meter using a glass electrode (780 pH meter, Deutsche METROHM GmbH & Co. KG) and verified with a pH meter using a InLab Micro electrode (FiveGo pH meter F2, Mettler Toledo GmbH). These pH meters were calibrated at 25 °C with standard buffers of pH = 10.01, 7.01, and 4.01 (Mettler Toledo GmbH) in three-point calibrations.

Particle size and zeta potential. A Zetasizer (Malvern Nano ZS, Malvern Panalytical) was used to determine the zeta potential and the particle size (hydrodynamic diameter) of the nanosensor by DLS. For particle size measurement and the determination of the PDI, 2 µl of the 25 mg/ml nanosensor stock suspension was added to 1 ml MilliQ Water in a quartz glass cuvette. Thermal equilibration time was set to 60 s at 25 °C. Each intensity-weighted size distribution represents the average of ten individual DLS analyses and three independent replicates. For the determination of the zeta potential a Dip cell kit (Malvern Panalytical) was used. The NP dispersion was diluted in the same manner as done for the particle size determination. Again, the average of ten individual zeta potential analyses and three independent replicates were determined. The particle size was also assessed using a transmission electron microscope (TEM). 400 mesh 3.5 mm Formvar coated copper grids (Plano GmbH, Germany) were hydrophilized with 0.2% alcian blue (Sigma Aldrich, Germany) in 0.03% acetic acid solution. The grids were floated on alcian blue droplets for 10 min, and dried using a filter paper. The hydrophilized grids were used on the same day. 5 µl of a 5 mg/ml sample dispersion was applied on each grid, incubated for 1 min and the excess liquid was removed with a filter paper. Samples on the copper grids were observed in a Jeol 1400 Plus TEM (Jeol GmbH, Germany) operated at 120 kV. Material identification was done using diffraction pattern from published resources. Imaging was performed using a Veleta G2 camera (Olympus, Germany). Particle size was measured using iTEM software provided by Olympus. At least 4 different areas of each grid were examined per sample.

Bacterial strain and biofilm cultivation. *Escherichia coli* TG1 DSM 6056 was used as biofilm forming microorganism [56]. *Escherichia coli* were cultivated on Luria–Bertani (LB) medium agar plates and passaged every 3–4 weeks. For all biofilm experiments, 20 ml LB liquid medium was inoculated with single colonies and cultured overnight at 37 °C with shaking at 120 rpm on an orbital shaker (Incubating orbital shaker, Professional 3500, VWR) [57]. The culture was diluted 1:100 in fresh LB medium and incubated for additional 1–2 h at 37 °C until cells reached the exponential growth phase. Then, 2 ml of the culture was centrifuged (2 min, 3300 g) and resuspended in 2 ml PBS. For biofilm formation, the optical density of the suspension was measured at 600 nm (Novaspec Plus, Amershan Biosciences) and adjusted to 0.01 (corresponding to approx. 1.2×10^6 cells/ml) in M9 minimal medium, supplemented with 1 mM thiamine and 20 mg/L proline. For biofilm formation on the glass/liquid medium interface, 300 µl of cell suspension were then added to each well of Ibidi slides with glass bottom (8 well chamber slide, Ibidi GmbH). NP dispersions were added to a final concentration of 1 mg/ml. The slides were incubated at 37 °C on an orbital shaker, first for 60 min without shaking and then 24 h at 60 rpm for biofilm formation. Prior to imaging, biofilms were washed twice with BR-buffer to remove unbound nanosensor, and fresh buffer was added to each well.

Imaging. All biofilms, except the 4 °C control experiments, were imaged at 37 °C in Ibidi slides using a Leica SP8 X CLSM equipped with a supercontinuum white light laser and a monochromator (Leica Microsystems). A 100 ×/(N.A.1.4) objective with oil immersion was used for imaging. XY images were acquired with 2048 × 2048 or 8192 × 8192 pixels and Z-stacks in XYZ mode with 512 × 512 pixels, respectively. To obtain the Z-stacks, images were taken at 0.1 µm spacing through the biofilm. Excitation and read out emission wavelengths for FITC and NR were 480 nm and 486–525 nm and 530 nm and 537–621 nm, respectively. This choice of the emission filter settings prevents spectral crosstalk of the dyes. Biofilms without nanosensor were imaged in the same way to determine background signals and autofluorescence. The settings for imaging (laser intensity, gain, contrast etc.) were optimized in the beginning, saved, and used unchanged for all imaging procedures to establish comparability between the reference experiments and experiments for pH analysis.

Image analysis and pH calibration in biofilm. All images were acquired with identical microscope settings. A background correction was not done as autofluorescence was not observed for the chosen measurement conditions. For the following image analysis routine with ImageJ FITC and NR Z-stacks were used. The mean FI of the entire stack was calculated using the maximum intensity function for Z-stacks. The FITC FI divided by the NR FI yields the fluorescence ratio. For referencing, a calibration curve was created using BR-buffers with 8 different pH values ranging from 4.15 to 9.33. The biofilms were washed twice with a buffer of the pH of interest and imaged with 300 µl of the buffer as supernatant. This was carried out in independent triplicates for all 8 buffers in 8 different wells. To obtain the calibration curve, a four-parameter curve was fitted to the pH calibration data using Supplementary Equation S1. Fitting was performed with a non-linear least square regression in R (V4.0.3). The fitting parameters (Supplementary Table S2) were then used to perform an inverse pH estimation from the observed value. The inverse estimation was performed in R using the *investr* package [58]. For significance testing an unpaired two-sample *t*-test was performed.

pH analysis in biofilms. In order to analyze changes of pH over time, glucose inoculation experiments were done. A 10 mM glucose solution in K_2HPO_4/KH_2PO_4 buffer was prepared and the pH adjusted to 9. For each well containing biofilm, buffer, and glucose, a control containing only the biofilm and buffer was imaged in the same manner. Two images were taken at each time point starting at 0 min, directly after glucose addition to the well. Then, the images of the biofilm were taken after 30, 60, 120, 180 and 240 min. After the 240-min imaging step, the biofilms were imaged for a final time to demonstrate, that the nanosensor dyes do not bleach and can be reactivated. For this final imaging step, the supernatant of the biofilm was removed and K_2HPO_4/KH_2PO_4 buffer without glucose was added to each well. For the 4 °C control experiments the microscope was cooled to 10 °C, slides were kept in the fridge at 4 °C for 30 min prior to adding the glucose solution. In between imaging the slides were kept on ice. The 3 control samples for the 37 °C and 4 °C were later combined to one control with n = 6.

Data availability

The datasets generated and/or analyzed during the current study are available in the Figshare repository https://doi.org/10.6084/m9.figshare.19213824.

Received: 16 February 2022; Accepted: 25 May 2022

References

1. Donlan, R. M. Biofilms: microbial life on surfaces. *Emerg. Infect. Dis.* **8**, 881–890. https://doi.org/10.3201/eid0809.020063 (2002).
2. Donlan, R. M. & Costerton, J. W. Biofilms: survival mechanisms of clinically relevant microorganisms. *Clin. Microbiol. Rev.* **15**, 167–193. https://doi.org/10.1128/CMR.15.2.167-193.2002 (2002).
3. Francolini, I. & Donelli, G. Prevention and control of biofilm-based medical-device-related infections. *FEMS Immunol. Med. Microbiol.* **59**, 227–238. https://doi.org/10.1111/j.1574-695X.2010.00665.x (2010).
4. Galié, S., García-Gutiérrez, C., Miguélez, E. M., Villar, C. J. & Lombó, F. Biofilms in the food industry: health aspects and control methods. *Front. Microbiol.* **9**, 898–898. https://doi.org/10.3389/fmicb.2018.00898 (2018).
5. Abberton, C. L., Bereschenko, L., van der Wielen, P. W. & Smith, C. J. Survival, Biofilm formation, and growth potential of environmental and enteric *Escherichia coli* strains in drinking water microcosms. *Appl. Environ. Microbiol.* **82**, 5320–5331. https://doi.org/10.1128/aem.01569-16 (2016).
6. Ch'ng, J.-H., Chong, K. K. L., Lam, L. N., Wong, J. J. & Kline, K. A. Biofilm-associated infection by enterococci. *Nat. Rev. Microbiol.* **17**, 82–94. https://doi.org/10.1038/s41579-018-0107-z (2019).
7. Dunne, W. M. Jr. & Burd, E. M. The effects of magnesium, calcium, EDTA, and pH on the in vitro adhesion of staphylococcus epidermidis to plastic. *Microbiol. Immunol.* **36**, 1019–1027. https://doi.org/10.1111/j.1348-0421.1992.tb02106.x (1992).
8. Rumbaugh, K. P. & Sauer, K. Biofilm dispersion. *Nat. Rev. Microbiol.* **18**, 571–586. https://doi.org/10.1038/s41579-020-0385-0 (2020).
9. McEldowney, S. & Fletcher, M. Effect of pH, temperature, and growth conditions on the adhesion of a gliding bacterium and three nongliding bacteria to polystyrene. *Microb. Ecol.* **16**, 183–195. https://doi.org/10.1007/bf02018913 (1988).
10. Guilhen, C., Forestier, C. & Balestrino, D. Biofilm dispersal: multiple elaborate strategies for dissemination of bacteria with unique properties. *Mol. Microbiol.* **105**, 188–210. https://doi.org/10.1111/mmi.13698 (2017).
11. Mathlouthi, A., Pennacchietti, E. & De Biase, D. Effect of temperature, pH and plasmids on in vitro biofilm formation in *Escherichia coli*. *Acta Nat.* **10**, 129–132 (2018).
12. Stewart, P. S. & Franklin, M. J. Physiological heterogeneity in biofilms. *Nat. Rev. Microbiol.* **6**, 199–210. https://doi.org/10.1038/nrmicro1838 (2008).
13. Eriksson, L., Lif Holgerson, P. & Johansson, I. Saliva and tooth biofilm bacterial microbiota in adolescents in a low caries community. *Sci. Rep.* **7**, 5861. https://doi.org/10.1038/s41598-017-06221-z (2017).
14. Au-Schlafer, S. & Au-Dige, I. Ratiometric imaging of extracellular pH in dental biofilms. *JoVE* https://doi.org/10.3791/53622 (2016).
15. Marquis, R. E. Oxygen metabolism, oxidative stress and acid-base physiology of dental plaque biofilms. *J. Ind. Microbiol.* **15**, 198–207. https://doi.org/10.1007/bf01569826 (1995).
16. Little, B. J. *et al.* Microbially influenced corrosion—Any progress?. *Corros. Sci.* **170**, 108641. https://doi.org/10.1016/j.corsci.2020.108641 (2020).
17. Aktas, D. F. *et al.* Anaerobic metabolism of biodiesel and its impact on metal corrosion. *Energy Fuels* **24**, 2924–2928. https://doi.org/10.1021/ef100084j (2010).
18. Chen, S., Deng, H., Liu, G. & Zhang, D. Corrosion of Q235 carbon steel in seawater containing *Mariprofundus ferrooxydans* and *Thalassospira* sp. *Front. Microbiol.* https://doi.org/10.3389/fmicb.2019.00936 (2019).
19. Tribollet, B. Electrochemical sensors for biofilm and biocorrosion. *Mater. Corros.* **54**, 527–534. https://doi.org/10.1002/maco.200390116 (2003).

20. Hidalgo, G. *et al.* Functional tomographic fluorescence imaging of pH microenvironments in microbial biofilms by use of silica nanoparticle sensors. *Appl. Environ. Microbiol.* **75**, 7426. https://doi.org/10.1128/AEM.01220-09 (2009).
21. Sissons, C. H., Wong, L., Hancock, E. M. & Cutress, T. W. pH gradients induced by urea metabolism in "artificial mouth" microcosm plaques. *Arch. Oral Biol.* **39**, 507–511. https://doi.org/10.1016/0003-9969(94)90147-3 (1994).
22. Schäferling, M. Nanoparticle-based luminescent probes for intracellular sensing and imaging of pH. *WIREs Nanomed. Nanobiotechnol.* **8**, 378–413. https://doi.org/10.1002/wnan.1366 (2016).
23. Borisov, S. M., Gatterer, K. & Klimant, I. Red light-excitable dual lifetime referenced optical pH sensors with intrinsic temperature compensation. *Analyst* **135**, 1711–1717. https://doi.org/10.1039/C0AN00180E (2010).
24. Alford, R. *et al.* Toxicity of organic fluorophores used in molecular imaging: literature review. *Mol. Imaging* **8**, 341–354. https://doi.org/10.2310/7290.2009.00031 (2009).
25. Radunz, S. *et al.* Simple Self-referenced luminescent pH sensors based on upconversion nanocrystals and pH-sensitive fluorescent BODIPY dyes. *Anal. Chem.* **91**, 7756–7764. https://doi.org/10.1021/acs.analchem.9b01174 (2019).
26. Hollmann, B., Perkins, M., Chauhan, V. M., Aylott, J. W. & Hardie, K. R. Fluorescent nanosensors reveal dynamic pH gradients during biofilm formation. *NPJ Biofilms Microbiomes* **7**, 50. https://doi.org/10.1038/s41522-021-00221-8 (2021).
27. Fulaz, S. *et al.* Ratiometric Imaging of the in Situ pH Distribution of Biofilms by Use of Fluorescent Mesoporous Silica Nanosensors. *ACS Appl. Mater. Interfaces* **11**, 32679–32688. https://doi.org/10.1021/acsami.9b09978 (2019).
28. Montalti, M., Prodi, L., Rampazzo, E. & Zaccheroni, N. Dye-doped silica nanoparticles as luminescent organized systems for nanomedicine. *Chem. Soc. Rev.* **43**, 4243–4268. https://doi.org/10.1039/C3CS60433K (2014).
29. Wolfbeis, O. S. An overview of nanoparticles commonly used in fluorescent bioimaging. *Chem. Soc. Rev.* **44**, 4743–4768. https://doi.org/10.1039/C4CS00392F (2015).
30. Clark, H. A., Kopelman, R., Tjalkens, R. & Philbert, M. A. Optical nanosensors for chemical analysis inside single living cells. 2. Sensors for pH and calcium and the intracellular application of PEBBLE sensors. *Anal. Chem.* **71**, 4837–4843. https://doi.org/10.1021/ac990630n (1999).
31. Krämer, J. *et al.* Molecular probes, chemosensors, and nanosensors for optical detection of biorelevant molecules and ions in aqueous media and biofluids. *Chem. Rev.* https://doi.org/10.1021/acs.chemrev.1c00746 (2022).
32. Napp, J. *et al.* Targeted luminescent near-infrared polymer-nanoprobes for in vivo imaging of tumor hypoxia. *Anal. Chem.* **83**(23), 9039–9046 (2011).
33. Behnke, T. *et al.* Encapsulation of hydrophobic dyes in polystyrene micro- and nanoparticles via swelling procedures. *J. Fluoresc.* **21**, 937–944. https://doi.org/10.1007/s10895-010-0632-2 (2011).
34. Behnke, T., Würth, C., Laux, E.-M., Hoffmann, K. & Resch-Genger, U. Simple strategies towards bright polymer particles via one-step staining procedures. *Dyes Pigments* **94**, 247–257. https://doi.org/10.1016/j.dyepig.2012.01.021 (2012).
35. Miyazaki, J. *et al.* Bacterial toxicity of functionalized polystyrene latex nanoparticles toward *Escherichia coli*. *Adv. Mater. Res.* **699**, 672–677 (2013).
36. Ning, Q. *et al.* Combined effects of nanosized polystyrene and erythromycin on bacterial growth and resistance mutations in *Escherichia coli*. *J. Hazard. Mater.* **422**, 126858. https://doi.org/10.1016/j.jhazmat.2021.126858 (2022).
37. Wang, C., Otto, S., Dorn, M., Heinze, K. & Resch-Genger, U. Luminescent TOP nanosensors for simultaneously measuring temperature, oxygen, and pH at a single excitation wavelength. *Anal. Chem.* **91**, 2337–2344. https://doi.org/10.1021/acs.analchem.8b05060 (2019).
38. Özelci, E. *et al.* Quantitative measurements of the ph-sensitive quantum yield of fluorophores in mesoporous silica thin films using a drexhage-type experiment. *J. Phys. Chem. C* **123**, 20468–20475. https://doi.org/10.1021/acs.jpcc.9b03917 (2019).
39. Le Guern, F., Mussard, V., Gaucher, A., Rottman, M. & Prim, D. Fluorescein derivatives as fluorescent probes for pH monitoring along recent biological applications. *Int. J. Mol. Sci.* https://doi.org/10.3390/ijms21239217 (2020).
40. Sjöback, R., Nygren, J. & Kubista, M. Characterization of fluorescein–oligonucleotide conjugates and measurement of local electrostatic potential. *Biopolymers* **46**, 445–453. https://doi.org/10.1002/(SICI)1097-0282(199812)46:7%3c445::AID-BIP2%3e3.0.CO;2-5 (1998).
41. Martinez, K. A. 2nd. *et al.* Cytoplasmic pH response to acid stress in individual cells of *Escherichia coli* and *Bacillus subtilis* observed by fluorescence ratio imaging microscopy. *Appl. Environ. Microbiol.* **78**, 3706–3714. https://doi.org/10.1128/AEM.00354-12 (2012).
42. Fulaz, S., Vitale, S., Quinn, L. & Casey, E. Nanoparticle-biofilm interactions: the role of the EPS matrix. *Trends Microbiol.* **27**, 915–926. https://doi.org/10.1016/j.tim.2019.07.004 (2019).
43. Wang, H., Ma, R., Nienhaus, K. & Nienhaus, G. U. Formation of a monolayer protein corona around polystyrene nanoparticles and implications for nanoparticle agglomeration. *Small* **15**, 1900974. https://doi.org/10.1002/smll.201900974 (2019).
44. Stan, M. S. *et al.* Dynamic analysis of the interactions between Si/SiO$_2$ quantum dots and biomolecules for improving applications based on nano-bio interfaces. *Sci. Rep.* **8**, 5289. https://doi.org/10.1038/s41598-018-23621-x (2018).
45. Flores-Mireles, A. L., Walker, J. N., Caparon, M. & Hultgren, S. J. Urinary tract infections: epidemiology, mechanisms of infection and treatment options. *Nat. Rev. Microbiol.* **13**, 269–284. https://doi.org/10.1038/nrmicro3432 (2015).
46. Ali, A. H., Reda, D. Y. & Ormago, M. D. Prevalence and antimicrobial susceptibility pattern of urinary tract infection among pregnant women attending Hargeisa Group Hospital, Hargeisa, Somaliland. *Sci. Rep.* **12**, 1419. https://doi.org/10.1038/s41598-022-05452-z (2022).
47. Allocati, N., Masulli, M., Alexeyev, M. F. & Di Ilio, C. Escherichia coli in Europe: an overview. *Int. J. Environ. Res. Public Health* **10**, 6235–6254. https://doi.org/10.3390/ijerph10126235 (2013).
48. Ciani, M., Comitini, F. & Mannazzu, I. in *Encyclopedia of Ecology* (eds Jørgensen, S. E. & Fath, B. D.) 1548–1557 (Academic Press, 2008).
49. Nevius, B. A., Chen, Y. P., Ferry, J. L. & Decho, A. W. Surface-functionalization effects on uptake of fluorescent polystyrene nanoparticles by model biofilms. *Ecotoxicology* **21**, 2205–2213. https://doi.org/10.1007/s10646-012-0975-3 (2012).
50. Dai, X., Fan, Z., Lu, Y. & Ray, P. C. Multifunctional nanoplatforms for targeted multidrug-resistant-bacteria theranostic applications. *ACS Appl. Mater. Interfaces* **5**, 11348–11354. https://doi.org/10.1021/am403567k (2013).
51. Price, P. B. & Sowers, T. Temperature dependence of metabolic rates for microbial growth, maintenance, and survival. *Proc. Natl. Acad. Sci. U. S. A.* **101**, 4631–4636. https://doi.org/10.1073/pnas.0400522101 (2004).
52. Mcneill, K. D. & Hamilton, I. R. Effect of acid stress on the physiology of biofilm cells of Streptococcus mutans. *Microbiology* **150**(Pt 3), 735–742 (2004).
53. Hwang, G. *et al.* Simultaneous spatiotemporal mapping of in situ pH and bacterial activity within an intact 3D microcolony structure. *Sci. Rep.* **6**, 32841. https://doi.org/10.1038/srep32841 (2016).
54. Radunz, S., Tschiche, H. R., Moldenhauer, D. & Resch-Genger, U. Broad range ON/OFF pH sensors based on pKa tunable fluorescent BODIPYs. *Sens. Actuators B Chem.* **251**, 490–494. https://doi.org/10.1016/j.snb.2017.05.080 (2017).
55. Moser, M., Nirmalananthan, N., Behnke, T., Geißler, D. & Resch-Genger, U. Multimodal cleavable reporters versus conventional labels for optical quantification of accessible amino and carboxy groups on nano- and microparticles. *Anal. Chem.* **90**, 5887–5895. https://doi.org/10.1021/acs.analchem.8b00666 (2018).
56. Ghigo, J. M. Natural conjugative plasmids induce bacterial biofilm development. *Nature* **412**, 442–445. https://doi.org/10.1038/35086581 (2001).
57. Schwibbert, K., Menzel, F., Epperlein, N., Bonse, J. & Krüger, J. Bacterial adhesion on femtosecond laser-modified polyethylene. *Materials (Basel, Switzerland)* **12**, 3107. https://doi.org/10.3390/ma12193107 (2019).

58. Greenwell, B. M. & Schubert Kabban, C. M. Investr: an R package for inverse estimation. *R J.* **6**, 90–100. https://doi.org/10.32614/RJ-2014-009 (2014).

Acknowledgements

We gratefully acknowledge Aaron Katz who helped greatly with data evaluation. This research was funded by the German Federal Institute for Risk Assessment, Grant Number: SFP 1322-721.

Author contributions

The study was designed by C.K., U.R.-G., A.L. and H.R.T. All experiments were performed by C.K., K.S., A.K.G., D.T. and N.N.-B. C.K. and H.R.T. performed the data analysis. C.K., U.R.-G., and H.R.T. wrote the manuscript and K.S., P.L., and A.L. were involved in critically reviewing the manuscript.

Funding

Open Access funding enabled and organized by Projekt DEAL.

Competing interests

The authors declare no competing interests.

Additional information

Supplementary Information The online version contains supplementary material available at https://doi.org/10.1038/s41598-022-13518-1.

Correspondence and requests for materials should be addressed to U.R.-G. or H.R.T.

3.2. A fluorescent nanosensor for ratiometric pH sensing at the cell surface

Charlotte Kromer, Aaron Katz, Ines Feldmann, Peter Laux, Andreas Luch, Harald R. Tschiche

Submitted on 3 March 2024 to:
Scientific Reports

Published online after revisions on 29 May 2024 in:
Scientific Reports 14, 12302, 2024
DOI: 10.1038/s41598-024-62976-2
https://doi.org/10.1038/s41598-024-62976-2

Involvement of the author within this publication: Study design, project execution, data analysis, writing and visualisation of the manuscript.

Author contributions as published: The study was designed by C.K. and H.R.T. Experiments were performed by C.K. and I.F. The data analysis was performed by C.K. and A.K. The manuscript was written by C.K. and H.R.T. and critically reviewed by A.K., I.F., P.L., and A.L.

Supplementary Material is presented in Annex II.

A targeted fluorescent nanosensor for ratiometric pH sensing at the cell surface

Charlotte Kromer[1,2]*, Aaron Katz[1], Ines Feldmann[3], Peter Laux[1], Andreas Luch[1,2], Harald R. Tschiche[1]

[1]Product Materials and Nanotechnology, Department Chemical and Product Safety, German Federal Institute for Risk Assessment, Berlin, Germany

[2]Institute of Pharmacy, Freie Universität Berlin, Berlin, Germany

[3]Material-Microbiome Interactions, Department Materials and the Environment, Federal Institute for Materials Research and Testing, Berlin, Germany

***Correspondence:**
Charlotte Kromer
Product Materials and Nanotechnology, Department Chemical and Product Safety, German Federal Institute for Risk Assessment, Max-Dohrn-Str. 8-10, 10589 Berlin, Germany
Charlotte.Kromer@bfr.bund.de

ORCID
Charlotte Kromer: 0000-0003-4823-4714
Aaron Katz: 0009-0002-5681-847X
Ines Feldmann: 0000-0003-2650-9270
Peter Laux: 0000-0002-0351-3392
Andreas Luch: 0000-0002-5866-901X
Harald R. Tschiche: 0000-0002-6766-9804

ABSTRACT

The correlation between altered extracellular pH and various pathological conditions, including cancer, inflammation and metabolic disorders, is well known. Bulk pH measurements cannot report the extracellular pH value at the cell surface. However, there is a limited number of suitable tools for measuring the extracellular pH of cells with high spatial resolution, and none of them are commonly used in laboratories around the world. In this study, a versatile ratiometric nanosensor for the measurement of extracellular pH was developed. The nanosensor consists of biocompatible polystyrene nanoparticles loaded with the pH-inert reference dye Nile red and is surface functionalized with a pH-responsive fluorescein dye. Equipped with a targeting moiety, the nanosensor can adhere to cell membranes, allowing direct measurement of extracellular pH at the cell surface. The nanosensor exhibits a sensitive ratiometric pH response within the range of 5.5-9.0, with a calculated pKa of 7.47. This range optimally covers the extracellular pH (pH_e) of most healthy cells and cells in which the pH_e is abnormal, such as cancer cells. In combination with the nanosensors ability to target cell membranes, its high robustness, reversibility and its biocompatibility, the pH_e nanosensor proves to be well suited for in-situ measurement of extracellular pH, even over extended time periods. This pH nanosensor has the potential to advance biomedical research by improving our understanding of cellular microenvironments, where extracellular pH plays an important role.

Keywords: pH sensor, pH, pHe, nanosensor, extracellular pH, targeting, nanoparticles

INTRODUCTION

Cellular pH regulation is a fundamental aspect of cellular homeostasis and crucial for maintaining normal cellular function and survival. The precise control of intracellular and extracellular pH can be divided into the combination of two types of processes: I) passive processes such as diffusion and selective ion channels and II) active processes involving proton pumps, bicarbonate transporters and buffer systems, triggered by feedback mechanisms. The main purpose is to ensure that intracellular pH (pH_i) levels remain within a narrow, tightly regulated range, typically between 6.8 and 7.2, depending on the cell type [1, 2]. This is essential for maintaining the stability of numerous physiological processes, including enzyme activity, ion transport, and protein conformation. Therefore, intracellular pH regulation is a key factor influencing basic cell functions such as cell signaling, cell growth, and apoptosis [3].

The extracellular pH (pH_e) of the microenvironment surrounding cells is equally critical, both for the individual cell function but also for the functioning of tissues and organs as a whole. Aberrations in pH_e can impact cell-cell communication, metabolic processes, and even the immune response, contributing to the pathogenesis of numerous diseases [4, 5].
Extracellular pH imbalances can arise from various factors, including metabolic disorders leading to conditions like diabetic ketoacidosis, respiratory acidosis, or hypoxia-induced acidosis. Other pathomechanisms leading to tissue acidification are inflammation or carcinogenesis. While normal cells typically maintain a neutral pH_e (within the range of pH 7.2-7.4), the pH_e in tumor microenvironments is more dynamic [6, 7]. The extracellular milieu in tumors often becomes acidic, with pH levels ranging from 6.2 to 6.9, primarily attributed to increased glycolysis and lactic acid production [8]. Studies have also indicated the presence of pH_e gradients and local pH_e heterogeneities within the tumor microenvironment [9, 10]. These phenomena and the acidic microenvironment not only foster an invasive and metastatic tumor phenotype but also exert an influence on therapeutic resistance [11-14]. Therefore, accurate assessment of extracellular pH may help in evaluating the extent of tumor invasion, immune response and treatment strategies [15, 16].

Understanding the function and importance of extracellular pH regulation is essential for unraveling the intricacies of normal cellular and tissue function, as well as the pathogenesis of various diseases. Consequently, there is a pressing need for innovative and non-invasive methods that can provide real-time, high-resolution pH_e data for cells and tissues under physiological and pathophysiological conditions [17].

While pH_i regulation has been extensively studied, the pH_e environment is often overlooked, possibly attributed to the substantial challenges associated with precise measurement of pH_e directly in cell's proximity. Conventional methods, such as pH microelectrodes, are invasive, often lack the required spatial resolution as they only detect one point at a time and are not suitable for measuring local pH fluctuations in complex biological systems [18, 19]. Nuclear Magnetic Resonance Imaging and Positron Emission Computed Tomography have also been reported for pH_e measurement [9, 20]. These methods are limited by their high operation cost, low spatial resolution and their reliance on the distribution of the probes within the tissue of interest. Fluorescence-based techniques using fluorescent probes have the advantages of high sensitivity and excellent spatiotemporal resolution, as well as wide applications in 3D and even *in vivo* biosensing [21, 22]. While conventional fluorescent dyes for sensing applications underlie limitations, like their susceptibility to fluctuations in excitation light intensity, changes in dye concentration and high background levels, ratiometric fluorescent sensors have been developed circumventing these limitations [21, 23, 24].

Sensors based on fluorescent dyes [22], proteins, lipids and nanoparticles [23, 25, 26] share a common characteristic: their properties facilitate cellular uptake. However, concerning extracellular measurements this ease of cellular entry is also their primary drawback [6]. Consequently, most of them are better suited for intracellular rather than extracellular pH sensing applications [27]. One possible approach is the immobilization of the probe encased in thin films or gels [28, 29]. This does enable pH sensing in the extracellular region but confines measurement to the interface where the gel adheres to the cell surface. However, accurately delivering extracellular pH data within three-dimensional cellular structures and *in vivo* settings presents an unresolved challenge. Therefore, an ideal and highly functional sensor would involve a sensor equipped with a targeting moiety, allowing precise localization on the cell membrane, the intended site for pH_e sensing. Nevertheless, there are only a few tools suitable for measuring the pH_e of adherently growing cells with high spatial resolution, and none of them is widely used in laboratories [30]. Consequently, the development of a cell-anchored ratiometric fluorescent sensor with high sensitivity emerges as a desirable solution for extracellular pH measurements.

This study describes the development of a highly functional pH_e nanosensor with a straightforward design concept utilizing readily available commercial components. The nanosensor is comprised of biocompatible polystyrene (PS) nanoparticles (NP), incorporating a reference dye in its core and a pH-responsive dye on its surface. For targeting the cell surface, the lectin wheat germ agglutinin (WGA) was utilized enabling the active targeting of the cell membranes and therefore the sensing of pH_e in close proximity to the cell. This versatile pH_e nanosensor has demonstrated the ability to perform non-invasive pH measurements within a pH range of 5.5 – 9, while preserving the integrity of the biological systems under investigation. The successful application of the pH_e nanosensor in three distinct eukaryotic cell lines (A549, BeWo, HaCaT) underscores its suitability to be utilized across diverse types of cell lines. Thus, a cell-anchored ratiometric fluorescent nanosensor with high sensitivity, quick response times and universal applicability was developed as a valuable tool for real-time monitoring of pH_e. This pH_e nanosensor holds great potential for advancing the understanding of cellular physiology, disease mechanisms, and the development of targeted therapeutic interventions.

EXPERIMENTAL SECTION

Materials and reagents

The solvents tetrahydrofuran (THF) and ethanol (EtOH) were purchased from Sigma-Aldrich (UV-spectroscopic grade) and used as received. The PS NP (100 nm) were purchased from Kisker Biotech and were ultrasonically treated for 10 minutes prior to use. The fluorescent dye Nile Red (NR) and WGA labeled with fluorescein isothiocyanate (FITC) were purchased from Merck and employed without further purification. The cell culture materials and ingredients were purchased from Thermo Fisher Scientific, Carl Roth and Merck. All cell culture media components were purchased from Pan-Biotech (Aidenbach, Germany).

pH_e nanosensor preparation

The pH_e nanosensor was prepared from commercially available carboxylated PS NP following a modified method which was previously described by Kromer et al [31]. The PS NP had a size of 100 nm and a reported loading of carboxylic groups of 390 nmol/mg [32]. The reference dye NR was incorporated into the PS NP via a swelling procedure published by Behnke et al. [33]. In brief, 100 µL of a NR solution in THF (50 µmol/L) were added to 600 µL of an aqueous suspension of the PS NP (0.5 w%). After 30 minutes of shaking at RT, the suspension was centrifuged for 40 minutes at 16,000 g (5415D, Eppendorf). The supernatant consisting of unembedded NR dye was removed, followed by a washing step with 50 v% EtOH, a washing step with 10 v% EtOH and two washing steps with MilliQ H_2O. Subsequently, the FITC-labeled protein WGA was conjugated to the NP. For that purpose, 1.2 mg of 1-Ethyl-3-(3-dimethylaminopropyl)carbodiimide and 2.4 mg of N-Hydroxysuccinimide in MES buffer were added to 300 µL NR-PS NP suspension (2.5 w%) and shaken for 30 minutes. After centrifugation at 16,000 g for 40 minutes, the supernatant was removed and a subsequent washing step with MilliQ H_2O was performed. Then, 300 µL of the FITC-labeled protein WGA in PBS (1 mg/mL) were added to the NP suspension and allowed to react for 3 hours with continuous shaking. After another centrifugation step and removal of the supernatant, 120 µL of a 25 µM glycine solution were added and shaken for 30 minutes to block unspecific binding sites followed by three washing steps with MilliQ H_2O. Finally, the concentration of the suspension was adjusted to 25 mg/mL before being stored in the fridge until further use.

Particle size and zeta potential

The zeta potential and the particle size (hydrodynamic diameter) of the pH_e nanosensor were determined by dynamic light scattering (DLS) using a Zetasizer (Malvern Nano ZS, Malvern Panalytical). For particle size measurement and the determination of the polydispersity index (PDI), 2 µL of the NP suspension (25 mg/mL) was added to 1 mL MilliQ H_2O in a Hellma quartz glass cuvette. The thermal equilibration time was set to 30 s at 25 °C. The intensity-weighted size distribution represents the average of three independent replicates, each consisting of three measurements with ten individual analyses. The dip cell kit (Malvern Panalytical) was used for the determination of the zeta potential. The NP dispersion was diluted as described above for the particle size determination. The zeta potential was determined as an average of three independent replicates, each consisting of three measurements with ten individual analyses. The particle size was also assessed using a transmission electron microscope (TEM) as described before [31]. 400 mesh 3.5 mm Formvar coated copper grids (Plano GmbH, Germany) were hydrophilized with 0.2 % alcian blue (Sigma Aldrich, Germany) in 0.03% acetic acid solution. The grids were floated on alcian blue droplets for 10 min, and dried using a filter paper. The hydrophilized grids were used on the same day. 5 µL of a 5 mg/mL sample dispersion was applied on each grid, incubated for 1 minute and the excess liquid was removed with a filter paper. Samples on the copper grids were observed in a Jeol 1400 Plus TEM (Jeol GmbH, Germany) operated at 120 kV. Material identification was done using diffraction pattern from published resources. Imaging was performed using a Veleta G2 camera (Olympus, Germany). Particle size was measured using iTEM software provided by Olympus. At least 4 different areas of each grid were examined per sample.

pH dependent fluorescence measurements

Fluorescence spectra were recorded with a fluorospectrometer (LS 55, Perkin Elmer). Fluorescence measurements were carried out using an integration time of 0.1 s and slit widths for excitation and emission of 2 and 6 nm, respectively. To observe the pH-dependent fluorescence behavior of the pH_e nanosensor, 2 µL of nanosensor suspension (25 mg/mL) was added to 1 mL of buffer solution. The fluorescence spectra were recorded with excitation at 485 nm, with 21 different pH values ranging from 4.15 to 10.94, using the Britton-Robinson (BR) buffer in Hellma quartz cuvettes. The pH values of the BR buffer solutions were measured using a pH meter with an InLab Micro electrode (FiveGo F2 pH meter, Mettler Toledo GmbH). The pH meter was calibrated at 25 °C with standard buffers of pH = 9.21, 7.01, and 4.01 in a three-point calibration.

Dye and protein loading

Dye loading was determined using a spectrophotometric method as previously described by Kromer et al [34]. A calibration curve for the absorbance of NR in 50 v% THF in H_2O at 530 nm was prepared. The concentration range of 1.25-15 nmol/mL was determined to be linear with R=0.9985 using a linear regression model. As a second step, a defined volume of nanosensor suspension was added to an Eppendorf tube and centrifuged at 16,000 g for 40 minutes. The supernatant was removed, and the NPs were dissolved in 500 µL THF and 500 µL H_2O was added. The absorption at 530 nm was determined in a spectrophotometer (FoodALYT, Germany). The dye concentration was calculated as dye equivalents by using the calibration curve and used to calculate the dye loading per mg nanosensor.

For the determination of the protein loading (equiv. of WGA per mg particle) a modified indirect Coomassie assay was performed [35]. The NP suspensions were prepared by adding 20 µL NP suspension (0.5 mg NP) to 880 µL MilliQ H_2O and 100 µL of Coomassie blue concentrate (Protein Assay Kit, Bio Rad). As a control 20 µL of NP without lectin were prepared in the same manner. The mixture was incubated for 10 minutes and then centrifuged at 16,000 g for 40 minutes. The supernatant, containing unbound Coomassie blue, was collected and 50.4 µL of BSA solution (8 mg/mL in MilliQ H_2O) was added to 700 µL supernatant. 100 µL of the resulting solution was transferred to a 96-well plate in triplicates. Titration of the Coomassie Blue was performed by adding different volumes of Coomassie blue (0, 1, 5, 10, 50, and 100 µL) to 700 µL of MilliQ H_2O in Eppendorf tubes, followed by the addition of 50.4 µL of the BSA solution. Triplicates of each sample were transferred to the same 96-well plate. Similarly, BSA titration was carried out by setting up a standard series of Coomassie blue. 10, 20, and 50 µL of Coomassie Blue were made up to 700 µL with MilliQ H_2O and variable amounts of BSA (0, 1, 2, 4, 6, 8, 10, or 15 µL) were added. Triplicates of each sample were then transferred to the second 96-well plate. For both plates the absorbance at 595 nm was measured using a plate reader (BioTek Synergy Neo 2, Agilent Technologies). The amount of conjugated lectin as BSA equivalents was calculated.

Cell culture

The human lung epithelial cell line A549 and the human placenta cell line BeWo were purchased from ATTC (American Type Culture Collection). The human immortal keratinocyte cell line HaCaT was purchased from DSMZ (German Collection of Microorganisms and Cell Cultures GmbH). All cells were cultivated in 5 % CO_2 at 37 °C and grown in DMEM medium, containing 10 v% FCS for A549 and BeWo and 5 v% for HaCaT, 100 U/mL penicillin, 100 mg/mL streptomycin, and 2 mM L-glutamine.

Cell viability

To assess the viability of the cells after incubation of the NP the colorimetric viability assay kit WST-1 (Roche Diagnostics GmbH) was used. Here, the amount of formazan dye formed is directly related to the metabolic activity of cells. The assay was carried out as described in the manufacturer's instructions. In brief, cells were seeded at 2×10^4 cells/well in transparent 96-well plates and incubated with the NP for various time periods. After addition of 10% WST-1 reagent and incubation for 30 min, the absorbance was measured at 450 nm (620 nm was used as reference wavelength) in a multiplate reader (BioTek Synergy Neo 2, Agilent Technologies). To account for potential absorbance of the NP at 450 nm, the absorbance of each well was also measured before addition of the WST-1 reagent and subtracted from the final value. Results are reported as relative WST-1 activity, where 100% corresponds to the absorbance measured in control cultures and 0% to the dead-control treated with 1% Triton-X for 30 minutes.

Cell binding assay

To evaluate the cell adhesion of the WGA-conjugated nanosensor, binding studies were performed on the 3 cell lines A549, HaCaT and BeWo. For this purpose, the suspended cells were incubated for 5 minutes at 37°C with WGA-conjugated NP at 1.25 mg/mL in Eppendorf tubes. NP without WGA served as a control. After the incubation, the cells were centrifuged at 300 g for 6 minutes. The supernatant containing the unbound NP was removed. The cell pellet was resuspended in cell culture medium, transferred to a 96 well plate, followed by measurement of the NP fluorescence (NR, 530 nm) in a plate reader. Cells with NP without centrifugation served as 100% control for calculating the relative amount of NP bound to the cells.

Scanning electron microscopy (SEM) imaging

For SEM imaging, A549 and HaCaT cells were grown on 1 x1 cm glass slides and incubated for 10 minutes with 0.825 mg/ml pH_e nanosensor. The samples underwent three washing steps with PBS and were then fixed with 2% glutaraldehyde for 2 hours. After three more washing steps with PBS, the cell specimens were dehydrated using a graded series of alcohol (30%, 50%, 70%, 90%, and 99% ethanol). Liquid carbon dioxide was used as a transitional fluid for critical point drying (EM CPD300, Leica, Germany). The cell specimens were sputter-coated with a 30 nm conductive gold layer (EM ACE600 table-top coater, Leica, Germany) and examined with an environmental scanning electron microscope (XL 30 ESEM, FEI, Netherlands) equipped with a secondary electron detector and operated at an electron accelerating voltage of 25 kV. At least three random sections per sample were analyzed.

CLSM imaging

All cells were live cell imaged in Ibidi μ-dishes at 37 °C using a confocal laser scanning microscope (LSM 700, Carl Zeiss Jena GmbH, Jena, Germany). A 63 × /N.A. 1.4 objective with oil immersion was used for imaging. XY images were acquired with 1024 × 1024 pixels. The standard laser and filter set for FITC and NR were used. Cells without nanosensor were imaged in the same way to determine background signals and autofluorescence. The imaging settings, such as laser intensity, gain, and contrast, were first optimized, saved, and then used for all imaging procedures to ensure comparability.

Image analysis and pH calibration

As describe above, all images were acquired with identical microscope settings. No background correction was performed as autofluorescence was not observed under the chosen measurement conditions. For the image analysis the fluorescence intensities (FI) of the FITC and NR channel of the whole image were calculated with ImageJ. The FITC FI divided by the NR FI yields the total FI ratio of the pH_e nanosensor. A calibration curve was generated using BR buffers with 11 different pH values ranging from 4.15 to 10.05. For imaging, the cells were washed twice with PBS before adding the nanosensor at a concentration of 0.825 mg/mL. After incubating the nanosensor for 10 minutes, the supernatant containing unbound nanosensor was removed. Subsequently, the cells were washed with BR buffer of the pH of interest and imaged. This procedure was carried out in three independent triplicates for all three cells lines and all 11 buffers. To obtain the calibration curve, a four-parameter sigmoidal curve was fitted to the pH calibration data using Graph Pad Prism. A reverse pH estimation can also be performed with this function, allowing for determination of unknown pH values from the FI ratio of an image.

Statistics

Statistical analysis was carried out with GraphPad Prism 9. All data are presented as mean ± standard deviation and were acquired in triplicates. Groups were compared using the t-test and one-way ANOVA. P values ≤ 0.05 were considered statistically significant.

RESULTS AND DISCUSSION

Fabrication of the pH_e nanosensor

For the preparation of the pH_e nanosensor, a straight forward two-step strategy was carried out as shown in Fig. 1. First, the reference dye NR was embedded into PS NP by a previously established swelling method [33, 34]. The PS NP were chosen as the platform for the pH_e nanosensor, as they are readily available with different surface functionalizations. Here, NP with carboxylic surface groups were chosen, as they are hydrophilic and allow conjugation of dye molecules as well as proteins. These negatively charged PS NP are biocompatible and stable in cell culture media [36, 37]. As a second step, the protein WGA, labelled with the pH-responsive dye FITC, was covalently attached to the carboxylic groups of the PS NP surface via carbodiimide coupling. WGA is a lectin, which is a carbohydrate-binding protein that specifically binds to N-acetylglucosamine and sialic acid residues. WGA conjugated to fluorophores are frequently used to label and identify specific glycoproteins or glycolipids on cell membranes in microscopy studies [38, 39]. Here, the WGA was applied to facilitate the targeting of the cell membranes by the pH_e nanosensor. The protein loading was optimized, with respect to optimal binding of the NP to the cells and optimal signal intensities of FITC (dye and protein loading data in SI, table A1). For ratiometric fluorescence sensing of pH in the visible wavelength region, hydrophobic red emissive NR was chosen as a pH-inert reference dye and hydrophilic and biocompatible FITC as a pH-responsive dye [31, 40]. Upon incorporation into the NP, NR showed a homogeneous particle loading without leakage in aqueous dispersions, high photochemical stability and brightness. FITC reveals a strong green fluorescence solely at basic and neutral pH values with an optimal working range for pH sensing for working in eukaryotic cells. The dyes exhibit spectrally discriminable emission bands and can be read out with a standard CLSM setup using standard lasers and filter settings. While FITC exhibits its excitation maximum at approximately 490 nm, NR, on the other hand, has its excitation maximum at 530 nm. Notably, the excitation range of NR is broad and overlaps with the excitation maximum of FITC. Therefore, both dyes can be excited at the same wavelength, but the emission can be read out at different wavelengths, enabling ratiometric pH measurement with only one excitation wavelength. This simplifies the equipment needed to do measurements, and thus there are less error sources. The chosen ratiometric design concept allows a correlation of the calculated intensity ratios of the pH_e nanosensor FITC and NR fluorescence with pH neglecting local concentration differences of the sensor. Hence, the pH_e nanosensor is a useful tool for pH detection that can be used in a standard laboratory environment under a wide range of conditions. Despite its efficient performance, there is no need for advanced techniques or materials other than a CLSM. In this study, functionality and practicality was prioritized over complexity and novelty, as this provides the greatest benefit to the ever-growing need for easy and ready-to-use methods.

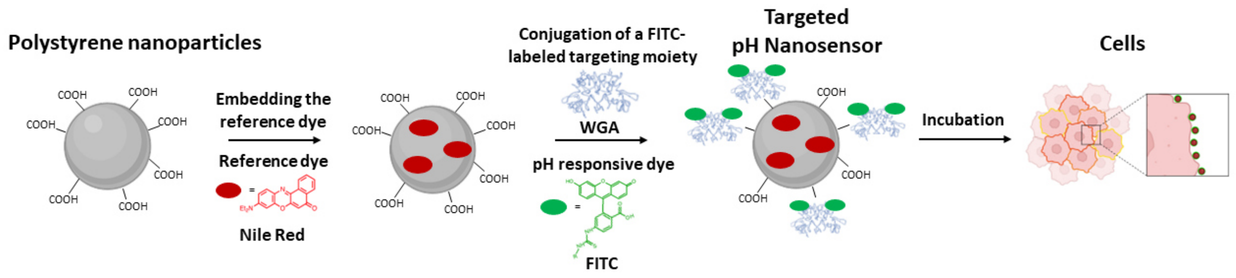

Fig. 1 Schematic illustration of the pH_e nanosensor fabrication starting from a functionalized PS NP. The reference dye NR is embedded into the particle by a swelling procedure. The lectin WGA labeled with the pH-responsive dye FITC is conjugated to the NP as targeting moiety therefore enabling the pH_e nanosensor to target the cell membrane of eukaryotic cells

Characterization of the pH_e nanosensor

The precursor PS NP size was determined to be 114.1 ± 3.9 nm through DLS and 94.0 ± 8.5 nm through TEM, a result that matches the value of 100 nm provided by the manufacturer (Table 1). The size of the particles remained unchanged after incorporation of NR dye and the hydrodynamic diameter increased only slightly after the conjugation of the protein WGA. The particles have a spherical morphology and low aggregation behavior, which also remains unchanged after functionalization of the particles (Fig. 2e). The consistency of particle size and morphology is critical as it excludes the aggregation of particles and thus ensures the sensor's reliability and performance [41]. Furthermore, the small size of the particles allows local pH imaging with high resolution. This is in contrast to other particulate sensors, which have larger particles in the µm range, hindering the ability to image and detect pH at a cellular resolution [29]. The zeta potential analysis revealed a negative charge of approximately -63 mV and -66 mV for the precursor NP and the NR-loaded NP, respectively. This indicates a high stability of the suspension, as suspensions with zeta potentials more positive than +30 mV or more negative than −30 mV are considered to have a high colloidal stability maintained by electrostatic repulsion [42-44]. Furthermore, after WGA-FITC conjugation, while the zeta potential increased, it remained negative at around -31 mV. Importantly, the critical properties for suspension stability, namely size and zeta potential remain stable even after functionalization, underscoring the suitability of the nanosensor for the imaging of pH_e in cells.

Table 1 Comparison of the particle size and zeta potential of the precursor PS NP with the NR-loaded NP and the pH_e nanosensor by TEM and DLS

	Size (TEM) [nm]	Size (DLS) [nm]	PDI (DLS)	Zeta potential [mV]
PS NP	94.0 ± 8.5	114.1 ± 3.9	0.012	-62.7 ± 1.1
NR-loaded NP	92.2 ± 9.7	113.8 ± 2.6	0.018	-66.0 ± 5.3
pH_e nanosensor	86.5 ± 9.2	125.8 ± 6.5	0.050	-30.6 ± 1.4

Fluorescence Characterization

The fluorescence properties of the pH_e nanosensor were examined at different pH values in BR buffer to assess its ability for pH determination in cellular systems. As shown in Fig. 2a, the pH_e nanosensor is excited at 485 nm and exhibits a strong fluorescence signal of with maxima of NR at 600 nm and of FITC at 520 nm under neutral and basic pH conditions. The pH-dependent fluorescence measurements confirmed that the FI of FITC correlates with changes in pH while the FI of NR is pH-independent. The FITC fluorescence signal is highest at pH 10.05, decreases upon acidification, and eventually disappears at $pH \leq 4.5$. Integrating the FI of FITC in the peak area and plotting against pH reveals a sigmoidal behavior (Fig. 2b), whereas that of NR remains constant (Fig. 2c). The plot of the ratio of the integrated FI of FITC and NR as function of pH (Fig. 2d) derives a pKa value of 7.69 that is slightly shifted to basic pH values compared to FITC conjugated only to WGA with a pKa value of 6.7. This shift is attributed to the coupling of FITC to a negatively charged particle [24]. However, due to it being comparatively small no changes in protein structure and activity are expected. The working range of pH 5.5 – 9 is rather broad when compared to other pH sensors, due to the relatively flat slope of the curve. Thus, the working range of the nanosensor for pH detection is well suited for fluorometric pH sensing in the physiological pH range of eukaryotic cells.

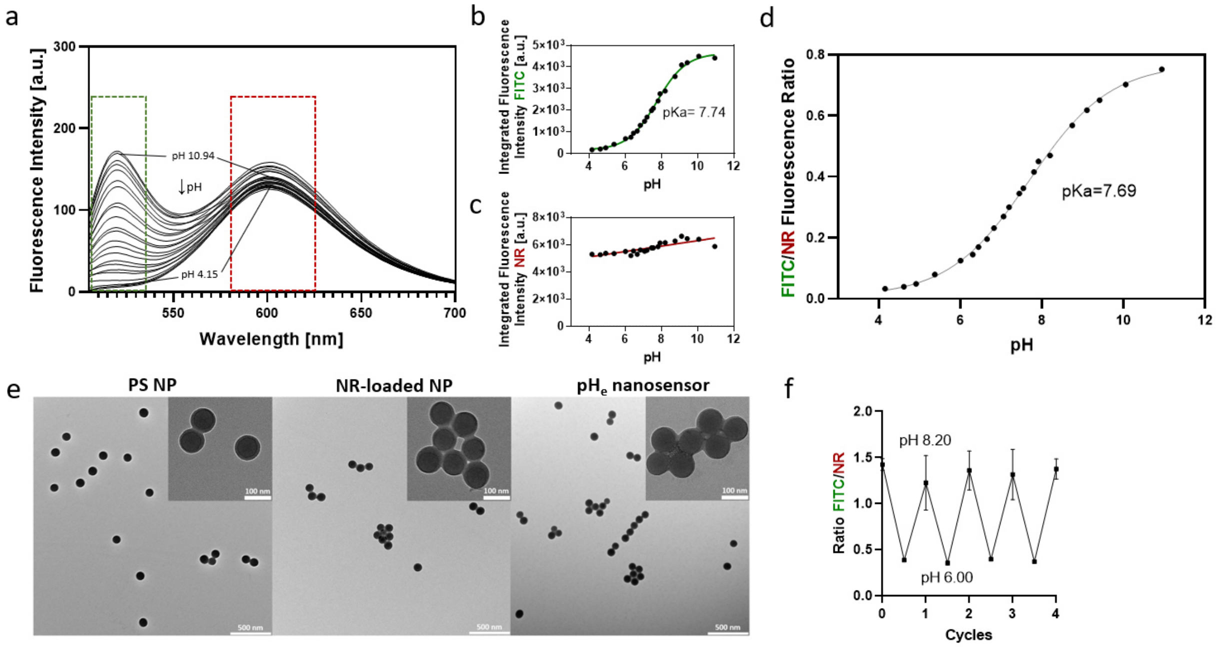

Fig. 2 Characterization of the pH_e nanosensor. **a** Fluorescence spectra of the pH_e nanosensor excited at 485 nm in different buffers with known pH. **b** Sigmoidal fit of the integrated FI of FITC (green box = area of signal integration) plotted against the pH value of the respective buffer. **c** Integrated FI of NR (red box = area of signal integration) plotted against the pH value of the respective buffer and derived pKa value. **d** Ratio of the integrated FI of the FITC and the NR emission plotted against the corresponding pH with sigmoidal curve fit. **e** TEM images of the precursor PS NP (left), the NR-loaded NP (middle), and the pH_e nanosensor consisting of NR-loaded NP conjugated to WGA-FITC (right). **f** pH reversibility study of the pH_e nanosensor between pH 6.0 and 8.2

The reversibility of the pH sensing capabilities of the pH_e nanosensor was tested by imaging the FI ratio of FITC to NR at different pH in the CLSM. After repetitive changes of the extracellular pH between 8.2 and 6.0, the FI ratio of the pH_e nanosensor was not affected (Fig. 2f). Therefore, leaching of the dyes from the sensor and bleaching of the dyes can be excluded, as this would change the FI ratio over time. This reversible response is a prerequisite of pH_e nanosensors to be utilized for tracking continuous pH fluctuations in biological systems over extended periods of time.

Screening target cell lines

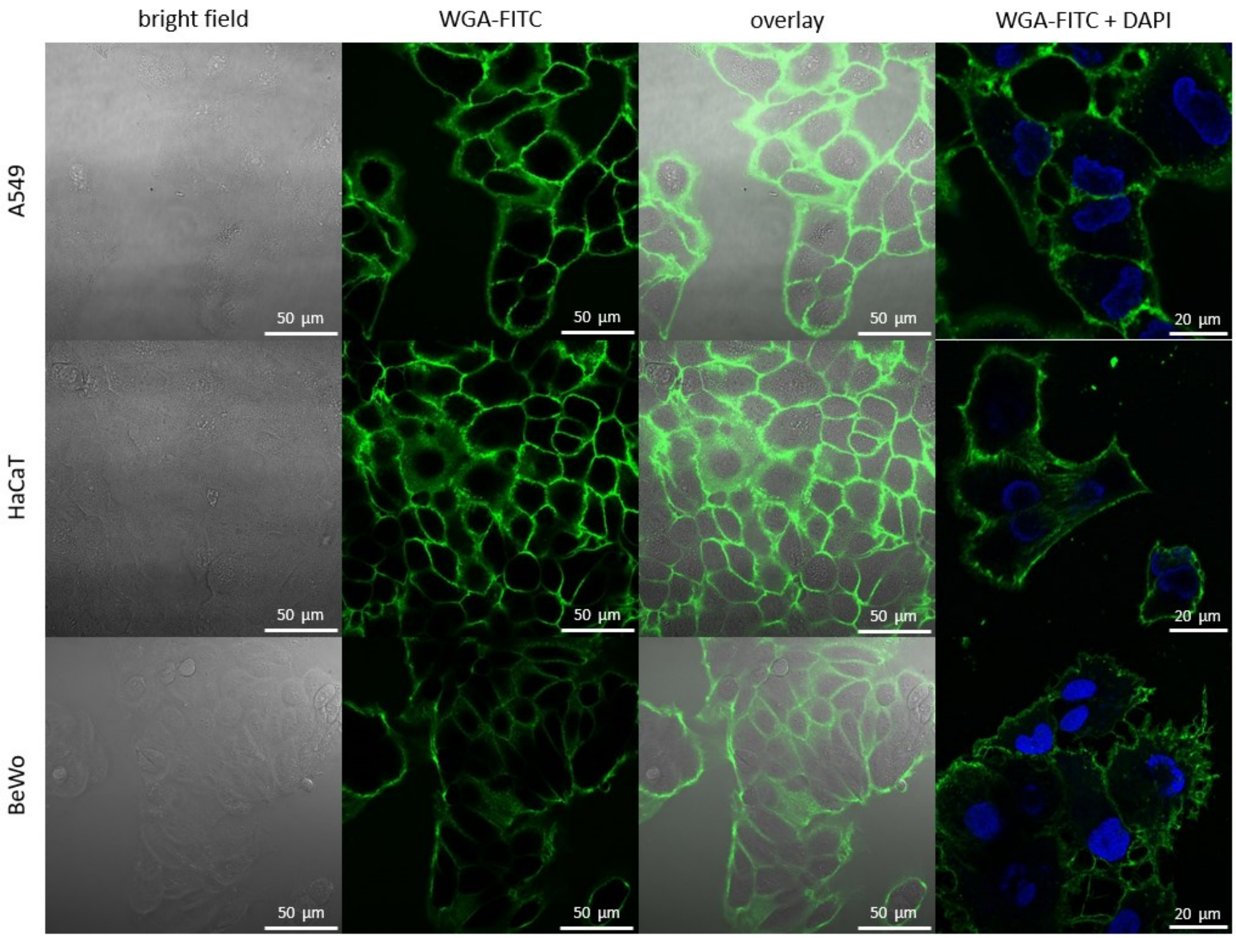

Fig. 3 Screening of targeting capabilities of WGA as a targeting moiety. CLSM images of the lung cell line A549, skin cell line HaCaT and placenta cell line BeWo incubated with 5 µg/mL WGA-FITC (green) and Hoechst for nuclei stain (blue)

To measure the pH_e, the pH_e nanosensor has to be in close proximity to the target cells. Therefore, the pH_e nanosensor was adhered to the cell surface by using the protein WGA as targeting moiety. To first evaluate the suitability of WGA as a cell membrane targeting component, three different cell lines from different tissues were incubated with FITC-labeled WGA and examined with CLSM (Fig. 3). Here, the selection of A549 (human lung epithelial cells), BeWo (human placenta cells), and HaCaT (human skin keratinocytes) aimed to ensure tissue diversity. This selection was made with the understanding that the pH_e is highly relevant across different tissues in an organism. As it can be seen in the CLSM images, WGA exclusively labels the cell membranes of all 3 cell lines without entering the cells. This proves its suitability as a targeting moiety for the cell surfaces of various cell types, enabling the utilization for measuring the pH_e.

To assess the effectiveness of WGA as a targeting moiety when conjugated to the NP, a cell binding assay was performed, quantifying the amount of NP that bind to the cells with and without conjugated WGA (Fig. 4a). For this purpose, suspended cells of the 3 cell lines were incubated with WGA-conjugated nanosensor (WGA NP) and the precursor NP before WGA labeling was used as a non-targeted control sample (control NP). After incubation, the cells were centrifuged, and the supernatant containing unbound NP was removed. The cell-bound NP were quantified via the fluorescence signal of the embedded NR in the NP and were related to the total fluorescence signal of the NP before centrifugation. The largest fraction of the control NP was removed by centrifugation, and only approximately 10 % of the particles were found in the cell pellets. This might be due to electrostatic affinity or other unspecific bindings of the NP to the cells. For the WGA NP, approximately 75-85 % of the particles were found to be bound to the cells, indicating that a large fraction of the WGA NP binds to the cells via specific protein binding. These numbers align with literature values of BSA-WGA binding to, e.g., Caco-2 cells [45]. This indicates that the activity of WGA to act as a targeting moiety in conjunction with the NP is not compromised when the protein is conjugated. To further characterize the targeting properties, the cells were investigated with SEM after incubation with the pH$_e$ nanosensor (Fig. 4c, additional SEM images in the SI). The images revealed that the spherical nanosensors bind to the cell membrane, creating a sensor layer that uniformly covers the cell surface. This uniform distribution is crucial for obtaining strong signal intensities at the area of interest in fluorescence experiments and accurately measuring pH levels locally.

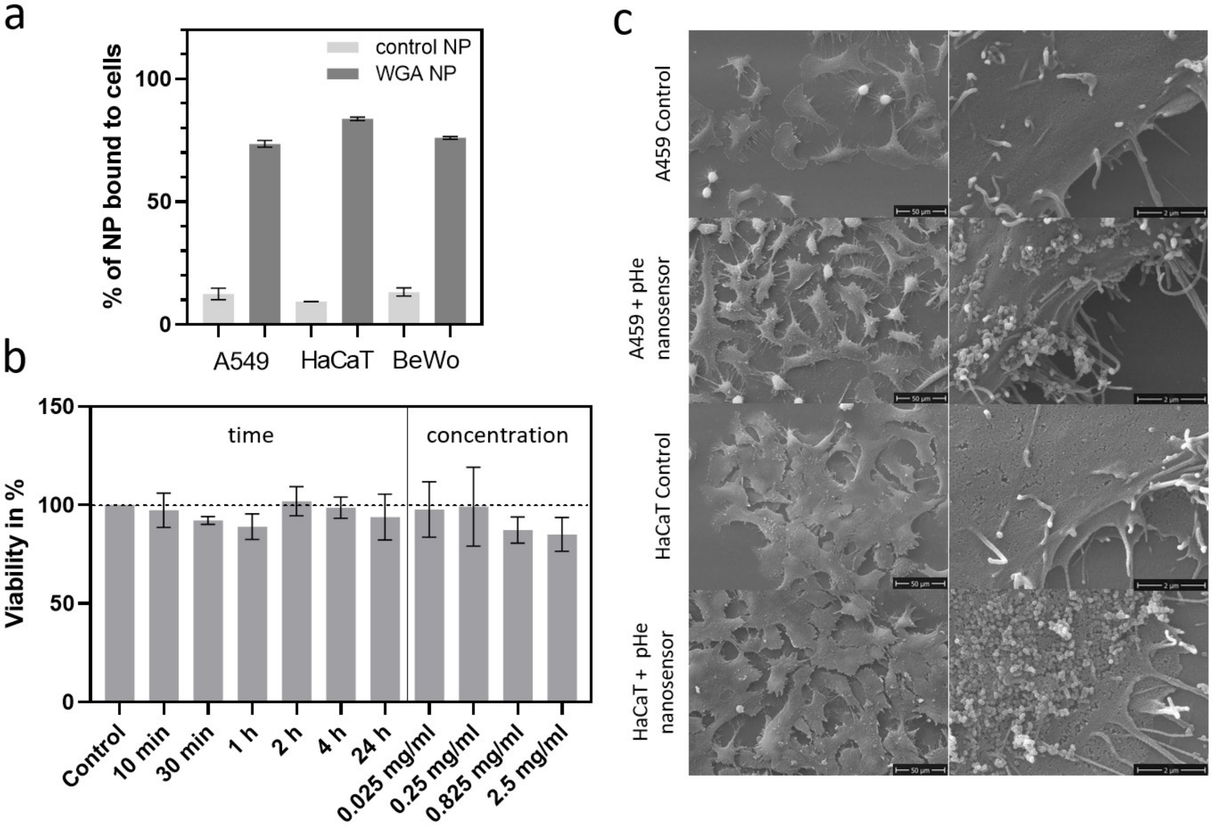

Fig. 4 a pH$_e$ nanosensor cell binding assay with WGA-conjugated nanosensor (WGA NP) and precursor nanosensor without WGA as non-targeted control NP (control NP). The amount of NP bound to the cells was quantified via the NR fluorescence signal and correlated to the total amount of NP (100%) **b** Viability of A549 cells after exposure of the pH$_e$ nanosensor for different time points and different concentrations related to the control without pH$_e$ nanosensor **c** SEM images of A549 and HaCaT cells. Samples without (control) and with the pH$_e$ nanosensor (0.825 mg/ml)

To utilize the nanosensor as a tool for pH$_e$ sensing in *in vitro* applications such as cell cultures, tissues or organoids, it is important that the pH$_e$ nanosensor does not affect the target cells or their viability. Despite the selection of the components used for the pH$_e$ nanosensor being based on components to be known as non-toxic in the concentrations used, a cell viability assay was performed. Here, a WST-1 assay was selected to assess whether exposure of the pH$_e$ nanosensor influences the cell viability (Fig. 4b). Different concentrations and incubation times were tested, ranging from 10 minutes to 24 hours, to cover a variety of application times subsequent for imaging experiments. It was found that no concentration up to the tested maximal concentration of 2.5 mg/mL and none of the incubation times tested showed a significantly toxic effect on the cells. Additionally, no morphological changes were observed in the cells in the SEM images, compared to the control (Fig. 4c, additional SEM images in the SI). Therefore, the pH$_e$ nanosensor was found to be cell-compatible, enabling its safe application, particularly for brief time periods of several minutes or hours in cell culture experiments.

Ideally, pH$_e$ nanosensors should function with minimal impact on cellular processes to avoid disrupting the natural cell environment. Some studies have shown local pH$_e$ measurements with high resolution through the expression of fluorescent sensor molecules by the target cells [46, 47]. Although this method is highly effective, the expression of fluorescent dyes represents a significant intervention in cell physiology. To maintain a cell's natural state during imaging, it is preferable to opt for minimally invasive pH sensing methods. Anderson et al. developed a pH_e measurement tool by attaching a dye to a low-insertion protein that inserts into the cell membrane [48]. The study yielded precise surface pH values with relatively little impact on the cell function. However, local pH determination at the cellular level, which is the ultimate goal of surface pH determination, especially in environments with pH heterogeneities, was lacking.

Imaging of the pH_e nanosensor and determination of pH_e

To investigate the pH_e nanosensors functionality and robustness in cellular applications, its capability to determine the pH on the cell surface was investigated. For this purpose, the three different cell lines were incubated with the pH_e nanosensor and imaged with CLSM in different pH buffers with pH values from 4.15 to 10.05 (Fig. 5). Here, the fluorescence signals of the pH_e nanosensor, were found to localize at the cell membranes, as it can be seen in the overlay images of the BF, the NR (red) and the FITC (green) channel. This shows effective targeting of the cell membranes of all three kinds of cell lines by the pH_e nanosensor, ultimately enabling the direct sensing of pH_e on the surface of the cell. Furthermore, the co-localization of the FITC and NR fluorescence signals shows that both dyes are located at the pH_e nanosensor, and that the dyes did not leak but are stable, hence allowing ratiometric determination of $pH_{e.}$

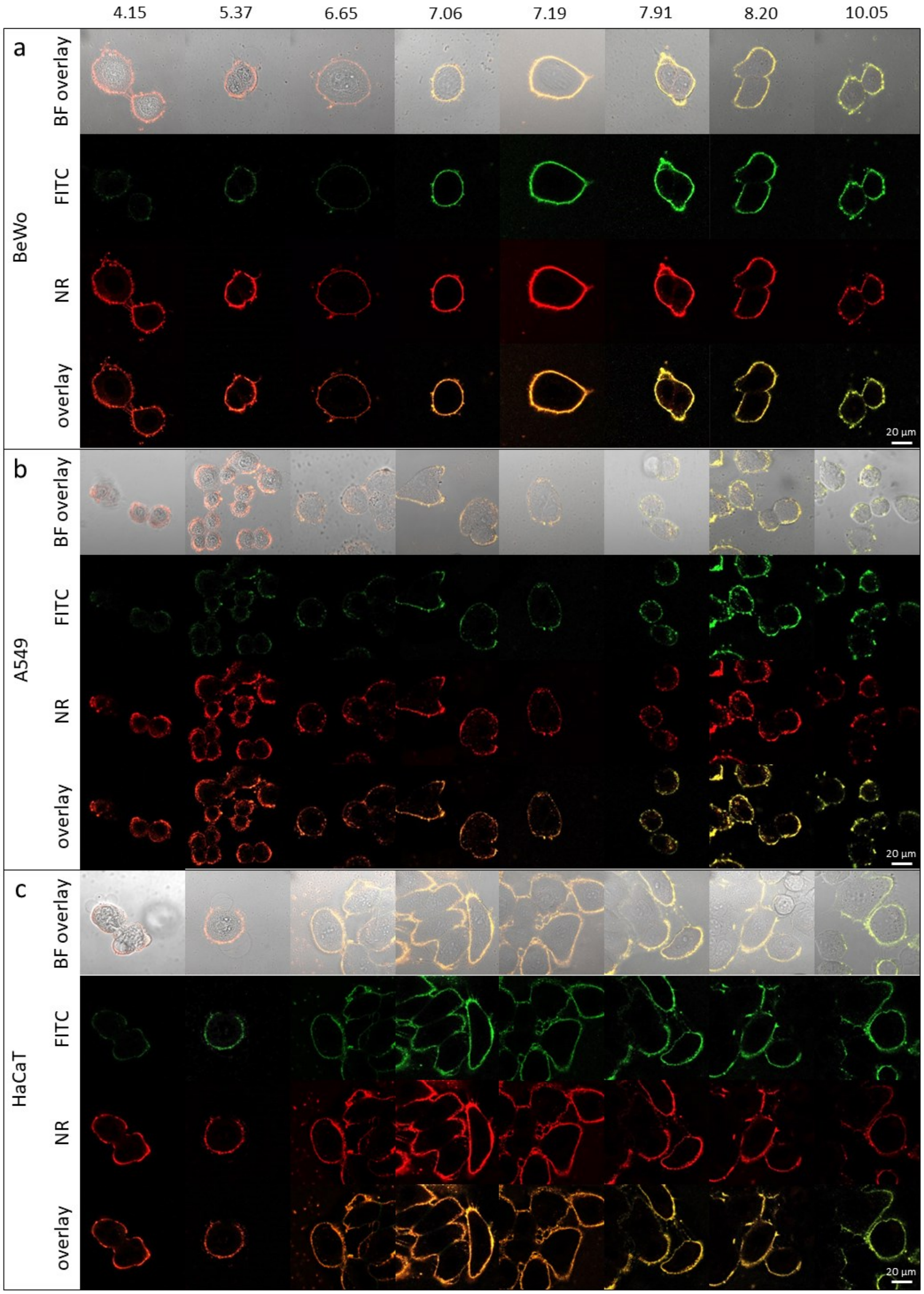

Fig. 5 CLSM images of the 3 different cell lines **a** BeWo, **b** A549 and **c** HaCaT with the pH_e nanosensor. The cells were imaged in 8 different buffers with pH values from 4.15-10.05. Displayed are the FITC (green) and NR (red) channels, the fluorescence overlay and the bright field channel with fluorescence overlay. The 20 µm scale bar applies to all images

When imaging the pH_e nanosensor and the cells in buffers with known pH, the FI of FITC does respond according to the pH value with high FI in basic pH and low FI in acidic pH. This also can be seen in the overlay of the FITC and NR fluorescence channels showing the ratio of the two channels as a color change from red to yellow for acidic to basic pH. The mathematical realization of this overlay is the calculation of the FI ratio, by dividing the FITC FI through the NR FI. This ratiometric concept allows a correlation of the calculated FI ratio with pH, neglecting local concentration differences of the pH_e nanosensor. Plotting the FI ratio against each corresponding pH, yields a calibration curve for each individual cell line tested (Fig. 6). Notably, the pH curves and pKa values observed in the cell culture experiments align with those determined in the acellular assay, highlighting the pH_e nanosensor's robustness. The pH_e nanosensor's functionality is not compromised by the biological system despite variations in experimental conditions, including salt concentrations, protein interactions, matrix effects, and cellular autofluorescence. This robustness is essential to affirm the sensor's suitability for biological applications, demonstrating its ability to remain functional even in complex biological environments.

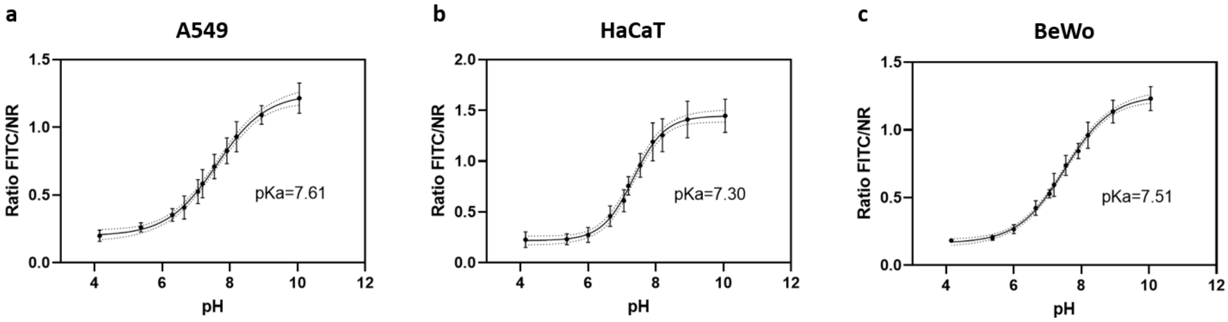

Fig. 6 The calibration curves derived from the CLSM experiments in the pH range from 4.15 to 10.05 with sigmoidal curve fit in the three cell lines **a** A549, **b** HaCaT and **c** BeWo and the respective derived pKa values

The advantage of the pH_e nanosensor is its remarkably simple experimental procedure for labeling cell surfaces and therefore the target cell line. In contrast to some sensors that need to be genetically encoded to be expressed on the cells surface [46, 47] or extensivly incubated (several hours to overnight) [40], the pH_e nanosensor's application only required a single step: just adding it to the cell culture medium for 10 minutes. Regarding the simplicity of the labeling procedure, a PEG-FITC-based probe by Ohgaki et al [49] is comparable to the pH_e nanosensor. A drawback of the aforementioned probe is its narrow pH measuring range of aprox. 5.5 – 7. Chen et al also report a sensor with a similar limited pH measuring range of 6.4 to 5.9 [50]. Such a narrow pH range reduces a sensors applicability to very specific areas of interest. Nevertheless, their sensor system exhibits great potential for pH_e measurement through anchoring a lipid to the cell membrane.

CONCLUSIONS

In this study, a ratiometric pH_e nanosensor for the determination of extracellular pH was developed. The measurement of pH_e with this nanosensor is fast, robust, fully reversible, and the nanosensor showed no leaching of dyes even after long periods of time. By conjugating the nanosensor with a protein that binds to cell surfaces, the pH_e nanosensor can rapidly target different cell lines of interest such as lung, skin and placenta cells. As demonstrated by CLSM and SEM experiments, the active targeting approach proves to be highly effective, thus enabling the pH_e nanosensor to accurately measure pH levels on the surface of cells. This approach enables a very precise and locally resolved measurement of the pH_e whilst being cell-compatible and universally applicable in cell lines of different tissues.

In the future, this pH_e nanosensor can further advance the understanding of cellular microenvironments. The nanosensor can be utilized for a variety of applications in biomedical research in which the extracellular pH level may be of critical importance, such as cancer research, studies on metabolic disorders, and for diagnostic and treatment applications.

Acknowledgments
The authors want to thank Ashish Gadicherla for carrying out the TEM analysis.

Authors' contributions
The study was designed by C.K. and H.R.T. Experiments were performed by C.K. and I.F. The data analysis was performed by C.K. and A.K. The manuscript was written by C.K. and H.R.T. and critically reviewed by A.K., I.F., P.L., and A.L.

Supplementary Information
Table with dye and protein loading of the pH_e nanosensor
SEM images of the cells with and without pH_e nanosensor

Data availability
Data underlying the results presented in this paper can be found in the Supplementary Information or obtained from the corresponding author upon reasonable request.

Funding
This study was funded by the German Federal Institute for Risk Assessment, Grant Number: SFP 1322-721.

Competing interests
The authors have no relevant financial or non-financial competing interests to disclose.

REFERENCES

1. Casey, J.R., S. Grinstein, and J. Orlowski, *Sensors and regulators of intracellular pH.* Nat Rev Mol Cell Biol, 2010. **11**(1): p. 50-61.
2. Putnam, R.W., *Chapter 17 - Intracellular pH Regulation*, in *Cell Physiology Source Book (Fourth Edition)*, N. Sperelakis, Editor. 2012, Academic Press: San Diego. p. 303-321.
3. Lagadic-Gossmann, D., L. Huc, and V. Lecureur, *Alterations of intracellular pH homeostasis in apoptosis: origins and roles.* Cell Death & Differentiation, 2004. **11**(9): p. 953-961.
4. Swietach, P., R.D. Vaughan-Jones, and A.L. Harris, *Regulation of tumor pH and the role of carbonic anhydrase 9.* Cancer Metastasis Rev, 2007. **26**(2): p. 299-310.
5. Lardner, A., *The effects of extracellular pH on immune function.* J Leukoc Biol, 2001. **69**(4): p. 522-30.
6. Ke, G., et al., *A Cell-Surface-Anchored Ratiometric Fluorescent Probe for Extracellular pH Sensing.* ACS Applied Materials & Interfaces, 2014. **6**(17): p. 15329-15334.
7. Lim, H., et al., *Longitudinal Measurements of Intra- and Extracellular pH Gradient in a Rat Model of Glioma.* Tomography, 2018. **4**(2): p. 46-54.
8. Hashim, A.I., et al., *Imaging pH and metastasis.* NMR Biomed, 2011. **24**(6): p. 582-91.
9. Delli Castelli, D., et al., *In vivo maps of extracellular pH in murine melanoma by CEST–MRI.* Magnetic Resonance in Medicine, 2014. **71**(1): p. 326-332.
10. Lutz, N.W., et al., *Quantitative in vivo characterization of intracellular and extracellular pH profiles in heterogeneous tumors: a novel method enabling multiparametric pH analysis.* Cancer Res, 2013. **73**(15): p. 4616-28.
11. Swietach, P., et al., *The role of carbonic anhydrase 9 in regulating extracellular and intracellular ph in three-dimensional tumor cell growths.* J Biol Chem, 2009. **284**(30): p. 20299-310.
12. Korenchan, D.E. and R.R. Flavell, *Spatiotemporal pH Heterogeneity as a Promoter of Cancer Progression and Therapeutic Resistance.* Cancers (Basel), 2019. **11**(7).
13. Martínez-Zaguilán, R., et al., *Acidic pH enhances the invasive behavior of human melanoma cells.* Clin Exp Metastasis, 1996. **14**(2): p. 176-86.

14. Sutoo, S., et al., *Adaptation to chronic acidic extracellular pH elicits a sustained increase in lung cancer cell invasion and metastasis.* Clin Exp Metastasis, 2020. **37**(1): p. 133-144.
15. Swietach, P., et al., *The chemistry, physiology and pathology of pH in cancer.* Philos Trans R Soc Lond B Biol Sci, 2014. **369**(1638): p. 20130099.
16. Parks, S.K., J. Chiche, and J. Pouyssegur, *pH control mechanisms of tumor survival and growth.* J Cell Physiol, 2011. **226**(2): p. 299-308.
17. Zhang, X., Y. Lin, and R.J. Gillies, *Tumor pH and its measurement.* J Nucl Med, 2010. **51**(8): p. 1167-70.
18. Zhao, X., et al., *Branched Au Nanoparticles on Nanofibers for Surface-Enhanced Raman Scattering Sensing of Intracellular pH and Extracellular pH Gradients.* ACS Sensors, 2020. **5**(7): p. 2155-2167.
19. Zhang, Y., et al., *High-resolution label-free 3D mapping of extracellular pH of single living cells.* Nature Communications, 2019. **10**(1): p. 5610.
20. Huang, Y., et al., *Towards longitudinal mapping of extracellular pH in gliomas.* NMR in Biomedicine, 2016. **29**(10): p. 1364-1372.
21. Chan, Y.-H., et al., *Development of Ultrabright Semiconducting Polymer Dots for Ratiometric pH Sensing.* Analytical Chemistry, 2011. **83**(4): p. 1448-1455.
22. Chen, S., et al., *Full-Range Intracellular pH Sensing by an Aggregation-Induced Emission-Active Two-Channel Ratiometric Fluorogen.* Journal of the American Chemical Society, 2013. **135**(13): p. 4926-4929.
23. Marín, M.J., et al., *Localized Intracellular pH Measurement Using a Ratiometric Photoinduced Electron-Transfer-Based Nanosensor.* Angewandte Chemie International Edition, 2012. **51**(38): p. 9657-9661.
24. Steinegger, A., O.S. Wolfbeis, and S.M. Borisov, *Optical Sensing and Imaging of pH Values: Spectroscopies, Materials, and Applications.* Chemical Reviews, 2020. **120**(22): p. 12357-12489.
25. Shi, W., X. Li, and H. Ma, *A tunable ratiometric pH sensor based on carbon nanodots for the quantitative measurement of the intracellular pH of whole cells.* Angew Chem Int Ed Engl, 2012. **51**(26): p. 6432-5.
26. Pang, C., et al., *The Establishment and Application Studies on Precise Lysosome pH Indicator Based on Self-Decomposable Nanoparticles.* Nanoscale Research Letters, 2020. **15**(1): p. 143.
27. Nandi, N., et al., *Ratiometric Multimode Detection of pH and Fe3+ by Dual-Emissive Heteroatom-Doped Carbon Dots for Living Cell Applications.* ACS Applied Nano Materials, 2022. **5**(11): p. 17315-17324.
28. Tian, Y., et al., *A series of naphthalimide derivatives as intra and extracellular pH sensors.* Biomaterials, 2010. **31**(29): p. 7411-7422.
29. Li, F., et al., *Ratiometric Fluorescent Microgels for Sensing Extracellular Microenvironment pH during Biomaterial Degradation.* ACS Omega, 2020. **5**(31): p. 19796-19804.
30. Munteanu, R.-E., et al., *Measurement of the Extracellular pH of Adherently Growing Mammalian Cells with High Spatial Resolution Using a Voltammetric pH Microsensor.* Analytical Chemistry, 2018. **90**(11): p. 6899-6905.
31. Kromer, C., et al., *Monitoring and imaging pH in biofilms utilizing a fluorescent polymeric nanosensor.* Scientific Reports, 2022. **12**(1): p. 9823.
32. You, Z., et al., *Separation of polystyrene nanoparticles bearing different carboxyl group densities and functional groups quantification with capillary electrophoresis and asymmetrical flow field flow fractionation.* Journal of Chromatography A, 2020. **1626**: p. 461392.
33. Behnke, T., et al., *Encapsulation of hydrophobic dyes in polystyrene micro- and nanoparticles via swelling procedures.* J Fluoresc, 2011. **21**(3): p. 937-44.
34. Kromer, C., et al., *ROS generating BODIPY loaded nanoparticles for photodynamic eradication of biofilms.* Frontiers in Microbiology, 2023. **14**.

35. Oviedo, M.J., et al., *Determination of conjugated protein on nanoparticles by an adaptation of the Coomassie blue dye method.* MethodsX, 2019. **6**: p. 2134-2140.
36. Loos, C., et al., *Functionalized polystyrene nanoparticles as a platform for studying bio-nano interactions.* Beilstein J Nanotechnol, 2014. **5**: p. 2403-12.
37. Hesler, M., et al., *Multi-endpoint toxicological assessment of polystyrene nano- and microparticles in different biological models in vitro.* Toxicology in Vitro, 2019. **61**: p. 104610.
38. Bensley, J.G., et al., *Three-dimensional direct measurement of cardiomyocyte volume, nuclearity, and ploidy in thick histological sections.* Scientific Reports, 2016. **6**(1): p. 23756.
39. Mohammadpour, R., et al., *Comparative Endocytosis Mechanisms and Anticancer Effect of HPMA Copolymer- and PAMAM Dendrimer-MTCP Conjugates for Photodynamic Therapy.* Macromolecular Bioscience, 2017. **17**(4): p. 1600333.
40. Yang, Y., et al., *A Cell-Surface-Specific Ratiometric Fluorescent Probe for Extracellular pH Sensing with Solid-State Fluorophore.* ACS Sensors, 2018. **3**(11): p. 2278-2285.
41. Xiao, D., et al., *Advances and Challenges of Fluorescent Nanomaterials for Synthesis and Biomedical Applications.* Nanoscale Research Letters, 2021. **16**(1): p. 167.
42. Cho, E.J., et al., *Nanoparticle Characterization: State of the Art, Challenges, and Emerging Technologies.* Molecular Pharmaceutics, 2013. **10**(6): p. 2093-2110.
43. Varsou, D.-D., et al., *Zeta-Potential Read-Across Model Utilizing Nanodescriptors Extracted via the NanoXtract Image Analysis Tool Available on the Enalos Nanoinformatics Cloud Platform.* Small, 2020. **16**(21): p. 1906588.
44. Ramaye, Y., et al., *Development and Validation of Optical Methods for Zeta Potential Determination of Silica and Polystyrene Particles in Aqueous Suspensions.* Materials (Basel), 2021. **14**(2).
45. Gabor, F., A. Schwarzbauer, and M. Wirth, *Lectin-mediated drug delivery: binding and uptake of BSA-WGA conjugates using the Caco-2 model.* International Journal of Pharmaceutics, 2002. **237**(1): p. 227-239.
46. Goryashchenko, A.S., et al., *FLIM-Based Intracellular and Extracellular pH Measurements Using Genetically Encoded pH Sensor.* Biosensors, 2021. **11**(9): p. 340.
47. Urra, J., et al., *A genetically encoded ratiometric sensor to measure extracellular pH in microdomains bounded by basolateral membranes of epithelial cells.* Pflugers Arch, 2008. **457**(1): p. 233-42.
48. Anderson, M., et al., *Probe for the measurement of cell surface pH in vivo and ex vivo.* Proceedings of the National Academy of Sciences, 2016. **113**(29): p. 8177-8181.
49. Ohgaki, R., et al., *Ratiometric fluorescence imaging of cell surface pH by poly(ethylene glycol)-phospholipid conjugated with fluorescein isothiocyanate.* Sci Rep, 2017. **7**(1): p. 17484.
50. Chen, B., et al., *A Mimosa-Inspired Cell-Surface-Anchored Ratiometric DNA Nanosensor for High-Resolution and Sensitive Response of Target Tumor Extracellular pH.* Analytical Chemistry, 2020. **92**(22): p. 15104-15111.

3.3. ROS generating BODIPY loaded NPs for photodynamic eradication of biofilms

Charlotte Kromer, Karin Schwibbert, Sebastian Radunz, Dorothea Thiele, Peter Laux, Andreas Luch, and Harald R. Tschiche

Published online on 12 October 2023 in:
Frontiers in Microbiology 14:1274715
DOI: 10.3389/fmicb.2023.1274715
Link: https://doi.org/10.3389/fmicb.2023.1274715

Involvement of the author within this publication: Conceptualization, Data curation, Formal Analysis, Investigation, Visualization, Writing of the manuscript.

Author contributions as published: CK: Conceptualization, Data curation, Formal Analysis, Investigation, Visualization, Writing – original draft. KS: Supervision, Writing – original draft. SR: Investigation, Writing – review & editing. DT: Investigation, Writing – review & editing. PL: Writing – review & editing. AL: Supervision, Writing – review & editing. HT: Conceptualization, Supervision, Writing–original–draft.

Online Supplementary Material is presented in Annex III.

Frontiers in Microbiology

TYPE Original Research
PUBLISHED 12 October 2023
DOI 10.3389/fmicb.2023.1274715

OPEN ACCESS

EDITED BY
Lichong Xu,
The Pennsylvania State University, United States

REVIEWED BY
Jiang Yuan,
Nanning Normal University, China
Shakir Khan,
Harvard Medical School, United States

*CORRESPONDENCE
Charlotte Kromer
✉ Charlotte.Kromer@bfr.bund.de

RECEIVED 08 August 2023
ACCEPTED 19 September 2023
PUBLISHED 12 October 2023

CITATION
Kromer C, Schwibbert K, Radunz S, Thiele D, Laux P, Luch A and Tschiche HR (2023) ROS generating BODIPY loaded nanoparticles for photodynamic eradication of biofilms.
Front. Microbiol. 14:1274715.
doi: 10.3389/fmicb.2023.1274715

ROS generating BODIPY loaded nanoparticles for photodynamic eradication of biofilms

Charlotte Kromer[1,2]*, Karin Schwibbert[3], Sebastian Radunz[4], Dorothea Thiele[3], Peter Laux[1], Andreas Luch[1,2] and Harald R. Tschiche[1]

[1]Department Chemicals and Product Safety, Product Materials and Nanotechnology, German Federal Institute for Risk Assessment, Berlin, Germany, [2]Institute of Pharmacy, Freie Universität Berlin, Berlin, Germany, [3]Department Materials and the Environment, Biodeterioration and Reference Organisms, Federal Institute for Materials Research and Testing, Berlin, Germany, [4]nanoPET Pharma GmbH, Berlin, Germany

Bacterial biofilms can pose a serious health risk to humans and are less susceptible to antibiotics and disinfection than planktonic bacteria. Here, a novel method for biofilm eradication based on antimicrobial photodynamic therapy utilizing a nanoparticle in conjunction with a BODIPY derivative as photosensitizer was developed. Reactive oxygen species are generated upon illumination with visible light and lead to a strong, controllable and persistent eradication of both planktonic bacteria and biofilms. One of the biggest challenges in biofilm eradication is the penetration of the antimicrobial agent into the biofilm and its matrix. A biocompatible hydrophilic nanoparticle was utilized as a delivery system for the hydrophobic BODIPY dye and enabled its accumulation within the biofilm. This key feature of delivering the antimicrobial agent to the site of action where it is activated resulted in effective eradication of all tested biofilms. Here, 3 bacterial species that commonly form clinically relevant pathogenic biofilms were selected: *Escherichia coli*, *Staphylococcus aureus* and *Streptococcus mutans*. The development of this antimicrobial photodynamic therapy tool for biofilm eradication takes a promising step towards new methods for the much needed treatment of pathogenic biofilms.

KEYWORDS

biofilm, disinfection, antimicrobials, photodynamic therapy, aPDT, nanoparticles, BODIPY

1. Introduction

Biofilms are microbial communities adhered to surfaces and surrounded by a self-produced matrix, mainly composed of water and extracellular polymeric substances (EPS) (Flemming and Wingender, 2010). The matrix plays an important role in biofilm formation by providing the biofilm with structural integrity as well as increased resistance to external influences such as temperature changes, desiccation, shear forces and also disinfection (Donlan and Costerton, 2002; Flemming and Wingender, 2010). In addition, it forms a reservoir for nutrients and allows the microorganisms to establish long-term synergistic associations characterized by social interactions and community evolution (Hansen et al., 2007; Flemming et al., 2016).

Infections caused by bacteria including those involving biofilms pose a global threat to human health. Particularly devastating is the ever-evolving resistance of bacteria to existing treatments. Biofilm formation protects bacteria from common cleaning procedures like disinfection and allows further colonization (Dang and Lovell, 2016). Strategies for biofilm control currently used include cleaning and disinfection, material selection and surface treatments such as application of ultraviolet light, plasma, and ultrasonic treatment. In the medical field and for application in humans, the use of antibiotics plays a fundamental role. Most of these methods are primarily aimed at killing planktonic bacteria or inhibiting their growth and are, therefore, not sufficient to control biofilms entirely (Ciofu et al., 2022). Two problems are recognized to be inextricably linked to this approach: (I) the frequently observed development of resistance to antimicrobial agents and (II) the fact that therapeutic agents are much less effective on bacteria growing in biofilms compared to planktonic cells (Mah and O'Toole, 2001). The latter point is of particular importance because in recent years there has been mounting evidence that most chronic bacterial infections are associated with biofilms (Macia et al., 2014; Kolpen et al., 2022). The rapid development of resistance in many bacterial species is also highly problematic as it makes future eradication even more challenging. Therefore, strategies to overcome bacterial persistence by inhibiting biofilm formation or removing mature biofilms that are effective and can be used long term are urgently needed.

A great hope lies in the utilization of *in situ* generated reactive oxygen species (ROS). This concept is already applied in photodynamic therapy (PDT). PDT uses photosensitizers (PS) that are activated by visible or near-infrared light but are non-toxic without illumination. The PS first forms an excited singlet state, followed by a transition to the long-lived excited triplet state, which undergoes photochemical reactions in the presence of oxygen and generates ROS (Bekmukhametova et al., 2020). The ROS can then destroy biological targets such as cancer cells and microbes including bacteria (Hu et al., 2018). When PDT is applied to combat microbes, such as bacteria, it is often referred to as antimicrobial photodynamic therapy (aPDT). A key advantage of aPDT is that ROS damage is completely non-specific and, thus, can be used on all bacteria, as there is no known resistance to ROS (Hughes and Webber, 2017). Commonly used classes of PS are porphyrins, squarains, phenothiazines and boron-dipyrromethene (BODIPY) (Bekmukhametova et al., 2020). BODIPY dyes are excellent candidates for the development of modern aPDT strategies due to their particularly remarkable photophysical properties, such as high molar absorption coefficients, high quantum yields for ROS generation and high photostability (Rebeca and Jorge, 2018; Boens et al., 2019; Radunz et al., 2020). Additionally, they are a highly versatile dye class that can be easily prepared and structurally altered to benefit various applications (Bañuelos, 2016; Sheng et al., 2019; Radunz et al., 2020).

Generally, the applicability of many PS molecules is limited by their poor water solubility, aggregation behavior and impaired ability to sufficiently penetrate tissues and biofilms (Abrahamse and Hamblin, 2016; Songca and Adjei, 2022). In addition, the lifetime of the generated singlet oxygen is very short, limiting its diffusion to only 10–55 nm (Dysart and Patterson, 2005). Therefore, the photodynamic damage is likely to occur only in close proximity to the location of the PS, thus, the ROS generation has to be induced at the target site, e.g., inside the biofilm (Moan et al., 1989). The higher the concentration of the PS inside the biofilm, the better the therapeutic performance (Bekmukhametova et al., 2020).

Nanoparticles (NPs) can be utilized to act as carriers for the PS to facilitate the delivery and accumulation within the biofilm. By using hydrophilic particles in which the dye is embedded, the solubility issues of the mostly hydrophobic PS can be circumvented. In addition, there is the possibility of using NPs that can enable active targeting, e.g., by binding to specific cell components or biofilm structures, e.g., by utilizing protein conjugation. However, the NPs accumulation in the biofilm is also possible in a passive manner through diffusion, influenced by their charge, size or hydrophobicity (De-la-Pinta et al., 2019; Hollmann et al., 2021). This allows high amounts of PS to be concentrated locally at the target site, especially if the particles have a high dye loading.

Several studies have shown the bactericidal effect of aPDT utilizing NPs, e.g., methylen blue-loaded gold NPs (Khan et al., 2017) and chitosan NPs (Yaghoubi et al., 2020), curcumin-loaded PLGA NPs (Raschpichler et al., 2019) toluidine blue-loaded alginate NPs (Usacheva et al., 2016) and rose bengal-loaded chitosan NPs (Shrestha et al., 2014). However, there are limitations to the published methods that constrain their successful use for biofilm removal. For example, elimination rates lower than 2 log units achieved with toluidine blue or methylen blue-loaded NPs cannot be viewed as sufficient biofilm removal (Klepac-Ceraj et al., 2011; Usacheva et al., 2016; Anju et al., 2019). This is particularly important as biofilms can proliferate and rebuild their population quickly, even if only a few bacterial cells survive. The commonly used PS Rose Bengal was also used in several NPs applications but showed relevant dark toxicity interfering with the aPDT treatment (Shrestha et al., 2014; Anju et al., 2018). The use of highly effective yet controllable PS for photodynamic eradication of biofilms is therefore urgently needed.

In general, the effect of aPDT on planktonic bacterial cells is higher than on biofilms. Most published methods are able to eradicate planktonic bacteria by several log units; however, for biofilms, the reduction is only in the double-digit percentage range (Anju et al., 2018; Dai et al., 2018; Anju et al., 2019). Reasons for this are the more difficult penetration of PS into biofilms due to EPS and the generally higher concentration of bacteria in the biofilm compared to a suspension in medium (Li et al., 2023). In addition, bacteria in different physiological stages are present in a biofilm, which means that not all of them are in a vulnerable, proliferating state (Ciofu et al., 2022). Some may be in a dormant state with a lower metabolism, which also limits the internalization of substances and thus the effectiveness of many treatment agents. It is therefore important to develop systems that are also highly effective in biofilms.

It is well-known, that gram-positive bacteria are more susceptible to aPDT than gram-negative bacteria, due to their cell wall composition (Bekmukhametova et al., 2020). Studies have confirmed this fact and shown that gram-negative bacteria are up to 10 times less sensitive than gram-positive bacteria (Yang et al., 2012; Kirar et al., 2018). Therefore, investigations for utilizing aPDT for biofilm eradication should also be carried out on gram-negative as well as gram-positive bacteria. On top, the functionality and also the limitations of aPDT in relation to the composition of the cell wall should be investigated further.

The efficacy of aPDT systems can be significantly increased by the development of more complex and sophisticated aPDT systems, for example in combination with other antibacterial agents (Pérez-Laguna et al., 2019; Songca and Adjei, 2022). However, when considering these developments in terms of their practicability, it is at least as important to develop systems that are easy to manufacture and use and yet highly effective.

In this study, a highly effective PS combined with a facile NP delivery system was utilized to overcome the limitations of previously described aPDT systems to achieve effective eradication of both, planktonic bacteria and biofilms. For this purpose, a highly effective diiodinated BODIPY derivative that can be excited with visible light with a wavelength of 530 nm was embedded in polystyrene NPs. Both Gram-positive and Gram-negative biofilm-forming bacteria with high clinical relevance were selected to evaluate the effectiveness of the BODIPY-loaded NPs for aPDT of planktonic bacteria and biofilms.

2. Methods

2.1. Materials and reagents

All solvents (tetrahydrofuran (THF), ethanol, acetonitrile and dimethylsulfoxide) were of analytical grade, purchased from Merck and Thermo Fisher Scientific, and used as received. The 100 nm polystyrene NPs were purchased from Kisker Biotech and ultrasonicated prior to use. *Escherichia coli* (*E. coli*), *Staphylococcus aureus* (*S. aureus*), and *Streptococcus mutans* (*S. mutans*) were purchased from DSMZ-German collection of microorganisms and cell cultures. All cell culture materials and ingredients were obtained from Merck, VWR, and Thermo Fisher Scientific.

2.2. BODIPY synthesis

The synthesis as well as analytical and optical characterization of the iodinated BODIPY dye has been reported previously (Radunz et al., 2020). For this study, 4,4-difluoro-1,3,5,7-tetramethyl-8-(4-hydroxyphenyl)-bora-3a, 4a-diaza-s-indacene was used as precursor dye for the synthesis of the diiodinated singlet oxygen-generating BODIPY (Radunz et al., 2017). All compounds subjected to biological assays were of >95% purity (ultra performance liquid chromatography). All reagents and solvents employed for the synthesis and characterization were used without further purification.

N-Iodosuccinimide (2.2 equiv.) was added slowly in small portions to a stirred solution of the precursor BODIPY (1 equiv.) in 100 mL of dichloromethane. After complete addition of the N-Iodosuccinimide, the reaction mixture was stirred for further 60 min. Then, the reaction mixture was washed with deionized water and subsequently dried over $MgSO_4$. Purification was performed by column chromatography in the dark using dichloromethane/petroleum ether (1/1, v/v) as eluents followed by recrystallization by chloroform/n-hexane.

4,4-Difluoro-2,6-diiodo-1,3,5,7-tetramethyl-8-(4-hydroxyphenyl) -bora-3a,4a-diaza-s-indacene. Yield 23%; UPLC: >95% purity; 1H NMR (500 MHz, CDCl3) [ppm]: $\delta = 7.04$ (d, $2H_{aryl}$), 6.98 (d, $2H_{aryl}$), 2.63 (s, $6H_{methyl}$), 1.48 (s, $6H_{methyl}$); 13C NMR (125 MHz, CDCl3) [ppm]: $\delta = 158.2$, 156.3, 145.5, 142.2, 131.8, 129.0, 125.4, 116.3, 85.3, 17.0, 15.8; MS (ESI-TOF): m/z calculated for $C19H17BF2I2N2NaO^+$ [M + Na]+: 614.9389; found: 614.9417.

2.3. Nanoparticle preparation

The nanosensor was prepared from commercially available polystyrene NPs and a diiodinated BODIPY derivative. The BODIPY dye was incorporated into the NPs via a swelling procedure published by Behnke et al. (2011). In brief, BODIPY was first dissolved in THF in a concentration of 3 nmol/1 µL. Dye loading of the NPs was performed by addition of 100 µL of the BODIPY-containing solution to 600 µL of an aqueous suspension of the NPs (5 mg/mL). The suspension was shaken for 30 min at room temperature, followed by 40 min centrifugation at 16,000 g (Eppendorf centrifuge 5415D). The supernatant consisting of unembedded BODIPY dye was removed from the BODIPY-loaded NPs. The purification steps consisted of a total of 5 washing steps starting with MilliQ water, followed by 2 washing steps with ethanol and 2 final washing steps with MilliQ water.

2.4. Particle size and zeta potential

The particle size (hydrodynamic diameter) and polydispersity index (PDI) of the NPs was determined by dynamic light scattering (DLS) (Zetasizer Malvern Panalytical, Malvern Nano ZS). Measurements were carried out in MilliQ water at 50 µg/mL in a quartz glass cuvette. Thermal equilibration time was set to 60 s at 25°C. Each intensity-weighted size distribution represents the average of 10 individual DLS analyses and three independent replicates. A Dip cell kit (Malvern Panalytical) was used for the determination of the zeta potential. The average of 10 individual zeta potential analyses and three independent replicates were determined. The particle size was also assessed using a transmission electron microscope (TEM). Formvar coated copper and gold grids with 400 mesh and 3.5 mm diameter (Plano GmbH, Germany) were hydrophilized with 0.2% alcian blue (Sigma Aldrich, Germany) in 0.03% acetic acid solution. The grids were floated on alcian blue droplets for 10 min, and dried using a filter paper. 5 µL of a 1 mg/mL NPs dispersion was applied immediately on each hydrophilized grid, incubated for 1 min and the excess liquid was removed with a filter paper. Samples on the copper and gold grids were observed in a Jeol 1,400 Plus TEM (Jeol GmbH, Germany) operated at 120 kV. Material identification was done using diffraction pattern from published resources. Imaging was performed using a Veleta G2 camera (Olympus, Germany). Particle size was measured using iTEM software provided by Olympus. At least 4 different areas of each grid were examined per sample.

2.5. Dye loading

Dye loading was determined by a spectrophotometric method (FoodALYT, Germany). A calibration curve for the absorbance of BODIPY in THF at 530 nm was prepared to evaluate the dye loading. The concentration range of 2.5–20 nmol/mL was linear with $R = 0.9813$ determined by a linear regression model. As a second step, three different volumes of BODIPY-loaded NPs suspension were added to Eppendorf tubes and centrifuged at 16.000 g for 40 min. The supernatant was removed, and the NPs were dissolved in 1000 µL THF. The absorption at 530 nm was determined in a spectrophotometer. The dye concentration in 1000 µL THF was calculated as dye equivalents to the calibration curve. Lastly, the dye loading per mg NPs was calculated.

2.6. ROS assay

Singlet oxygen generation by the BODIPY dye was quantified by an indirect method using 1,3-diphenylisobenzofuran (DPBF) as singlet oxygen quencher (Krieg, 1993; You, 2018). The decrease of absorbance of DPBF at 410 nm upon quenching of singlet oxygen produced by excitation of the BODIPY dye was monitored. Therefore, the absorbance of DPBF was set to values of about 0.8 at the absorption maximum and the absorbance of the respective dye was set to absorbances of 0.1 which was approx. 15 nmoL/mL. Subsequently, the samples were illuminated stepwise using a 530 nm LED array (LEDA-G, Teleopto Bio Research Center Co., Japan). The initial LED light power of 43.5 mW/cm^2 was adjusted with regard to the sensitivity of the assay molecule and scaled down to around 8.7 mW/cm^2. After each illumination step, an absorption spectrum was recorded and the rate constants k were determined assuming pseudo-first-order kinetics with $[\mathrm{DPBF}]_0$ being the absorbance (area under the curve) at time point 0 and [DPBF] at the measured time point (Wang et al., 2015; Hu et al., 2018).

$$kt = \ln \frac{[\mathrm{DPBF}]_0}{[\mathrm{DPBF}]}$$

2.7. Bacterial cell culture and biofilm growth

Escherichia coli TG1 DSM 6056, *Staphylococcus aureus* BAM 480 and *Streptococcus mutans* DSM 20523 were used as biofilm forming microorganisms (Schwibbert et al., 2019). *E. coli* and *S. aureus* were cultivated on Luria–Bertani (LB) medium agar plates and passaged every 3–4 weeks. *S. mutans* was cultivated on Columbian blood agar plates and passaged every 1–2 weeks. For all biofilm experiments, 20 mL liquid medium was inoculated with single colonies and cultured overnight at 37°C with shaking at 120 rpm on an orbital shaker (Incubating orbital shaker, Professional 3,500, VWR) 57. LB medium was used for *E. coli*, AB medium for *S. aureus* and M92 medium for *S. mutans*. The cultures were diluted 1:100 in fresh medium and incubated for additional 1–2 h at 37°C until cells reached the exponential growth phase. For biofilm formation, the optical density of the suspension was measured at 600 nm (Novaspec Plus, Amershan Biosciences) and adjusted to 0.01 (corresponding to approx. 1.2×10^6 cells/mL for *E. coli*, 1.5×10^6 cells/mL for *S. aureus* and 6×10^5 cells/mL for *S. mutans*). *E. coli* biofilms were grown in M9 minimal medium, supplemented with 1 mM thiamine and 20 mg/L proline. *S. aureus* biofilms were grown in M9 minimal medium, supplemented with 1 mM thiamine, 20 mg/L proline, 0.5 g/L protein hydrolysate amicase (acid hydrolyzed casein), and 0.5 g/L yeast extract. *S. mutans* biofilms were grown in M92 medium. For the biofilm assay, biofilms were grown in 96 well plates (100 µL per well) on the well/liquid medium interface for 24 h with constant shaking at 100 rpm for *E. coli* and 60 rpm for *S. aureus* and *S. mutans*. For microscopy, biofilms were formed in ibidi glass slides (8 well chamber slide, Ibidi GmbH) on the glass/liquid medium interface.

2.8. Biofilm assay and illumination

For the biofilm assay, the supernatant of the biofilms was removed, and the biofilms were washed with PBS before the NPs were added at a final concentration of 1 mg/mL. The well plate containing the samples and control samples without NPs were staged on top of an LED array standing inside a shaking incubator. The excitation wavelength of the LED array (LEDA-G, Teleopto Bio Research Center Co., Japan) was 530 nm. Samples were illuminated at 43.5 mW/cm^2 for 30 min, 2 h and 4 h with light doses of 81 J/cm^2, 324 J/cm^2 and 648 J/cm^2, respectively. For each illuminated plate, a dark control was conducted with identical samples without illumination. After the illumination, the plates were taken from the shaker and the supernatant was removed from each well. For quantification of bacteria per biofilm, all samples were washed with PBS and the biofilms were resuspended in 100 µL PBS. Crystal violet staining (0.1%, 10 min incubation, 3 × washing with MilliQ water) and microscopy of the empty wells revealed no leftover biofilm in the wells after this procedure. The PBS containing the biofilm bacteria was serially diluted in a new 96 well plate. These serial dilutions were seeded on LB agar plates, incubated at 37°C over night and the Colony forming units (CFU) were counted.

2.9. Imaging (CLSM and SEM)

For confocal laser scanning microscopy (CLSM), all biofilms were imaged at 37°C in Ibidi slides using a Leica SP8 X CLSM equipped with a supercontinuum white light laser and a monochromator (Leica Microsystems). A 100 × / (N.A.1.4) objective with oil immersion was used for imaging. XY images were acquired with 2048 × 2048 or 8,192 × 8,192 pixels and Z-stacks in XYZ mode with 512 × 512 pixels, respectively. To obtain the Z-stacks, images were taken at 1 µm spacing through the biofilm.

For scanning electron microscopy (SEM) imaging, biofilms were grown on 1 × 1 cm glass slides, washed three times with PBS and fixed with 2% glutaraldehyde for 2 h. After three additional washing steps with PBS, specimens were dehydrated in a graded alcohol series (30, 50, 70, 90, and 99% ethanol). Critical point drying was performed with liquid carbon dioxide as a transitional fluid (EM CPD300, Leica, Germany). Biofilm specimens were sputter coated with a 30 nm conducting layer of gold (EM ACE600 table-top coater, Leica, Germany) and examined with an emission scanning electron microscope (XL 30 ESEM, FEI, Netherlands) using secondary electron detector and operated at an electron accelerating voltage of 20 kV and 25 kV. A minimum of three random sections per sample were analyzed.

2.10. Statistics

Data analysis was performed with Graph Pad Prism 9. Error bars indicate the standard error of the mean of three independent experiments performed in triplicates. *, **, and *** represent the significant difference to the control determined with an unpaired *t* test with $p < 0.05$, $p < 0.01$, and $p < 0.001$, respectively.

3. Results

3.1. Design and preparation of the NPs

BODIPY dyes are highly versatile, can be easily prepared and chemically modified and are well suited as PS for aPDT (Ziessel et al., 2007; Bañuelos, 2016). Not only do they exhibit very high photostability, but they also have remarkable photophysical properties, such as their high absorption coefficients and high quantum yields for ROS generation, especially when halogens are introduced to the chromophore core (Gorbe et al., 2019). Here, a diiodinated BODIPY derivative was used due to its highly effective ROS generation, in comparison, to, e.g., the commonly used PS rose bengal (Radunz et al., 2020). Furthermore, BODIPY dyes enable dual use as PS for aPDT and as reporter for fluorescence imaging. One major limitation of BODIPYs is their often very poor water solubility. Thus, the direct application of BODIPYs in aqueous media in relevant concentrations is not feasible. The use of cosolvents (e.g., DMSO) would theoretically be possible, but relatively high concentrations are needed to dissolve adequate amounts of BODIPY. Thus, the risk of the cosolvent influencing the biological system under investigation is high (Summer et al., 2022). Here, the hydrophobic BODIPY dye was embedded into polystyrene NPs that are readily suspendable in aqueous media due to their hydrophilic surface functionalization. The NPs are commercially available, cost effective and have a wide range of applications especially for nano-sized applications such as biosensors or as self-assembling nanostructures (Velev and Kaler, 1999; Kromer et al., 2022). Here, 100 nm polystyrene NPs with a hydrophilic surface functionalization of carboxyl and amine groups were chosen. These NPs are biocompatible, stable in cell culture media and reportedly non-toxic to bacterial cells (Miyazaki et al., 2013; Loos et al., 2014). Especially in the concentration range required for use as a nanocarrier for PS, no negative effects have been reported on the viability or physiology of biofilms (Supplementary Figure S1) (Kromer et al., 2022). The main advantage for the application of these NPs as nanocarriers is their previously reported ability to accumulate well in biofilms (Kromer et al., 2022). The rational design of our approach includes the following steps. First the PS dye was embedded in 100 nm NPs by a previously established dye loading protocol using a swelling method (Behnke et al., 2011). Upon illumination with visible light (530 nm) ROS are generated (Figure 1). For eradication of biofilms the BODIPY-loaded NPs are incubated and accumulated in the biofilm. Photosensitization and ROS generation inside the biofilm leads to the destruction of the bacteria and in case of high effectiveness ultimately the biofilm. The NPs can be applied for the eradication of planktonic cells and subsequently the prevention of biofilm formation or for the eradication of existing biofilms (Figure 2).

3.2. Characterization of the NPs and ROS generation

Since the size of the NPs is of major importance influencing the capability of the particles to accumulate in the biofilm, the size of the NPs was determined before and after loading the PS. A change in size could be associated with agglomeration of the particles, which in turn could decrease the stability of the suspension and, subsequently, could affect the accumulation of the NPs in the biofilm. Hence, the dye loading would have had to be limited if these parameters had changed due to the introduction of the dye. The particle size determined by DLS and TEM showed that the size the BODIPY-loaded NPs was not altered (Table 1). Furthermore, TEM images revealed, that the particle shape was also not altered by the incorporation of the dye and remained spherical (Figures 3A,B). The PDI assessment revealed that both the precursor NPs and the dye-containing NPs show a very narrow and comparable size distribution and there was no indication of particle agglomeration. Consequently, the introduction of the BODIPY dye did not affect the particle size, shape, and agglomeration behavior of the NPs. The zeta potential of the precursor NPs and the BODIPY-loaded NPs was determined to -30.7 ± 1.1 mV and -22.1 ± 0.6 mV, respectively. It is favorable that the zeta potential is still in the negative range after the incorporation of the dye, since a negative zeta potential is considered biocompatible for polystyrene NPs (Miyazaki et al., 2013; Frankel et al., 2020). Moreover, the diffusion rate of negatively charged nanoparticles is higher than that of positively charged nanoparticles, since the latter are retained via electrostatic interactions (Blanco-Cabra et al., 2022). The diffusion rate is relevant for the accumulation of the particles in the biofilm.

The dye loading of the particles was determined by dissolving the BODIPY-loaded NPs in THF and photometrical analysis, comparing the BODIPY absorbance with the free dye at 530 nm (Supplementary Figure S2). The dye loading was determined to

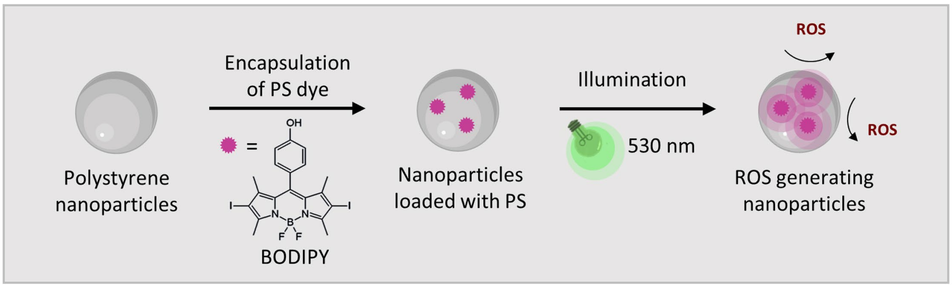

FIGURE 1
The BODIPY dye embedded in polystyrene NPs generates ROS when activated by visible light (530 nm).

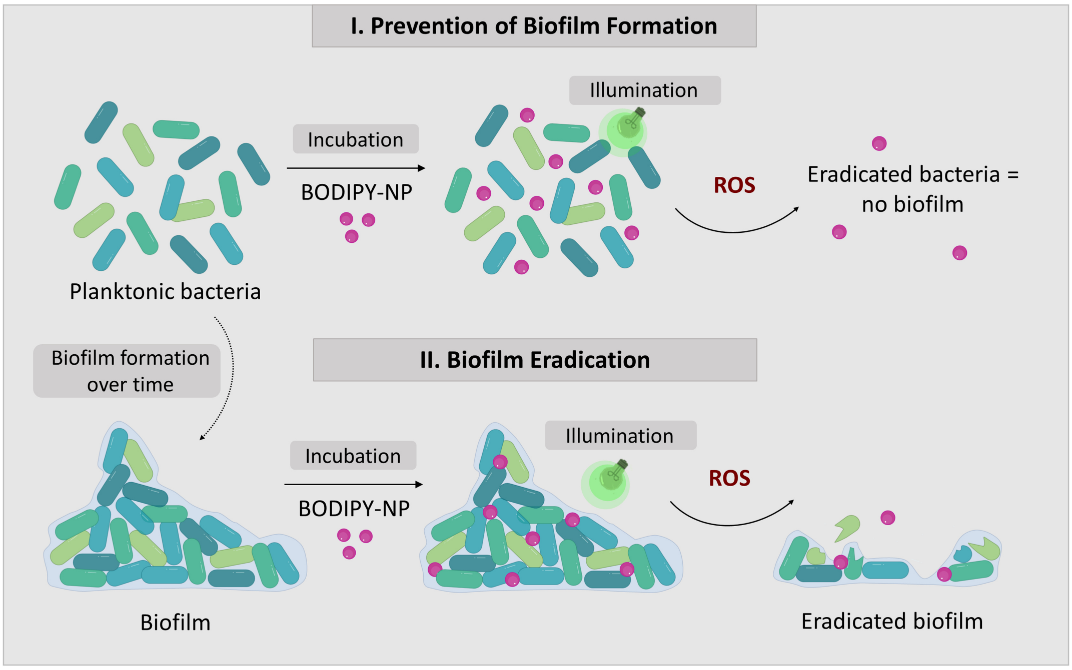

FIGURE 2
The concept of biofilm eradication utilizing aPDT with BODIPY-loaded NPs. The two approaches to combat biofilms: I. Prevention of biofilm formation by eradication of planktonic bacteria; II. Eradication of existing biofilms.

TABLE 1 **Particle size and zeta potential of the precursor NPs and dye-loaded NPs.**

	Size (TEM) [nm]	Size (DLS) [nm]	PDI	Zeta potential [mV]	Dye loading
NPs	96 ± 12	130 ± 1	0.008 ± 0.006	− 30.7 ± 1.1	–
NPs + BODIPY	90 ± 9	137 ± 2	0.111 ± 0.018	− 22.1 ± 0.6	61.3 ± 5.1 nmol/mg NPs

be 61.3 ± 5.1 nmol per mg NPs (Table 1). No leaking of BODIPY dye from the NPs was observed after 24 h and 72 h in cell culture medium, here M9 minimal medium. This is critical with respect to long-term stability and applicability of the NPs for aPDT. The main factors governing undesired dye leaking are the hydrophilicity of the dye and its solubility in the solvent or matrix surrounding the NPs (Behnke et al., 2011). The absorption and emission spectra of the BODIPY dye were not significantly changed by incorporation into the NPs (Supplementary Figure S3). It was investigated whether embedding the BODIPY dye in the NPs affects or limits the dyes ability to generate ROS. In the case of a compromised ROS generation due to the incorporation of BODIPY dye into the NPs, the effectiveness of the aPDT would be lowered. It would also pose the question if embedding BODIPYs in NPs is a suitable way of application for photodynamic applications or even aPDT. Therefore, DPBF was used as detection molecule in a singlet oxygen assay. In the presence of singlet oxygen, DPBF degrades to a colorless product, thus, the decrease of DPBFs absorption at 410 nm can be used to determine the rate of singlet oxygen generation of the sensitizer (Figures 3C,D). The determined singlet oxygen generation rates prove a similar DPBF degradation of 0.08020/s and 0.08115/s for the free dye and the dye embedded in the NPs, respectively (Figures 3C,D insets). Accordingly, embedding BODIPY into NPs in the concentration tested does not alter the ability of the PS to produce singlet oxygen. It can be assumed that the good oxygen and light transmission of the NPs contributes to the fact that ROS generation is not impaired, even though the dye is loaded in high local concentrations inside the particle. Additionally, effects such as degradation of the dye and inner filter effect seem to be negligible at this concentration.

3.3. Eradication of planktonic bacteria and prevention of biofilm formation

The eradication of planktonic bacteria can be an important step in preventing biofilm formation. When planktonic bacteria are present in aqueous media, they can form biofilms. This is not only very problematic in medical environments, but also in water or food processing facilities (Zwirzitz et al., 2020). Especially when affected areas cannot be cleaned with conventional disinfection methods, e.g., due to alcohol-sensitive materials or limited accessibility. Therefore, the performance of BODIPY-loaded NPs was tested against planktonic bacterial cultures and the subsequent biofilm formation was evaluated. Three bacterial species were selected that are known to frequently form pathological biofilms and are of high relevance in the medical field, namely *E. coli, S. aureus,* and *S. mutans. E. coli* is a major cause

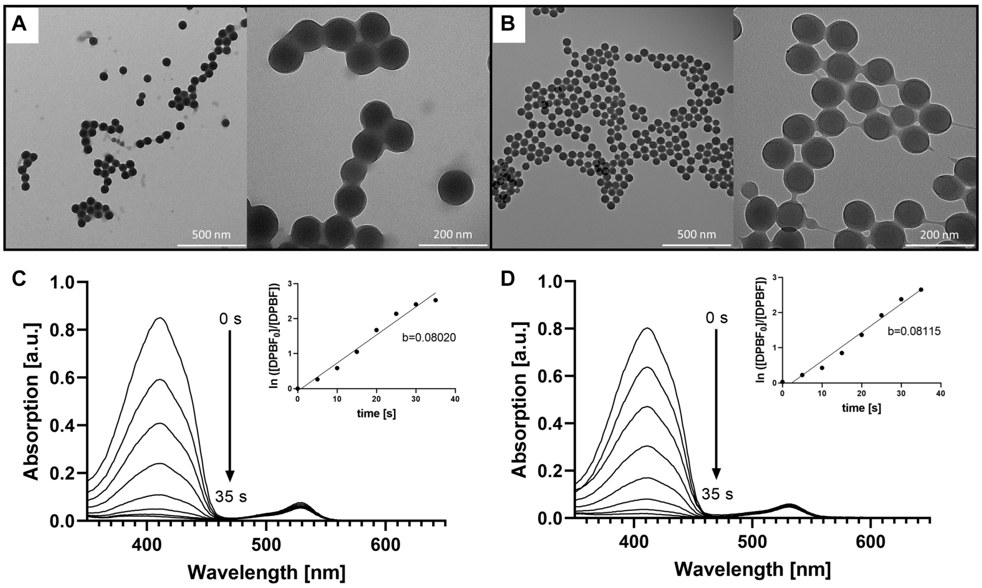

FIGURE 3
Comparison of the precursor NPs, the free BODIPY dye and the BODIPY-loaded NPs. TEM images of **(A)** the precursor NPs and **(B)** the NPs after incorporation of the BODIPY dye. **(C)** Determination of singlet oxygen generation of the free BODIPY dye. Absorption spectra of DPBF showing decomposition by singlet oxygen generated by free BODIPY dye upon stepwise (7 × 5 s) illumination with a 530 nm LED array. Inset: illumination time-dependent changes in absorbance of DPBF derived from the absorption spectra. **(D)** Determination of singlet oxygen generation of the BODIPY-loaded NPs with the same setup as in **(C)**. Inset: illumination time-dependent changes in absorbance of DPBF derived from the absorption spectra in presence of BODIPY-loaded NPs.

of urinary tract infections, and its biofilms often lead to chronification of the infection (Eberly et al., 2017). *S. aureus* is a common infector of medical equipment such as catheters or endotracheal tubes (Machado et al., 2012; Zheng et al., 2018) and of surgical sites and burn wounds (Plumet et al., 2022). Contamination of endotracheal tubes often leads to ventilator-associated pneumonia, which most often prolongs the hospital stay in the ICU and has a mortality rate of up to a 20–30%. *S. aureus* and its biofilms are feared in hospitals and intensive care units, especially because of its high pathogenicity and tendency to become multidrug resistant. *S. mutans* is omnipresent in the human oral cavity, but its ability to form biofilms that create an acidic milieu contributes to its high pathogenicity. *S. mutans* is the main cause of dental caries.

The effectiveness of aPDT with BODIPY-loaded NPs against planktonic bacterial cultures and the subsequent biofilm formation was evaluated for the three bacterial test strains. For this purpose, exponentially growing planktonic bacterial cultures were treated with the BODIPY-loaded NPs and illuminated for 30 min with an LED array at 530 nm. The advantages of this LED array are the easy handling (96 well plates can be mounted on top) and the low susceptibility to errors generated by, e.g., intensity fluctuations. The illumination intensity can be adjusted on the device and ensures good comparability. Unlike lasers, which are often used and are defocused with a lens, the LED array does not need to be readjusted each time. Biofilm formation was observed after 24 h, and the resulting biomass of the biofilm was determined (Figure 4). For this purpose, the biofilms were washed to remove planktonic cells, resuspended in PBS, serially diluted and seeded on agar plates to determine the CFU. For the dark controls, the biofilms were grown for 24 h without NPs and without illumination. When either only the light (illum control) or only the BODIPY-loaded NPs (dark BODIPY) are used, no eradication effect was observed. Only when both are used in combination (illum BODIPY), a strong eradication effect is achieved, leading to the prevention of biofilm formation, even after 24 h post incubation. The eradication of the planktonic cultures results in 100% prevention of biofilm formation for *E. coli* and *S. aureus* and > 99.9% for *S. mutans*. This demonstrates, that aPDT with the BODIPY-loaded NPs is a highly effective method for the treatment of planktonic bacterial cultures and a suitable method for the prevention of biofilm formation.

3.4. Biofilm eradication

Although eradicating planktonic bacteria and thus preventing biofilm formation is a valid option, there must also be systems that can combat existing biofilms. Once biofilms have formed and matured, they pose a much greater threat, as they are then very difficult to remove (Koo and Yamada, 2016). One reason for this is that the EPS matrix protects the biofilm by providing structural integrity, thereby increasing its resistance to external influences such as disinfection. It also forms a reservoir for nutrients, hence only a few bacteria need to survive for a biofilm to regrow quickly.

To investigate whether the BODIPY-loaded NPs are able to eradicate biofilms, treatment against *E. coli*, *S. aureus*, and *S. mutans* biofilms was tested and their effect determined. Additionally, planktonic cultures were treated and the subsequent biofilm formation was examined. Each bacterial strain was cultivated separately on glass for 24 h, then incubated with the dye-loaded NPs and illuminated with an LED array at 530 nm. Afterwards, the biofilms were fixed and examined by SEM to investigate the effects of aPDT treatment on the

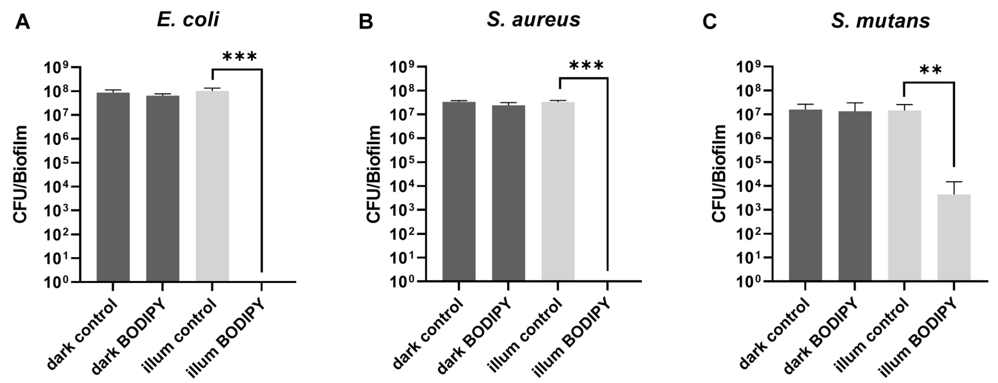

FIGURE 4
Prevention of biofilm formation after aPDT of planktonic bacteria and determination of subsequent biofilm formation after 24 h. **(A)** Planktonic *E. coli*, **(B)** *S. aureus*, and **(C)** *S. mutans* after 30 min of illumination with a 530 nm LED array. CFU, colony forming units; illum, illuminated. Three independent replicates were performed for each sample. Error bars indicate the standard error of the mean of three independent experiments performed in triplicates. *, **, and *** represent the significant difference to the control determined with an unpaired *t* test with $p < 0.05$, $p < 0.01$, and $p < 0.001$, respectively.

bacteria and biofilm structure (Figure 5). Furthermore, planktonic bacterial cultures were treated as described before (Figure 5D). Controls without NPs and controls with NPs but without illumination were included (Figures 5A,B). Due to the sample preparation for SEM imaging, which includes numerous washing steps, and the loose and fluffy structure of the *S. aureus* and *S. mutans* biofilms, a large proportion of the biofilms were detached from the slides. Therefore, the SEM results can only be used for a comparison between treatment and controls, but not as an indicator for the natural morphology of the biofilms. For all three biofilm test strains, the biofilm structure was not disrupted or altered by the presence of the NPs without illumination compared to the control without nanoparticles. Therefore, dark toxicity of the NPs is not expected. As treatment groups, both biofilms and planktonic cultures were exposed to the NPs and then illuminated. In the treated planktonic samples (Figure 5D), no bacteria or biofilm structures were found in any of the samples. This indicates 100% eradication of planktonic bacteria, as biofilm formation was completely prevented. The results are consistent with the previously obtained results from the biofilm CFU assays and thus demonstrate a good performance of the aPDT NPs in preventing biofilm formation.

In the treated biofilm samples, the number of bacteria and the biofilm structures appear to be reduced (Figure 5C). A determination whether the bacteria present are alive or dead by SEM is very difficult. Although it is normal for dead cells to remain structurally intact during fixation and thus are visible by SEM imaging, the morphology of the cell and the surface structure of the dead cells can be altered (Cheng et al., 2011). The cells can become deformed and wrinkled, indicating that the intracellular content had leaked out (García-Salinas et al., 2018). Studies have also found, that dead cells emptied of their cellular content can still have almost intact cell walls (Diogo et al., 2017). In this case, however, the structural change of the membrane is difficult to observe due to the membrane of the bacteria being completely covered with NPs after the treatment. This is a very unusual observation revealing a significant change in comparison to the NPs controls. The attachment of NPs to the bacterial membranes is eminent in all three bacterial species.

Since it was not possible to distinguish the live from the dead bacteria with SEM, the dead cells were visualized by staining with propidium iodide and investigation with CLSM after aPDT treatment (Figure 6). In an untreated control, the living cells were additionally stained with Syto9. A Syto9 stain is not possible in the BODIPY-loaded NPs treated samples due to an overlap of the emission of BODIPY and Syto9. The NPs accumulated in the biofilm can be imaged by the fluorescence of BODIPY. The control biofilm shows a large number of live cells (green signal) and a small number of dead cells (red signal) (Figure 6A). The NPs control (Figure 6B) incubated only with BODIPY-loaded NPs but not illuminated shows few dead cells, comparable to the control without NPs. When the biofilm and the NPs accumulated within are illuminated, a very high number of dead cells is observed (Figure 6C). This indicates that the bacteria and the biofilm structure itself are still intact, but the cells are dead after the aPDT treatment. This is consistent with the SEM images where bacterial structures were also visible after treatment, but most likely dead.

The microscopic images revealed that treatment of biofilms with aPDT leads to a high number of dead cells in the biofilm. Treatment of planktonic cultures with aPDT can even prevent biofilm formation altogether. To determine the effectiveness of biofilm eradication by aPDT treatment with BODIPY-loaded NPs, the number of viable bacteria in the biofilms after treatment was quantified. For this purpose, biofilms of three bacterial species were grown in 96-well plates for 24 h. After a washing step with PBS, the BODIPY-loaded NPs were added to the biofilms, incubated for a given time period and were illuminated with the LED array. To determine the viable fraction of the biofilms after aPDT treatment, the biofilms were then washed, resuspended in PBS, serially diluted and the resulting CFU determined (Figure 7). The empty 96-well plates were then stained with crystal violet to ensure a complete removal of biofilm from the plate. Previous studies have found a clear correlation between illumination intensity and eradication efficiency, with higher intensity leading to greater bacterial eradication (Shrestha et al., 2014; Gillespie et al., 2017; Sun et al., 2019). Considering the goal of our study to achieve the highest possible eradication efficiency, we opted for the highest illumination intensity of the LED array. Initially, the biofilms were illuminated for 30 min as with the planktonic cultures. However, although an illumination time of 30 min resulted in effective eradication for the planktonic cultures, this was not the case for the much more robust

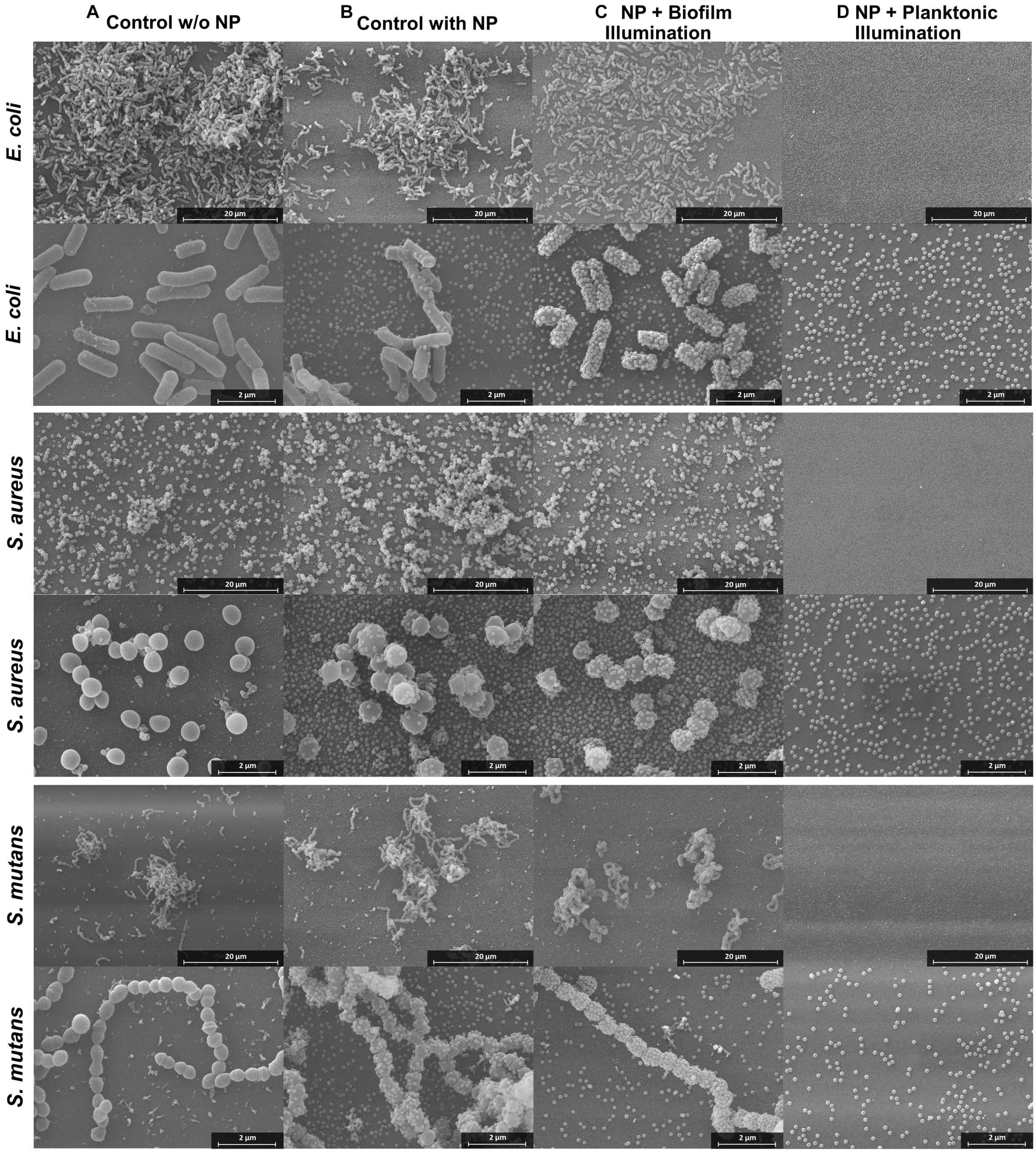

FIGURE 5
SEM images of *E. coli*, *S. aureus*, and *S. mutans* biofilms treated with aPDT. The four columns display the different treatments from left to right: biofilm control without NPs, biofilm control with NPs and without illumination, biofilm with NPs and illumination, biofilm grown for 24 h after treatment of planktonic culture with NPs and illumination. Additional SEM images can be found in Supplementary Figures S5–S7.

biofilms. Here, only ~0.3–0.4 log units of bacteria in the biofilms were eradicated after 30 min of illumination. Increased illumination times of 2 h and 4 h resulted in significantly better eradication of the biofilms. After 4 h, the aPDT treatment was able to eradicate 0.65 log units of *E. coli*, 5.8 log units of *S. aureus* and 3.3 log units of *S. mutans* compared to the control.

Since a successful eradication method aims for 100% eradication, the setup was further optimized. For this purpose, the NPs were first incubated in the biofilm and then irradiated. The optimal incubation time was determined using CLSM by determining the accumulation of BODIPY-loaded NPs into the biofilm at different time points. The time point up to which an increase of particles in the biofilm could be observed was determined as the needed incubation time. It was observed that the time required for the NPs to accumulate in the biofilm varies depending on the biofilm test strain, therefore different incubation times were chosen. Incubation times of 3 h were sufficient

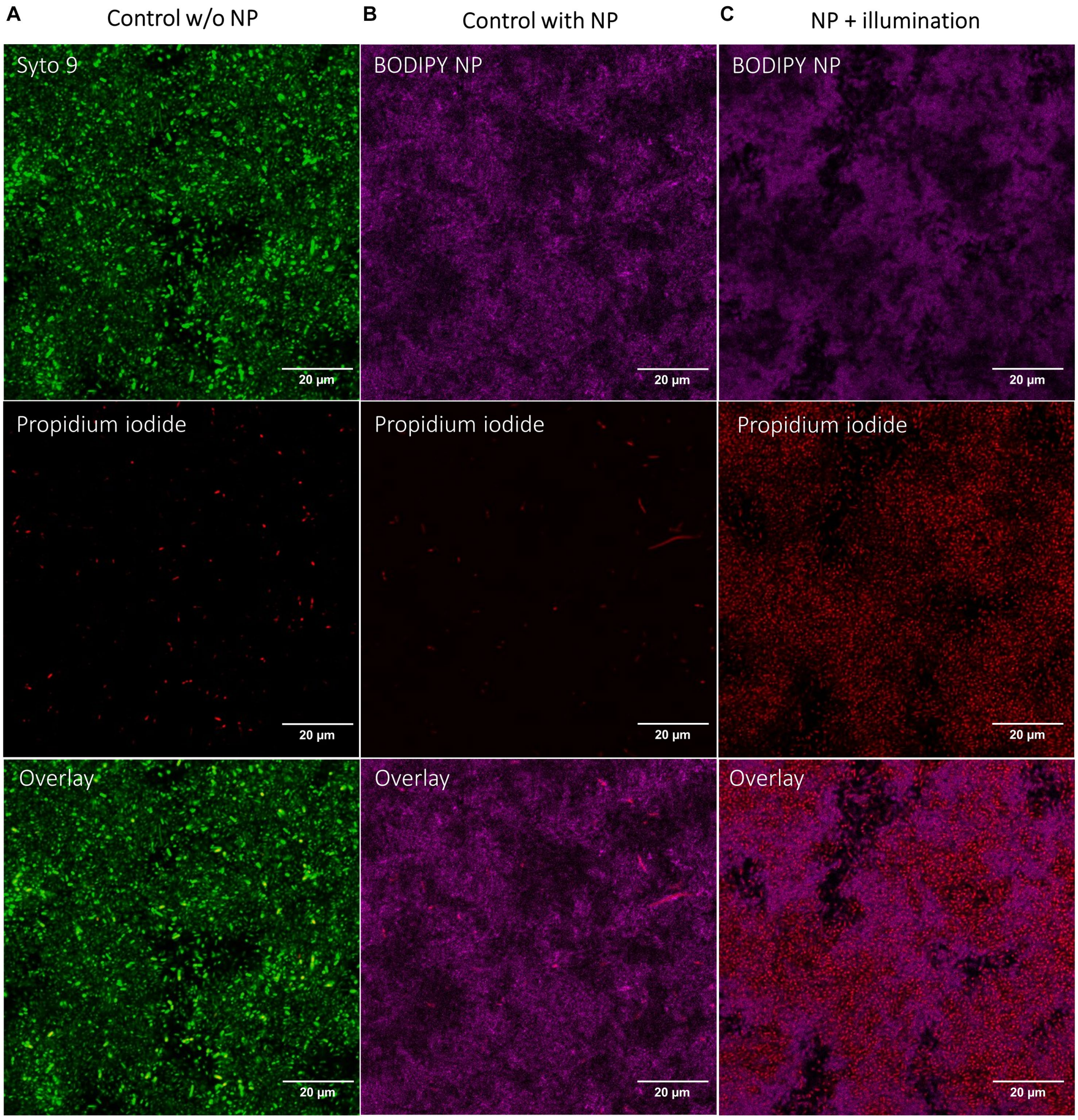

FIGURE 6
CLSM images of *E. coli* biofilms after aPDT with BODIPY-loaded NPs. **(A)** Control biofilm without NPs with illumination, **(B)** Biofilm incubated with NPs without illumination, **(C)** Biofilm incubated with NPs and with illumination. BODIPY-loaded NPs (magenta), Live/Dead stain of bacteria with propidium iodide for dead cells (red) and Syto9 for live cells (green). Scale bar is 20 µm.

for *S. aureus* and *S. mutans* biofilms. For the *E. coli* biofilms, a significantly longer incubation time of 24 h was required to achieve sufficient accumulation in the biofilm. Representative images of optimizing the incubation time of *E. coli* biofilms are shown in Supplementary Figure S4.

For all three biofilms tested, the eradication effect increased with increasing illumination time and is generally higher when the NPs were previously incubated into the biofilm. No dark toxicity of the BODIPY-loaded NPs is observed in the dark controls for any of the three bacterial biofilm types. This confirms that the eradication effect is exclusively achieved by aPDT. Remarkably, after 4 h of treatment, two of the three biofilm species, namely *S. aureus* and *S. mutans*, were eradicated by 100%. *E. coli* biofilms were eradicated by 6.65 log units corresponding to 99.99986%.

4. Discussion

This study has demonstrated that nanoparticles for aPDT can be a powerful tool for the eradication of planktonic bacteria and bacterial biofilms. It was shown that the aPDT eradication effect increased with increasing illumination time and was generally higher when the NPs were previously incubated into the biofilm. The efficiency of the BODIPY-loaded NPs is thus higher when ROS generation takes place in close proximity to the bacteria inside the biofilm and not in the medium. Since the generated ROS have a short lifespan and thus a short diffusion distance, the spatial proximity to the bacteria is a very important factor for the effectiveness. Additionally, it was found that the incubation times needed for a sufficient accumulation in the biofilm vary

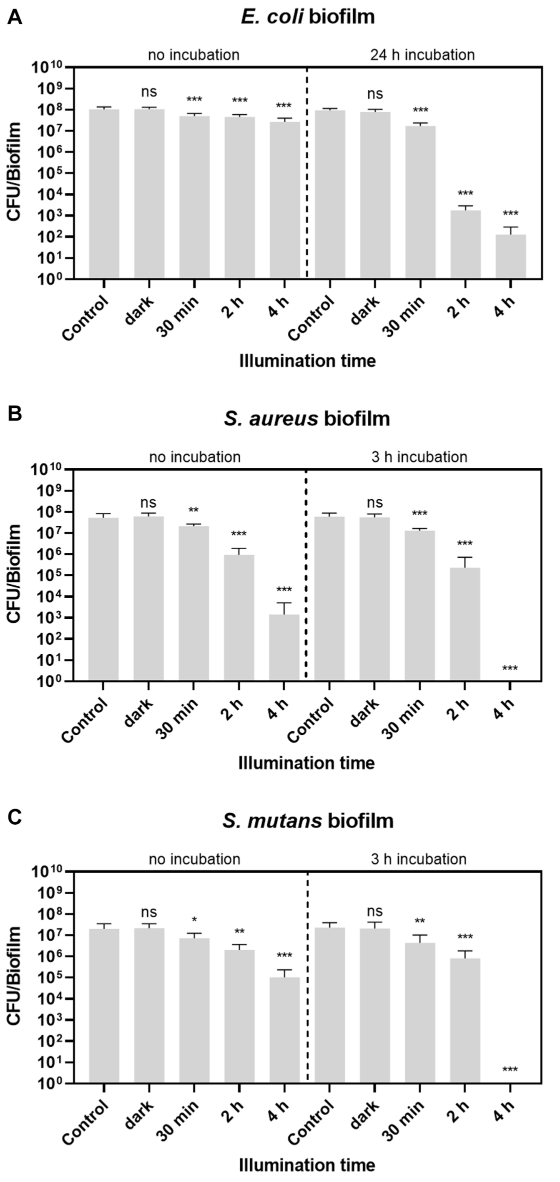

FIGURE 7
Biofilm eradication with BODIPY-loaded NPs. **(A)** *E. coli*, **(B)** *S. aureus*, and **(C)** *S. mutans* biofilms were illuminated either with or without previous incubation of the dye-loaded NPs. The CFU per biofilm were determined after different illumination times (30 min, 2 h and 4 h), biofilm samples without NPs after 30 min and 4 h (control), and biofilms exposed to NPs but without illumination after 30 min and 4 h (dark). Error bars indicate the standard error of the mean of three independent experiments performed in triplicates. *, **, and *** represent the significant difference to the control determined with an unpaired *t* test with $p < 0.05$, $p < 0.01$, and $p < 0.001$, respectively.

depending on the biofilm species. The NPs penetration into and movement within the biofilm is considered to be driven primarily by diffusion (Ikuma et al., 2015). The most important factors influencing the diffusion of NPs into the biofilm are particle properties such as size, charge and hydrophobicity (Hollmann et al., 2021). However, the nature of the biofilm also plays a very important role. Here, the pore size and hydrophobicity of the biofilm are particularly important, but also the charge and chemical gradient of the biofilm and its matrix (Peulen T. O. and Wilkinson, 2011; Sahle-Demessie and Tadesse, 2011). Since the same NPs were used here for all three biofilms, the structure and nature of the biofilms is most likely the main factor for the kinetic of NPs penetration in the biofilms. *E. coli* forms very dense biofilms with quite small extracellular spaces and with smaller pore size. Hence, longer incubation times were needed for *E. coli* biofilms than for *S. aureus* and *S. mutans*. These biofilms tend to have a looser structure with more extracellular matrix and larger pore size (Hou et al., 2019). This finding aligns with the previously stated hypotheses that the pore size of a biofilm significantly influences penetration of NPs into that biofilm.

A main feature of the aPDT method described here are the very high eradication rates of up to 100%. Biofilms have the ability to quickly rebuild large populations, even if only a few specimens survive a disinfection treatment. Not eliminating all bacteria in a biofilm is a major shortcoming of most published studies utilizing PS-loaded NPs (Klepac-Ceraj et al., 2011; Usacheva et al., 2016; Anju et al., 2018, 2019). Therefore, a key feature of a successful eradication method is to achieve 100% eradication to permanently eliminate biofilms. In this study, 100% eradication was achieved for, *S. aureus* and *S. mutans*. In the case of *E. coli* biofilms, a very small fraction of the biofilm survives the treatment regardless. Since the rate of surviving bacteria in *E. coli* biofilms decreases steadily with the illumination time, it is reasonable to assume that 100% eradication can be achieved with longer illumination times for *E. coli* as well. In general, the difference in the susceptibility of gram-negative and gram-positive bacteria to aPDT can be attributed to the different cell wall structure of the bacteria (Malik et al., 1992; Bekmukhametova et al., 2020). Gram-negative bacteria, in contrast to gram-positive bacteria, have a more complex cell wall structure due to an additional lipopolysaccharide containing membrane as the outermost layer. This membrane provides additional protection against ROS, as it is not enough to disturb the outer-membrane structure alone, but the cytoplasmic membrane must be disrupted as well (Malik et al., 1992). Gram-negative bacteria and biofilms can be just as harmful as gram-positive bacteria. Therefore, aPDT agents that are able to successfully eliminate gram-negative bacteria need to be further developed and optimized.

These studies also include SEM images that revealed that the NPs attach to the bacterial membranes after the illumination. This observation was eminent in all three bacterial species. The lack of membrane potential, as it occurs in dead cells, could be a reason for the adhesion of the NPs to the cells. Furthermore, changes in the cell membrane could be involved as well. The outer cell membranes of viable bacteria are typically negatively charged due to the presence of molecules such as lipopolysaccharides and carboxylate substituents on their surface (Wilson et al., 2001). Thus, the NPs, which are also negatively charged, have no electrostatic attraction to the bacteria. However, when the bacteria are damaged by aPDT leading to cell wall ruptures, substances can leak from inside the bacteria. The release of intracellular components might result in the exposure of positively charged molecules or ions on the bacterial surface, causing a shift in the overall charge from negative to neutral or positive (Kłodzińska et al., 2010; Ferreyra Maillard et al., 2021). This might lead to the binding of NPs to the bacterial surfaces by electrostatic attraction, as observed by SEM. It is therefore reasonable to conclude that bacteria with a large number of NPs adhering to their surface are dead.

In summary, the design, preparation, characterization, and application of a BODIPY-loaded NPs tool for aPDT of bacteria and their corresponding biofilms was described. The BODIPY-NPs proved to be highly effective for the prevention of biofilm formation as well as the eradication of biofilms. With its simple preparation and easy application, the aPDT system stands in contrast to existing methods, which most often require a complex manufacturing and application and therefore lack practical suitability. It has the potential to be used as a seminal and universal disinfection agent for the much-needed treatment of pathogenic bacteria and biofilms. Furthermore, the multitargeted mechanism of action of aPDT leads to a demonstrably lower development of bacterial resistance (Vatansever et al., 2013; Bekmukhametova et al., 2020). By combining the NPs with substances that enable active targeting, such as lectins or antibodies, aPDT can potentially be applied more selective. Thus, in a mixed bacterial population, only the pathogenic bacteria could be eradicated, allowing potential applications where bacteria are beneficial such as the skin or gut microbiome. The BODIPY-loaded NPs could also be used for theranostic applications, where not only eradication but also diagnosis of the bacteria via imaging techniques (here by fluorescence) is given. It is also possible to combine the PS with a bactericidal drug in one particle to achieve a dual mode of action, thus further increasing the efficiency.

Data availability statement

The original contributions presented in the study are included in the article/Supplementary material, further inquiries can be directed to the corresponding author/s.

Author contributions

CK: Conceptualization, Data curation, Formal Analysis, Investigation, Visualization, Writing – original draft. KS: Supervision, Writing – original draft. SR: Investigation, Writing – review & editing. DT: Investigation, Writing – review & editing. PL: Writing – review & editing. AL: Supervision, Writing – review & editing. HT: Conceptualization, Supervision, Writing–original–draft.

Funding

The author(s) declare financial support was received for the research, authorship, and/or publication of this article. This research was funded by the German Federal Institute for Risk Assessment, grant number: SFP 1322–721 and by the Federal Institute for Materials Research and Testing.

Acknowledgments

The authors would like to thank Ines Feldmann (BAM 4.2) for help with the SEM sample preparation and SEM characterizations of the biofilms. We thank Franziska Riedel and Konstantin Simon for proof reading and fruitful discussions.

Conflict of interest

SR is an employee of a company producing and marketing substances for diagnostic imaging.

The remaining authors declare that the research was conducted in the absence of any commercial or financial relationships that could be construed as a potential conflict of interest.

Publisher's note

Supplementary material

The Supplementary material for this article can be found online at: https://www.frontiersin.org/articles/10.3389/fmicb.2023.1274715/full#supplementary-material

References

Abrahamse, H., and Hamblin, M. R. (2016). New photosensitizers for photodynamic therapy. *Biochem. J.* 473, 347–364. doi: 10.1042/BJ20150942

Anju, V. T., Paramanantham, P., Sb, S. L., Sharan, A., Alsaedi, M. H., Dawoud, T. M. S., et al. (2018). Antimicrobial photodynamic activity of rose bengal conjugated multi walled carbon nanotubes against planktonic cells and biofilm of *Escherichia coli*. *Photodiagn. Photodyn. Ther.* 24, 300–310. doi: 10.1016/j.pdpdt.2018.10.013

Anju, V. T., Paramanantham, P., Sruthil Lal, S. B., Sharan, A., Syed, A., Bahkali, N. A., et al. (2019). Antimicrobial photodynamic activity of toluidine blue-carbon nanotube conjugate against Pseudomonas aeruginosa and *Staphylococcus aureus* – understanding the mechanism of action. *Photodiagn. Photodyn. Ther.* 27, 305–316. doi: 10.1016/j.pdpdt.2019.06.014

Bañuelos, J. (2016). BODIPY dye, the Most versatile fluorophore ever? *Chem. Rec.* 16, 335–348. doi: 10.1002/tcr.201500238

Behnke, T., Würth, C., Hoffmann, K., Hübner, M., Panne, U., and Resch-Genger, U. (2011). Encapsulation of hydrophobic dyes in polystyrene micro-and nanoparticles via swelling procedures. *J. Fluoresc.* 21, 937–944. doi: 10.1007/s10895-010-0632-2

Bekmukhametova, A., Ruprai, H., Hook, J. M., Mawad, D., Houang, J., and Lauto, A. (2020). Photodynamic therapy with nanoparticles to combat microbial infection and resistance. *Nanoscale* 12, 21034–21059. doi: 10.1039/D0NR04540C

Blanco-Cabra, N., Movellan, J., Marradi, M., Gracia, R., Salvador, C., Dupin, D., et al. (2022). Neutralization of ionic interactions by dextran-based single-chain nanoparticles improves tobramycin diffusion into a mature biofilm. *NPJ Biofilms Microbiom.* 8:52. doi: 10.1038/s41522-022-00317-9

Boens, N., Verbelen, B., Ortiz, M. J., Jiao, L., and Dehaen, W. (2019). Synthesis of BODIPY dyes through postfunctionalization of the boron dipyrromethene core. *Coord. Chem. Rev.* 399:213024. doi: 10.1016/j.ccr.2019.213024

Cheng, X., Imai, T., Teeka, J., Yamaguchi, J., Hirose, M., Higuchi, T., et al. (2011). Inactivation of Escherichia coli and bacteriophage T4 by high levels of dissolved CO2. *Appl. Microbiol. Biotechnol.* 90, 1493–1500. doi: 10.1007/s00253-011-3163-0

Ciofu, O., Moser, C., Jensen, P. Ø., and Høiby, N. (2022). Tolerance and resistance of microbial biofilms. *Nat. Rev. Microbiol.* 20, 621–635. doi: 10.1038/s41579-022-00682-4

Dai, X., Chen, X., Zhao, Y., Yu, Y., Wei, X., Zhang, X., et al. (2018). A water-soluble galactose-decorated cationic photodynamic therapy agent based on BODIPY to selectively eliminate biofilm. *Biomacromolecules* 19, 141–149. doi: 10.1021/acs.biomac.7b01316

Dang, H., and Lovell, C. R. (2016). Microbial surface colonization and biofilm development in marine environments. *Microbiol. Mol. Biol. Rev.* 80, 91–138. doi: 10.1128/MMBR.00037-15

De-la-Pinta, I., Cobos, M., Ibarretxe, J., Montoya, E., Eraso, E., Guraya, T., et al. (2019). Effect of biomaterials hydrophobicity and roughness on biofilm development. *J. Mater. Sci. Mater. Med.* 30:77. doi: 10.1007/s10856-019-6281-3

Diogo, P., Fernandes, C., Caramelo, F., Mota, M., Miranda, I. M., Faustino, M. A. F., et al. (2017). Antimicrobial photodynamic therapy against endodontic enterococcus faecalis and *Candida albicans* mono and mixed biofilms in the presence of photosensitizers: a comparative study with classical endodontic Irrigants. *Front. Microbiol.* 8:498. doi: 10.3389/fmicb.2017.00498

Donlan, R. M., and Costerton, J. W. (2002). Biofilms: survival mechanisms of clinically relevant microorganisms. *Clin. Microbiol. Rev.* 15, 167–193. doi: 10.1128/CMR.15.2.167-193.2002

Dysart, J. S., and Patterson, M. S. (2005). Characterization of Photofrin photobleaching for singlet oxygen dose estimation during photodynamic therapy of MLL cells in vitro. *Phys. Med. Biol.* 50, 2597–2616. doi: 10.1088/0031-9155/50/11/011

Eberly, A. R., Floyd, K. A., Beebout, C. J., Colling, S. J., Fitzgerald, M. J., Stratton, C. W., et al. (2017). Biofilm formation by Uropathogenic *Escherichia coli* is favored under oxygen conditions that mimic the bladder environment. *Int. J. Mol. Sci.* 18:2077. doi: 10.3390/ijms18102077

Ferreyra Maillard, A. P. V., Espeche, J. C., Maturana, P., Cutro, A. C., and Hollmann, A. (2021). Zeta potential beyond materials science: applications to bacterial systems and to the development of novel antimicrobials. *Biochim. Biophys. Acta Biomembr.* 1863:183597. doi: 10.1016/j.bbamem.2021.183597

Flemming, H. C., and Wingender, J. (2010). The biofilm matrix. *Nat. Rev. Microbiol.* 8, 623–633. doi: 10.1038/nrmicro2415

Flemming, H. C., Wingender, J., Szewzyk, U., Steinberg, P., Rice, S. A., and Kjelleberg, S. (2016). Biofilms: an emergent form of bacterial life. *Nat. Rev. Microbiol.* 14, 563–575. doi: 10.1038/nrmicro.2016.94

Frankel, R., Ekvall, M. T., Kelpsiene, E., Hansson, L.-A., and Cedervall, T. (2020). Controlled protein mediated aggregation of polystyrene nanoplastics does not reduce toxicity towards *Daphnia magna*. *Environ. Sci. Nano* 7, 1518–1524. doi: 10.1039/C9EN01236B

García-Salinas, S., Elizondo-Castillo, H., Arruebo, M., Mendoza, G., and Irusta, S. (2018). Evaluation of the antimicrobial activity and cytotoxicity of different components of natural origin present in essential oils. *Molecules* 23:1399. doi: 10.3390/molecules23061399

Gillespie, J. B., Maclean, M., Given, M. J., Wilson, M. P., Judd, M. D., Timoshkin, I. V., et al. (2017). Efficacy of pulsed 405-nm light-emitting diodes for antimicrobial photodynamic inactivation: effects of intensity, frequency, and duty cycle. *Photomed. Laser Surg.* 35, 150–156. doi: 10.1089/pho.2016.4179

Gorbe, M., Costero, A. M., Sancenón, F., Martínez-Máñez, R., Ballesteros-Cillero, R., Ochando, L. E., et al. (2019). Halogen-containing BODIPY derivatives for photodynamic therapy. *Dyes Pigments* 160, 198–207. doi: 10.1016/j.dyepig.2018.08.007

Hansen, S. K., Rainey, P. B., Haagensen, J. A. J., and Molin, S. (2007). Evolution of species interactions in a biofilm community. *Nature* 445, 533–536. doi: 10.1038/nature05514

Hollmann, B., Perkins, M., Chauhan, V. M., Aylott, J. W., and Hardie, K. R. (2021). Fluorescent nanosensors reveal dynamic pH gradients during biofilm formation. *NPJ Biofilms Microbiomes.* 7:50. doi: 10.1038/s41522-021-00221-8

Hou, J., Wang, C., Rozenbaum, R. T., Gusnaniar, N., de Jong, E. D., Woudstra, W., et al. (2019). Bacterial density and biofilm structure determined by optical coherence tomography. *Sci. Rep.* 9:9794.

Hu, W., Zhang, X.-F., Lu, X., Lan, S., Tian, D., Li, T., et al. (2018). Attaching electron donating groups on the meso-phenyl and meso-naphthyl make aryl substituted BODIPYs act as good photosensitizer for singlet oxygen formation. *J. Lumin.* 194, 185–192. doi: 10.1016/j.jlumin.2017.10.018

Hu, X., Huang, Y.-Y., Wang, Y., Wang, X., and Hamblin, M. R. (2018). Antimicrobial photodynamic therapy to control clinically relevant biofilm infections. *Front. Microbiol.* 9:1299. doi: 10.3389/fmicb.2018.01299

Hughes, G., and Webber, M. A. (2017). Novel approaches to the treatment of bacterial biofilm infections. *Br. J. Pharmacol.* 174, 2237–2246. doi: 10.1111/bph.13706

Ikuma, K., Decho, A. W., and Lau, B. L. T. (2015). When nanoparticles meet biofilms—interactions guiding the environmental fate and accumulation of nanoparticles. *Front. Microbiol.* 6:591. doi: 10.3389/fmicb.2015.00591

Khan, S., Khan, S. N., Meena, R., Dar, A. M., Pal, R., and Khan, A. U. (2017). Photoinactivation of multidrug resistant bacteria by monomeric methylene blue conjugated gold nanoparticles. *J. Photochem. Photobiol. B* 174, 150–161. doi: 10.1016/j.jphotobiol.2017.07.011

Klepac-Ceraj, V., Patel, N., Song, X., Holewa, C., Patel, C., Kent, R., et al. (2011). Photodynamic effects of methylene blue-loaded polymeric nanoparticles on dental plaque bacteria. *Lasers Surg. Med.* 43, 600–606. doi: 10.1002/lsm.21069

Kirar, S., Thakur, N. S., Laha, J. K., Bhaumik, J., and Banerjee, U. C. (2018). Development of gelatin nanoparticle-based biodegradable Phototheranostic agents: advanced system to treat infectious diseases. *ACS Biomater Sci. Eng.* 4, 473–482. doi: 10.1021/acsbiomaterials.7b00751

Krieg, M. (1993). Determination of singlet oxygen quantum yields with 1, 3-diphenylisobenzofuran in model membrane systems. *J. Biochem. Bioph. Meth.* 27, 143–149. doi: 10.1016/0165-022X(93)90058-V

Kromer, C., Schwibbert, K., Gadicherla, A. K., Thiele, D., Nirmalananthan-Budau, N., Laux, P., et al. (2022). Monitoring and imaging pH in biofilms utilizing a fluorescent polymeric nanosensor. *Sci. Rep.* 12:9823. doi: 10.1038/s41598-022-13518-1

Kolpen, M., Kragh, K. N., Enciso, J. B., Faurholt-Jepsen, D., Lindegaard, B., Egelund, G. B., et al. (2022). Bacterial biofilms predominate in both acute and chronic human lung infections. *Thorax* 77:1015. doi: 10.1136/thoraxjnl-2021-217576

Koo, H., and Yamada, K. M. (2016). Dynamic cell-matrix interactions modulate microbial biofilm and tissue 3D microenvironments. *Curr. Opin. Cell Biol.* 42, 102–112. doi: 10.1016/j.ceb.2016.05.005

Kłodzińska, E., Szumski, M., Dziubakiewicz, E., Hrynkiewicz, K., Skwarek, E., Janusz, W., et al. (2010). Effect of zeta potential value on bacterial behavior during electrophoretic separation. *Electrophoresis* 31, 1590–1596. doi: 10.1002/elps.200900559

Li, Y., Sun, G., Xie, J., Xiao, S., and Lin, C. (2023). Antimicrobial photodynamic therapy against oral biofilm: influencing factors, mechanisms, and combined actions with other strategies. *Front. Microbiol.* 14:1192955. doi: 10.3389/fmicb.2023.1192955

Loos, C., Syrovets, T., Musyanovych, A., Mailänder, V., Landfester, K., Nienhaus, G. U., et al. (2014). Functionalized polystyrene nanoparticles as a platform for studying bio-nano interactions. *Beilstein J. Nanotechnol.* 5, 2403–2412. doi: 10.3762/bjnano.5.250

Mah, T. F., and O'Toole, G. A. (2001). Mechanisms of biofilm resistance to antimicrobial agents. *Trends Microbiol.* 9, 34–39. doi: 10.1016/S0966-842X(00)01913-2

Macia, M. D., Rojo-Molinero, E., and Oliver, A. (2014). Antimicrobial susceptibility testing in biofilm-growing bacteria. *Clin. Microbiol. Infect.* 20, 981–990. doi: 10.1111/1469-0691.12651

Miyazaki, J., Kuriyama, Y., Miyamoto, A., Tokumoto, H., Konishi, Y., and Nomura, T. (2013). Bacterial toxicity of functionalized polystyrene latex nanoparticles toward *Escherichia coli*. *Adv. Mater. Res.* 699, 672–677. doi: 10.4028/www.scientific.net/AMR.699.672

Machado, M. C., Tarquinio, K. M., and Webster, T. J. (2012). Decreased *Staphylococcus aureus* biofilm formation on nanomodified endotracheal tubes: a dynamic airway model. *Int. J. Nanomedicine* 7, 3741–3750. doi: 10.2147/IJN.S28191

Malik, Z., Ladan, H., and Nitzan, Y. (1992). Photodynamic inactivation of gram-negative bacteria: problems and possible solutions. *J. Photochem. Photobiol. B* 14, 262–266. doi: 10.1016/1011-1344(92)85104-3

Moan, J., Berg, K., Kvam, E., Western, A., Malik, Z., Rück, A., et al. (1989). Intracellular localization of photosensitizers. *Ciba Foundation symposium*, 146, 95–111. doi: 10.1002/9780470513842.ch7

Pérez-Laguna, V., Gilaberte, Y., Millán-Lou, M. I., Agut, M., Nonell, S., Rezusta, A., et al. (2019). A combination of photodynamic therapy and antimicrobial compounds to treat skin and mucosal infections: a systematic review. *Photochem. Photobiol. Sci.* 18, 1020–1029. doi: 10.1039/c8pp00534f

Plumet, L., Ahmad-Mansour, N., Dunyach-Remy, C., Kissa, K., Sotto, A., Lavigne, J. P., et al. (2022). Bacteriophage therapy for *Staphylococcus Aureus* infections: a review of animal models, treatments, and clinical trials. *Front. Cell. Infect. Microbiol.* 12:907314. doi: 10.3389/fcimb.2022.907314

Peulen, T. O., Wilkinson, K. J. (2011). Diffusion of nanoparticles in a biofilm. *Environ. Sci. Technol.* 45, 3367–3373. doi: 10.1021/es103450g

Radunz, S., Wedepohl, S., Röhr, M., Calderón, M., Tschiche, H. R., and Resch-Genger, U. (2020). pH-Activatable singlet oxygen-generating boron-dipyrromethenes (BODIPYs) for photodynamic therapy and bioimaging. *J. Med. Chem.* 63, 1699–1708. doi: 10.1021/acs.jmedchem.9b01873

Rebeca, S.-L., and Jorge, B. (2018). "Introductory chapter: BODIPY dye, an all-in-one molecular scaffold for (bio)photonics" in *BODIPY Dyes*. eds. B.-P. Jorge and L. Rebeca Sola (Rijeka: Intech Open)

Radunz, S., Kraus, W., Bischoff, F. A., Emmerling, F., Tschiche, H. R., and Resch-Genger, U. (2020). Temperature-and structure-dependent optical properties and Photophysics of BODIPY dyes. *J. Phys. Chem. A* 124, 1787–1797. doi: 10.1021/acs.jpca.9b11859

Raschpichler, M., Agel, M. R., Pinnapireddy, S. R., Duse, L., Baghdan, E., Schäfer, J., et al. (2019). In situ intravenous photodynamic therapy for the systemic eradication of blood stream infections. *Photochem. Photobiol. Sci.* 18, 304–308. doi: 10.1039/c8pp00267c

Radunz, S., Tschiche, H. R., Moldenhauer, D., and Resch-Genger, U. (2017). Broad range ON/OFF pH sensors based on pKa tunable fluorescent BODIPYs. *Sens. Actuators B Chem.* 251, 490–494. doi: 10.1016/j.snb.2017.05.080

Sheng, W., Lv, F., Tang, B., Hao, E., and Jiao, L. (2019). Toward the most versatile fluorophore: direct functionalization of BODIPY dyes via regioselective C–H bond activation. *Chin. Chem. Lett.* 30, 1825–1833. doi: 10.1016/j.cclet.2019.08.004

Songca, S. P., and Adjei, Y. (2022). Applications of antimicrobial photodynamic therapy against bacterial biofilms. *Int. J. Mol. Sci.* 23:3209. doi: 10.3390/ijms23063209

Shrestha, A., Hamblin, M. R., and Kishen, A. (2014). Photoactivated rose bengal functionalized chitosan nanoparticles produce antibacterial/biofilm activity and stabilize dentin-collagen. *Nanomed.* 10, 491–501. doi: 10.1016/j.nano.2013.10.010

Schwibbert, K., Menzel, F., Epperlein, N., Bonse, J., and Krüger, J. (2019). Bacterial adhesion on femtosecond laser-modified polyethylene. *Materials.* 12:3107. doi: 10.3390/ma12193107

Summer, K., Browne, J., Hollanders, M., and Benkendorff, K. (2022). Out of control: the need for standardised solvent approaches and data reporting in antibiofilm assays incorporating dimethyl-sulfoxide (DMSO). *Biofilms* 4:100081. doi: 10.1016/j.bioflm.2022.100081

Sun, L., Jiang, W., Zhang, H., Guo, Y., Chen, W., Jin, Y., et al. (2019). Photosensitizer-loaded multifunctional chitosan nanoparticles for simultaneous in situ imaging, highly efficient bacterial biofilm eradication, and tumor ablation. *ACS Appl. Mater. Interfaces* 11, 2302–2316. doi: 10.1021/acsami.8b19522

Sahle-Demessie, E., and Tadesse, H. (2011). Kinetics and equilibrium adsorption of nano-TiO2 particles on synthetic biofilm. *Surf. Sci.* 605, 1177–1184. doi: 10.1016/j.susc.2011.03.022

Usacheva, M., Layek, B., Rahman Nirzhor, S. S., and Prabha, S. (2016). Nanoparticle-mediated photodynamic therapy for mixed biofilms. *J. Nanomater.* 2016:4752894. doi: 10.1155/2016/4752894

Velev, O. D., and Kaler, E. W. (1999). In situ assembly of colloidal particles into miniaturized biosensors. *Langmuir* 15, 3693–3698. doi: 10.1021/la981729c

Vatansever, F., de Melo, W. C., Avci, P., Vecchio, D., Sadasivam, M., Gupta, A., et al. (2013). Antimicrobial strategies centered around reactive oxygen species--bactericidal antibiotics, photodynamic therapy, and beyond. *FEMS Microbiol. Rev.* 37, 955–989. doi: 10.1111/1574-6976.12026

Wang, P., Qin, F., Zhang, Z., and Cao, W. (2015). Quantitative monitoring of the level of singlet oxygen using luminescence spectra of phosphorescent photosensitizer. *Opt. Express* 23, 22991–23003. doi: 10.1364/OE.23.022991

Wilson, W. W., Wade, M. M., Holman, S. C., and Champlin, F. R. (2001). Status of methods for assessing bacterial cell surface charge properties based on zeta potential measurements. *J. Microbiol. Methods* 43, 153–164. doi: 10.1016/S0167-7012(00)00224-4

Yaghoubi, M., Rahimi, F., Negahdari, B., Rezayan, A. H., and Shafiekhani, A. (2020). A lectin-coupled porous silicon-based biosensor: label-free optical detection of bacteria in a real-time mode. *Sci. Rep.* 10:16017. doi: 10.1038/s41598-020-72457-x

Yang, K., Gitter, B., Rüger, R., Albrecht, V., Wieland, G. D., and Fahr, A. (2012). Wheat germ agglutinin modified liposomes for the photodynamic inactivation of bacteria. *Photochem. Photobiol.* 88, 548–556. doi: 10.1111/j.1751-1097.2011.00983.x

You, Y. (2018). Chemical tools for the generation and detection of singlet oxygen. *Org. Biomol. Chem.* 16, 4044–4060. doi: 10.1039/C8OB00504D

Ziessel, R., Ulrich, G., and Harriman, A. (2007). The chemistry of Bodipy: a new El Dorado for fluorescence tools. *New J. Chem.* 31, 496–501. doi: 10.1039/b617972j

Zwirzitz, B., Wetzels, S. U., Dixon, E. D., Stessl, B., Zaiser, A., Rabanser, I., et al. (2020). The sources and transmission routes of microbial populations throughout a meat processing facility. *NPJ Biofilms Microbiomes.* 6:26. doi: 10.1038/s41522-020-0136-z

Zheng, Y., He, L., Asiamah, T. K., and Otto, M. (2018). Colonization of medical devices by staphylococci. *Environ. Microbiol.* 20, 3141–3153. doi: 10.1111/1462-2920.14129

Glossary

EPS	extracellular polymeric substances
ROS	Reactive oxygen species
PDT	Photodynamic therapy
PS	Photosensitizer
aPDT	Antimicrobial photodynamic therapy
BODIPY	Boron-dipyrromethene
NPs	Nanoparticles
THF	Tetrahydrofuran
PDI	Polydispersity index
DLS	Dynamic light scattering
TEM	Transmission electron microscope
DPBF	1, 3-diphenylisobenzofuran
LB	Luria–Bertani
CFU	Colony forming units
CLSM	Confocal laser scanning microscopy
SEM	Scanning electron microscopy

4. Discussion

4.1. Designing functional nanoparticles for sensing and treatment

The properties of a NP are essential for its function. For example, the surface hydrophilicity of a particle determines whether it can be suspended in water or if it will have the tendency to aggregate. The types of surface groups determine which molecules are suitable as binding partners for further surface functionalisations and interactions within a biological system. Therefore, the NPs should be selected and modified depending on the intended application, and their functionality should be thoroughly checked.

In this thesis, PS NPs with different surface functionalisations were employed for the fabrication of various nanoscale tools. In the first study, pH nanosensors were fabricated for application in biofilms. The NPs needed to be highly hydrophilic to be used in aqueous media and have surface groups to which the sensor dye could be conjugated. Carboxylated and aminated particles were used for this purpose, as they are hydrophilic, and the amine groups allow for conjugation with the pH-sensitive dye FITC. Both before and after dye conjugation to the amine groups on the surface, the particles exhibited a slightly negative zeta potential (Table 1). Zeta potential, along with particle size and polydispersity index, is an important indicator of suspension stability. Maintaining a constant particle size before and after embedding and conjugating of the dyes is crucial for the stability of the suspension. The particle size was monitored before and after the introduction of the dyes and no significant changes were observed. A small particle size and a narrow size distribution I also crucial for high-resolution localized pH imaging. In addition, particle size is also an important factor that determines particle diffusion and accumulation into a biofilm. Thus, it is essential to ensure that all properties remain stable after embedding and conjugation of dyes and proteins to guarantee the functionality of the particles. If any of these parameters changed significantly, the dye loading might have to be limited.

For the second study, the pH_e nanosensors were designed and fabricated for use with eukaryotic cells. This required the NPs to be conjugated with a targeting moiety to attach the sensor to the cells. The lectin wheat germ agglutinin (WGA) was used for this purpose.

Hydrophilic carboxylated PS NPs were chosen because they allow easy conjugation of the lectin via carboxyl groups. To maintain a good suspension stability after lectin conjugation, particles with a highly negative zeta potential were selected. The zeta potential was slightly increased by conjugating the lectin to the carboxyl groups. However, the final value was intended to be in the optimum negative range for stability of around -30 mV (Table 1). This resulted in a long-term stable nanoparticle suspension for the pH_e nanosensor.

Table 1. Overview of the properties of the precursor nanoparticles (NP) and the nanoparticles after embedding and conjugation of the dyes determined with transmission electron microscopy (TEM) and dynamic light scattering (DLS). PS – polystyrene; PDI – polydispersity index; NR – nile red; BODIPY – boron-dipyrromethene.

Type of PS NP	Size (TEM) [nm]	Size (DLS) [nm]	PDI	Zeta potential [mV]
NP (COOH NH_2)	103 ± 9	133 ± 3	0.038 ± 0.023	−30.6 ± 0.6
pH nanosensor	101 ± 8	132 ± 1	0.017 ± 0.011	−38.0 ± 1.3
PS NP (COOH)	94 ± 9	114 ± 4	0.012 ± 0.020	−62.7 ± 1.1
NR-loaded NP	92 ± 10	114 ± 3	0.018 ± 0.015	−66.0 ± 5.3
pH_e nanosensor	88 ± 9	126 ± 7	0.050 ± 0.015	−30.6 ± 1.4
NP (COOH NH_2)	96 ± 12	130 ± 1	0.008 ± 0.006	−30.7 ± 1.1
BODIPY NP	90 ± 9	137 ± 2	0.111 ± 0.018	−22.1 ± 0.6

The third study focused on developing ROS-generating NPs for aPDT in biofilms. To achieve this, the NPs needed to have good water-suspendability, the ability to incorporate a lipophilic PTS, and the capability to passively diffuse into and accumulate in biofilms. In the previous study on pH nanosensors for the use in biofilms, carboxylated and aminated NPs were used and demonstrated excellent diffusion behavior in different biofilms. Therefore, the same precursor PS NPs were used in this study. The lipophilic PTS BODIPY was embedded in the NPs and, subsequently, the diffusion into three different biofilms was evaluated. The results showed good diffusion into all three biofilms, which is important for an effective aPDT method. Accordingly, the carboxylated and aminated precursor NPs were considered suitable candidates for embedding the PTS and achieving aPDT in the biofilm.

All three studies presented in this thesis demonstrate successful embedding of dyes in NPs without significant changes in particle size or negative impact on the zeta potential, therefore indicating no loss of function. The dyes (NR for both types of pH nanosensors and the BODIPY dye for the ROS-generating NPs) showed homogeneous particle loading upon incorporation into the NPs with no leakage in aqueous dispersions, a high photochemical stability, and brightness for imaging. Leakage or photobleaching of dyes can impair the functionality of a nanosensor and lead to incorrect interpretation of NPs fluorescence. Free dye may cause apparent cellular uptake to be observed and the distribution of the dye may not correspond to that of the NPs [196,197]. None of the three studies presented in this thesis showed any dye leakage from the NPs, nor photobleaching, or other loss of function.

This demonstrates that the selected PS NPs, in combination with appropriate dyes used in the three studies, are suitable to be used as nanosensors and nanocarriers.

4.2. Biosensing with nanosensors

A ratiometric nanosensor typically requires three main components: a sensor dye, a reference dye, and a NP that contains both dyes while maintaining their function. The functionality of nanosensors in biological systems can be limited by various factors, such as interaction with the matrix components of a biofilm. It is known that NPs in biological fluids form a dynamic layer of biomolecules, mainly proteins, but also polysaccharides, nucleic acids or lipids, also termed protein corona [11,198]. The presence of a protein corona may promote particle agglomeration or impair the functionality of the incorporated dyes. This could result in changes to the absorption or fluorescence maxima, fluorescence intensities, and/or pH dependence of the optical properties used as readout parameters. Therefore, it is necessary to verify the functionality of these parameters in the biological medium before the nanosensor can be successfully used.

In the pH nanosensor study for monitoring pH in biofilms, transmission electron microscopy images were taken after 24 hours of incubation in the biofilm to check for particle agglomeration. The images showed that the particles did not aggregate or agglomerate even after this long time. This is an advantage over previously published nanosensors, which often show a high aggregation tendency in biological media, limiting their biosensing performance [78]. Furthermore, the fluorescence properties of the pH nanosensor were evaluated both before and after incubation in the biofilm. This is crucial as the pH nanosensor's function relies on the fluorescence of two dyes. The fluorescence of the reference dye NR needs to remain constant over the entire pH measuring range, while that of the sensor dye FITC changes as a function of pH. The pH can be determined by calculating the ratio of fluorescence intensities between the sensor and reference dyes after calibration. The fluorescence maxima, intensities, and pH dependencies remained unchanged even after 24 hours of incubation. In another experiment, the change in pH value within a biofilm after glucose metabolization was monitored. The decrease in pH value, an acidification of the biofilm, was shown as a relative decrease in FITC fluorescence compared to NR fluorescence. To ensure the reliability of the measurement, it was confirmed that the observed decrease in FITC fluorescence was not caused by dye bleaching or nanosensor leakage from the biofilm. For this purpose, a standard buffer was used to reverse the pH value of the biofilm. The functionality of the nanosensor was confirmed by demonstrating the complete reversibility of the fluorescence of the sensor dye, even after 4 hours of measurement. The study demonstrated that the nanosensor's functionality remains unaffected by the presence of a complex biological matrix, pH changes, or long measurement intervals. This makes the nanosensor a highly robust and suitable tool for pH determinations in biofilms, even over extended periods of time.

Eukaryotic cells and tissues differ physiologically from bacterial biofilms in several ways. Eukaryotic cells and tissues are denser, have more direct cell-cell contacts, and lack the slimy extracellular matrix typical for biofilms. Without this matrix, passive diffusion of the nanosensor into the eukaryotic cell tissue was not possible. Therefore, the pH nanosensor needed to be structurally adapted to measure the pH_e of eukaryotic cells. For this purpose, the nanosensor was equipped with a targeting moiety, which enables anchoring the sensor to the cell surface. The lectin WGA was chosen as a targeting moiety due to its ability to bind to *N*-acetyl-D-glucosamine and *N*-acetylneuraminic acid residues present on cell surfaces [199,200]. The theoretical suitability of WGA as a cell surface targeting molecule was confirmed in cell culture using three cell lines originated from different tissues (lung: A549, placenta: BeWo, skin: HaCaT). In a screening experiment, WGA bound exclusively to cell membranes, demonstrating its suitability as a targeting molecule. The NPs were then conjugated with WGA to test whether the lectin anchors the NPs to the cells. In all three cell lines used, approximately 75-80% of the targeted NPs bound specifically to the cells. These results are consistent with literature values for the binding of WGA coupled to BSA to Caco-2 cells [201]. This indicates that the activity of WGA as a targeting moiety in conjunction with the NPs is not compromised when the protein is conjugated.

For ratiometric imaging, the nanosensor requires a reference dye embedded in the core and a sensor dye, usually conjugated to the NPs surface. To avoid competition between FITC and WGA on the particle surface, FITC-labelled WGA was conjugated to the NPs. It is commercially available and has the advantage of requiring only a single conjugation step. It was also verified that the fluorescence properties and the functionality for pH sensing of FITC are not affected when conjugated to WGA instead of the NPs.

The dyes NR and FITC have spectrally distinct emission bands. FITC has a narrow excitation range with a maximum at approximately 490 nm, while NR has a broad excitation range with a maximum at 530 nm. The excitation maxima of NR and FITC partly overlap. Therefore, both dyes can be excited at the same wavelength, but the emission can be read at different wavelengths, enabling a ratiometric pH_e measurement with only one excitation wavelength. This simplifies the equipment required for the measurements, reduces sources of error, and shortens measurement time, particularly in confocal microscopy. The chosen ratiometric design concept allows for a correlation between the calculated intensity ratios of the FITC and NR fluorescence of the pH_e nanosensor with the pH value, while neglecting local concentration differences of the sensor. The pH_e nanosensor's robustness and reversibility were tested by repeatedly changing the pH with subsequent fluorescence measurement. The reversibility of the fluorescence intensity ratio was demonstrated, ruling out any leaking or bleaching of the dyes. This reversible reaction is a prerequisite for the pH_e nanosensor to be used for monitoring continuous pH fluctuations in biological systems over long time periods.

The pH_e nanosensor had a working range in cell culture of pH 5.5–9.0. This range is quite wide compared to other pH sensors e.g., from Ohgaki et al. with a range of approx. 5.5–7.0 [202] and from Chen et al. with a range of only 5.9–6.4 [203]. Thus, the working range of the nanosensor for pH detection is well suited for fluorometric pH sensing in the physiological pH_e range of eukaryotic cells.

Despite its efficient performance, no advanced techniques or materials other than a confocal laser scanning microscopy are required. Therefore, the pH_e nanosensor is a useful instrument for pH_e detection that can be used in a standard laboratory environment.

Ideally, nanosensors should function with minimal impact on cellular processes to avoid disturbing the natural cellular environment. It is important to exclude any potential toxicity of the NPs to the system under investigation. Therefore, the cell viability at incubation times of up to 24 hours and concentrations of up to 2.5 mg/ml was investigated. The results showed no significant toxic effects of the NPs, indicating that the pH_e nanosensor is safe for use in cell culture experiments.

Furthermore, the pH_e nanosensor's functionality for sensing pH_e in cell culture was assessed. The results showed that the pH_e nanosensor effectively targeted the cell membranes of all three types of cell lines, enabling direct measurement of pH_e at the cell surface. The pH curves and pK_a values observed in the cell culture experiments were consistent with those obtained in the acellular assays, indicating the robustness of the pH_e nanosensor. The functionality of the pH_e nanosensor is not affected by the biological system despite varying experimental conditions, including salt concentrations, protein interactions, matrix effects, and cellular autofluorescence. This confirms the suitability of the pH_e nanosensor for biological applications, as it demonstrates that the sensor remains functional even in complex biological environments.

Using an active targeting moiety has the added benefit of allowing the pH_e nanosensor to be applied in a single step by adding it to the cell culture medium for ten minutes. This makes the application of the pH_e nanosensor a simple experimental procedure, which sets it apart from other sensors used for pH_e measurement on the cell surface. These sensors must either be genetically encoded to be expressed on the cell surface [204,205] or require long incubation times (several hours to overnight) [206]. Easy experimental procedures have also been achieved in other studies, e.g. by Anderson et al. [207]. They developed a sensor for determining the surface pH of cancer cells based on the conjugation of a dye to a low-insertion protein. The protein penetrates the cell membrane and enables the detection of the pH at the cell surface. Although this method has a high degree of accuracy, the resolution is not good enough to detect local pH values at a cellular level. This is important if the method is to be used universally, for example to determine and map the pH microenvironments typical for cancer tissue.

The pH_e nanosensor study presented here highlights the functionality and practicality of simple and user-friendly yet powerful instruments that are in high demand in biochemical and cancer research. This pH_e nanosensor is a useful tool for pH_e detection of cells that can be used in many laboratories across different research disciplines.

4.3. Nanoparticles as carries for antimicrobial photodynamic therapy treatment

In the third study, an aPDT method was developed using PS NPs as carriers for the ROS-generating PTS BODIPY. It was demonstrated that when activated, these NPs can effectively eliminate both planktonic bacteria and bacterial biofilms. It is widely recognized that aPDT has a greater impact on planktonic bacterial cells than on biofilms. This is because the EPS matrix makes it more difficult for PS NPs to penetrate into biofilms. On top, the concentration of bacteria in biofilms is generally higher than in suspensions in the medium [191]. Furthermore, bacteria in biofilms exist in different physiological stages, meaning that not all of the bacteria are in a susceptible, proliferating state [145]. Some bacteria may exist in a dormant state with reduced metabolism, which also limits the internalisation of substances and thus the efficacy of many treatment agents. Several published studies have shown that while planktonic bacteria can be effectively eradicated, the reduction of biofilms is significantly lower [171,186,193]. While this phenomenon is partly observed in this study, the results regarding the eradication of biofilms contrast with those of other studies. Longer illumination times allowed for complete elimination of the biofilms. Complete eradication is critical as even a few surviving specimens can quickly rebuild large populations, making it essential for a successful disinfection treatment. Generally, the eradication effect increased as the illumination time increased and was particularly high when the BODIPY-loaded NPs were previously incubated in the biofilm. This suggests that BODIPY-loaded NPs are more effective when ROS generation occurs in close proximity to the bacteria within the biofilm rather than in the medium. The main reason for this is the short lifetime of ROS and therefore a limited diffusion distance. The effectiveness of the ROS-generating PTS is highly dependent on its proximity to the bacteria. Therefore, carriers, such as NPs, are needed to transport the PTS into the biofilm.

Here, the required incubation times for sufficient accumulation in the biofilm vary depending on the type of biofilm. It is assumed that NPs penetrate the biofilm mainly by diffusion [208]. Particle properties, such as size, charge, and hydrophobicity, influence the diffusion of NPs into the biofilm [38]. However, the structure and composition of the biofilm also play an important role for the time the NPs need to diffuse into the biofilm. The pore size and hydrophobicity of the biofilm are particularly important, but also the charge and chemical gradient of the biofilm and its matrix [209,210]. As identical NPs were used in all three biofilm experiments, it is likely that the structure of the biofilms themselves is the most important factor in the kinetics of NP penetration. Some bacteria such as *Escherichia coli* form dense biofilms with small extracellular spaces and pore sizes, making it more difficult for the NPs to diffuse into the biofilm. Therefore, longer incubation times were required for *Escherichia coli* compared to *Staphylococcus aureus* and *Streptococcus mutans*. These biofilms typically have a less dense structure with a greater amount of extracellular matrix and larger pore size, which facilitates the diffusion of NPs into the biofilm [211]. The results are therefore consistent with the hypothesis that the structure and pore size of a biofilm can significantly influence the penetration of NPs.

According to the literature, gram-negative bacteria have been reported to be up to ten times less sensitive to aPDT than gram-positive bacteria [180,182]. This difference in sensitivity is thought to be due to differences in cell wall composition between gram-positive and gram-negative bacteria [167,212]. Although gram-positive bacteria have a thicker cell wall, gram-negative bacteria have a more complex cell wall structure. They have an additional lipopolysaccharide-containing membrane as their outermost layer, which offers additional protection against ROS. In order to cause a membrane disruption, ROS not only have to destroy the outer membrane structure but also the cytoplasmic membrane [212].

In this study, it was found that biofilms of gram-positive bacteria, as reported in the literature, were more sensitive than those of gram-negative bacteria. However, this was not observed for planktonic bacteria. It is assumed that other factors, such as the generation time of the bacteria (also known as the doubling time), may be decisive for the sensitivity of planktonic bacteria to aPDT. During the time of cell division, the bacterial membranes are thinner, particularly at the division site and not yet fully functional [213]. This suggests that the bacteria are particularly susceptible to ROS in this phase, as these can destroy the cell membranes much more easily, regardless of whether they are gram-negative or gram-positive. Bacteria with short doubling times undergo the vulnerable cycle of cell division more often within the same time. The bacterial species used in this study have doubling times of approximately 20 minutes for *Escherichia coli* as well as *Staphylococcus aureus* and 60 minutes for *Streptococcus mutans* [214-217]. As the illumination time was 30 minutes for all planktonic samples, it can be assumed, that all *Escherichia coli* and *Staphylococcus aureus* bacteria underwent at least one cell division, but only about half of the *Streptococcus mutans* bacteria did. Therefore, *Streptococcus mutans* bacteria were in a less vulnerable state, making them less susceptible to ROS damage. The study's results confirm the previous assumption and demonstrate that, while *Escherichia coli* and *Staphylococcus aureus* were both completely eradicated, the population of *Streptococcus mutans* was only reduced from 10^7 to 10^3 cells. This suggests that bacteria with slower cell division may be less susceptible to aPDT than rapidly dividing bacteria. To confirm this hypothesis, further investigation is required using different bacterial species with varying cell division times. However, if this effect proves to be true, it seems possible to estimate the optimal treatment duration in advance based on the division time of the bacteria. This can significantly increase the chances of successful eradication.

In addition to eradication efficacy, the study also investigated the interactions between biofilms and NPs. Scanning electron microscopy (SEM) images of control biofilms, biofilms with non-activated NPs, and biofilms exposed to activated ROS-producing NPs were obtained. The images showed that non-activated NPs had little interaction with the bacteria, whereas the bacteria exposed to ROS-generating NPs had a large number of NPs attached to the bacterial surface. The death of the bacteria by aPDT may cause the loss of membrane potential in the bacteria, which could explain the adhesion of the NPs to the cells. Additionally, changes in the cell membrane itself may also contribute to this phenomenon. Typically, viable bacteria have negatively charged outer cell membranes due to the presence of molecules such as lipopolysaccharides and carboxylate substituents on their surface [218]. The negatively charged NPs are not electrostatically attracted to the bacteria. However, if ROS damage the bacteria and their cell membranes, it can lead to a disruption of membrane integrity. This process can cause substances and intracellular components to leak from the bacteria, resulting in the release of positively charged molecules or ions on the bacterial surface. As a result, the overall charge of the bacteria may shift from negative to neutral or positive [219,220]. This could lead to the binding of NPs to the bacterial surface through electrostatic attraction, as observed in the SEM images.

It is worth investigating whether the efficacy of aPDT could be improved by conjugating the NPs with a targeting moiety similar to the pH_e nanosensor. This could potentially lead to shorter incubation or irradiation times or extend the applicability of the system by only being effective against a targeted bacterial strain.

It has been demonstrated that NPs are valuable tools for the design and fabrication of nanosensors, but also as carriers of PTS for PDT. Their versatility allows for tuning of their properties to suit the desired application. It is a unique feature that a nanosensor with only minimal structural modifications can be used for imaging in both bacterial biofilms and eukaryotic cells.

While PS NPs demonstrate good biocompatibility over short and medium time periods, it is important to note that they are not biodegradable (yet [221]). This characteristic raises concerns about potential accumulation in living organisms, leading to adverse effects. Therefore, its use in medical applications *in vivo* is currently discouraged. However, PS NPs are valuable tools for manufacturing *in vitro* diagnostic and therapeutic instruments and for the testing of pharmaceutical compounds, PDT candidates and more. By addressing and understanding the potential risks associated with PS NPs, researchers can make informed decisions to maximize their benefits while mitigating potential harm in specific contexts.

5. Conclusion and outlook

This thesis presents three studies that demonstrate the diverse use and application of PS NPs as nanosensors for biosensing in cellular research and for the treatment of pathogenic biofilms.

In the first study, the design and fabrication of a pH-responsive ratiometric nanosensor using biocompatible PS NPs is described. The pH nanosensor employs the ratio of the fluorescence intensities of the pH-insensitive dye NR and the pH-sensitive dye FITC to determine and monitor the pH in biofilms by confocal microscopic imaging. The study demonstrated the function of the nanosensors by monitoring time-dependent pH changes induced by the metabolic activity of *Escherichia coli* biofilms. The smart but straightforward design concept, combined with the ease of fabrication and use of the sensor, create numerous application possibilities in the characterization of the chemical microenvironment of biofilms. Particularly with regard to automated imaging and automated image and data processing, the quantity and quality of data that can be obtained with such nanosensors far exceeds that of conventional methods. Future applications of these nanosensors include the investigation of microbially induced corrosion processes on surfaces, *in vitro* investigations of dental caries, and monitoring of other biotechnological processes accompanied by pH changes. These nanosensors offer promising avenues for advancing our understanding of biofilm dynamics and facilitating improved strategies to combat biofilm-associated health issues in natural, industrial, and clinical environments.

The second study presents a ratiometric pH_e nanosensor developed for the determination of pH_e of eukaryotic cells. The nanosensor contains the same fluorophores as the first nanosensor, but by conjugating the nanosensor to a cell membrane-targeting lectin, this nanosensor can effectively label the cell surface of different cell lines. This feature enables precise and spatially resolved measurements of the pH_e of individual cells directly on their cell surface. The study illustrates the versatility and compatibility of the pH_e nanosensor with different cell lines from different organs. The pH_e nanosensor holds great potential as a tool for exploring cellular microenvironments and gaining a deeper comprehension of cellular processes. Its applications in biomedical research, particularly in cancer research, for understanding and investigating metabolic disorders, diagnostic or therapeutic applications highlight its potential impact on diverse fields.

The third study focuses on the use of PS NPs as carriers of PTS for aPDT. The study demonstrated the high efficacy of BODIPY-loaded NPs against both planktonic bacteria and bacterial biofilms. The NPs performed several crucial functions: (1) solubilizing the lipophilic PTS making it applicable in aqueous media, (2) delivering the PTS directly into the biofilm for activation at the target site, and (3) having a high loading resulting in a high local concentration of PTS. The study found that the BODIPY-loaded NPs were highly effective in preventing and eliminating biofilms. This provides a practical and straightforward alternative to existing methods. Additionally, aPDT reduces the risk of developing bacterial resistance in the future. Furthermore, active targeting using lectins or antibodies could be utilized for selective bacterial eradication, enabling beneficial bacteria to thrive in certain applications. In the future, this approach could also be combined with other bactericidal or imaging agents to enhance the NPs efficiency and potentially be developed as a dual-action or theranostic application.

In summary, all three studies collectively underscore the potential of NPs to be utilized as sensors and carriers in providing valuable insights into biofilm microenvironments. They also enable precise pH_e measurements in diverse cell lines and offer effective strategies for antimicrobial treatment. These advancements hold promise for future research and applications in fields ranging from biofilm characterization to biomedical research and antimicrobial therapy.

6. Literature

1 Altug, H., Oh, S.-H., Maier, S. A. & Homola, J. Advances and applications of nanophotonic biosensors. *Nature Nanotechnology* **17**, 5-16 (2022). https://doi.org:10.1038/s41565-021-01045-5

2 Srivastava, A. K., Dev, A. & Karmakar, S. Nanosensors and nanobiosensors in food and agriculture. *Environmental Chemistry Letters* **16**, 161-182 (2018). https://doi.org:10.1007/s10311-017-0674-7

3 Abdel-Karim, R., Reda, Y. & Abdelfatah, A. Review—Nanostructured Materials-Based Nanosensors. *Journal of The Electrochemical Society* **167**, 037554 (2020). https://doi.org:10.1149/1945-7111/ab67aa

4 Namikuchi, E. A., Gaspar, R. D. L., Raimundo, I. M. & Mazali, I. O. A fluorescent magnetic core–shell nanosensor for detection of copper ions in natural waters. *Spectrochimica Acta Part A: Molecular and Biomolecular Spectroscopy* **300**, 122915 (2023). https://doi.org:10.1016/j.saa.2023.122915

5 Ishida, T., Murayama, T., Taketoshi, A. & Haruta, M. Importance of Size and Contact Structure of Gold Nanoparticles for the Genesis of Unique Catalytic Processes. *Chemical Reviews* **120**, 464-525 (2020). https://doi.org:10.1021/acs.chemrev.9b00551

6 Carabineiro, S. A. C. Supported Gold Nanoparticles as Catalysts for the Oxidation of Alcohols and Alkanes. *Frontiers in Chemistry* **7** (2019). https://doi.org:10.3389/fchem.2019.00702

7 Alkilany, A. M. & Murphy, C. J. Toxicity and cellular uptake of gold nanoparticles: what we have learned so far? *J Nanopart Res* **12**, 2313-2333 (2010). https://doi.org:10.1007/s11051-010-9911-8

8 Pastoriza-Santos, I., Kinnear, C., Pérez-Juste, J., Mulvaney, P. & Liz-Marzán, L. M. Plasmonic polymer nanocomposites. *Nature Reviews Materials* **3**, 375-391 (2018). https://doi.org:10.1038/s41578-018-0050-7

9 Visaveliya, N. R. & Köhler, J. M. Softness Meets with Brightness: Dye-Doped Multifunctional Fluorescent Polymer Particles via Microfluidics for Labeling. *Advanced Optical Materials* **9**, 2002219 (2021). https://doi.org:10.1002/adom.202002219

10 Mitchell, M. J. *et al.* Engineering precision nanoparticles for drug delivery. *Nature Reviews Drug Discovery* **20**, 101-124 (2021). https://doi.org:10.1038/s41573-020-0090-8

11 Xia, X.-R., Monteiro-Riviere, N. A. & Riviere, J. E. An index for characterization of nanomaterials in biological systems. *Nature Nanotechnology* **5**, 671-675 (2010). https://doi.org:10.1038/nnano.2010.164

12 Nguyen, V. H. & Lee, B. J. Protein corona: a new approach for nanomedicine design. *Int J Nanomedicine* **12**, 3137-3151 (2017). https://doi.org:10.2147/ijn.S129300

13 Zayas, H. A., Truong, N. P., Valade, D., Jia, Z. & Monteiro, M. J. Narrow molecular weight and particle size distributions of polystyrene 4-arm stars synthesized by RAFT-mediated miniemulsions. *Polym Chem-Uk* **4**, 592-599 (2013). https://doi.org:10.1039/C2PY20709E

14 Liao, J. *et al.* Kinetically Controlled Synthesis of Nonspherical Polystyrene Nanoparticles with Manipulatable Morphologies. *Langmuir* **38**, 12132-12139 (2022). https://doi.org:10.1021/acs.langmuir.2c01326

15 Wang, Y.-F. *et al.* Spatiotemporal Tracing of the Cellular Internalization Process of Rod-Shaped Nanostructures. *ACS Nano* **16**, 4059-4071 (2022). https://doi.org:10.1021/acsnano.1c09684

16 Dasgupta, S., Auth, T. & Gompper, G. Shape and Orientation Matter for the Cellular Uptake of Nonspherical Particles. *Nano Letters* **14**, 687-693 (2014). https://doi.org:10.1021/nl403949h

17 Champion, J. A. & Mitragotri, S. Shape induced inhibition of phagocytosis of polymer particles. *Pharm Res* **26**, 244-249 (2009). https://doi.org:10.1007/s11095-008-9626-z

18 Chanteau, B., Fresnais, J. & Berret, J. F. Electrosteric Enhanced Stability of Functional Sub-10 nm Cerium and Iron Oxide Particles in Cell Culture Medium. *Langmuir* **25**, 9064-9070 (2009). https://doi.org:10.1021/la900833v

19 Ivanov, V. B., Behnisch, J., Holländer, A., Mehdorn, F. & Zimmermann, H. Determination of Functional Groups on Polymer Surfaces Using FluorescenceLabelling. *Surface and Interface Analysis* **24**, 257-262 (1996). https://doi.org:10.1002/(SICI)1096-9918(199604)24:4<257::AID-SIA107>3.0.CO;2-1

20 Kik, K., Bukowska, B. & Sicińska, P. Polystyrene nanoparticles: Sources, occurrence in the environment, distribution in tissues, accumulation and toxicity to various organisms. *Environmental Pollution* **262**, 114297 (2020). https://doi.org:10.1016/j.envpol.2020.114297

21 Wang, Y. *et al.* Effects of ingested polystyrene microplastics on brine shrimp, Artemia parthenogenetica. *Environmental Pollution* **244**, 715-722 (2019). https://doi.org:10.1016/j.envpol.2018.10.024

22 Ašmonaitė, G., Sundh, H., Asker, N. & Carney Almroth, B. Rainbow Trout Maintain Intestinal Transport and Barrier Functions Following Exposure to Polystyrene Microplastics. *Environmental Science & Technology* **52**, 14392-14401 (2018). https://doi.org:10.1021/acs.est.8b04848

23 Kim, J. *et al.* Surface charge determines the lung inflammogenicity: A study with polystyrene nanoparticles. *Nanotoxicology* **10**, 94-101 (2016). https://doi.org:10.3109/17435390.2015.1022887

24 Miyazaki, J. *et al.* Bacterial Toxicity of Functionalized Polystyrene Latex Nanoparticles Toward Escherichia coli</i. *Advanced Materials Research* **699**, 672-677 (2013). https://doi.org:10.4028/www.scientific.net/AMR.699.672

25 Schröter, L. *et al.* A Multisystemic Approach Revealed Aminated Polystyrene Nanoparticles-Induced Neurotoxicity. *Small* **n/a**, 2302907 https://doi.org:10.1002/smll.202302907

26 Weiss, M. *et al.* Density of surface charge is a more predictive factor of the toxicity of cationic carbon nanoparticles than zeta potential. *Journal of Nanobiotechnology* **19**, 5 (2021). https://doi.org:10.1186/s12951-020-00747-7

27 Fröhlich, E. The role of surface charge in cellular uptake and cytotoxicity of medical nanoparticles. *Int J Nanomedicine* **7**, 5577-5591 (2012). https://doi.org:10.2147/ijn.S36111

28 Li, R. *et al.* Surface charge and cellular processing of covalently functionalized multiwall carbon nanotubes determine pulmonary toxicity. *ACS Nano* **7**, 2352-2368 (2013). https://doi.org:10.1021/nn305567s

29 Wei, X. *et al.* Cationic nanocarriers induce cell necrosis through impairment of Na+/K+-ATPase and cause subsequent inflammatory response. *Cell Research* **25**, 237-253 (2015). https://doi.org:10.1038/cr.2015.9

30 Murali, K. *et al.* Uptake and bio-reactivity of polystyrene nanoparticles is affected by surface modifications, ageing and LPS adsorption: in vitro studies on neural tissue cells. *Nanoscale* **7**, 4199-4210 (2015). https://doi.org:10.1039/c4nr06849a

31 Loos, C. *et al.* Functionalized polystyrene nanoparticles as a platform for studying bio-nano interactions. *Beilstein Journal of Nanotechnology* **5**, 2403-2412 (2014). https://doi.org:10.3762/bjnano.5.250

32 Sargazi, S. *et al.* Fluorescent-based nanosensors for selective detection of a wide range of biological macromolecules: A comprehensive review. *International Journal of Biological Macromolecules* **206**, 115-147 (2022). https://doi.org:10.1016/j.ijbiomac.2022.02.137

33 Huang, X., Zhu, Y. & Kianfar, E. Nano Biosensors: Properties, applications and electrochemical techniques. *Journal of Materials Research and Technology* **12**, 1649-1672 (2021). https://doi.org:10.1016/j.jmrt.2021.03.048

34 Steinegger, A., Wolfbeis, O. S. & Borisov, S. M. Optical Sensing and Imaging of pH Values: Spectroscopies, Materials, and Applications. *Chemical Reviews* **120**, 12357-12489 (2020). https://doi.org:10.1021/acs.chemrev.0c00451

35 Han, J. & Burgess, K. Fluorescent indicators for intracellular pH. *Chem Rev* **110**, 2709-2728 (2010). https://doi.org:10.1021/cr900249z

36 Shamsipur, M., Barati, A. & Nematifar, Z. Fluorescent pH nanosensors: Design strategies and applications. *Journal of Photochemistry and Photobiology C: Photochemistry Reviews* **39**, 76-141 (2019). https://doi.org:10.1016/j.jphotochemrev.2019.03.001

37 Radunz, S. *et al.* Simple Self-Referenced Luminescent pH Sensors Based on Upconversion Nanocrystals and pH-Sensitive Fluorescent BODIPY Dyes. *Anal Chem* **91**, 7756-7764 (2019). https://doi.org:10.1021/acs.analchem.9b01174

38 Hollmann, B., Perkins, M., Chauhan, V. M., Aylott, J. W. & Hardie, K. R. Fluorescent nanosensors reveal dynamic pH gradients during biofilm formation. *NPJ Biofilms Microbiomes* **7**, 50 (2021). https://doi.org:10.1038/s41522-021-00221-8

39 Fulaz, S. *et al.* Ratiometric Imaging of the in Situ pH Distribution of Biofilms by Use of Fluorescent Mesoporous Silica Nanosensors. *ACS Applied Materials & Interfaces* **11**, 32679-32688 (2019). https://doi.org:10.1021/acsami.9b09978

40 Reisch, A. & Klymchenko, A. S. Fluorescent Polymer Nanoparticles Based on Dyes: Seeking Brighter Tools for Bioimaging. *Small* **12**, 1968-1992 (2016). https://doi.org:10.1002/smll.201503396

41 Woo, J. *et al.* Novel fluorescein polymer-based nanoparticles: facile and controllable one-pot synthesis, assembly, and immobilization of biomolecules for application in a highly sensitive biosensor. *RSC Advances* **10**, 2998-3004 (2020). https://doi.org:10.1039/C9RA09106H

42 Behnke, T., Würth, C., Laux, E.-M., Hoffmann, K. & Resch-Genger, U. Simple strategies towards bright polymer particles via one-step staining procedures. *Dyes Pigments* **94**, 247-257 (2012). https://doi.org:10.1016/j.dyepig.2012.01.021

43 Behnke, T. *et al.* Encapsulation of hydrophobic dyes in polystyrene micro- and nanoparticles via swelling procedures. *Journal of fluorescence* **21**, 937-944 (2011). https://doi.org:10.1007/s10895-010-0632-2

44 Montalti, M., Prodi, L., Rampazzo, E. & Zaccheroni, N. Dye-doped silica nanoparticles as luminescent organized systems for nanomedicine. *Chemical Society Reviews* **43**, 4243-4268 (2014). https://doi.org:10.1039/C3CS60433K

45 Wolfbeis, O. S. An overview of nanoparticles commonly used in fluorescent bioimaging. *Chemical Society Reviews* **44**, 4743-4768 (2015). https://doi.org:10.1039/C4CS00392F

46 Litvinov, I. K. *et al.* The Dual Luminescence Lifetime pH/Oxygen Sensor: Evaluation of Applicability for Intravital Analysis of 2D- and 3D-Cultivated Human Endometrial Mesenchymal Stromal Cells. *Int J Mol Sci* **24** (2023). https://doi.org:10.3390/ijms242115606

47 Srivastava, P. *et al.* Dual color pH probes made from silica and polystyrene nanoparticles and their performance in cell studies. *Scientific Reports* **13**, 1321 (2023). https://doi.org:10.1038/s41598-023-28203-0

48 Demchenko, A. P. Dual emission and its λ-ratiometric detection in analytical fluorimetry. Pt. I. Basic mechanisms of generating the reporter signal. *Methods and Applications in Fluorescence* **11**, 033002 (2023). https://doi.org:10.1088/2050-6120/acc714

49 Borisov, S. M., Seifner, R. & Klimant, I. A novel planar optical sensor for simultaneous monitoring of oxygen, carbon dioxide, pH and temperature. *Anal Bioanal Chem* **400**, 2463-2474 (2011). https://doi.org:10.1007/s00216-010-4617-4

50 Flemming, H.-C. & Wingender, J. The biofilm matrix. *Nature reviews. Microbiology* **8**, 623-633 (2010). https://doi.org:10.1038/nrmicro2415

51 Donlan, R. M. & Costerton, J. W. Biofilms: survival mechanisms of clinically relevant microorganisms. *Clin Microbiol Rev* **15**, 167-193 (2002). https://doi.org:10.1128/CMR.15.2.167-193.2002

52 Hansen, S. K., Rainey, P. B., Haagensen, J. A. J. & Molin, S. Evolution of species interactions in a biofilm community. *Nature* **445**, 533-536 (2007). https://doi.org:10.1038/nature05514

53 Flemming, H.-C., Neu, T. R. & Wingender, J. *The Perfect Slime: Microbial Extracellular Polymeric Substances (EPS)*. (IWA Publishing, 2016).

54 Stoica, P., Chifiriuc, M. C., Rapa, M. & Lazăr, V. in *Biofilms and Implantable Medical Devices* (eds Ying Deng & Wei Lv) 3-23 (Woodhead Publishing, 2017).

55 Nguyen, A. T., Goswami, S., Ferracane, J. & Koley, D. Real-time monitoring of the pH microenvironment at the interface of multispecies biofilm and dental composites. *Anal Chim Acta* **1201**, 339589 (2022). https://doi.org:10.1016/j.aca.2022.339589

56 Yeor-Davidi, E., Zverzhinetsky, M., Krivitsky, V. & Patolsky, F. Real-time monitoring of bacterial biofilms metabolic activity by a redox-reactive nanosensors array. *Journal of Nanobiotechnology* **18**, 81 (2020). https://doi.org:10.1186/s12951-020-00637-y

57 Hunter, R. C. & Beveridge, T. J. Application of a pH-sensitive fluoroprobe (C-SNARF-4) for pH microenvironment analysis in Pseudomonas aeruginosa biofilms. *Appl Environ Microbiol* **71**, 2501-2510 (2005). https://doi.org:10.1128/aem.71.5.2501-2510.2005

58 Jo, J., Price-Whelan, A. & Dietrich, L. E. P. Gradients and consequences of heterogeneity in biofilms. *Nature Reviews Microbiology* **20**, 593-607 (2022). https://doi.org:10.1038/s41579-022-00692-2

59 Lin, Q., Pilewski, J. M. & Di, Y. P. Acidic Microenvironment Determines Antibiotic Susceptibility and Biofilm Formation of Pseudomonas aeruginosa. *Frontiers in Microbiology* **12** (2021). https://doi.org:10.3389/fmicb.2021.747834

60 Eriksson, L., Lif Holgerson, P. & Johansson, I. Saliva and tooth biofilm bacterial microbiota in adolescents in a low caries community. *Scientific Reports* **7**, 5861 (2017). https://doi.org:10.1038/s41598-017-06221-z

61 Takahashi, N. & Nyvad, B. The role of bacteria in the caries process: ecological perspectives. *J Dent Res* **90**, 294-303 (2011). https://doi.org:10.1177/0022034510379602

62 Marquis, R. E. Oxygen metabolism, oxidative stress and acid-base physiology of dental plaque biofilms. *J Ind Microbiol* **15**, 198-207 (1995). https://doi.org:10.1007/bf01569826

63 Xiao, J. *et al.* Biofilm three-dimensional architecture influences in situ pH distribution pattern on the human enamel surface. *Int J Oral Sci* **9**, 74-79 (2017). https://doi.org:10.1038/ijos.2017.8

64 Liu, Y., Ren, Z., Hwang, G. & Koo, H. Therapeutic Strategies Targeting Cariogenic Biofilm Microenvironment. *Advances in Dental Research* **29**, 86-92 (2018). https://doi.org:10.1177/0022034517736497

65 Vargel, C. in *Corrosion of Aluminium (Second Edition)* (ed Christian Vargel) 289-294 (Elsevier, 2020).

66 Little, B. J. *et al.* Microbially influenced corrosion—Any progress? *Corrosion Science* **170**, 108641 (2020). https://doi.org:10.1016/j.corsci.2020.108641

67 Aktas, D. F. *et al.* Anaerobic Metabolism of Biodiesel and Its Impact on Metal Corrosion. *Energy & Fuels* **24**, 2924-2928 (2010). https://doi.org:10.1021/ef100084j

68 Chen, S., Deng, H., Liu, G. & Zhang, D. Corrosion of Q235 Carbon Steel in Seawater Containing Mariprofundus ferrooxydans and Thalassospira sp. *Frontiers in Microbiology* **10** (2019). https://doi.org:10.3389/fmicb.2019.00936

69 Kim, T., Kwon, S., Lee, J., Lee, J. S. & Kang, S. A metallic anti-biofouling surface with a hierarchical topography containing nanostructures on curved micro-riblets. *Microsystems & Nanoengineering* **8**, 6 (2022). https://doi.org:10.1038/s41378-021-00341-3

70 Puentes-Cala, E. *et al.* Microbiologically influenced corrosion: The gap in the field. *Frontiers in Environmental Science* **10** (2022). https://doi.org:10.3389/fenvs.2022.924842

71 The National Biofilms Innovation Centre Annual Report 2021. (National Biofilms Innovation Centre, 2021).

72 Chaudhari, B., Panda, B., Šavija, B. & Chandra Paul, S. Microbiologically Induced Concrete Corrosion: A Concise Review of Assessment Methods, Effects, and Corrosion-Resistant Coating Materials. *Materials* **15**, 4279 (2022). https://doi.org:10.3390/ma15124279

73 Tribollet, B. Electrochemical sensors for biofilm and biocorrosion. *Materials and Corrosion* **54**, 527-534 (2003). https://doi.org:10.1002/maco.200390116

74 Knisz, J. *et al.* Microbiologically influenced corrosion—more than just microorganisms. *FEMS Microbiology Reviews* **47** (2023). https://doi.org:10.1093/femsre/fuad041

75 Highmore, C. J. *et al.* Translational challenges and opportunities in biofilm science: a BRIEF for the future. *NPJ Biofilms Microbiomes* **8**, 68 (2022). https://doi.org:10.1038/s41522-022-00327-7

76 Vonau, W. & Guth, U. pH Monitoring: a review. *Journal of Solid State Electrochemistry* **10**, 746-752 (2006). https://doi.org:10.1007/s10008-006-0120-4

77 Saccomano, S. C., Jewell, M. P. & Cash, K. J. A review of chemosensors and biosensors for monitoring biofilm dynamics. *Sensors and Actuators Reports* **3**, 100043 (2021). https://doi.org:10.1016/j.snr.2021.100043

78 Hidalgo, G. *et al.* Functional Tomographic Fluorescence Imaging of pH Microenvironments in Microbial Biofilms by Use of Silica Nanoparticle Sensors. *Appl Environ Microbiol* **75**, 7426 (2009). https://doi.org:10.1128/AEM.01220-09

79 Sissons, C. H., Wong, L., Hancock, E. M. & Cutress, T. W. pH gradients induced by urea metabolism in 'artificial mouth' microcosm plaques. *Archives of oral biology* **39**, 507-511 (1994). https://doi.org:10.1016/0003-9969(94)90147-3

80 Dai, X., Fan, Z., Lu, Y. & Ray, P. C. Multifunctional nanoplatforms for targeted multidrug-resistant-bacteria theranostic applications. *ACS Appl Mater Interfaces* **5**, 11348-11354 (2013). https://doi.org:10.1021/am403567k

81 Gashti, M. P., Asselin, J., Barbeau, J., Boudreau, D. & Greener, J. A microfluidic platform with pH imaging for chemical and hydrodynamic stimulation of intact oral biofilms. *Lab on a Chip* **16**, 1412-1419 (2016). https://doi.org:10.1039/C5LC01540E

82 Merkl, P., Aschtgen, M.-S., Henriques-Normark, B. & Sotiriou, G. A. Biofilm interfacial acidity evaluation by pH-Responsive luminescent nanoparticle films. *Biosensors and Bioelectronics* **171**, 112732 (2021). https://doi.org:10.1016/j.bios.2020.112732

83 Moßhammer, M. *et al.* Design and Application of an Optical Sensor for Simultaneous Imaging of pH and Dissolved O2 with Low Cross-Talk. *ACS Sensors* **1**, 681-687 (2016). https://doi.org:10.1021/acssensors.6b00071

84 Schäferling, M. Nanoparticle-based luminescent probes for intracellular sensing and imaging of pH. *WIREs Nanomedicine and Nanobiotechnology* **8**, 378-413 (2016). https://doi.org:10.1002/wnan.1366

85 Borisov, S. M., Gatterer, K. & Klimant, I. Red light-excitable dual lifetime referenced optical pH sensors with intrinsic temperature compensation. *Analyst* **135**, 1711-1717 (2010). https://doi.org:10.1039/C0AN00180E

86 Alford, R. *et al.* Toxicity of Organic Fluorophores Used in Molecular Imaging: Literature Review. *Molecular imaging* **8**, 341-354 (2009). https://doi.org:10.2310/7290.2009.00031

87 Au - Schlafer, S. & Au - Dige, I. Ratiometric Imaging of Extracellular pH in Dental Biofilms. *JoVE*, e53622 (2016). https://doi.org:10.3791/53622

88 Napp, J. *et al.* Targeted luminescent near-infrared polymer-nanoprobes for in vivo imaging of tumor hypoxia. *Anal Chem* **83**, 9039-9046 (2011). https://doi.org:10.1021/ac201870b

89 Flinck, M., Kramer, S. H. & Pedersen, S. F. Roles of pH in control of cell proliferation. *Acta Physiologica* **223**, e13068 (2018). https://doi.org:10.1111/apha.13068

90 Madshus, I. H. Regulation of intracellular pH in eukaryotic cells. *Biochemical Journal* **250**, 1-8 (1988). https://doi.org:10.1042/bj2500001

91 Hersey, S. J. Intracellular pH measurements in gastric mucosa. *Am J Physiol* **237**, E82-89 (1979). https://doi.org:10.1152/ajpendo.1979.237.1.E82

92 Lagadic-Gossmann, D., Huc, L. & Lecureur, V. Alterations of intracellular pH homeostasis in apoptosis: origins and roles. *Cell Death & Differentiation* **11**, 953-961 (2004). https://doi.org:10.1038/sj.cdd.4401466

93 Hashim, A. I., Zhang, X., Wojtkowiak, J. W., Martinez, G. V. & Gillies, R. J. Imaging pH and metastasis. *NMR Biomed* **24**, 582-591 (2011). https://doi.org:10.1002/nbm.1644

94 Parks, S. K., Chiche, J. & Pouyssegur, J. pH control mechanisms of tumor survival and growth. *J Cell Physiol* **226**, 299-308 (2011). https://doi.org:10.1002/jcp.22400

95 Delli Castelli, D., Ferrauto, G., Cutrin, J. C., Terreno, E. & Aime, S. In vivo maps of extracellular pH in murine melanoma by CEST–MRI. *Magnetic Resonance in Medicine* **71**, 326-332 (2014). https://doi.org:10.1002/mrm.24664

96 Lutz, N. W., Le Fur, Y., Chiche, J., Pouysségur, J. & Cozzone, P. J. Quantitative in vivo characterization of intracellular and extracellular pH profiles in heterogeneous tumors: a novel method enabling multiparametric pH analysis. *Cancer Res* **73**, 4616-4628 (2013). https://doi.org:10.1158/0008-5472.Can-13-0767

97 Swietach, P., Patiar, S., Supuran, C. T., Harris, A. L. & Vaughan-Jones, R. D. The role of carbonic anhydrase 9 in regulating extracellular and intracellular ph in three-dimensional tumor cell growths. *J Biol Chem* **284**, 20299-20310 (2009). https://doi.org:10.1074/jbc.M109.006478

98 Korenchan, D. E. & Flavell, R. R. Spatiotemporal pH Heterogeneity as a Promoter of Cancer Progression and Therapeutic Resistance. *Cancers (Basel)* **11** (2019). https://doi.org:10.3390/cancers11071026

99 Martínez-Zaguilán, R. *et al.* Acidic pH enhances the invasive behavior of human melanoma cells. *Clin Exp Metastasis* **14**, 176-186 (1996). https://doi.org:10.1007/bf00121214

100 Sutoo, S., Maeda, T., Suzuki, A. & Kato, Y. Adaptation to chronic acidic extracellular pH elicits a sustained increase in lung cancer cell invasion and metastasis. *Clin Exp Metastasis* **37**, 133-144 (2020). https://doi.org:10.1007/s10585-019-09990-1

101 Swietach, P., Vaughan-Jones, R. D., Harris, A. L. & Hulikova, A. The chemistry, physiology and pathology of pH in cancer. *Philos Trans R Soc Lond B Biol Sci* **369**, 20130099 (2014). https://doi.org:10.1098/rstb.2013.0099

102 Casey, J. R., Grinstein, S. & Orlowski, J. Sensors and regulators of intracellular pH. *Nat Rev Mol Cell Biol* **11**, 50-61 (2010). https://doi.org:10.1038/nrm2820

103 Chen, S. *et al.* Full-Range Intracellular pH Sensing by an Aggregation-Induced Emission-Active Two-Channel Ratiometric Fluorogen. *J Am Chem Soc* **135**, 4926-4929 (2013). https://doi.org:10.1021/ja400337p

104 He, C. B., Lu, K. D. & Lin, W. B. Nanoscale Metal-Organic Frameworks for Real-Time Intracellular pH Sensing in Live Cells. *J Am Chem Soc* **136**, 12253-12256 (2014). https://doi.org:10.1021/ja507333c

105 Shi, W., Li, X. & Ma, H. A tunable ratiometric pH sensor based on carbon nanodots for the quantitative measurement of the intracellular pH of whole cells. *Angew Chem Int Ed Engl* **51**, 6432-6435 (2012). https://doi.org:10.1002/anie.201202533

106 Korzeniowska, B. *et al.* Intracellular pH-Sensing Using Core/Shell Silica Nanoparticles. *J Biomed Nanotechnol* **10**, 1336-1345 (2014). https://doi.org:10.1166/jbn.2014.1815

107 Zhang, Y. *et al.* High-resolution label-free 3D mapping of extracellular pH of single living cells. *Nature Communications* **10**, 5610 (2019). https://doi.org:10.1038/s41467-019-13535-1

108 Zhang, Q. *et al.* Gold-Photodeposited Silver Nanowire Endoscopy for Cytosolic and Nuclear pH Sensing. *Acs Appl Nano Mater* **4**, 9886-9894 (2021). https://doi.org:10.1021/acsanm.1c02363

109 Huang, Y. *et al.* Towards longitudinal mapping of extracellular pH in gliomas. *NMR in Biomedicine* **29**, 1364-1372 (2016). https://doi.org:10.1002/nbm.3578

110 Chan, Y.-H. *et al.* Development of Ultrabright Semiconducting Polymer Dots for Ratiometric pH Sensing. *Anal Chem* **83**, 1448-1455 (2011). https://doi.org:10.1021/ac103140x

111 Marín, M. J., Galindo, F., Thomas, P. & Russell, D. A. Localized Intracellular pH Measurement Using a Ratiometric Photoinduced Electron-Transfer-Based Nanosensor. *Angewandte Chemie International Edition* **51**, 9657-9661 (2012). https://doi.org:10.1002/anie.201203866

112 Pang, C. *et al.* The Establishment and Application Studies on Precise Lysosome pH Indicator Based on Self-Decomposable Nanoparticles. *Nanoscale Research Letters* **15**, 143 (2020). https://doi.org:10.1186/s11671-020-03367-0

113 Ke, G. *et al.* A Cell-Surface-Anchored Ratiometric Fluorescent Probe for Extracellular pH Sensing. *ACS Applied Materials & Interfaces* **6**, 15329-15334 (2014). https://doi.org:10.1021/am503818n

114 Nandi, N., Choudhury, K., Sarkar, P., Barnwal, N. & Sahu, K. Ratiometric Multimode Detection of pH and Fe3+ by Dual-Emissive Heteroatom-Doped Carbon Dots for Living Cell Applications. *Acs Appl Nano Mater* **5**, 17315-17324 (2022). https://doi.org:10.1021/acsanm.2c04531

115 Clark, H. A., Kopelman, R., Tjalkens, R. & Philbert, M. A. Optical Nanosensors for Chemical Analysis inside Single Living Cells. 2. Sensors for pH and Calcium and the Intracellular Application of PEBBLE Sensors. *Anal Chem* **71**, 4837-4843 (1999). https://doi.org:10.1021/ac990630n

116 Rosenblum, D., Joshi, N., Tao, W., Karp, J. M. & Peer, D. Progress and challenges towards targeted delivery of cancer therapeutics. *Nature Communications* **9**, 1410 (2018). https://doi.org:10.1038/s41467-018-03705-y

117 Alexis, F., Pridgen, E., Molnar, L. K. & Farokhzad, O. C. Factors Affecting the Clearance and Biodistribution of Polymeric Nanoparticles. *Molecular Pharmaceutics* **5**, 505-515 (2008). https://doi.org:10.1021/mp800051m

118 Wilhelm, S. *et al.* Analysis of nanoparticle delivery to tumours. *Nature Reviews Materials* **1**, 16014 (2016). https://doi.org:10.1038/natrevmats.2016.14

119 Byrne, J. D., Betancourt, T. & Brannon-Peppas, L. Active targeting schemes for nanoparticle systems in cancer therapeutics. *Advanced Drug Delivery Reviews* **60**, 1615-1626 (2008). https://doi.org:10.1016/j.addr.2008.08.005

120 Suk, J. S., Xu, Q., Kim, N., Hanes, J. & Ensign, L. M. PEGylation as a strategy for improving nanoparticle-based drug and gene delivery. *Adv Drug Deliv Rev* **99**, 28-51 (2016). https://doi.org:10.1016/j.addr.2015.09.012

121 Green, A. E. & Rose, P. G. Pegylated liposomal doxorubicin in ovarian cancer. *Int J Nanomedicine* **1**, 229-239 (2006).

122 Patra, J. K. *et al.* Nano based drug delivery systems: recent developments and future prospects. *Journal of Nanobiotechnology* **16**, 71 (2018). https://doi.org:10.1186/s12951-018-0392-8

123 Szebeni, J. *et al.* Insights into the Structure of Comirnaty Covid-19 Vaccine: A Theory on Soft, Partially Bilayer-Covered Nanoparticles with Hydrogen Bond-Stabilized mRNA-Lipid Complexes. *ACS Nano* **17**, 13147-13157 (2023). https://doi.org:10.1021/acsnano.2c11904

124 White, B. E. *et al.* Nanotechnology approaches to addressing HER2-positive breast cancer. *Cancer Nanotechnology* **11**, 12 (2020). https://doi.org:10.1186/s12645-020-00068-2

125 Ledermann, J. A., Canevari, S. & Thigpen, T. Targeting the folate receptor: diagnostic and therapeutic approaches to personalize cancer treatments. *Ann Oncol* **26**, 2034-2043 (2015). https://doi.org:10.1093/annonc/mdv250

126 Kesharwani, P., Chadar, R., Sheikh, A., Rizg, W. Y. & Safhi, A. Y. CD44-Targeted Nanocarrier for Cancer Therapy. *Front Pharmacol* **12**, 800481 (2021). https://doi.org:10.3389/fphar.2021.800481

127 Jamal, M. *et al.* Bacterial biofilm and associated infections. *J Chin Med Assoc* **81**, 7-11 (2018). https://doi.org:10.1016/j.jcma.2017.07.012

128 Lewis, K. Riddle of biofilm resistance. *Antimicrob Agents Chemother* **45**, 999-1007 (2001). https://doi.org:10.1128/aac.45.4.999-1007.2001

129 Macia, M. D., Rojo-Molinero, E. & Oliver, A. Antimicrobial susceptibility testing in biofilm-growing bacteria. *Clinical Microbiology and Infection* **20**, 981-990 (2014). https://doi.org:10.1111/1469-0691.12651

130 Kolpen, M. *et al.* Bacterial biofilms predominate in both acute and chronic human lung infections. *Thorax* **77**, 1015 (2022). https://doi.org:10.1136/thoraxjnl-2021-217576

131 Flores-Mireles, A. L., Walker, J. N., Caparon, M. & Hultgren, S. J. Urinary tract infections: epidemiology, mechanisms of infection and treatment options. *Nature reviews. Microbiology* **13**, 269-284 (2015). https://doi.org:10.1038/nrmicro3432

132 Eberly, A. R. *et al.* Biofilm Formation by Uropathogenic Escherichia coli Is Favored under Oxygen Conditions That Mimic the Bladder Environment. *Int J Mol Sci* **18** (2017). https://doi.org:10.3390/ijms18102077

133 McLaughlin-Borlace, L., Stapleton, F., Matheson, M. & Dart, J. K. Bacterial biofilm on contact lenses and lens storage cases in wearers with microbial keratitis. *Journal of applied microbiology* **84**, 827-838 (1998). https://doi.org:10.1046/j.1365-2672.1998.00418.x

134 Niedzielski, A., Chmielik, L. P. & Stankiewicz, T. The Formation of Biofilm and Bacteriology in Otitis Media with Effusion in Children: A Prospective Cross-Sectional Study. *Int J Environ Res Public Health* **18** (2021). https://doi.org:10.3390/ijerph18073555

135 Sousa, C., Henriques, M. & Oliveira, R. Mini-review: Antimicrobial central venous catheters--recent advances and strategies. *Biofouling* **27**, 609-620 (2011). https://doi.org:10.1080/08927014.2011.593261

136 Machado, M. C., Tarquinio, K. M. & Webster, T. J. Decreased Staphylococcus aureus biofilm formation on nanomodified endotracheal tubes: a dynamic airway model. *Int J Nanomedicine* **7**, 3741-3750 (2012). https://doi.org:10.2147/ijn.S28191

137 Zheng, Y., He, L., Asiamah, T. K. & Otto, M. Colonization of medical devices by staphylococci. *Environ Microbiol* **20**, 3141-3153 (2018). https://doi.org:10.1111/1462-2920.14129

138 Gil-Perotin, S. *et al.* Implications of endotracheal tube biofilm in ventilator-associated pneumonia response: a state of concept. *Critical Care* **16**, R93 (2012). https://doi.org:10.1186/cc11357

139 Holliday, R., Preshaw, P. M., Bowen, L. & Jakubovics, N. S. The ultrastructure of subgingival dental plaque, revealed by high-resolution field emission scanning electron microscopy. *BDJ Open* **1**, 15003 (2015). https://doi.org:10.1038/bdjopen.2015.3

140 World-Health-Organization. Prioritization of pathogens to guide discovery, research and development of new antibiotics for drug-resistant bacterial infections, including tuberculosis., (World Health Organization Geneva: World Health Organization 2017).

141 Tacconelli, E. *et al.* Discovery, research, and development of new antibiotics: the WHO priority list of antibiotic-resistant bacteria and tuberculosis. *The Lancet*

Infectious Diseases **18**, 318-327 (2018). https://doi.org:10.1016/S1473-3099(17)30753-3

142 Kang, X. *et al.* Strategies and materials for the prevention and treatment of biofilms. *Materials Today Bio* **23**, 100827 (2023). https://doi.org:10.1016/j.mtbio.2023.100827

143 Narayana, P. S. V. V. S. & Srihari, P. S. V. V. A Review on Surface Modifications and Coatings on Implants to Prevent Biofilm. *Regenerative Engineering and Translational Medicine* **6**, 330-346 (2020). https://doi.org:10.1007/s40883-019-00116-3

144 Mah, T. F. & O'Toole, G. A. Mechanisms of biofilm resistance to antimicrobial agents. *Trends Microbiol* **9**, 34-39 (2001). https://doi.org:10.1016/s0966-842x(00)01913-2

145 Ciofu, O., Moser, C., Jensen, P. Ø. & Høiby, N. Tolerance and resistance of microbial biofilms. *Nature Reviews Microbiology* (2022). https://doi.org:10.1038/s41579-022-00682-4

146 Peterson, E. & Kaur, P. Antibiotic Resistance Mechanisms in Bacteria: Relationships Between Resistance Determinants of Antibiotic Producers, Environmental Bacteria, and Clinical Pathogens. *Frontiers in Microbiology* **9** (2018). https://doi.org:10.3389/fmicb.2018.02928

147 Bai, J., Kim, Y. T., Ryu, S. & Lee, J. H. Biocontrol and Rapid Detection of Food-Borne Pathogens Using Bacteriophages and Endolysins. *Front Microbiol* **7**, 474 (2016). https://doi.org:10.3389/fmicb.2016.00474

148 Donlan, R. M. Preventing biofilms of clinically relevant organisms using bacteriophage. *Trends in Microbiology* **17**, 66-72 (2009). https://doi.org:10.1016/j.tim.2008.11.002

149 Hughes, G. & Webber, M. A. Novel approaches to the treatment of bacterial biofilm infections. *British Journal of Pharmacology* **174**, 2237-2246 (2017). https://doi.org:10.1111/bph.13706

150 Fu, W. *et al.* Bacteriophage cocktail for the prevention of biofilm formation by Pseudomonas aeruginosa on catheters in an in vitro model system. *Antimicrob Agents Chemother* **54**, 397-404 (2010). https://doi.org:10.1128/aac.00669-09

151 Kifelew, L. G. *et al.* Efficacy of phage cocktail AB-SA01 therapy in diabetic mouse wound infections caused by multidrug-resistant Staphylococcus aureus. *BMC Microbiol* **20**, 204 (2020). https://doi.org:10.1186/s12866-020-01891-8

152 McVay, C. S., Velásquez, M. & Fralick, J. A. Phage therapy of Pseudomonas aeruginosa infection in a mouse burn wound model. *Antimicrob Agents Chemother* **51**, 1934-1938 (2007). https://doi.org:10.1128/aac.01028-06

153 Kusradze, I. *et al.* Characterization and Testing the Efficiency of Acinetobacter baumannii Phage vB-GEC_Ab-M-G7 as an Antibacterial Agent. *Front Microbiol* **7**, 1590 (2016). https://doi.org:10.3389/fmicb.2016.01590

154 O'Flaherty, S. *et al.* Potential of the polyvalent anti-Staphylococcus bacteriophage K for control of antibiotic-resistant staphylococci from hospitals. *Appl Environ Microbiol* **71**, 1836-1842 (2005). https://doi.org:10.1128/aem.71.4.1836-1842.2005

155 Ross, A., Ward, S. & Hyman, P. More Is Better: Selecting for Broad Host Range Bacteriophages. *Frontiers in Microbiology* **7** (2016). https://doi.org:10.3389/fmicb.2016.01352

156 Hentzer, M., Eberl, L., Nielsen, J. & Givskov, M. Quorum Sensing. *BioDrugs* **17**, 241-250 (2003). https://doi.org:10.2165/00063030-200317040-00003

157 Coughlan, L. M., Cotter, P. D., Hill, C. & Alvarez-Ordóñez, A. New Weapons to Fight Old Enemies: Novel Strategies for the (Bio)control of Bacterial Biofilms in the Food

Industry. *Frontiers in Microbiology* **7** (2016). https://doi.org:10.3389/fmicb.2016.01641

158 Dufour, D. & Lévesque, C. M. Cell death of Streptococcus mutans induced by a quorum-sensing peptide occurs via a conserved streptococcal autolysin. *J Bacteriol* **195**, 105-114 (2013). https://doi.org:10.1128/jb.00926-12

159 Enwemeka, C. S., Williams, D., Enwemeka, S. K., Hollosi, S. & Yens, D. Blue 470-nm light kills methicillin-resistant Staphylococcus aureus (MRSA) in vitro. *Photomed Laser Surg* **27**, 221-226 (2009). https://doi.org:10.1089/pho.2008.2413

160 O'Loughlin, C. T. *et al.* A quorum-sensing inhibitor blocks Pseudomonas aeruginosa virulence and biofilm formation. *Proc Natl Acad Sci U S A* **110**, 17981-17986 (2013). https://doi.org:10.1073/pnas.1316981110

161 Vera, C., Tulli, F. & Borsarelli, C. D. Photosensitization With Supramolecular Arrays for Enhanced Antimicrobial Photodynamic Treatments. *Frontiers in Bioengineering and Biotechnology* **9** (2021). https://doi.org:10.3389/fbioe.2021.655370

162 Pfeifer, G. P., You, Y. H. & Besaratinia, A. Mutations induced by ultraviolet light. *Mutat Res* **571**, 19-31 (2005). https://doi.org:10.1016/j.mrfmmm.2004.06.057

163 Abrahamse, H. & Hamblin, M. R. New photosensitizers for photodynamic therapy. *The Biochemical journal (IF 4.1)* **473**, 347-364 (2016). https://doi.org:10.1042/BJ20150942

164 Wormald, R., Evans, J., Smeeth, L. & Henshaw, K. Photodynamic therapy for neovascular age-related macular degeneration. *Cochrane Database Syst Rev*, Cd002030 (2003). https://doi.org:10.1002/14651858.Cd002030

165 Dysart, J. S. & Patterson, M. S. Characterization of Photofrin photobleaching for singlet oxygen dose estimation during photodynamic therapy of MLL cells in vitro. *Phys Med Biol* **50**, 2597-2616 (2005). https://doi.org:10.1088/0031-9155/50/11/011

166 Moan, J. *et al.* Intracellular localization of photosensitizers. *Ciba Found Symp* **146**, 95-107; discussion 107-111 (1989). https://doi.org:10.1002/9780470513842.ch7

167 Bekmukhametova, A. *et al.* Photodynamic therapy with nanoparticles to combat microbial infection and resistance. *Nanoscale* **12**, 21034-21059 (2020). https://doi.org:10.1039/d0nr04540c

168 Cieplik, F., Tabenski, L., Buchalla, W. & Maisch, T. Antimicrobial photodynamic therapy for inactivation of biofilms formed by oral key pathogens. *Front Microbiol* **5**, 405 (2014). https://doi.org:10.3389/fmicb.2014.00405

169 Ash, C., Dubec, M., Donne, K. & Bashford, T. Effect of wavelength and beam width on penetration in light-tissue interaction using computational methods. *Lasers in Medical Science* **32**, 1909-1918 (2017). https://doi.org:10.1007/s10103-017-2317-4

170 Shrestha, A., Hamblin, M. R. & Kishen, A. Photoactivated rose bengal functionalized chitosan nanoparticles produce antibacterial/biofilm activity and stabilize dentin-collagen. *Nanomedicine (IF 5.3)* **10**, 491-501 (2014). https://doi.org:10.1016/j.nano.2013.10.010

171 Anju V.T *et al.* Antimicrobial photodynamic activity of rose bengal conjugated multi walled carbon nanotubes against planktonic cells and biofilm of Escherichia coli. *Photodiagnosis and Photodynamic Therapy* **24**, 300-310 (2018). https://doi.org:10.1016/j.pdpdt.2018.10.013

172 Rebeca, S.-L. & Jorge, B. in *BODIPY Dyes* (eds Bañuelos-Prieto Jorge & Llano Rebeca Sola) Ch. 1 (IntechOpen, 2018).

173 Radunz, S. *et al.* Temperature- and Structure-Dependent Optical Properties and Photophysics of BODIPY Dyes. *The journal of physical chemistry. A* **124**, 1787-1797 (2020). https://doi.org:10.1021/acs.jpca.9b11859

174 Boens, N., Verbelen, B., Ortiz, M. J., Jiao, L. & Dehaen, W. Synthesis of BODIPY dyes through postfunctionalization of the boron dipyrromethene core. *Coordination Chemistry Reviews* **399**, 213024 (2019). https://doi.org:10.1016/j.ccr.2019.213024

175 Radunz, S. *et al.* pH-Activatable Singlet Oxygen-Generating Boron-dipyrromethenes (BODIPYs) for Photodynamic Therapy and Bioimaging. *Journal of Medicinal Chemistry (IF 7.4)* **63**, 1699-1708 (2020). https://doi.org:10.1021/acs.jmedchem.9b01873

176 Bañuelos, J. BODIPY Dye, the Most Versatile Fluorophore Ever? *Chem Rec* **16**, 335-348 (2016). https://doi.org:10.1002/tcr.201500238

177 Sheng, W., Lv, F., Tang, B., Hao, E. & Jiao, L. Toward the most versatile fluorophore: Direct functionalization of BODIPY dyes via regioselective C–H bond activation. *Chinese Chemical Letters* **30**, 1825-1833 (2019). https://doi.org:10.1016/j.cclet.2019.08.004

178 Songca, S. P. & Adjei, Y. Applications of Antimicrobial Photodynamic Therapy against Bacterial Biofilms. *Int J Mol Sci* **23** (2022). https://doi.org:10.3390/ijms23063209

179 Usacheva, M., Layek, B., Rahman Nirzhor, S. S. & Prabha, S. Nanoparticle-Mediated Photodynamic Therapy for Mixed Biofilms. *Journal of Nanomaterials* **2016**, 4752894 (2016). https://doi.org:10.1155/2016/4752894

180 Yang, K. *et al.* Wheat germ agglutinin modified liposomes for the photodynamic inactivation of bacteria. *Photochem Photobiol* **88**, 548-556 (2012). https://doi.org:10.1111/j.1751-1097.2011.00983.x

181 Khan, S. *et al.* Photoinactivation of multidrug resistant bacteria by monomeric methylene blue conjugated gold nanoparticles. *J Photochem Photobiol B* **174**, 150-161 (2017). https://doi.org:10.1016/j.jphotobiol.2017.07.011

182 kirar, s., Thakur, N., Laha, J., Bhaumik, J. & Banerjee, U. Development of Gelatin Nanoparticle Based Biodegradable Phototheranostic Agents: Advanced System to Treat Infectious Diseases. *ACS Biomaterials Science & Engineering* **4** (2018). https://doi.org:10.1021/acsbiomaterials.7b00751

183 Zhang, H. *et al.* Dual-Mode Antibacterial Conjugated Polymer Nanoparticles for Photothermal and Photodynamic Therapy. *Macromol Biosci* **20**, e1900301 (2020). https://doi.org:10.1002/mabi.201900301

184 Raschpichler, M. *et al.* In situ intravenous photodynamic therapy for the systemic eradication of blood stream infections. *Photochemical & Photobiological Sciences* **18**, 304-308 (2019). https://doi.org:10.1039/C8PP00267C

185 Klepac-Ceraj, V. *et al.* Photodynamic effects of methylene blue-loaded polymeric nanoparticles on dental plaque bacteria. *Lasers Surg Med* **43**, 600-606 (2011). https://doi.org:10.1002/lsm.21069

186 Anju, V. T. *et al.* Antimicrobial photodynamic activity of toluidine blue-carbon nanotube conjugate against Pseudomonas aeruginosa and Staphylococcus aureus - Understanding the mechanism of action. *Photodiagnosis Photodyn Ther* **27**, 305-316 (2019). https://doi.org:10.1016/j.pdpdt.2019.06.014

187 Garcez, A. S. *et al.* Effects of photodynamic therapy on Gram-positive and Gram-negative bacterial biofilms by bioluminescence imaging and scanning electron microscopic analysis. *Photomed Laser Surg* **31**, 519-525 (2013). https://doi.org:10.1089/pho.2012.3341

188 Fontana, C. R. *et al.* The antibacterial effect of photodynamic therapy in dental plaque-derived biofilms. *J Periodontal Res* **44**, 751-759 (2009). https://doi.org:10.1111/j.1600-0765.2008.01187.x
189 Mamone, L. *et al.* Photodynamic inactivation of planktonic and biofilm growing bacteria mediated by a meso-substituted porphyrin bearing four basic amino groups. *Journal of Photochemistry and Photobiology B: Biology* **161**, 222-229 (2016). https://doi.org:10.1016/j.jphotobiol.2016.05.026
190 Sedlacek, M. J. & Walker, C. Antibiotic resistance in an in vitro subgingival biofilm model. *Oral Microbiol Immunol* **22**, 333-339 (2007). https://doi.org:10.1111/j.1399-302X.2007.00366.x
191 Li, Y., Sun, G., Xie, J., Xiao, S. & Lin, C. Antimicrobial photodynamic therapy against oral biofilm: influencing factors, mechanisms, and combined actions with other strategies. *Front Microbiol* **14**, 1192955 (2023). https://doi.org:10.3389/fmicb.2023.1192955
192 Gad, F., Zahra, T., Hasan, T. & Hamblin, M. R. Effects of growth phase and extracellular slime on photodynamic inactivation of gram-positive pathogenic bacteria. *Antimicrob Agents Chemother* **48**, 2173-2178 (2004). https://doi.org:10.1128/aac.48.6.2173-2178.2004
193 Dai, X. *et al.* A Water-Soluble Galactose-Decorated Cationic Photodynamic Therapy Agent Based on BODIPY to Selectively Eliminate Biofilm. *Biomacromolecules* **19**, 141-149 (2018). https://doi.org:10.1021/acs.biomac.7b01316
194 De-la-Pinta, I. *et al.* Effect of biomaterials hydrophobicity and roughness on biofilm development. *Journal of Materials Science: Materials in Medicine* **30**, 77 (2019). https://doi.org:10.1007/s10856-019-6281-3
195 Pérez-Laguna, V. *et al.* A combination of photodynamic therapy and antimicrobial compounds to treat skin and mucosal infections: a systematic review. *Photochemical & Photobiological Sciences* **18**, 1020-1029 (2019). https://doi.org:10.1039/c8pp00534f
196 Snipstad, S. *et al.* Labeling nanoparticles: Dye leakage and altered cellular uptake. *Cytometry Part A* **91**, 760-766 (2017). https://doi.org:10.1002/cyto.a.22853
197 Andreozzi, P., Martinelli, C., Carney, R. P., Carney, T. M. & Stellacci, F. Erythrocyte incubation as a method for free-dye presence determination in fluorescently labeled nanoparticles. *Mol Pharm* **10**, 875-882 (2013). https://doi.org:10.1021/mp300530c
198 Wang, H., Ma, R., Nienhaus, K. & Nienhaus, G. U. Formation of a Monolayer Protein Corona around Polystyrene Nanoparticles and Implications for Nanoparticle Agglomeration. *Small* **15**, 1900974 (2019). https://doi.org:10.1002/smll.201900974
199 Monsigny, M., Roche, A.-C., Sene, C., Maget-Dana, R. & Delmotte, F. Sugar-Lectin Interactions: How Does Wheat-Germ Agglutinin Bind Sialoglycoconjugates? *European Journal of Biochemistry* **104**, 147-153 (1980). https://doi.org:10.1111/j.1432-1033.1980.tb04410.x
200 Biari, K. e., Gaudioso, Á., Fernández-Alonso, M. C., Jiménez-Barbero, J. & Cañada, F. J. Peptidoglycan Recognition by Wheat Germ Agglutinin. A View by NMR. *Natural Product Communications* **14**, 1934578X19849240 (2019). https://doi.org:10.1177/1934578x19849240
201 Gabor, F., Schwarzbauer, A. & Wirth, M. Lectin-mediated drug delivery: binding and uptake of BSA-WGA conjugates using the Caco-2 model. *International Journal of Pharmaceutics* **237**, 227-239 (2002). https://doi.org:10.1016/S0378-5173(02)00049-2

202 Ohgaki, R. *et al.* Ratiometric fluorescence imaging of cell surface pH by poly(ethylene glycol)-phospholipid conjugated with fluorescein isothiocyanate. *Sci Rep* **7**, 17484 (2017). https://doi.org:10.1038/s41598-017-17459-y

203 Chen, B. *et al.* A Mimosa-Inspired Cell-Surface-Anchored Ratiometric DNA Nanosensor for High-Resolution and Sensitive Response of Target Tumor Extracellular pH. *Anal Chem* **92**, 15104-15111 (2020). https://doi.org:10.1021/acs.analchem.0c03250

204 Goryashchenko, A. S. *et al.* FLIM-Based Intracellular and Extracellular pH Measurements Using Genetically Encoded pH Sensor. *Biosensors* **11**, 340 (2021). https://doi.org:10.3390/bios11090340

205 Urra, J. *et al.* A genetically encoded ratiometric sensor to measure extracellular pH in microdomains bounded by basolateral membranes of epithelial cells. *Pflugers Arch* **457**, 233-242 (2008). https://doi.org:10.1007/s00424-008-0497-2

206 Yang, Y., Xia, M., Zhao, H., Zhang, S. & Zhang, X. A Cell-Surface-Specific Ratiometric Fluorescent Probe for Extracellular pH Sensing with Solid-State Fluorophore. *ACS Sensors* **3**, 2278-2285 (2018). https://doi.org:10.1021/acssensors.8b00514

207 Anderson, M., Moshnikova, A., Engelman, D. M., Reshetnyak, Y. K. & Andreev, O. A. Probe for the measurement of cell surface pH in vivo and ex vivo. *Proceedings of the National Academy of Sciences* **113**, 8177-8181 (2016). https://doi.org:10.1073/pnas.1608247113

208 Ikuma, K., Decho, A. W. & Lau, B. L. T. When nanoparticles meet biofilms—interactions guiding the environmental fate and accumulation of nanoparticles. *Frontiers in Microbiology* **6** (2015). https://doi.org:10.3389/fmicb.2015.00591

209 Peulen, T. O. & Wilkinson, K. J. Diffusion of nanoparticles in a biofilm. *Environ Sci Technol* **45**, 3367-3373 (2011). https://doi.org:10.1021/es103450g

210 Sahle-Demessie, E. & Tadesse, H. Kinetics and equilibrium adsorption of nano-TiO2 particles on synthetic biofilm. *Surface Science* **605**, 1177-1184 (2011). https://doi.org:10.1016/j.susc.2011.03.022

211 Hou, J. *et al.* Bacterial Density and Biofilm Structure Determined by Optical Coherence Tomography. *Scientific Reports* **9**, 9794 (2019). https://doi.org:10.1038/s41598-019-46196-7

212 Malik, Z., Ladan, H. & Nitzan, Y. Photodynamic inactivation of Gram-negative bacteria: problems and possible solutions. *J Photochem Photobiol B* **14**, 262-266 (1992). https://doi.org:10.1016/1011-1344(92)85104-3

213 Egan, A. J. F. Bacterial outer membrane constriction. *Molecular microbiology* **107**, 676-687 (2018). https://doi.org:10.1111/mmi.13908

214 Tuttle, A. R., Trahan, N. D. & Son, M. S. Growth and Maintenance of Escherichia coli Laboratory Strains. *Curr Protoc* **1**, e20 (2021). https://doi.org:10.1002/cpz1.20

215 Missiakas, D. M. & Schneewind, O. Growth and laboratory maintenance of Staphylococcus aureus. *Curr Protoc Microbiol* **Chapter 9**, Unit 9C.1 (2013). https://doi.org:10.1002/9780471729259.mc09c01s28

216 Chen, Y. *et al.* Streptococcus mutans cell division protein FtsZ has higher GTPase and polymerization activities in acidic environment. *Molecular Oral Microbiology* **37**, 97-108 (2022). https://doi.org:10.1111/omi.12364

217 Jung, C.-J., Zheng, Q.-H., Shieh, Y.-H., Lin, C.-S. & Chia, J.-S. Streptococcus mutans autolysin AtlA is a fibronectin-binding protein and contributes to bacterial survival in the bloodstream and virulence for infective endocarditis. *Molecular microbiology* **74**, 888-902 (2009). https://doi.org:10.1111/j.1365-2958.2009.06903.x

218 Wilson, W. W., Wade, M. M., Holman, S. C. & Champlin, F. R. Status of methods for assessing bacterial cell surface charge properties based on zeta potential measurements. *J Microbiol Methods* **43**, 153-164 (2001). https://doi.org:10.1016/s0167-7012(00)00224-4

219 Kłodzińska, E. *et al.* Effect of zeta potential value on bacterial behavior during electrophoretic separation. *Electrophoresis* **31**, 1590-1596 (2010). https://doi.org:10.1002/elps.200900559

220 Ferreyra Maillard, A. P. V., Espeche, J. C., Maturana, P., Cutro, A. C. & Hollmann, A. Zeta potential beyond materials science: Applications to bacterial systems and to the development of novel antimicrobials. *Biochimica et Biophysica Acta (BBA) - Biomembranes* **1863**, 183597 (2021). https://doi.org:10.1016/j.bbamem.2021.183597

221 Zhang, Y., Pedersen, J. N., Eser, B. E. & Guo, Z. Biodegradation of polyethylene and polystyrene: From microbial deterioration to enzyme discovery. *Biotechnology Advances* **60**, 107991 (2022). https://doi.org:10.1016/j.biotechadv.2022.107991

7. List of publications

(1) Singh, A. V.; Maharjan, R. S.; **Kromer, C**.; Laux, P.; Luch, A.; Vats, T.; Chandrasekar, V.; Dakua, S. P.; Park, B. W. Advances in Smoking Related In Vitro Inhalation Toxicology: A Perspective Case of Challenges and Opportunities from Progresses in Lung-on-Chip Technologies. Chem Res Toxicol **2021**, 34 (9), 1984-2002. DOI: 10.1021/acs.chemrestox.1c00219

(2) Tschiche, H. R.; Bierkandt, F. S.; Creutzenberg, O.; Fessard, V.; Franz, R.; Giese, B.; Greiner, R.; Haas, K. H.; Haase, A.; Hartwig, A.; Hund-Rinke, K.; Iden, P.; **Kromer, C.**; Loeschner, K.; Mutz, D.; Rakow, A.; Rasmussen, K.; Rauscher, H.; Richter, H.; Schoon, J.; Schmid, O.; Som, C.; M. Tovar, G. E.; Westerhoff, P.; Wohlleben, W.; Luch, A.; Laux, P., Environmental considerations and current status of grouping and regulation of engineered nanomaterials. Environmental Nanotechnology, Monitoring and Management **2022**, 18, DOI: 10.1016/j.enmm.2022.100707

(3) Tschiche, H. R.; Bierkandt, F. S.; Creutzenberg, O.; Fessard, V.; Franz, R.; Greiner, R.; Gruber-Traub, C.; Haas, K. H.; Haase, A.; Hartwig, A.; Hesse, B.; Hund-Rinke, K.; Iden, P.; **Kromer, C.**; Loeschner, K.; Mutz, D.; Rakow, A.; Rasmussen, K.; Rauscher, H.; Richter, H.; Schoon, J.; Schmid, O.; Som, C.; Spindler, L. M.; Tovar, G. E. M.; Westerhoff, P.; Wohlleben, W.; Luch, A.; Laux, P., Analytical and toxicological aspects of nanomaterials in different product groups: Challenges and opportunities. NanoImpact **2022**, 28, 100416, DOI: 10.1016/j.impact.2022.100416

(4) **Kromer, C**.; Schwibbert, K.; Gadicherla, A. K.; Thiele, D.; Nirmalananthan-Budau, N.; Laux, P.; Resch-Genger, U.; Luch, A.; Tschiche, H. R. Monitoring and imaging pH in biofilms utilizing a fluorescent polymeric nanosensor. Scientific Reports **2022**, 12 (1), 9823. DOI: 10.1038/s41598-022-13518-1.

(5) Hachenberger, Y. U.; Rosenkranz, D.; **Kromer, C.;** Krause, B. C.; Dreiack, N.; Kriegel, F. L.; Koz'menko, E.; Jungnickel, H.; Tentschert, J.; Bierkandt, F. S.; et al. Nanomaterial

Characterization in Complex Media-Guidance and Application. Nanomaterials-Basel **2023**, 13 (5), 922. DOI: 10.3390/nano13050922

(6) **Kromer, C**.; Schwibbert, K.; Radunz, S.; Thiele, D.; Laux, P.; Luch, A.; Tschiche, H. R. ROS generating BODIPY loaded NPs for photodynamic eradication of biofilms. Frontiers in Microbiology **2023**, 14, Original Research. DOI: 10.3389/fmicb.2023.1274715.

(7) **Kromer, C**.; Katz, A.; Feldmann, I.; Laux, P.; Luch, A.; Tschiche H. R., A targeted fluorescent nanosensor for ratiometric pH sensing at the cell surface, manuscript submitted **2024** to Scientific Reports

Annex I: Supplementary Material

Research Paper: Monitoring and imaging pH in biofilms utilizing a fluorescent polymeric nanosensor

Charlotte Kromer, Karin Schwibbert, Ashish K. Gadicherla, Dorothea Thiele, Nithiya Nirmalananthan-Budau, Peter Laux, Ute Resch-Genger, Andreas Luch, Harald R. Tschiche

Published online on 14 June 2022 in:
Scientific Reports 12, 9823, 2022

Link: https://doi.org/10.1038/s41598-022-13518-1

Supplementary Information

Monitoring and imaging pH in biofilms utilizing a fluorescent polymeric nanosensor

Charlotte Kromer[1,2], Karin Schwibbert[3], Ashish K. Gadicherla[4], Dorothea Thiele[3], Nithiya Nirmalananthan-Budau[5], Peter Laux[1], Ute Resch-Genger[5]*, Andreas Luch[1,2], Harald R. Tschiche[1]*

$$ratio_{FI} = d + \left(\frac{a-d}{1+\left(\frac{pH}{c}\right)^{b}}\right)$$

Supplementary Equation S1. Curve fitting for pH calibration.

Supplementary Table S2. Parameters used for the inverse estimation.

Parameter	Estimate	Std. Error
a	0.13383	0.01005
b	0.71996	0.01539
c	7.16552	0.05673
d	0.68475	0.05915

The thickness of the biofilm was determined after a growth period of 24 h and 2 washing steps with RB-buffer (**Supplementary Table S3**). For the measurements, the focus plane of the CLSM was placed at the lower end of the biofilm in BF mode and a z-stack was recorded until the minimum and maximum upper ends were reached. Three measurement points were recorded for each of the three biological replicates. After a growth period of 24 hours, the E. coli biofilms had a uniform thickness and colonized the entire Ibidi glass slide without gaps.

Supplementary Table S3 Minimum and maximum biofilm thickness determined with CLSM and illustration of biofilm thickness.

Slide	Minimum thickness [µm]	Maximum thickness [µm]
1	6.45 ± 0.33	12.13 ± 1.35
2	7.82 ± 1.94	15.43 ± 4.43
3	7.88 ± 1.16	14.87 ± 3.28
Average	7.38 ± 0.81	14.14 ± 1.77

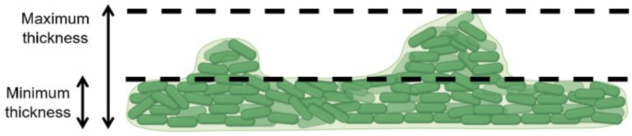

To visualize the structure and viability of the biofilm, a live/dead staining was performed using the BacLight kit (Thermo Fisher Scientific). **Supplementary Figure S4** shows the top and side view of a CLSM image obtained from a live/dead stained biofilm. A dense and homogeneous biofilm uniformly colonizes the slide. The high number of living bacteria (green) shows the high viability of the biofilm with is not altered when PS NP are incubated into the biofilm for 24 hours.

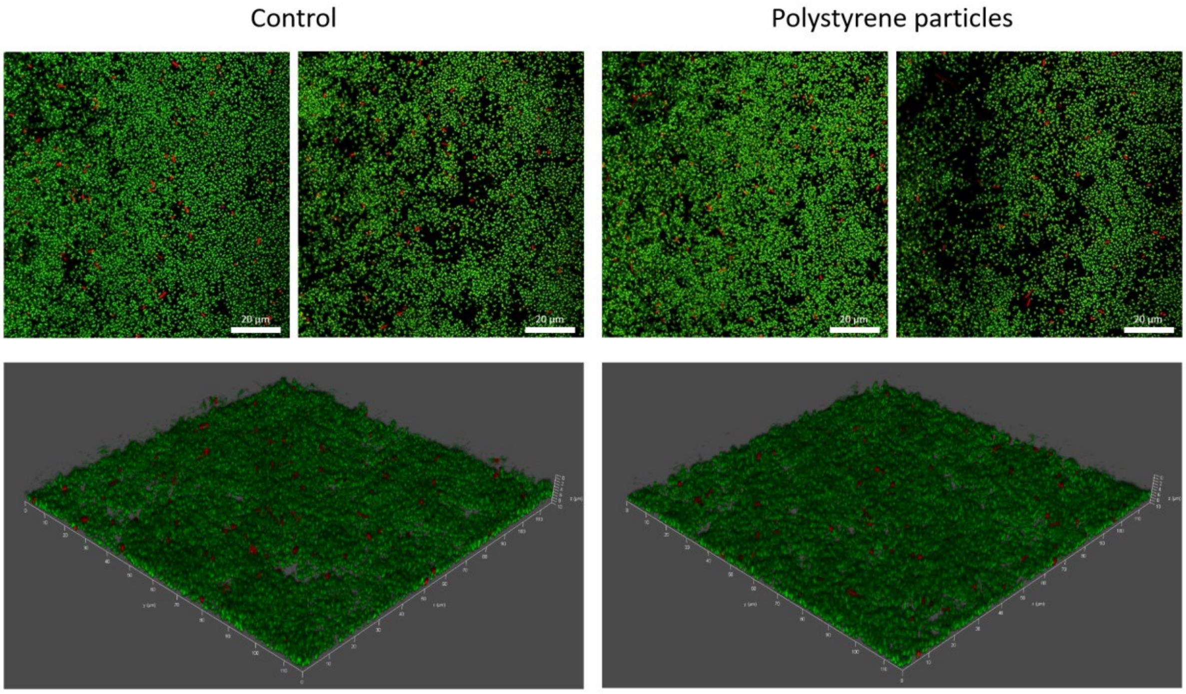

Supplementary Figure S4 CLSM image of a live/dead stained biofilm. The green SYTO9 stain represents living cells, the red propidium iodide stain represents dead cells. Left: biofilm grown without nanoparticles for 24 h. Right: biofilm incubated with 1 mg/ml polystyrene nanoparticles for 24 hours.

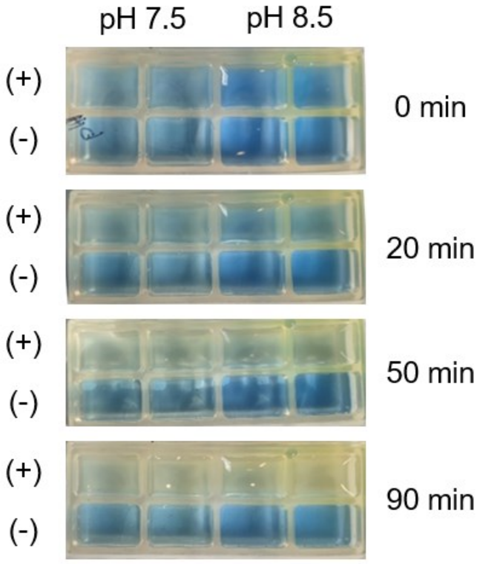

Supplementary Figure S5 Test for metabolic activity of *E. coli* biofilms in terms of acidification of growth media. Bromothymol blue was used as pH indicator solution. The upper row samples (+) were inoculated with glucose, the lower row samples (-) were control samples without glucose. The change of color from blue to yellow, indicates acidification of the samples containing glucose.

The localisation of the nanosensors in the biofilm was assessed by incubating PS particles stained with NR but without the pH-responsive dye FITC into the biofilm. This was followed by a live staining of the biofilm with Syto9. The reason for using these particles instead of the NR-stained and FITC-labeled pH nanosensor was to avoid spectral crosstalk of the fluorescence signals from FITC and the live stain Syto9.

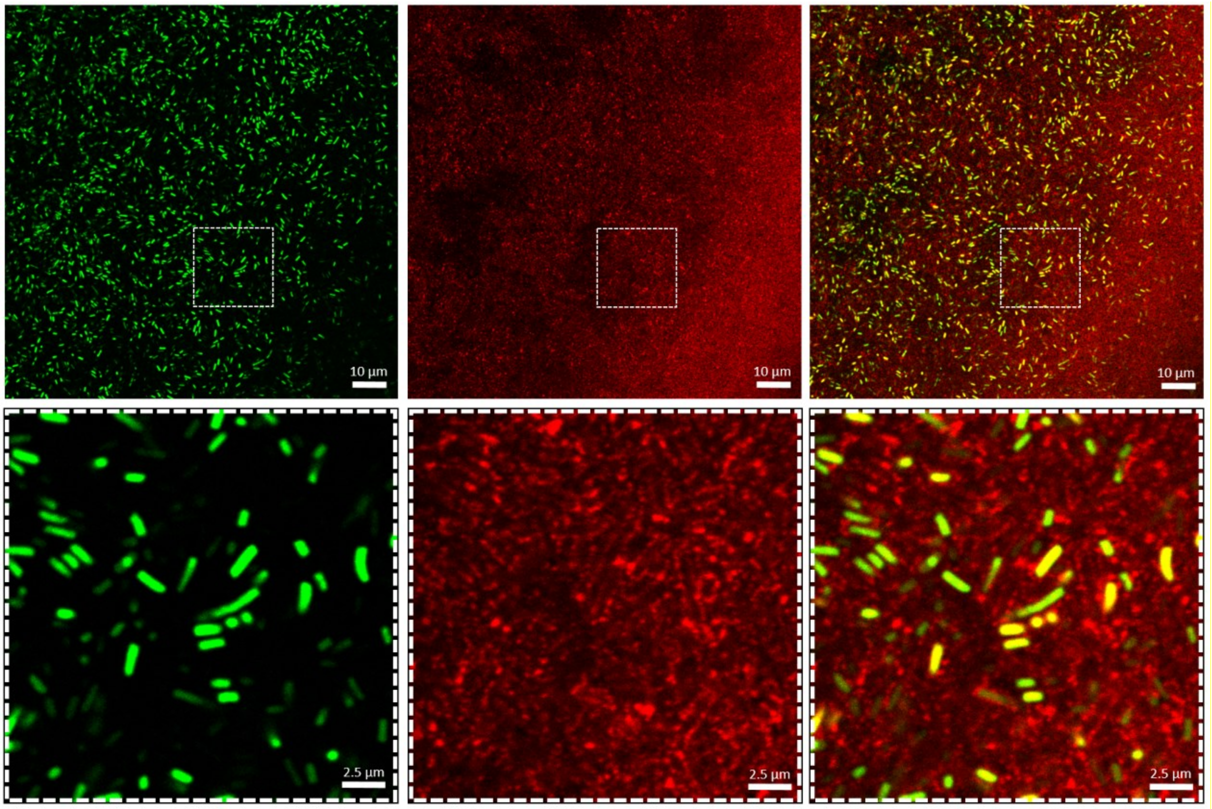

Supplementary Figure S6 CLSM images of the biofilm in fluorescence mode incubated with the NR-stained PS nanoparticles (red) for 24 h and subsequent live-staining of the cells with Syto9 (green). The NR fluorescence image (zoomed area, middle lower image) shows the highest fluorescence signals in extracellular regions, indicating that the nanoparticles are not taken up by the bacteria.

Annex II: Supplementary Material

Research Paper: A fluorescent nanosensor for ratiometric pH sensing at the cell surface

Charlotte Kromer, Aaron Katz, Ines Feldmann, Peter Laux, Andreas Luch, Harald R. Tschiche

Submitted on 3 March 2024 to:
Scientific Reports

Supporting Information for article:

A targeted fluorescent nanosensor for ratiometric pH sensing at the cell surface

Charlotte Kromer[1,2]*, Aaron Katz[1], Peter Laux[1], Andreas Luch[1,2], Harald R. Tschiche[1]

[1]Product Materials and Nanotechnology, Department Chemical and Product Safety, German Federal Institute for Risk Assessment, Berlin, Germany

[2]Institute of Pharmacy, Freie Universität Berlin, Berlin, Germany

* Correspondence:

Charlotte Kromer
Product Materials and Nanotechnology, Department Chemical and Product Safety, German Federal Institute for Risk Assessment, Max-Dohrn-Str. 8-10, 10589 Berlin, Germany
Charlotte.Kromer@bfr.bund.de

Table A1 Dye and protein loading of the pH_e nanosensor.

	Loading per mg PS [nmol]
NR	5.90 ± 0.58
FITC	0.848 ± 0.106
WGA	0.424 ± 0.053

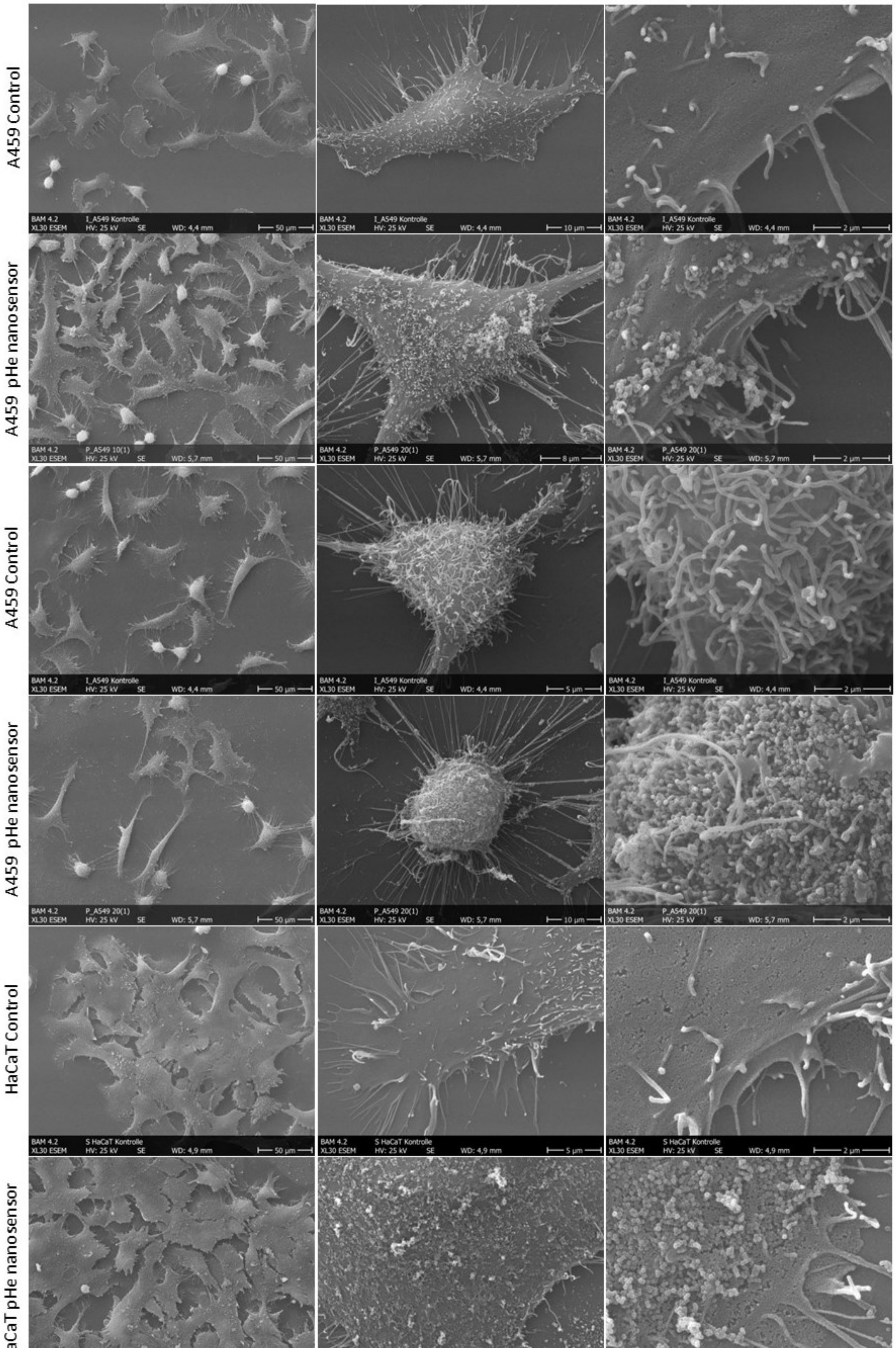

Figure A1 SEM images of A549 and HaCaT cells at different magnifications. Samples without (control) and with the pH_e nanosensor (0.825 mg/ml)

Annex III: Supplementary Material

Research Paper: ROS generating BODIPY loaded NPs for photodynamic eradication of biofilms

Charlotte Kromer, Karin Schwibbert, Sebastian Radunz, Dorothea Thiele, Peter Laux, Andreas Luch, and Harald R. Tschiche

Published online on 12 October 2023 in:
Frontiers in Microbiology 14:1274715

Link: https://doi.org/10.3389/fmicb.2023.1274715

Supplementary Material

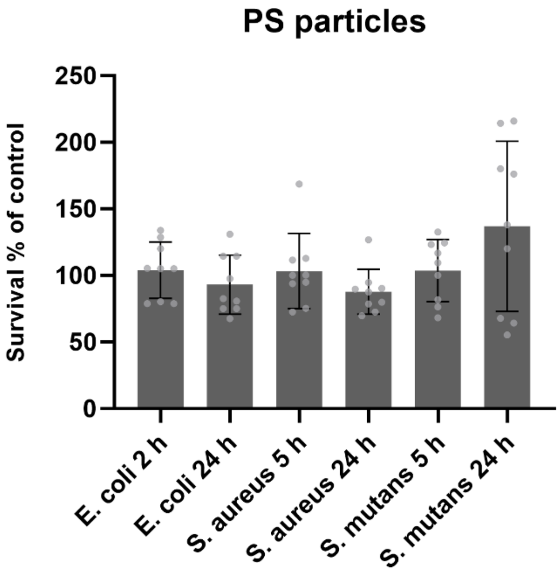

Supplementary Figure 1. Viability after incubation of PS NP without dye. Survival % of control of *E. coli*, *S. aureus* and *S. mutans* biofilms after various incubation times. All experiments were carried out as three independent replicates. None of the tested incubation times showed a significant toxic effect. Thus, within the testing conditions and experimental setup the PS NP are biocompatible and have no effect on the bacteria.

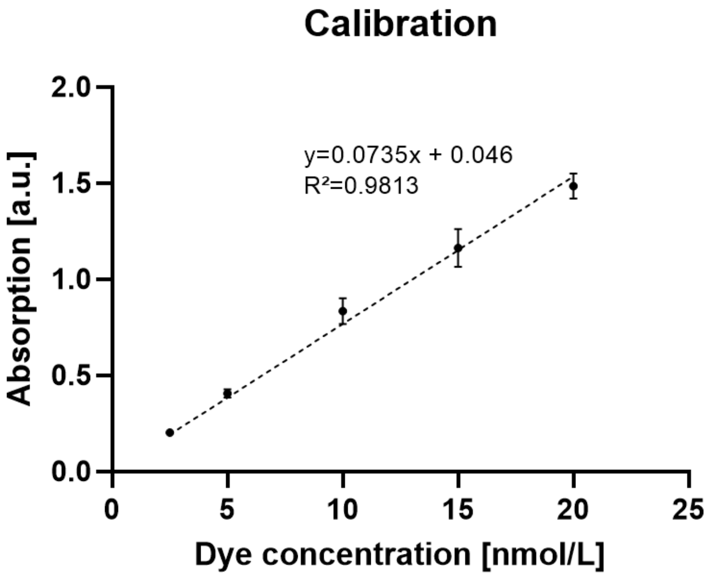

Supplementary Figure 2. Calibration curve for determination of BODIPY dye loading of the BODIPY-loaded NPs.

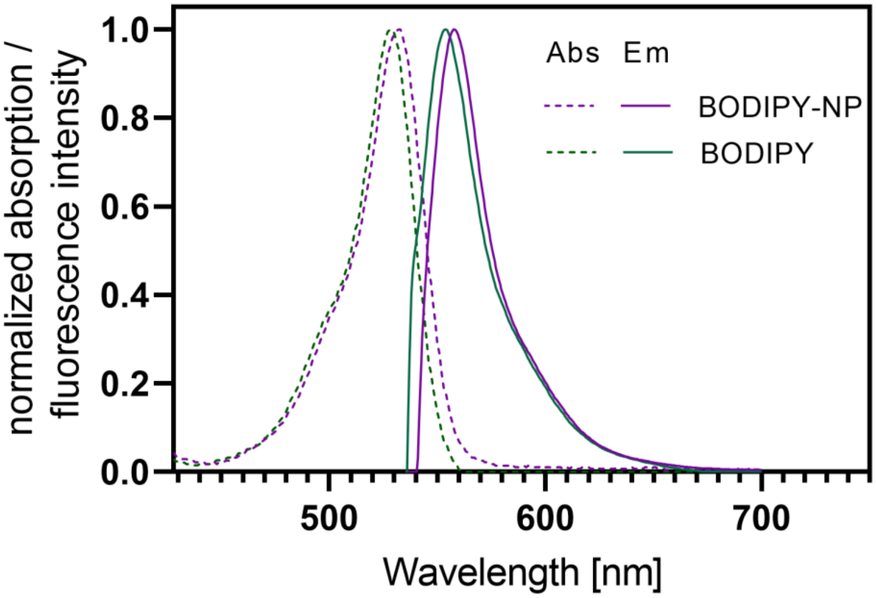

Supplementary Figure 3. Absorption and emission spectra of the free BODIPY dye and the BODIPY-loaded NPs in 50% ACN. Excitation for the Emission spectra was 530 nm.

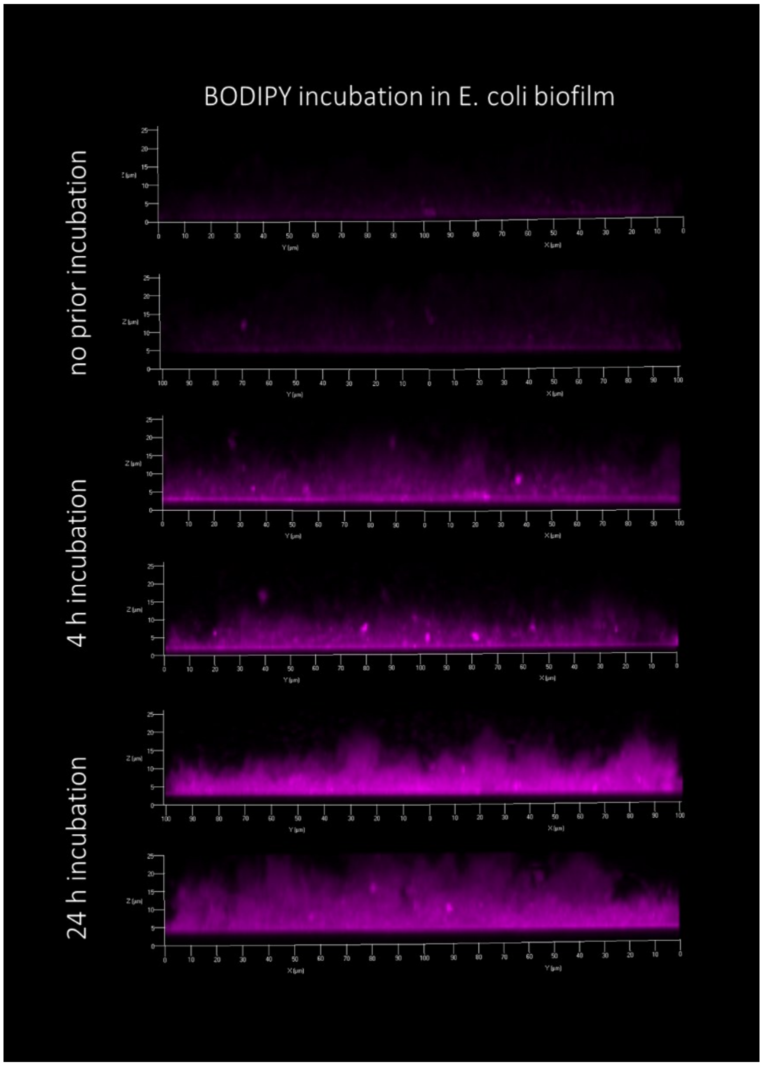

Supplementary Figure 4. CLSM images of the incubation time optimization for *E. coli* biofilms. BODIPY dye (magenta) was imaged in *E. coli* biofilms with no incubation, 4 hours incubation and 24 hours incubation. The goal was a sufficient penetration into the biofilm and accumulation in the biofilm.

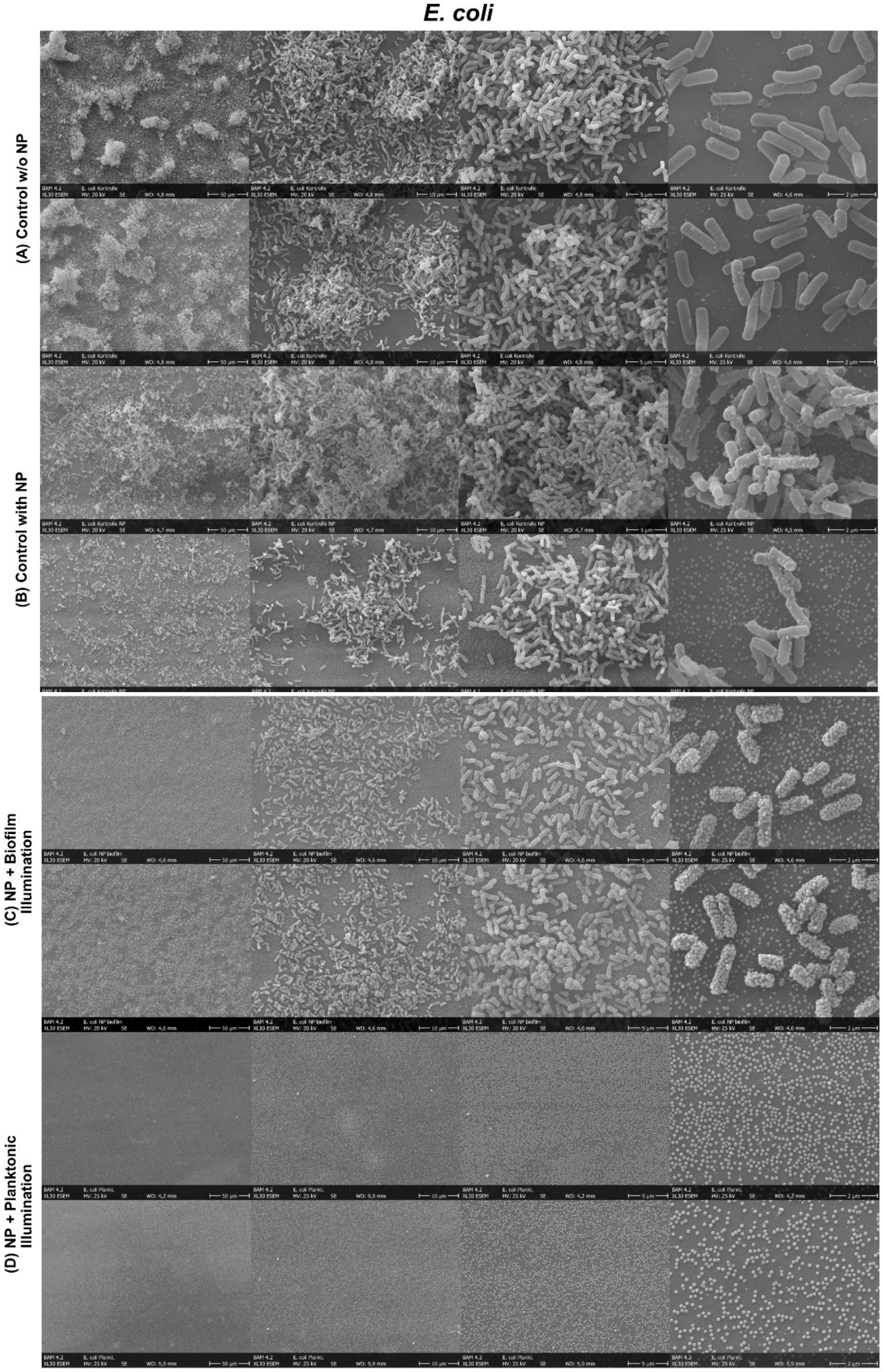

Supplementary Figure 5. SEM images of *E. coli* biofilms treated with aPDT. The four columns display increasing magnifications from left to right. a) Biofilm control without NP, b) biofilm control with NP and without illumination, c) biofilm with NP and illumination, d) biofilm grown for 24 hours after treatment of planktonic culture with NP and illumination.

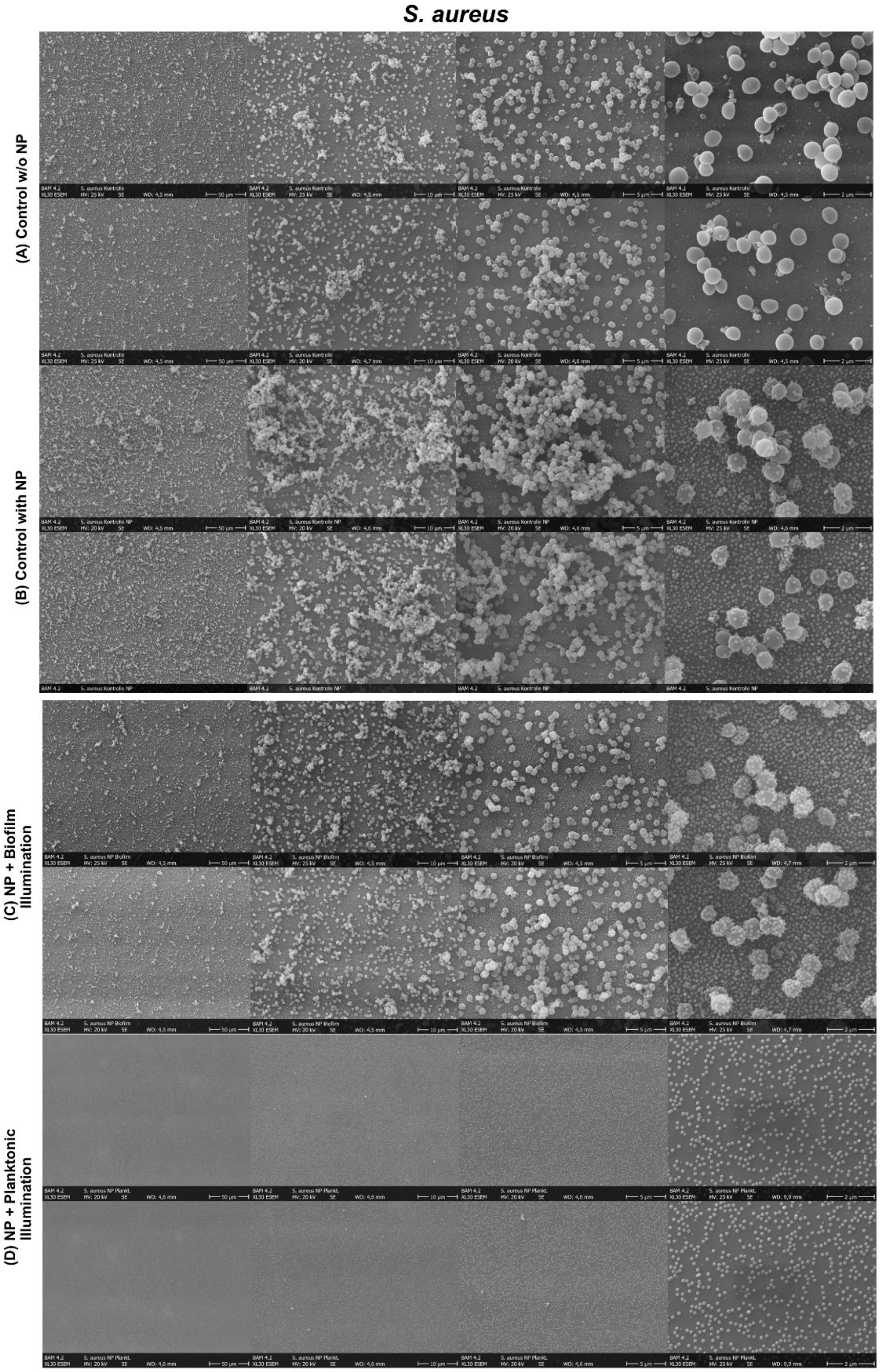

Supplementary Figure 6. SEM images of *S. aureus* biofilms treated with aPDT. The four columns display increasing magnifications from left to right. a) Biofilm control without NP, b) biofilm control with NP and without illumination, c) biofilm with NP and illumination, d) biofilm grown for 24 hours after treatment of planktonic culture with NP and illumination.

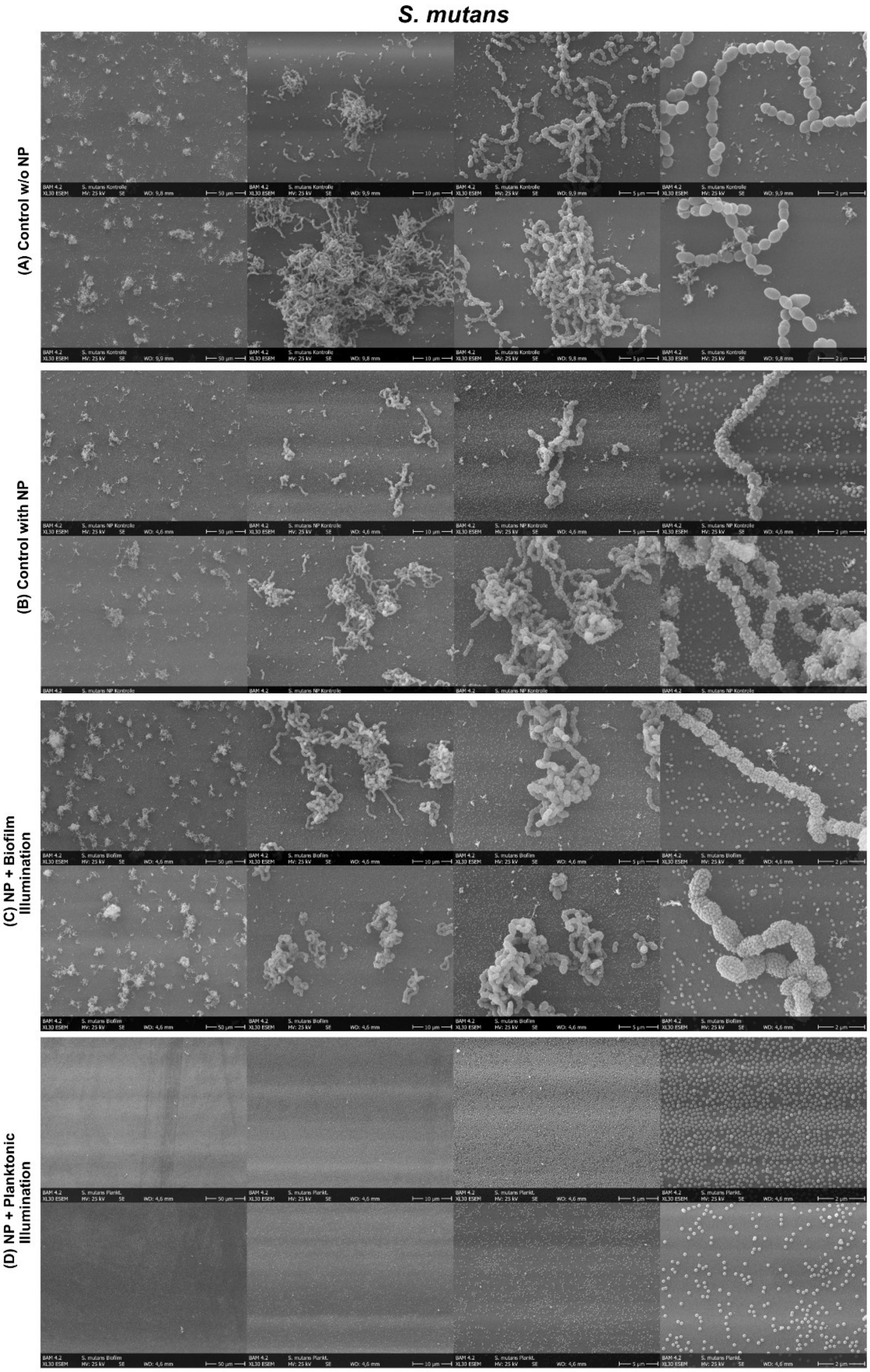

Supplementary Figure 7. SEM images of *S. mutans* biofilms treated with aPDT. The four columns display increasing magnifications from left to right. a) Biofilm control without NP, b) biofilm control with NP and without illumination, c) biofilm with NP and illumination, d) biofilm grown for 24 hours after treatment of planktonic culture with NP and illumination.